



Tropospheric corrections for Satellite Altimetry studies over coastal and inland water regions

Programa Doutoral em Engenharia Geográfica

Telmo André Pereira Vieira

Departamento de Geociências, Ambiente e Ordenamento do Território (DGAOT)
Faculdade de Ciências, Universidade do Porto (FCUP)

Supervisor

M. Joana Fernandes

Dissertation submitted to the University of Porto for the degree of Doctor of Philosophy in
Surveying Engineering

Porto, April 2021

Acknowledgements

To thank is to acknowledge the contribution and help of those who accompany us on the most diverse walks. And on this journey, I would like to thank many people.

Firstly, I am truly thankful to my supervisor Professor **Joana Fernandes** for all her guidance and support, and mainly for the opportunity to learn and discover the Earth Observation. I would also like to thank Professor **Clara Lázaro** for all discussions and scientific insight. In general, to the whole small **group of Satellite Altimetry at FCUP** for all scientific and non-scientific discussions and good moments throughout the last years, in particular **Eliana, Nelson** and **Pedro**.

I would also like to thank all my **friends** and **colleagues** who I had the opportunity to know throughout the last 10 years at FCUP.

A special word of gratitude to my cousin **Ana**, my uncles **Albertino** and **Emília** and their **family** for all their support in my academic life since 2010.

Lastly, I am deepest thankful to **Raquel, my sister, my parents, my godmother**, and my whole **family** for being the main spectators of the story that is my life and for being proud of me.

Thank you all.

Funding: During the first two years, this thesis was funded by FCUP, in the scope of projects supported by the European Space Agency. In the last two years, this thesis was funded by the Fundação para a Ciência e a Tecnologia (FCT) through the PhD grant SFRH/BD/135671/2018, funded by the European Social Fund and by Ministério da Ciência, Tecnologia e Ensino Superior (MCTES). The hosting R&D Centre of this PhD grant was the Centro Interdisciplinar de Investigação Marinha e Ambiental (CIIMAR).

Nowadays, satellite radar altimetry plays an essential role in the monitoring of the sea level rise, consequences of the climate changes that society presently faces. The determination, at a global scale, of the sea surface height (SSH), by means of this remote sensing technique, requires a set of corrections that impact directly this SSH estimation, as any error in the required fields can be wrongly interpreted as SSH variation. Among the required corrections of the altimeter observations, this thesis addresses the tropospheric corrections – dry tropospheric correction (DTC) and wet tropospheric correction (WTC), aiming at analysing and developing improved methodologies for their estimation, namely over coastal zones and inland waters, where their handling is still problematic.

The accurate determination of the DTC is quite simple, while the estimation of the WTC over these regions of interest is more challenging. The most accurate way to measure the WTC is from microwave radiometers (MWR) on board altimetry satellites. Since the algorithms to retrieve the WTC from these instruments are only tuned for open ocean observations, their retrievals deteriorate towards the non-oceanic surfaces and become invalid over coastal and continental waters.

Due to this limitation, alternative methods are required to estimate the WTC in these regions, e.g., by combining WTC measurements from external sources, which may be acquired at different altitudes. Thus, the combination of these observations requires an additional step: the conversion of the different WTC to the same reference altitude. Additionally, the WTC retrieval algorithms from MWR observations require regular updates and a specific tuning for each mission.

The general goal of this study is the development of enhanced methodologies to retrieve the DTC and WTC over coastal and continental water zones. In this context, the main objectives of this thesis are firstly the modelling of the WTC altitude dependence, to better combine the different WTC, and secondly the development of an improved WTC retrieval algorithm from MWR measurements with a focus on the Sentinel-3 mission.

Concerning the first objective, an improved modelling of the WTC vertical distribution was developed, considering exponential functions with decay coefficients dependent on geographic location and period of the year, by means of 3-D fields provided by an atmospheric model. Independent comparisons reveal that, with respect to the use of a single coefficient, the error reduction with the proposed modelling can be larger than 1 cm. Regarding the second objective, an improved WTC retrieval algorithm has been developed, better tuned for MWR on board Sentinel-3 satellites, showing a significant decrease in the WTC retrieval error, which can reach almost 1 cm over some regions. Both developments are a significant contribute to improve the accuracy of the WTC of altimetric satellites.

An additional set of studies have been conducted, aiming at the general goal of improving the tropospheric corrections for altimeter observations. These include the inspection of the tropospheric corrections of CryoSat-2 over inland waters, the comparison between Global Navigation Satellite Systems (GNSS) and MWR-derived WTC in coastal regions and the estimation of the WTC from the most recent atmospheric models. It has been shown that i) the accurate determination of the DTC is

straightforward, however some wrong procedures relative to its altitude dependence are still common, leading to significant systematic errors in current satellite products; ii) the comparison between GNSS and MWR shows the distance from coast (10-30 km) where MWR-derived WTC becomes invalid and iii) despite its improved temporal resolution (1h), the most recent atmospheric model (ERA5) is still not able to map WTC short space and time scales.

The overall contribution of this thesis is a better estimation of the sea surface height from satellite altimetry, both in open ocean and in coastal zones and inland waters, by means of proper methodologies and improved algorithms for the retrieval of tropospheric corrections, with direct impact on the SSH determination. Thus, improved water surface monitoring brings a better knowledge of the oceans and continental waters.

Atualmente, a altimetria radar por satélite desempenha um papel essencial na monitorização da subida do nível do mar, consequências das alterações climáticas que a sociedade enfrenta atualmente. A determinação global da altitude da superfície do mar (*sea surface height*, SSH), por meio desta técnica de deteção remota, requer um conjunto de correções que afetam diretamente esta estimação da SSH (qualquer erro nos campos necessários pode ser erradamente interpretado como uma variação da SSH). Entre as correções das observações altimétricas necessárias, esta tese aborda as correções troposféricas – a correção devida à componente seca (*dry tropospheric correction*, DTC) e a correção devida à componente húmida da troposfera (*wet tropospheric correction*, WTC), com o objetivo de analisar e desenvolver metodologias melhoradas para as suas estimativas, nomeadamente sobre zonas costeiras e águas interiores, onde os procedimentos ainda são problemáticos.

A determinação da DTC com grande exatidão é bastante simples, enquanto a determinação da WTC sobre estas regiões de interesse é mais desafiante. A forma mais precisa de medir a WTC é a partir de radiómetros de micro-ondas (*microwave radiometer*, MWR) a bordo dos satélites altimétricos. Uma vez que os algoritmos para determinar a WTC a partir destes instrumentos apenas são ajustados para observações sobre oceano aberto, as correspondentes correções deterioram-se em direção às superfícies não oceânicas e tornam-se inválidos sobre águas costeiras e continentais.

Devido a esta limitação, métodos alternativos são necessários para determinar a WTC nestas regiões, por exemplo, combinando medições de WTC de fontes externas, que podem ser adquiridas a diferentes altitudes. Assim, a combinação destas observações requer uma etapa adicional: a conversão das diferentes WTC para a mesma altitude de referência. Além disso, os algoritmos de determinação da WTC a partir das observações dos MWR requerem atualizações regulares e um ajuste específico para cada missão.

O objetivo geral deste estudo é o desenvolvimento de metodologias melhoradas para determinar a DTC e a WTC sobre zonas de águas costeiras e continentais. Neste contexto, os objetivos principais desta tese são, em primeiro lugar, a modelação da dependência da WTC com a altitude, para melhor combinar as diferentes WTC e, em segundo lugar, o desenvolvimento de um algoritmo melhorado para a determinação da WTC a partir de medidas de MWR, com foco na missão Sentinel-3.

Relativamente ao primeiro objetivo, foi desenvolvida uma modelação melhorada da distribuição vertical da WTC, considerando funções exponenciais com coeficientes de decaimento dependentes da localização geográfica e do período do ano, utilizando campos 3-D fornecidos por um modelo atmosférico. Comparações independentes revelam que, em relação ao uso de um único coeficiente, a redução do erro com a modelação proposta pode ser superior a 1 cm. Em relação ao segundo objetivo, foi desenvolvido um algoritmo melhorado para a determinação da WTC, ajustado para o MWR a bordo dos satélites da missão Sentinel-3, mostrando uma diminuição significativa no erro da WTC, que pode chegar a quase 1 cm em algumas regiões. Ambos os desenvolvimentos são uma contribuição significativa para melhorar a precisão da WTC dos satélites altimétricos.

Um conjunto adicional de estudos foi realizado, tendo como objetivo geral melhorar as correções troposféricas para as observações altimétricas. Estes incluem a análise das correções troposféricas do CryoSat-2 em águas interiores, a comparação entre a WTC obtida com Sistemas Globais de Navegação por Satélite (*Global Navigation Satellite Systems, GNSS*) e a derivada do MWR em regiões costeiras e o cálculo da WTC a partir dos modelos atmosféricos mais recentes. Foi demonstrado que i) a determinação precisa da DTC é simples, no entanto alguns procedimentos errados relativos à sua dependência com a altitude ainda são comuns, levando a erros sistemáticos significativos nos produtos de satélite atuais; ii) a comparação entre GNSS e MWR mostra a distância à costa (10-30 km) onde a WTC obtida com MWR se torna inválida e iii) apesar da sua resolução temporal melhorada (1h), o modelo atmosférico mais recente (ERA5) ainda não é capaz de mapear as pequenas escalas espaciais e temporais da WTC.

A contribuição geral desta tese é uma melhor determinação da altitude da superfície oceânica a partir de altimetria por satélite, tanto em oceano aberto como em zonas costeiras e águas interiores, por meio de metodologias adequadas e algoritmos melhorados para a determinação das correções troposféricas, com impacto direto na determinação da SSH. Assim, uma melhor monitorização da superfície da água traz um melhor conhecimento dos oceanos e das águas continentais.

Keywords

Brightness Temperature
Coastal zones
CryoSat-2
Dry Tropospheric Correction
ECMWF
ERA5
Global Navigation Satellite Systems
Inland waters
Microwave Radiometer
Modelling
Neural Network
Numerical Weather Model
Remote Sensing
Retrieval Algorithm
Satellite Radar Altimetry
Sentinel-3
Surveying Engineering
Tropospheric corrections
Water surface level determination
Wet Path Delay
Wet Tropospheric Correction
Zenith Tropospheric Delay

Contents

Acknowledgements.....	iii
Abstract.....	v
Resumo.....	vii
Keywords.....	ix
List of Figures.....	xv
List of Tables	xxi
List of Acronyms.....	xxiii
1. Introduction.....	1
1.1. Satellite Radar Altimetry	1
1.1.1. Dry Tropospheric Correction (DTC).....	4
1.1.2. Wet Tropospheric Correction (WTC).....	6
1.2. Objectives.....	9
1.3. Thesis Outline	9
1.3.1. Articles 1-3.....	10
1.3.2. Article 4.....	12
1.3.3. Article 5.....	13
2. Tropospheric Corrections of Satellite Altimetry observations over inland waters and coastal zones.....	15
2.1. Analysis and retrieval of tropospheric corrections for CryoSat-2 over inland waters (Article 1)	15
2.1.1. Introduction.....	16
2.1.2. Data and Methods	19
2.1.3. Assessment of tropospheric corrections present on CS-2 products	24
2.1.4. Conclusions	40
2.2. Independent Assessment of On-Board Microwave Radiometer Measurements in Coastal Zones Using Tropospheric Delays from GNSS (Article 2)	42
2.2.1. Introduction.....	42
2.2.2. Data set description.....	44
2.2.3. WTC derived from ZTD UPorto.....	48
2.2.4. Assessment of MWR-derived WTC.....	53

2.2.5.	Conclusion	64
2.3.	Impact of the New ERA5 Reanalysis in the Computation of Radar Altimeter Wet Path Delays (Article 3)	65
2.3.1.	Introduction.....	66
2.3.2.	WPD computation from NWM parameters.....	67
2.3.3.	Inter-comparisons of NWM-derived WPD.....	70
2.3.4.	Independent comparison between MWR and ERA5-derived WPD.....	76
2.3.5.	Conclusion.....	80
3.	Modelling the Altitude Dependence of the Wet Path Delay for Coastal Altimetry Using 3-D Fields from ERA5 (Article 4).....	83
3.1.	Introduction.....	83
3.2.	Data and Methods	86
3.2.1.	Data Sources for WPD Estimation.....	86
3.2.2.	Modelling the Altitude Dependence of the WPD	93
3.3.	Results and Discussion	95
3.3.1.	Comparison between WPD Computed Using Different ERA5 Data	95
3.3.2.	Modelling.....	96
3.3.3.	Assessment with ERA5 Data.....	99
3.3.4.	Validation with RS and GNSS.....	101
3.4.	Conclusions	103
4.	An enhanced Neural Network-based retrieval of the Wet Tropospheric Correction for Sentinel-3 (Article 5)	105
4.1.	Introduction.....	105
4.2.	MWR-derived WTC retrieval algorithms	109
4.2.1.	From MWR measurements to WTC.....	110
4.2.2.	Algorithms used in the reference missions.....	111
4.2.3.	Sentinel-3 Algorithm	111
4.3.	A new Sentinel-3 WTC retrieval algorithm	113
4.3.1.	Learning Database	113
4.3.2.	Learning of different Algorithms	121
4.4.	Evaluation of the different Sentinel-3 Wet Tropospheric Corrections.....	122
4.4.1.	Comparison with Scanning Imaging MWR.....	122

4.5. Conclusion.....	128
5. Conclusions.....	131
References.....	133

List of Figures

Figure 1. Satellite altimetry principle (image from AVISO)..... 2

Figure 2. Global mean sea level (GMSL) time series based on satellite altimetry data (Cazenave et al., 2018)..... 3

Figure 3. DTC in m (top left), altitude in m (bottom left) and planimetric view (right) of the S3A pass 13, cycle 10. Background colour of the right panel represents the surface pressure in hPa provided by ERA5..... 5

Figure 4. Mean (top panel) and standard deviation (bottom panel) of the WTC computed at surface level from an atmospheric model, considering 1 year of data. 6

Figure 5. Processing chain of the WTC retrieval from MWR measurements. 8

Article 1

Figure 1. Representation of the spatial coverage over Lake Titicaca of the various altimetric missions: 10-day repeat reference missions (yellow), 35-day ERS-1, ERS-2, ENVISAT and SARAL (black), Sentinel-3 (red) and CS-2 (blue). Light blue polygon represents Lake Titicaca. 18

Figure 2. Altitudes in meters above geoid of the ACE2 DEM 5' (left panel) and of the ECMWF model orography (right panel), over the Amazon basin. Black points represent the mean river profile and white points represent pass 20 of CS-2 sub-cycle 62. 26

Figure 3. Altitudes in meters above geoid of the ACE2 DEM 5' (top panel) and of the ECMWF model orography (bottom panel), over the Danube river. Black points represent the mean river profile and pink points represent the pass 188 of CS-2 sub-cycle 62..... 26

Figure 4. Altitudes in meters above geoid of the ACE2 DEM 5' (left panel) and of the ECMWF model orography (right panel), over Lake Titicaca. Black line represents the lake border. 27

Figure 5. Altitudes in meters above geoid of the ACE2 DEM 5' (top panel) and of the ECMWF model orography (bottom panel), over the Vanern lake. Black line represents the lake border. 27

Figure 6. Altitudes in meters above geoid of the ACE2 DEM 5' (left panel) and of the ECMWF model orography (right panel), over the Caspian Sea. Black line represents the sea border and pink and white points represent passes 489 of CS-2 sub-cycles 51 and 52, respectively. Note that on the right panel Gibbs effects mentioned above can be observed on the ECMWF orography inside the Caspian Sea. 28

Figure 7. Various altitudes (hdem – blue, hprofile and hmean – red, horo – green) above geoid, in meters, along the Amazon river profile (left) and along CS-2 sub-cycle 51, pass 489 over the Caspian Sea (right). In the right panel, larger altitude values exist close to the sea border: -24 m for hdem and 61 m for horo. 28

Figure 8. Various DTC (bottom left panel) and height surfaces (top left panel) for CS-2 sub-cycle 62, pass 188 (see also Fig. 3), over the Danube river. Various DTC in meters for CS-2 sub-cycle 51, pass 489 (see also Fig. 6), over the Caspian Sea (right panel). 31

Figure 9. Daily (blue points) and monthly (red points) means of the DTC computed at mean sea level over the Caspian Sea, spanning the year 2014..... 36

Figure 10. Various WTC for CS-2 sub-cycle 62, pass 20, over the Amazon river (left panel) function of distance to river profile and for CS-2 sub-cycle 52, pass 489, over the Caspian Sea (right panel), function of latitude. To represent both sides of the river, negative distances have been considered in one side of the Amazon. 37

Figure 11. Daily (blue points) and monthly (red points) means of the WTC computed at mean sea level over the Caspian Sea, spanning the year 2014. 40

Article 2

Figure 1. Spatial representation of the three subnetworks (UPorto-1—red triangles, UPorto-2—blue points, and UPorto-3—green squares). 49

Figure 2. ZTD differences for the ALBH station between ZTD computed in different subnetworks. (Top) UPorto1–UPorto2. (Middle) UPorto2–UPorto3. (Bottom) UPorto1–UPorto3. 50

Figure 3. Number of observations and stations per day since beginning of 1995 to end of 2016 for the UPorto-3 subnetwork. (Left axis) (blue) Number of observations per day. (Right axis) (red) Number of stations per day. 50

Figure 4. ZTD differences between UPorto and (Top) IGS and (bottom) EPN, in millimetres, for station MAS1, Gran Canaria, Spain. 52

Figure 5. Selected altimetry measurements around the Iberian Peninsula for (Top) EN cycle 73 and (Bottom) J2 cycle 10. 54

Figure 6. (Left axis) RMS (cm) of the WTC differences and (Right axis) number of altimetry measurements used for the ERS-1 mission. 56

Figure 7. (Left axis) RMS (cm) of the WTC differences and (Right axis) number of altimetry measurements used for the ERS-2 mission. 56

Figure 8. (Left axis) RMS (cm) of the WTC differences and (Right axis) number of altimetry measurements used for the EN mission. 56

Figure 9. (Left axis) RMS (cm) of the WTC differences and (Right axis) number of altimetry measurements used for the SA mission. 57

Figure 10. (Left axis) RMS (cm) of the WTC differences and (Right axis) number of altimetry measurements used for the TOPEX/Poseidon mission. 58

Figure 11. (Left axis) RMS (cm) of the WTC differences and (Right axis) number of altimetry measurements used for the Jason-1 mission. 58

Figure 12. (Left axis) RMS (cm) of the WTC differences and (Right axis) number of altimetry measurements used for the Jason-2 mission. 58

Figure 13. (Left axis) RMS (cm) of the WTC differences and (Right axis) number of altimetry measurements used for the GFO mission. Blue points represent the RMS of the differences between GNSS and GPD+ for the C2 mission. 59

Figure 14. Time evolution (averages) of the WTC differences (Top) between GNSS and MWR and (Bottom) between GNSS and GPD+ for ERS-2, EN, C2, and SA missions. 61

Figure 15. Time evolution (averages) of the WTC differences (Top) between GNSS and MWR and (Bottom) between GNSS and GPD+ for the reference missions and GFO. 62

Article 3

Figure 1. WPD mean (cm) computed from ERA5 single-level parameters, at the corresponding orography height, for the period 2010–2014 at 3°×3° spatial sampling. 68

Figure 2. WPD mean differences (mm) between 2-D and 3-D approaches at orography height for the year 2010. 69

Figure 3. RMS (cm) of WPD differences function of latitude for classes of 3° (top) and function of time computed for weighted daily and global differences (bottom). WPD differences are between the reference values and those interpolated using different temporal resolutions, both from ERA5. 71

Figure 4. RMS (cm) of the WPD differences when WPD is interpolated from ERA5 grids 6-h apart. 72

Figure 5. RMS (cm) of WPD differences function of latitude for classes of 3° (left) and function of time computed for each day (right). WPD differences are between the reference values and those interpolated using different spatial resolutions, both from ERA5. 74

Figure 6. RMS (cm) of the WPD differences when WPD is interpolated from ERA5 at 1.2° × 1.2° spatial sampling. 74

Figure 7. RMS (cm) of (Top) WPD differences function of latitude for classes of 3° and (Bottom) function of time computed for each day. WPD differences are between the reference values and those interpolated using different spatial resolutions, both from ECMWF operational model. 75

Figure 8. RMS (cm) of the WPD differences between (Left) MWR onboard EnviSat and (Right) Jason-2 and ERA5 at different temporal resolutions (1- and 6-h intervals), maintaining the same spatial resolution (0.3° × 0.3°). 77

Figure 9. Example of the WPD (cm) from ENVISAT MWR (black) and interpolated from ERA5 at 0.3° × 0.3° and 1-h (green) and 0.3° × 0.3° and 6-h (orange), showing only the effect of the temporal resolution. 78

Figure 10. RMS (cm) of the WPD differences between (Left) MWR onboard ENVISAT and (Right) Jason-2 and ERA5 at different spatial resolutions (0.3° × 0.3° and 0.6° × 0.6°), maintaining the same temporal resolution (6-h intervals). 78

Figure 11. Example of the WPD (cm) from ENVISAT MWR (black) and interpolated from ERA5 at 0.3° × 0.3° and 6 h (orange) and 0.6° × 0.6° and 6 h (blue), showing only the effect of the spatial resolution. 79

Article 4

Figure 1. Atmospheric variables provided by ERA5 on 1 January 2010, at 00:00 UTC on model levels (blue) and on pressure levels (orange): (a) temperature (T) in Kelvin and (b) specific humidity (q) in kg/kg at location 00°, 120°E. 88

Figure 2. Wet path delay (WPD) vertical profiles at (a) 10°N, 90°W; (b) 00°, 100°E; (c) 25°S, 65°E. Grey profiles represent those every 3h over the year 2010, solid line represents the annual mean profile, squares with dashed line and circles with dotted line represent the mean profiles for January and July, respectively. 90

Figure 3. Spatial representation of the radiosondes (RS) network from Integrated Global Radiosonde Data (IGRA). Blue points represent all RS since 1905, green squares represent the RS with valid

measurements of temperature and humidity over the year 2014, and red triangles represent those selected for the validation. 92

Figure 4. Time evolution of the α coefficients at locations: (a) 10°N, 90°W; (b) 00°, 100°E; (c) 25°S, 65°E. Grey points represent the α coefficients every 3h, orange line represents the overall mean (UP-01) and purple squares and green points represent the seasonally averaged (UP-04) and monthly averaged coefficients (UP-12), respectively. 97

Figure 5. Spatial representation of the α coefficient, computed as the mean for each point (UP-01) in a 5°x5° grid. 98

Figure 6. Root Mean Square (RMS) (cm) of the WPD differences between 3-D (WPD retrieved from the original ERA5 PL fields) and 2-D with Kouba reduction, using profiles every 3h in a 5°x5° grid over the year 2014. 99

Figure 7. RMS (cm) of the WPD differences between 3-D and 2-D with UP-01 reduction, using profiles every 3h in a 5°x5° grid over the year 2014. 100

Figure 8. RMS (cm) of the differences between WPD computed with 3-D approach and that computed at surface level and then reduced with UP-04 (left) and UP-12 (right) coefficients. 101

Figure 9. RMS (cm) of the differences between WPD computed with 3-D approach using atmospheric variables from IGRA and those computed at lowest level and then reduced with Kouba (blue bars), UP-01 (orange bars), UP-04 (purple bars), and UP-12 (green bars) coefficients. 101

Figure 10. RMS (cm) of the differences at Global Navigation Satellite Systems (GNSS) station height between WPD derived from GNSS and those computed at ERA5 orography level using single level atmospheric variables and then reduced with Kouba (blue bars), UP-01 (orange bars), UP-04 (purple bars), and UP-12 (green bars) coefficients to the height of each GNSS station (identified by its four characters). 102

Article 5

Figure 1. WPD computed from ERA5 versus S3A valid measurements stored in the learning database. 115

Figure 2. WPD computed from ERA5 versus additional inputs computed/interpolated from ERA5 stored in the learning database. 115

Figure 3. Spatial representation of mean values of TB23.8 (top panel), TB36.5 (middle panel) and σ_0 (bottom panel) from Sentinel-3A measurements considering the 104030 points over the year 2017 in the learning dataset. Brightness temperatures are in K, while σ_0 is in dB. 116

Figure 4. Annual mean of WTC in cm computed from vertical integration of temperature and humidity profiles from ERA5 on pressure levels, at 6h intervals and 0.5°x0.5° spatial sampling over the year 2017. 117

Figure 5. Mean (top panel) and standard deviation (bottom panel) for the year 2017 of SST in K from ERA5 at single level, every 6h, at 0.5°x0.5° spatial sampling. 118

Figure 6. Mean (top panel) and standard deviation (bottom panel) for year 2017 of γ_{800} in K/km computed using temperature from ERA5 at pressure levels, every 6h, at 0.5°x0.5° spatial sampling. 119

Figure 7. Mean for the year 2017 of u10 in m/s from ERA5 at single level, every 6h, at 0.5°x0.5° spatial sampling..... 120

Figure 8. Mean for the year 2017 of v10 in m/s from ERA5 at single level, every 6h, at 0.5°x0.5° spatial sampling..... 120

Figure 9. Global RMS of the WTC differences between SIMWR and the various S3 MWR retrievals. 123

Figure 10. Differences (in cm) between RMS of WPD differences for 3I-UP3S0 (top panel), 3I-UP3WS (middle panel) and UP3S0-UP3WS (bottom panel)..... 124

Figure 11. Differences (in cm) between RMS values for 5I-UP5S0 (top panel), 5I-UP5WS (middle panel) and UP5S0-UP5WS (bottom panel)..... 125

Figure 12. Differences (in cm) between RMS values for UP3S0-UP4S0 (top panel) and UP4S0-UP5S0 (bottom panel). 125

Figure 13. RMS of the WTC differences between SIMWR and the various MWR retrievals, considering only S3A along-track points with distances from coast in the range 30-250 km. 126

Figure 14. RMS of the WTC differences between SIMWR and 3I (green), 5I (orange) and UP4S0 (blue) function of distance from coast..... 127

List of Tables

Article 1

Table 1. Statistical parameters (minimum (min), maximum (max) and mean values and standard deviation (std)) of the altitude differences, considering only CS-2 points inside the Caspian Sea. ...	29
Table 2. Statistical parameters of the altitude differences along the Danube River mean profile.	30
Table 3. Statistical parameters of the DTC differences considering CS-2 measurements up to 20 km from the Amazon mean river profile.	32
Table 4. Statistical parameters of the DTC differences considering only CS-2 measurements inside the Caspian Sea.	33
Table 5. Root Mean Square (RMS) of the differences between DTC computed from SLP (ECMWF) reduced to surface elevation and DTC computed from pressure data from ISPD, in centimetres. ...	34
Table 6. Mean (in meters) and standard deviation (in centimetres) of the DTC computed at the level of mean river or mean lake (DTC profile or DTC mean) and maximum absolute error present in the DTC provided in CS-2 products, due to height dependence. The third column represents the maximum absolute difference between DTC alt and DTC mean or DTC profile.	35
Table 7. Statistical parameters of the WTC differences considering CS-2 measurements up to 2 km from the Danube river profile.	37
Table 8. Statistical parameters of the WTC differences considering only CS-2 measurements inside the Caspian Sea.	37
Table 9. Statistical parameters of the differences between ECMWF and GNSS-derived WTC, in centimetres.	39
Table 10. Mean (in meters) and standard deviation (std, in centimetres) of the WTC computed at the level of mean river or mean lake (WTC profile or WTC mean) and maximum absolute error present in the WTC provided in CS-2 products, due to height dependence. The third column represents the maximum absolute difference between WTC alt and WTC mean or WTC profile.	39

Article 2

Table 1. RMS (mm) of the ZTD differences for the common stations used in different subnetworks (UPorto-1, UPorto-2, and UPorto-3)	51
Table 2. Linear fitting values and time span for the 385-day averages of the GNSS–MWR differences for ESA missions and SA	61
Table 3. Linear fitting values and time span for the 385-day averages of the GNSS–GPD differences for ESA missions, C2, and SA	61
Table 4. Linear fitting values and time span for the 370-day averages of the GNSS–MWR differences for the reference missions and GFO	63
Table 5. Linear fitting values and time span for the 370-day averages of the GNSS–GPD differences for the reference missions and GFO	63

Article 3

Table 1. Temporal resolutions used to compute various WPDs from ERA5 model..... 71

Table 2. Spatial resolutions used to compute various WPDs from era5 and ECMWF operational models 73

List of Acronyms

ACE2	Altimeter Corrected Elevations 2
APC	Antenna Pattern Correction
ATK	Along-Track
ATSR	Along Track Scanning Radiometer
AVISO	Archiving, Validation and Interpretation of Satellite Oceanographic data
C3S	Copernicus Climate Change Service
CDS	Climate Data Store
CLS	Collecte Localisation Satellites
DEM	Digital Elevation Model
DTC	Dry Tropospheric Correction
ECMWF	European Centre for Medium-Range Weather Forecasts
EIGEN	European Improved Gravity model of the Earth by New techniques
EPN	EUREF Permanent Network
ERA5	ECMWF ReAnalysis 5
ERS	European Remote Sensing
ESA	European Space Agency
EUMETSAT	European Organisation for the Exploitation of Meteorological Satellites
GFO	GeoSat Follow-On
GMI	GPM Microwave Imager
GMSL	global mean sea level
GNSS	Global Navigation Satellite Systems
GPD	GNSS-derived Path Delay
GPM	Global Precipitation Measurement
GPT	Global Pressure and Temperature
IC	Ionospheric Correction
IGRA	Integrated Global Radiosonde Data
IGS	International GNSS Service
IPCC	Intergovernmental Panel on Climate Change
ISPD	International Surface Pressure Databank
ML	Model Levels
MPA	Mixed Pixel Algorithm
MWR	Microwave Radiometer
NN	Neural Network
NWM	Numerical Wether Model
PL	Pressure Level
RADS	Radar Altimeter Database System
RH	Relative Humidity
RMS	Root Mean Square
RMSE	Root Mean Square Error
ROI	Region of Interest
RS	Radiosonde

RTM	Radiative Transfer Model
S3A	Sentinel-3A
S3B	Sentinel-3B
SAR	Synthetic Aperture Radar
SARAL	Satellite with ARgos and ALtiKa
SHAPE	Sentinel-3 Hydrologic Altimetry Processor prototype
SIMWR	Scanning Imaging MWR
SIRAL	Synthetic Aperture Radar Interferometry Radar ALtimeter
SL	Single Level
SLP	Sea Level Pressure
SRAL	Synthetic Aperture Radar ALtimeter
SSH	Sea Surface Height
SSM/I	Special Sensor Microwave Imager
SST	Sea Surface Temperature
STD	Slant Total Delay
STM	Surface Topography Mission
SWH	Significant Wave Height
TB	Brightness Temperature
TCWV	Total Column Water Vapour
TOA	Top of Atmosphere
UN	United Nations
UTC	Universal Time Coordinated
VMF1	Vienna Mapping Functions 1
WMO	World Meteorological Organization
WPD	Wet Path Delay
WS	Wind Speed
WTC	Wet Tropospheric Correction
ZHD	Zenith Hydrostatic Delay
ZTD	Zenith Total Delay
ZWD	Zenith Wet Delay

1. Introduction

Nowadays, climate change is one of the most pressing issues for the society. The global climate system is complex and the Earth's dynamic processes, at a variety of scales, are fundamental in ensuring suitable conditions for the humankind. However, whether by natural fluctuations of the climate system or human activity, the Earth is changing. The extent and speed of climate changes, and consequently, the need for urgent climate action, plays a serious and imperative challenge for the human security.

To address the current climate crisis, several international organizations have been attentive to various climate change indicators. The World Meteorological Organization (WMO) report on the State of the Global Climate uses key indicators to describe the climate change, such as the temperature, the ocean heat, the sea level, the glacial mass, and the sea ice (WMO, 2020). On the other hand, to address the global challenges that humanity presently faces, including those related to climate and environmental degradation, United Nations (UN) defined clean water, climate action and life below water as some of the Sustainable Development Goals (UN, 2020).

Concerning the climate change and the environmental degradation, the global warming and the consequent global sea level rise are clear indicators of the alarming changes in the Earth (IPCC, 2019). Currently, satellite radar altimetry is a powerful space technique, which allows a wide range of applications, with particular and first interest in the global sea level measurement and monitoring (Chelton et al., 2001; Escudier et al., 2017). Over the last 28 years, different altimeter missions combined with each other have been the human's eyes on the oceans, guaranteeing a continuous and permanent monitoring. Thus, this technique can give crucial information, at global scale, about several climate indicators mentioned above (Hamlington et al., 2020), required by the scientists and dedicated international institutions.

1.1. Satellite Radar Altimetry

Satellite radar altimetry is a remote sensing technique, originally designed to map the ocean surface topography (Chelton et al., 2001). Consequently, several important geophysical phenomena impacting the ocean surface topography can also be observed by means of this Earth observation technique, providing essential information on Earth and ocean dynamics (Oziel et al., 2020).

Each space altimeter mission is composed of various instruments, which measurements, together with auxiliary data, modelling and several methodologies in a combined measurement system allow the determination of sea surface heights (SSH). While the principle of this determination is quite straightforward (Chelton et al., 2001; Escudier et al., 2017), measuring the SSH with an accuracy of a few centimetres (1-3 cm) is challenging, due to the complex observation system. Since the SSH

measurement is not simply the output of a single instrument, a wide variety of intermediate methodologies, data combination and processing are required.

The primary sensor of an altimetry mission is the radar altimeter. This active instrument emits a radar pulse in the nadir direction and analyses the return signal reflected in the water surface. This way, the altimeter determines the distance (R) from the satellite to the water surface (altimeter range) by measuring the satellite-to-surface round-trip time of the radar wave. The satellite's orbit altitude (S) above a reference Earth ellipsoid is known at each along-track point through precise orbit determination and the SSH is the difference between this altitude and the altimeter range, determined from the round-time of the altimeter signal ($SSH = S - R$). According to this altimetry principle, illustrated in Fig. 1, water surface height is determined above the same reference ellipsoid.

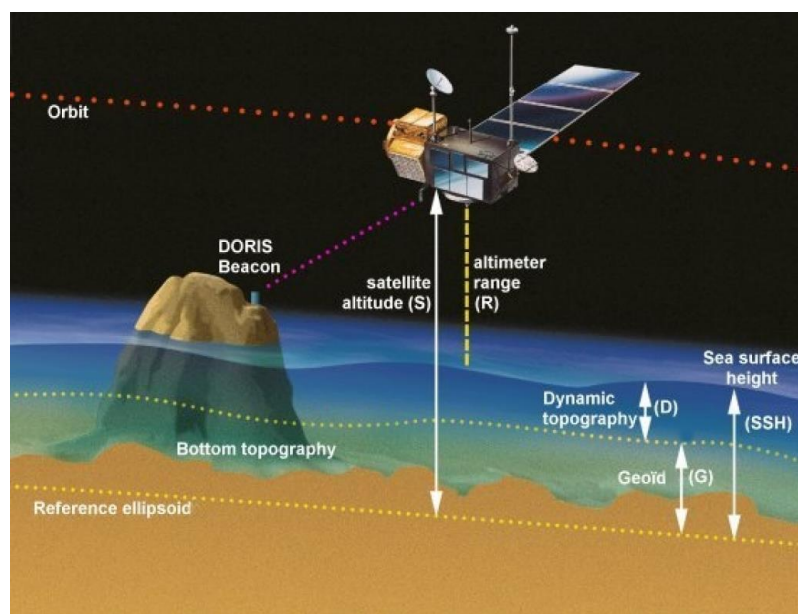


Figure 1. Satellite altimetry principle (image from AVISO).

Additionally, the processing of the return signal, known as retracking (Passaro et al., 2018), also allows to determine other geophysical parameters over the oceans, such as the significant wave heights (SWH) (Timmermans et al., 2020) and the modulus of the wind speed at sea surface, derived from the altimeter backscattering coefficient (σ_0) (Lillibridge et al., 2014). This altimeter-derived parameter is a measurement of the power of the return signal, containing information about the wind-induced sea surface roughness (Goddijn-Murphy et al., 2012). Calm waters generate high values of σ_0 , while rough waters generate low values of this altimeter-measured parameter.

Almost three decades of radar altimeter observations, combined with improvements in data processing, modelling and external data, allowed reaching a centimetric accuracy on SSH determination and demonstrated the capability to observe a global mean sea level (GMSL) rise of about 3 mm/year since 1993 (Ablain et al., 2019; Cazenave et al., 2018). This altimetry-based GMSL rise is shown in Fig. 2 (for more details see (Cazenave et al., 2018)).

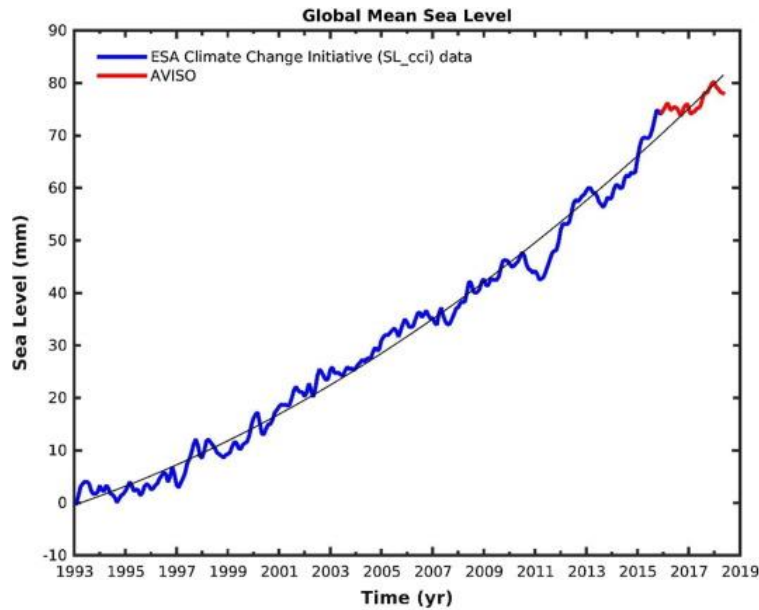


Figure 2. Global mean sea level (GMSL) time series based on satellite altimetry data (Cazenave et al., 2018).

This retrieval of water surface heights with centimetric accuracy from satellite observations requires the knowledge of all terms involved in the altimeter measurement system with the same level of accuracy (Benveniste et al., 2019; Vignudelli et al., 2019). Thus, to obtain accurate SSH from altimeter observations, several accurate measurements and corrections in a proper data processing are required. The following corrections are taken into account:

- i. range corrections – to account for the delay in the radar pulses propagating in the atmosphere (atmospheric corrections) and for the interaction with the sea surface (sea state bias);
- ii. geophysical corrections – to account for the sea level variability due to tides and atmospheric pressure;
- iii. instrumental corrections (relative positioning of antennas, internal delays, etc.).

The interaction of the altimeter signals with the atmosphere (troposphere and ionosphere) induces a delay in the signal propagation, due to the atmospheric refractivity (Fernandes et al., 2021). This effect is treated separately for the dry troposphere, wet troposphere and ionosphere, by means of the dry tropospheric correction (DTC), wet tropospheric correction (WTC) and ionospheric correction (IC), respectively, in the altimetric equation that calculates SSH. These corrections take into account the delay in the altimetric signal due to dry gases in the troposphere (DTC), water vapour and cloud liquid water in the troposphere (WTC) and electrons in the ionosphere (IC).

Concerning the ionospheric correction, it is determined using dual-frequency altimeters, since this effect is strongly dependent on frequency. The IC has mean values of 2–8 cm and a standard deviation of 1–3 cm for the frequencies and altitudes at which the current altimeters operate (Fernandes et al., 2021).

Among the range corrections, DTC and WTC are the focus of this thesis. These radar altimeter atmospheric path delays are significant error sources that must be properly accounted for (Vignudelli

et al., 2019), otherwise they may be the main source of uncertainty in the water surface level determination from radar altimetry (Fernandes et al., 2014).

Satellite radar altimetry was originally designed for ocean application. For this reason, the instrument data processing and every intermediate methodology were primarily tuned for ocean surfaces. However, this space technique started to be used over coastal and inland waters (Tong et al., 2016), where its application is more challenging than over open ocean. Concerning the tropospheric corrections, their determination over these regions of interest can be less accurate and require additional efforts. The specificity of each one, both in terms of determination and in terms of particular problems over non-ocean surfaces, will be addressed separately in the next sub-sections.

1.1.1. Dry Tropospheric Correction (DTC)

The dry tropospheric correction is the largest range correction in satellite altimetry, accounting for nearly 90% of the total delay caused by the troposphere. It accounts for the delay in the signal propagation due to the existence of dry neutral gases in the atmosphere and is proportional to the surface pressure (DTC in cm is roughly 0.23 times the surface pressure in hPa) (Chelton et al., 2001). While the sea level pressure (SLP) ranges approximately from 980 to 1035 hPa, the DTC has an absolute value at sea level of about 2.3 m and a range of about 0.2 m.

For the lower troposphere, DTC has an almost linear height dependence (nearly 1 cm per each 40 m) and it is determined with high accuracy from surface atmospheric pressure (in situ measurements or from a Numerical Weather Model (NWM)). Previous studies (Fernandes et al., 2014; Fernandes et al., 2013) have showed that the DTC can be computed from NWM with an accuracy better than 1 cm globally. In particular, over coastal and inland waters, the same accuracy can be achieved if the correction is computed at surface height, taking into account adequate procedures and accurate surface elevations.

The most common sources of atmospheric pressure used in the context of tropospheric corrections of altimeter observations are the atmospheric models from the European Centre for Medium-Range Weather Forecasts (ECMWF). Fernandes et al. (2013) showed that DTC can be estimated with an accuracy of a few millimetres from global grids of atmospheric pressure at sea level and an appropriate digital elevation model (DEM).

Fig. 3 shows an example of the DTC for pass 13 (cycle 10) of Sentinel-3A (S3A). The top left panel represents the DTC in meters, while the bottom left panel illustrates the corresponding altitude in meters. The right panel shows the planimetric representation of this S3A pass, where the background colour represents the surface pressure in hPa. The dry correction is that present in the S3A products (estimated from ECMWF model) and the altitude from Altimeter Corrected Elevations 2 (ACE2) DEM is also available in the same products. The corresponding surface pressure is that provided by ERA5. This example shows the main characteristics of the DTC:

- i. An absolute value at sea level of about 2.3 m;
- ii. Low variation at sea level;

- iii. A direct dependence on surface pressure (DTC is proportional to surface pressure);
- iv. A strong and almost linear dependence with altitude (an increase of 2500 m in altitude is equivalent to a decrease in the absolute value of the DTC of about 60 cm, roughly 1 cm in DTC for every 40 m in altitude).

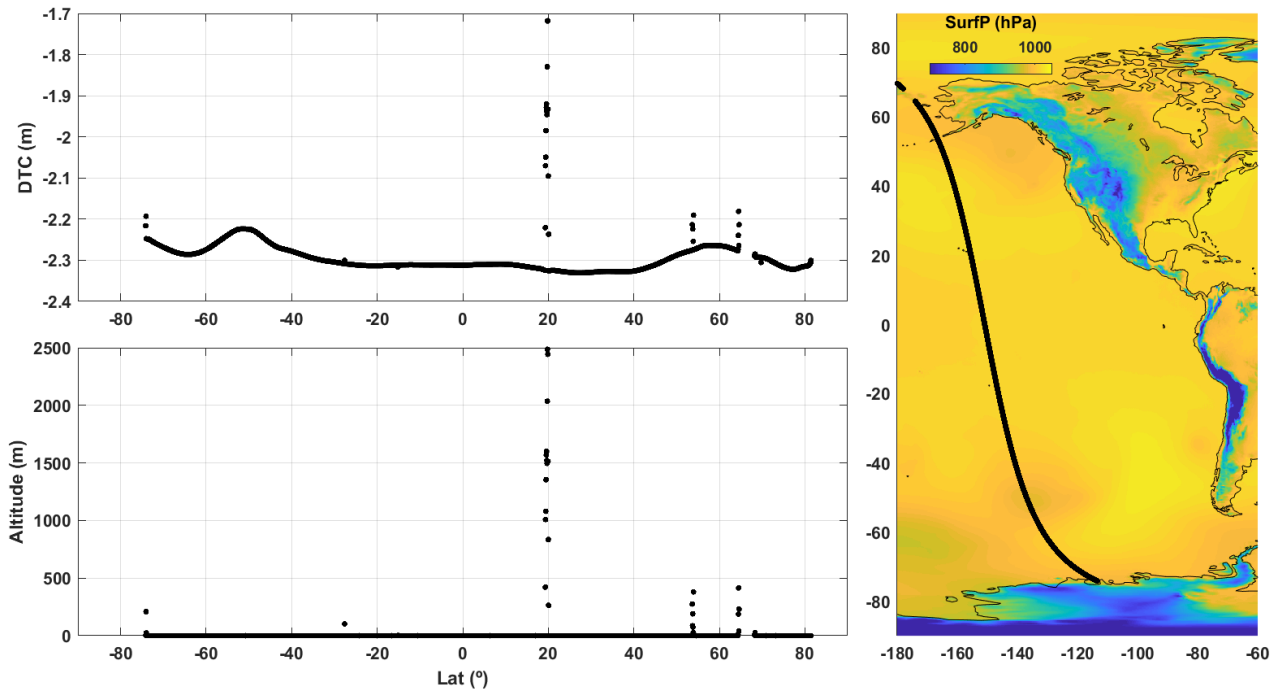


Figure 3. DTC in m (top left), altitude in m (bottom left) and planimetric view (right) of the S3A pass 13, cycle 10. Background colour of the right panel represents the surface pressure in hPa provided by ERA5.

Due to the strong height dependence of the DTC, some state-of-the-art methodologies (and altimeter products) fail to provide the DTC appropriate for coastal and inland water studies, due to inadequate handling of its height dependence (Fernandes et al., 2014). Since satellite altimetry is primarily designed for studies over the ocean, over this surface this dependence does not exist, and the methodologies are not suited for non-ocean surfaces. The DTC present in some altimetric products may have significant errors in coastal and inland water regions, which have been reported by several authors (Fernandes et al., 2014).

The main issue of this range correction is the adoption of the correct altitude of the measurement point, since once it is adopted, the DTC is easily determined with centimetric accuracy for altimeter observations. Despite being the largest range correction in satellite altimetry, if an adequate handling of its height dependence is adopted, errors below 1 cm are expected for this correction, either for open ocean or coastal zones.

More details about DTC are given in Sections 2.1 and 2.2, namely about its determination from global grids provided by an atmospheric model.

1.1.2. Wet Tropospheric Correction (WTC)

The wet tropospheric correction can be a major source of uncertainty in the determination of SSH from radar altimetry (Fernandes et al., 2015). It accounts for the delay in the signal's propagation in the atmosphere due to the water vapour and cloud liquid water. With an absolute value less than 50 cm, the WTC is highly variable, both in space and time (Vieira et al., 2019). This correction mainly depends on the integrated amount of atmospheric water vapour. The WTC also depends on the integrated amount of liquid water, however with a very small contribution (Fernandes et al., 2021). Typical values of this contribution are less than 5 mm, almost negligible compared to the dominant contribution from the integrated water vapour (Escudier et al., 2017).

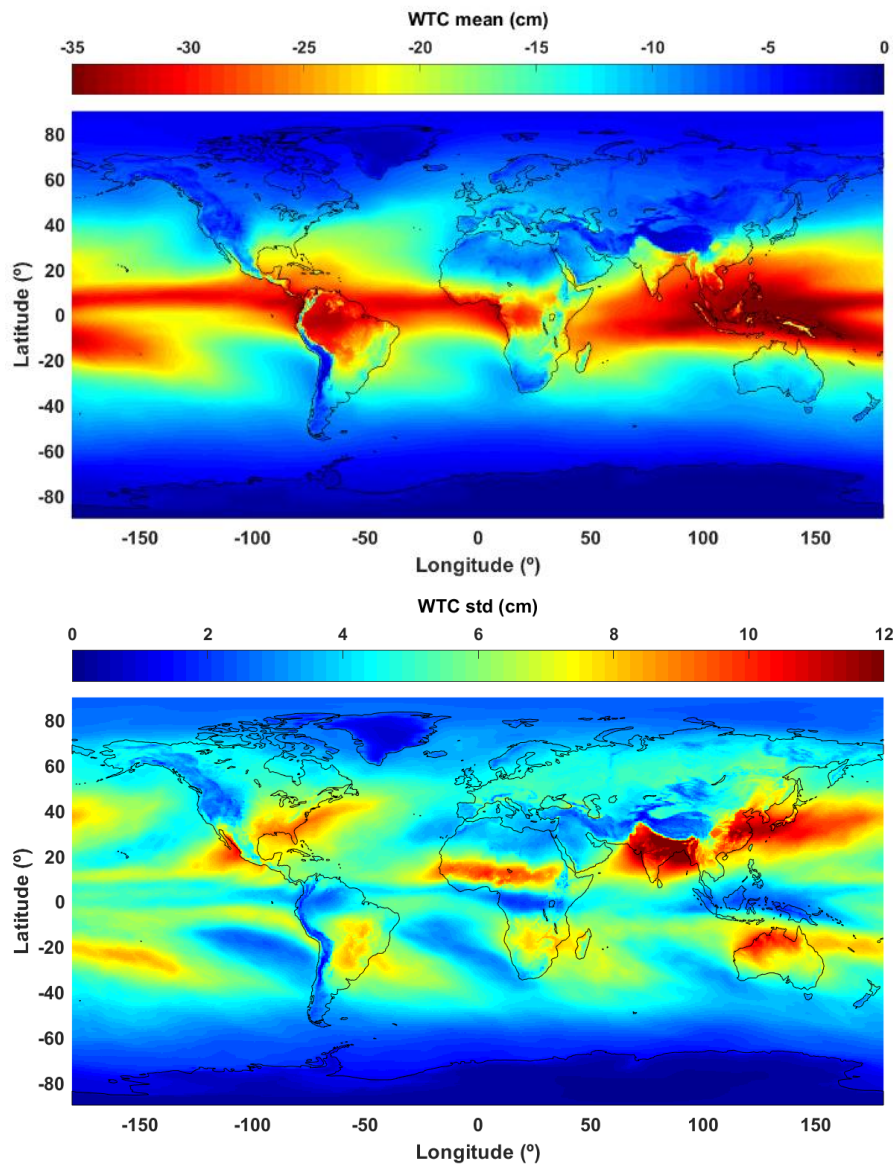


Figure 4. Mean (top panel) and standard deviation (bottom panel) of the WTC computed at surface level from an atmospheric model, considering 1 year of data.

Due to this major dependence on the integrated amount of water vapour, the spatial patterns of the WTC are very similar to those of the atmospheric humidity. Fig. 4 shows the mean (top panel) and standard deviation (bottom panel) of the WTC over an entire year (2017). While the maximum absolute mean values are around 35 cm for low latitudes, the standard deviation can reach 12 cm in the tropics, as represented in the bottom panel of Fig. 4. Unlike the DTC, the WTC has smaller absolute values (mean values in the range 0-35 cm) and much larger variability, up to 50% of the signal (Fernandes et al., 2021).

The WTC can be estimated using several sources, however considering the high spatial and temporal variability of the WTC, the most accurate way to retrieve the WTC over open-ocean is from collocated measurements from Microwave Radiometers (MWR) deployed on-board the altimetry satellites. Since WTC plays a major role in the altimeter error budget, dedicated retrieval techniques are required. Currently, for ocean altimetry missions, only microwave radiometers providing WTC retrievals collocated with the altimeter measurements can meet the stringent requirements (Legeais et al., 2014; Stum et al., 2011).

Despite this crucial role of the MWR-derived WTC over open-ocean, the MWR retrievals are not valid over non-ocean surfaces, as it will be stated below. Other alternatives exist for the determination of the WTC. It can also be derived from an NWM, this being the best approach for continental regions in the absence of alternative dedicated measurements (Fernandes et al., 2014; Legeais et al., 2014). Global Navigation Satellite Systems (GNSS) derived tropospheric delays are also alternative accurate data sources (Fernandes et al., 2013; Sibthorpe et al., 2011), namely in coastal zones and generally over the continents.

While MWR retrievals refer to sea level, the WTC derived from an atmospheric model are available at the level of the model orography, a smoothed DEM. The corresponding corrections from GNSS are computed at station height. Due to these different reference surfaces, the modelling of the height dependence of the WTC is a crucial step to combine these different data for satellite altimetry studies over these regions, where the difference between orography and water levels induces large WTC errors (Fernandes et al., 2014). The only known formula for the height dependence of the WTC available in the literature is an empirical expression by (Kouba, 2008) with various limitations, since it was derived from data over a single point and only between two heights.

Regarding the WTC from MWR, this retrieval uses the MWR measured top of the atmosphere (TOA) brightness temperatures (TB) at various frequencies around the 22.235 GHz water vapour absorption line. Every instrument on board the different altimetry satellites has a common 23.8-GHz channel (water vapour channel) that captures the major contribution of the water vapour to the WTC estimation. A higher frequency band is also used to capture the contribution of the cloud liquid water. This second channel, known as cloud liquid channel, ranges from 34 to 37 GHz, depending on the mission. Some radiometers use a third channel at 18.7 GHz that includes additional information about the surface contribution in the TBs measurements. These three MWR frequencies have shown to be the most well-suited for measuring the wet path delay (Keihm et al., 1995).

The lack of the third frequency in some radiometers brings the need of using other additional parameters in the retrieval algorithm as a proxy for the surface information (Obligis et al., 2006, 2009; Picard et al., 2015; Thao et al., 2015). More details are given in Section 4.2.

The conversion of raw MWR measurements into altimeter wet tropospheric corrections can be divided into three levels of processing (as illustrated in Fig. 5):

1. the antenna temperature calibration (Ruf et al., 1995), where the raw MWR data are converted into antenna temperatures;
2. the antenna pattern correction (APC), where the brightness temperature is derived from the antenna temperature (Janssen et al., 1995);
3. the retrieval algorithm, where the brightness temperatures at each MWR frequency are converted to wet tropospheric corrections (Ruf et al., 1996).

This thesis addresses this third step, illustrated in Fig. 5 with dark colours (where the previous steps are represented with light colours). The estimation of the WTC from the TBs is complex and cannot be solved by a purely physical approach. The retrieval needs an empirical inversion to establish the relation between TBs and WTC. Different methods exist in the building of the database, the empirical method used for the inversion, and the design of the retrieval algorithm. More details are given in Section 4.2.

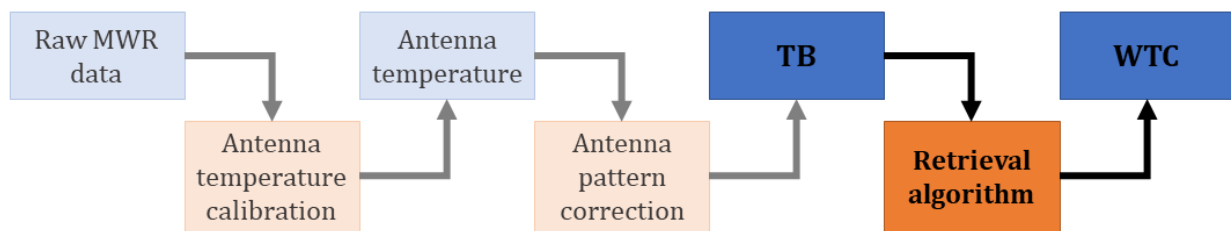


Figure 5. Processing chain of the WTC retrieval from MWR measurements.

The WTC derived from the measured brightness temperatures of the various MWR channels depends on the instruments and retrieval algorithms that can be different in each altimetric mission. Originally designed for the ocean, these algorithms are only tuned for ocean observations. In the presence of other surfaces, such as land or ice, the MWR measurements become invalid. This problem in coastal regions and high latitudes has been addressed by several authors and various algorithms have been designed for improving the WTC in these regions, e.g. (Brown, 2010; Fernandes et al., 2010, 2016). For a review of these methods see (Cipollini et al., 2017) and (Fernandes et al., 2021).

Requirements on accuracy and long-term stability of the WTC measurements are particularly challenging since altimetry missions require centimetric accuracy in WTC and a temporal stability better than 0.3 mm/year (Ablain et al., 2009).

More details about the WTC are given in the following sections, namely about its determination from global grids provided by an atmospheric model, GNSS and MWR measurements for radar altimetry.

1.2. Objectives

The focus of this thesis is the determination of tropospheric corrections for satellite radar altimetry over coastal regions and inland waters by developing improved techniques for retrieving these corrections and consequently improving the water surface height measurements in these regions.

In this context, the main objectives of this thesis are:

1. to model the altitude dependence of the wet tropospheric correction in coastal zones and inland waters and develop adequate methods for computing these corrections for satellite altimetry measurements over these regions;
2. to exploit and develop an improved algorithm for the retrieval of the WTC from MWR measurements, namely for two-band radiometers such that of Sentinel-3 (S3), by a suitable learning and appropriate handling of the contribution of the surface in the MWR measurements (a weakness in the 2-band MWR such as that of S3).

These topics are complementary, since a better modelling of the height dependence of the tropospheric corrections will improve data combination from different sources (MWR, GNSS and NWM), while the improvement of MWR retrieval algorithms will directly lead to more accurate surface heights in the target regions. Moreover, with the advent of more accurate high rate data sets from the new instrument modes, there is an increase demand for the retrieval of high rate range corrections using appropriate methodologies, both concerning the MWR retrieval and the handling of the height dependence of the tropospheric corrections.

Although the challenges posed by the coastal and inland water zones are the main motivation for the first objective, some of the potential improvements can be extended also to open-ocean. On the other hand, the second objective relative to the open ocean allows some initial exploitations and developments, useful for future WTC retrieval algorithms from MWR over coastal regions (ocean/land transition), known by their additional challenges.

The determination of altimeter-derived water surface heights either in open ocean or in e.g. rivers, lakes or enclosed seas with a better accuracy (by means of better tropospheric corrections) will support a proper use and management of the water resources, with effect in the climate changes and their impacts.

This thesis was carried out at FCUP, in the scope of various European Space Agency (ESA) funded projects, which aimed at developing methodologies for improving the CryoSat-2 (CS-2) and S3 data, mainly over coastal and inland water zones. The outcome of this thesis was a significant contribution to the improvement of the tropospheric corrections of these satellites over those regions.

1.3. Thesis Outline

The core of this thesis is a collection of five articles (at present, four already published and one under review) as described in what follows. Section 2, composed by the first three articles, describes the work mainly with a component of analysis and application. This section addresses the analysis of

tropospheric corrections over inland waters, the assessment of the land contamination in the MWR-derived WTC retrievals over coastal zones, as well as the study of the inability of the recent atmospheric models in mapping the small scales of the WTC, despite their increasing quality. After these analyses, Sections 3 and 4 (fourth and fifth articles, respectively) present the work performed in the scope of this thesis, with a component of development. These two sections correspond to the two main objectives of this thesis.

Overall, the research performed in the first three articles (Section 2) allowed the consolidation of the state-of-the-art and the identification of the current problems, the maturation of the objectives, as well as the motivation for the subsequent work described in Sections 3 and 4.

1.3.1. Articles 1-3

Section 2.1 contains the first article published in Advances in Space Research (ASR) on 9 September 2017. This analysis, carried out in the scope of the ESA-funded Sentinel-3 Hydrologic Altimetry Processor prototype (SHAPE) project, focuses on both tropospheric corrections over inland waters.

Different regions of interest (ROI) have been selected in the scope of this project, in order to assess the tropospheric corrections of the altimeter observations over these regions. The objectives of this study were firstly the analysis of the errors present on the DTC and WTC provided in the CryoSat-2 (CS-2) products and secondly the implementation of methodologies to derive improved corrections, aiming at getting improved products for CS-2. This analysis was conducted on five ROI: Amazon and Danube rivers, Titicaca and Vanern lakes and the Caspian Sea.

Different methodologies and data processing have been used, in order to compare the DTC and WTC from the CS-2 products with corrections computed from an ECMWF model at various levels (model orography, a DEM and mean sea/lake or river profile). Additionally, a validation of the corrections has also been performed by local comparisons with independent observations: DTC computed from in-situ surface pressure measurements and WTC derived from GNSS tropospheric path delays, according to the availability of these data over each region of interest.

Results of this paper showed that the tropospheric corrections present in CS-2 products are not referred to the correct surface elevation. Different reference altitudes may depart from the mean river profile or mean lake/sea heights (the levels of interest) by hundreds of meters, resulting on systematic errors, always with the same sign and magnitude for a given location (impacting directly the determination of the absolute water level). This paper also identifies the best reference surfaces for use in the DTC and WTC estimations from an atmospheric model, i.e., the corrections should be referred to the mean lake/sea level or to the mean river profile. Once this is ensured, the corresponding errors are expected to be less than 1 cm for the DTC and less than 2 cm for the WTC.

Focusing on the analysis of the tropospheric corrections over inland waters, where atmospheric models may be the only source available, the contribution of this article is the recommendation of a set of procedures for the proper handling of these corrections over these regions. Selecting the correct approach, large errors still present in the tropospheric corrections are easily avoidable.

Section 2.2 presents the second article published in IEEE Transactions on Geoscience and Remote Sensing (TGRS) on 5 October 2018. After analysing the tropospheric corrections over inland waters and ensuring a proper determination as far as an atmospheric model allows, this work addressed only the WTC over coastal zones, since the DTC estimation over these regions is not problematic and it is performed with enough accuracy (as in open ocean).

The contribution of this article is a complete coastal assessment of the MWR-derived WTC on board the various altimeter satellites. The GNSS-derived WTC is a useful independent source to inspect the land effects on MWR observations and to monitor the long-term stability of these instruments, very relevant for climate studies. This study determines the distance from coast at which the WTC retrievals become invalid and should not be used (10 to 30 km, depending on mission, due to their different frequencies, footprint sizes and different MWR retrieval algorithms). For this purpose, reference tropospheric delays are computed at a network of 60 global GNSS stations, from which WTC are derived. The comparison between the MWR-derived wet tropospheric correction and the GNSS-derived WTC at the nearby coastal stations, clearly illustrates the effect of land contamination in the MWR measurements. Aiming at inspecting the long-term stability of the MWR measurements, these comparisons with GNSS show negligible differences and drifts smaller than 0.3 mm/year. Another important contribution of this paper is to show the ability of the GNSS-derived path delay Plus (GPD+) algorithm developed at the University of Porto, to remove the land contamination in the WTC and to improve its retrieval.

Motivated by the new and improved temporal resolution of the latest ECMWF reanalysis model, an assessment of its impact in the WTC computation for satellite altimetry is the topic of the third article in Section 2.3 also published in IEEE TGRS on 9 August 2019.

This article concerns the analysis of the performance of the recent ECMWF reanalysis, ERA5, in the estimation of the WTC, namely a global assessment of the impact of the different temporal resolutions of ERA5 in the WTC computation. Despite the promising temporal high resolution (1h), this study revealed that the latest ECMWF reanalysis cannot also map the WTC short space and time scales, like its predecessor with a coarser temporal resolution (6h).

Results show that the RMS of the differences between MWR-derived WTC and ERA5 is 1.2 cm, showing that the global quality of the recent models has been increasing significantly, particularly this recent ECMWF reanalysis. However, the effect of using 1h instead of 6h intervals (the temporal resolution of the previous ECMWF reanalysis) is very small and hourly intervals do not have a significant impact on the WTC from ERA5. This work shows that ERA5 is currently the best ECMWF model and that a temporal resolution of 3h is high enough to ensure the same accuracy as 1h.

Despite the increasing quality of the atmospheric models, due to the high variation of the atmospheric humidity, valid retrievals of MWR and other observations are required to correct the altimetric measurements. This analysis reinforces the need of having observations from collocated MWR, since atmospheric models are not able to map the small space and time scales of the high variable water vapour.

1.3.2. Article 4

Section 3 contains the fourth article published in *MDPI Remote Sensing* on 11 December 2019. This work corresponds to the first main objective of this thesis and it is the first work with a component of development.

In the scope of the WTC retrievals, such as the GPD+ methodology, there is a need to combine observations from different sources and reference surfaces. For this purpose, a conversion of WTC values between different altitudes is required. This paper presents the modelling of the WTC altitude dependence, a crucial step to better combine these different WTC values in coastal and continental waters and thus, better determine water surface heights from satellite altimetry over these regions.

The only expression available for this altitude reduction, developed by Kouba (2008), is irrespective of geographic location and time. The objective of this paper is to develop improved expressions for this purpose. This modelling was performed from WTC vertical profiles computed globally from ERA5, using global 3-D fields of atmospheric temperature and humidity at pressure levels over 4 years (2010–2013). A thorough inspection of the shape of the WTC vertical profiles revealed that the most suitable adjusting function was an exponential, similar to that proposed by Kouba. Following this expression, the decay coefficient of this exponential function was modelled using least squares, considering a dependence on geographic location and period of the year.

The output of the developed modelling consists of three sets of decay coefficients:

- UP-01 – a single coefficient for each point (non-time-dependent), computed as the mean at each point;
- UP-04 – four seasonally averaged coefficients for each location;
- UP-12 – twelve monthly averaged coefficients for each point.

Despite a clear annual signal in the coefficients in some regions, suggesting the inclusion of a temporal dependence, the most striking feature of the time evolution of the coefficients at each location is the high variation of these coefficients, making this modelling a very difficult task. Due to the high WTC vertical variability, the adjustment of the WTC vertical profiles to a mathematical curve becomes inaccurate, particularly over regions with large WTC space-time variability. This is particularly difficult when the WTC at the height of interest (for example sea level) is much more variable than the WTC at the known altitude (for example station location).

An assessment using ERA5 data (not used in the modelling) and an independent validation of the proposed modelling was carried out, showing significant improvements when UP coefficients instead of Kouba are used. The most significant improvement appears when only spatially dependent coefficients are selected.

The motivation for this modelling was its inclusion in algorithms and methodologies to generate improved WTC that combine different WTC data sources for satellite altimetry application, mainly over coastal and continental waters. The contribution of the models developed in this study is a better determination of WTC over these challenging regions, and thus a better retrieval of water surface heights over these regions of interest.

1.3.3. Article 5

Section 4 pertains the fifth article, presently under review in *Journal of Geodesy (JOGE)*, submitted on 9 November 2020. This study addresses the second main objective of this thesis and it also involves a component of development.

The exploitation of the WTC retrieval algorithms from microwave radiometer observations is of particular interest for the Sentinel-3 mission for several reasons. Since the MWR on board Sentinel-3 does not possess a third band near 18 GHz, to account for the surface contribution in the MWR measurements, the design of the corresponding algorithms is more challenging and needs additional inputs to overcome this instrumental limitation. Moreover, preliminary results indicate that improvements are required in the MWR-derived WTC present in S3 products, suggesting that the corresponding current retrieval algorithms are not well tuned for this mission. After exploiting these algorithms adopted in the Sentinel-3 products, this paper describes an improved algorithm for the retrieval of the wet tropospheric correction from MWR measurements over open-ocean, specifically tuned for Sentinel-3. This is carried out considering a suitable learning, temporally closer to the S3 mission period and better accounting for the contribution of the surface in the MWR measurements (a weakness in the 2-band MWR such as that of S3), by means of including dynamic inputs, instead of seasonal tables as adopted in S3 products.

Adopting dynamic inputs interpolated from an atmospheric model, accounting for the contribution of the surface in the WTC retrieval, it was found that the fifth input currently used in the S3 algorithm becomes unnecessary. The proposed algorithm uses four inputs: the two brightness temperatures at 23.8 GHz and 36.5 GHz, the Ku-band backscattering coefficient (σ_0) and sea surface temperature fields from ERA5. Comparisons with reference and independent WTC show a significant improvement of this algorithm over the current algorithms (firstly designed for Envisat). The same comparisons show that the global RMS of the WTC differences between the independent source and the proposed algorithm is lower than 1 cm. Moreover, the improvement of this algorithm over those adopted in Sentinel-3 products is globally more significant for distances from coast between 30 and 250 km.

The contribution of the work described in this paper is a significant improvement in the quality of the WTC derived from the algorithm here developed over those adopted in the Sentinel-3 data records. Hence, this paper proposes the use of a new WTC retrieval algorithm, tuned for Sentinel-3, providing improved wet tropospheric corrections for this mission, as well as for the GNSS-derived Path Delay Plus algorithm which extends the validity of this crucial range correction to all surface types.

The sum of contributions of this thesis ends in a better and more accurate determination of water surface heights from satellite radar altimetry, by means of using improved tropospheric corrections. The main contributions of this thesis are therefore:

- Improve procedures for the computation of the DTC and WTC from atmospheric models over inland waters, adopting adequate formulae and ensuring their computation at correct water surface heights.
- Understand the land contamination in the MWR-retrieved WTC and the determination of threshold values of distance from coast where it appears, useful in the identification of invalid WTC values.
- Exploit the GNSS-derived WTC to assess the long-term stability of on-board MWR.
- Assess state-of-the-art NWM: recent atmospheric models are still not able to model the small scales of the WTC variability and are unable to produce WTC as accurate as that derived from MWR over open-ocean.
- Develop an improved climatology of the WTC vertical variation, considering its space-time dependence, generating an improved WTC estimation over regions where that derived from MWR is invalid, by means of a better combination of the available valid WTC.
- Implement an enhanced algorithm for retrieving the WTC of Sentinel-3 over open-ocean, based on the S3 on-board MWR observations, with additional dynamic inputs.

Since this thesis is a collection of five articles and each one has been published individually, the reader will find repeated information and ideas in different sections, mainly in the introductions of each article. Apart from the references and number of sections, which were unified throughout the whole document, the text in each article was kept in its original form.

2. Tropospheric Corrections of Satellite Altimetry observations over inland waters and coastal zones

2.1. Analysis and retrieval of tropospheric corrections for CryoSat-2 over inland waters (Article 1)

Abstract – The application of satellite altimetry over inland waters requires a proper modelling of the various error sources involved in the determination of precise surface water heights above a reference ellipsoid or above the geoid.

The objectives of this study are firstly the analysis of the errors present on the dry tropospheric correction (DTC) and on the wet tropospheric correction (WTC) provided in the CryoSat-2 (CS-2) products and secondly the development of methodologies to derive improved corrections, aiming at getting improved products for CS-2. This study is conducted on selected regions of interest, such as the Amazon and Danube rivers, Titicaca and Vanern lakes and the Caspian Sea. Since CS-2 has a geodetic orbit, its ground tracks allow the retrieval of precise surface water heights over regions not covered by any other satellite.

The DTC and WTC present in the CS-2 products have been compared against corrections computed from the European Centre for Medium-Range Weather Forecasts (ECMWF) operational model at various levels: (i) the level of ECMWF model orography; (ii) the level of the Altimetry Corrected Elevations 2 (ACE2) digital elevation model and (iii) the level of mean lake/sea or river profile.

An independent assessment of the corrections has also been performed by comparison with DTC derived from in situ surface pressure measurements and WTC retrieved from Global Navigation Satellite Systems (GNSS) data.

Results show that the model-derived corrections present on CS-2 products seem to be referred to the model orography, except for the Caspian Sea where corrections seem to be referred to mean sea level (zero level). Model orography can depart from the mean river profile or mean lake/sea heights by hundreds of meters. Overall, ACE2 DEM is a better altimetric surface than ECMWF orography, however height errors up to hundreds of meters exist in ACE2. Height errors induce DTC errors that can reach several centimetres (11 cm in the Danube River) and WTC errors up to 2–3 cm. These errors

are systematic, having always the same sign and magnitude for a given location, thus affecting the retrieval of the absolute water level.

For rivers, the mean profile is the best representation of the surface height in the river basin and is also the best reference surface for use in the DTC and WTC estimations from an atmospheric model. The same happens with lakes or closed seas, where the corrections should be referred to the mean lake/sea level.

Results show that, once computed at the correct mean river profile or mean lake/sea level, the DTC has a small variation, with a standard deviation going from 0.5 cm in the Amazon River to 3.0 cm in the Danube River. The DTC absolute values go from 1.48 m in Lake Titicaca to 2.32 m in the Caspian Sea. With a larger variability, once computed at mean river profile or mean lake/sea level, the standard deviation of the WTC goes from 2.7 cm in Lake Titicaca to 5–6 cm in all other regions and absolute values from only 6 cm in Lake Titicaca to 31 cm in the Amazon River.

Once computed at the correct surface elevation the corresponding errors are expected to be less than 1 cm for the DTC and less than 2 cm for the WTC.

2.1.1. Introduction

Satellite altimetry provides global information about sea and inland water levels and their variability. The principal objective is to measure the range from the satellite to the water surface (Chelton et al., 2001) and consequently to measure the sea surface height above a reference ellipsoid. Satellite altimetry was originally designed for applications over the ocean, however it has been used for applications over inland waters, which have a profound influence on human culture and society. The majority of the global population lives along the river system primarily due to easy access to water resources. Knowledge and prediction of the quantities of water flowing in rivers is of great importance in order to improve water allocation efficiency or to mitigate floods and droughts (Calmant et al., 2008).

The application of satellite altimetry over continental water surfaces, such as rivers, lakes or closed seas, has been addressed by several authors (Birkett, 1995; Calmant et al., 2006; Cazenave et al., 1997; Crétaux et al., 2006). Some important examples of these applications over inland water regions are the assessment of lake-level variation, such as the Lake Chad basin and the Caspian Sea (Coe et al., 2004; Sharifi et al., 2013), the inland water bodies monitoring over the Indian region (Chander et al., 2014) and the estimation of the Amazon and Ganges-Brahmaputra rivers discharges (Papa et al., 2010; Zakharova et al., 2006).

(Villadsen et al., 2016) addressed the application of SAR altimetry data from CryoSat-2 over inland waters, namely the improvement of water levels using different (empirical and physical) retracers. The authors present a selection of papers on inland water altimetry which include comparisons between water levels obtained with altimetry and with in situ gauges. This provides an independent assessment of the water levels obtained over inland waters with satellite altimetry, considering all errors sources involved.

Depending on the way how these water levels are derived with satellite altimetry (retracking algorithms, corrections used, etc.), these studies allow to give an independent indicator of the accuracy of these water levels. For instance, the most recent study mentioned above indicates a root mean square error (RMSE) from comparison of altimeter-derived water levels with in situ gauges below 4 cm for two lakes and a value of 15.3 cm for a river. Results over rivers vary much more due to several reasons, such as land contamination (caused by topography and shape of the river) or a lower number of observations due to river widths.

As over the ocean, the accuracy of the estimation of the water level for inland water bodies depends directly on the accuracy of the several corrections required to correct the measured range for various effects. For hydrological studies using satellite radar altimetry, various range and geophysical corrections, due to effects such as dry and wet troposphere, the ionosphere, solid earth tides, etc., should be taken into account. A proper modelling of the various corrections is a crucial step for satellite altimetry applications.

Many authors (Birkett et al., 2011; Crétaux et al., 2011; Fernandes et al., 2014) have reported various problems in the corrections present on the current standard altimeter products for several missions, namely on the tropospheric corrections. However, previous studies show that the agencies did not always take these reports into account and the tropospheric path delays present in these products are often not suitable for use in inland water regions (Fernandes et al., 2014). These studies show that the main errors in model-derived corrections, present in altimeter products, over inland water regions are on the tropospheric corrections – dry tropospheric correction (DTC) and wet tropospheric correction (WTC), due to the height dependence of these range corrections. Altimeter products often fail to provide valid tropospheric path delays over these water bodies, since DTC and WTC are provided at other level instead of at surface height. To overcome these problems, alternative sources of corrections have been used, namely in continental waters. For the DTC in situ data of surface pressure can be adopted, while for the wet correction, Global Navigation Satellite System (GNSS)-derived WTC from local stations can be used, when available (Birkett et al., 2010).

The focus of this study is the analysis of errors present in the dry and wet tropospheric corrections of the CryoSat-2 (CS-2) products over inland water bodies and the development of new improved corrections for this mission. Despite of the fact that this study is performed with CS-2 data, results can be applied to other altimetric missions, namely Sentinel-3.

The primary payload of this satellite is the Synthetic Aperture Radar Interferometry Radar ALtimeter (SIRAL). Conceived to measure and monitor the changing thickness of ice in polar regions, CryoSat-2 does not carry an on-board microwave radiometer (MWR), being the baseline wet tropospheric correction applied to the radar altimeter data a model based one, provided by the European Centre for Medium-Range Weather Forecasts (ECMWF) Operational model. The loss of Envisat in 2012 fostered the development of techniques for exploiting CS-2 data over ocean and inland water regions (Fernandes et al., 2016). This mission has a geodetic orbit with a 369 day repeat cycle and a sub-cycle close to 30 days (Francis, 2007). Thanks to its very long repeat cycle, this mission allows to cover many regions, namely inland waters, where CS-2 is operating in the Synthetic Aperture Radar (SAR) and SAR Interferometric (SARIn) modes, rarely covered by other missions,

such as the reference missions (see Fig. 1). With an inter-track spacing at the equator of 7.5 km (Francis, 2007), this mission allows to obtain measurements over small rivers and lakes.

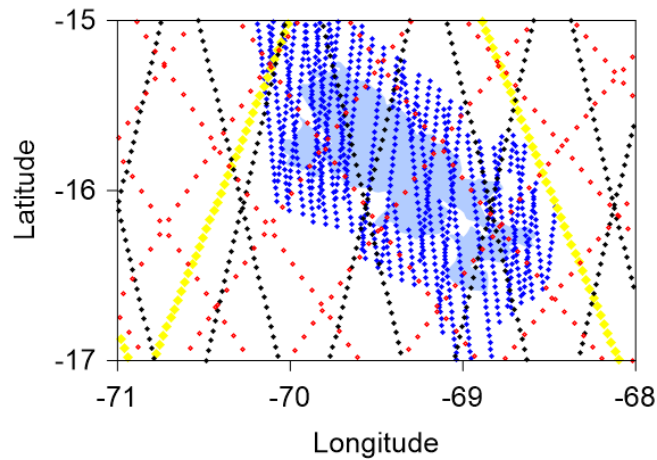


Figure 1. Representation of the spatial coverage over Lake Titicaca of the various altimetric missions: 10-day repeat reference missions (yellow), 35-day ERS-1, ERS-2, ENVISAT and SARAL (black), Sentinel-3 (red) and CS-2 (blue). Light blue polygon represents Lake Titicaca.

Previous studies (Fernandes et al., 2014; Fernandes et al., 2013) show that the DTC can be retrieved from atmospheric models with accuracy better than 1 cm globally. In particular, over inland waters, the same accuracy can be achieved if the correction is computed at surface height using adequate procedures and accurate surface elevations.

For the WTC, over ocean surfaces and central parts of large lakes the best source of information is the on-board microwave radiometer, with an accuracy close to 1 cm. Over rivers, small lakes and whenever the water body is small compared to the radiometer footprint size (10–40 km, depending on the instrument and frequency), the best source for the WTC retrieval is an atmospheric model such as the ECMWF operational (Miller et al., 2010), after 2004, or the ERA Interim (Dee et al., 2011), before 2004 (Fernandes et al., 2014; Legeais et al., 2014). Over these regions, even if a few radiometer measurements can be retrieved in the central parts of large river basins, they will be surrounded with noisy measurements due to land contamination and it will be almost impossible to discriminate between the good and bad measurements. For this reason the adoption of model-based WTC over rivers is recommended.

Alternative and accurate data source for WTC retrieval are GNSS-derived path delays, accurate to better than 1 cm (Fernandes et al., 2013).

It is important to note that these accuracies better than 1 cm for both DTC and WTC mentioned above neglect the effect of their height dependence.

Aiming at inspecting the errors in the tropospheric corrections present on CS-2 altimetry products over inland waters, some regions of interest (ROI) have been selected – Amazon and Danube Rivers, Titicaca and Vanern Lakes and the Caspian Sea. These regions have been chosen to be representative of the different variability conditions for the DTC and the WTC.

The assessment of the errors in the tropospheric corrections present in CS-2 products is performed by means of two complementary analyses. First, the errors related with the height dependence of the DTC and WTC are examined by comparing the corrections present in CS-2 products with those computed at ECMWF model orography and at surface height, as modelled by a digital elevation model (DEM) and by a previously determined mean river profile or mean lake/sea level. This allows assessing the effect of the altitude variation in the DTC and WTC at each ROI. Secondly, the assessment of the absolute errors present in model-derived corrections, once computed at the correct surface height, is achieved by comparison with those derived by independent sources: in situ surface pressure at barometric stations for the DTC and GNSS-derived wet path delays at GNSS permanent stations for the WTC. Altogether, these analyses provide a full assessment of the model-derived tropospheric path delays present in CS-2 products of the selected ROIs.

Section 2.1.2 presents a description of each tropospheric correction (DTC and WTC) and the data and methodology used to compute these path delays from an atmospheric model, at different surface heights. In Section 2.1.3, tropospheric path delays computed as described in Section 2.1.2 are used to assess the corresponding corrections provided on CS-2 products. Aiming at quantifying the errors related with the height dependence of the corrections, detailed altitude analysis has been performed for all regions of interest. Once the height variations in each region were quantified, the corresponding DTC and WTC errors were analysed. Secondly, an independent assessment of each correction is presented, with comparisons between model-derived tropospheric corrections from the ECMWF operational model, at surface height, using state-of-the-art methodologies and those computed from independent data (DTC from surface pressure and WTC from GNSS). Finally, Section 2.1.4 summarizes the main conclusions of this research.

2.1.2. Data and Methods

As mentioned above, previous studies show that the main errors in the altimeter products over inland water regions are on the tropospheric corrections, DTC and WTC. On the other hand, for consistency and due to data availability, model-derived tropospheric corrections, properly computed at surface height, are most suitable over inland water regions.

This Section describes both DTC and WTC and the way to compute these corrections from atmospheric model fields at different levels, since the altitude dependence of each correction is an important factor affecting their estimation. A description of the data used and the methodology adopted in the assessment of the tropospheric path delays in the various ROIs are also presented here.

2.1.2.1. Dry tropospheric correction

The dry tropospheric correction accounts for the delay in the signal propagation due to the existence of dry neutral gases in the atmosphere and it is the largest range correction in satellite altimetry. This correction, with an absolute value at sea level of about 2.3 m, accounts for nearly 90% of the total delay caused by the troposphere. It has an almost linear height dependence (nearly 2.5 cm per each 100 m) and it is usually modelled with high accuracy from in situ measurements of surface

pressure or from an atmospheric model (Fernandes et al., 2014; Fernandes et al., 2013), for example from the ECMWF, using the modified Saastamoinen model (Davis et al., 1985), according to Eq. (1) as described in (Fernandes et al., 2014).

$$DTC = -\frac{0.0022768p_s}{1 - 0.00266 \cos 2\varphi - 0.28 \times 10^{-6}h_s} \quad (1)$$

In Eq. (1), DTC results in meters, p_s is the surface pressure in hPa, φ is the geodetic latitude and h_s is the surface height above the geoid in meters. Surface pressure is computed from sea level pressure p_0 using Eq. (2) that represents the pressure variation with altitude.

$$p_s = p_0 \exp\left[-\frac{g_m(h_s - h_0)}{RT_m}\right] \quad (2)$$

In Eq. (2), R is the specific constant for dry air, T_m is the mean temperature in K of the layer between heights h_0 and h_s and g_m is the mean gravity, given by Eq. (3). T_m can be estimated as the mean value of temperatures T_0 and T_s at heights h_0 and h_s , respectively, given by a climatology such as the Global Pressure and Temperature (GPT) model (Boehm et al., 2007).

$$g_m = 9.784(1 - 0.00266 \cos 2\varphi - 0.28 \times 10^{-6}h_s) \quad (3)$$

Using this methodology and the expressions above, DTC can be estimated from an atmospheric model with an accuracy of a few millimetres, provided accurate surface heights are used. Although model-derived DTC errors are negligible, altitude-related errors depend directly on the surface elevation used, the latter having an almost linear height dependence (an error in altitude of about 100 m induces an error in DTC of about 2.5 cm).

2.1.2.2. Wet tropospheric correction

Unlike the DTC, the wet tropospheric correction that accounts for the path delay due to the presence of water vapour in the atmosphere has an absolute value less than 0.5 m, but it is highly variable, both in space and time. Due to this high variability, the most accurate way to model this effect is through the measurements of microwave radiometers on board the altimetric missions. Due to contamination on the MWR measurements of the surrounding lands, valid MWR observations are available only over the ocean and in the central parts of large lakes. In inland water regions such as small lakes or rivers, these valid measurements are not available. For the case of CryoSat-2, MWR measurements are inexistent, since this mission does not carry a microwave radiometer on board.

For regions with permanent GNSS stations in the surrounding areas, GNSS-derived WTC can be obtained with the same accuracy as MWR-derived WTC (Fernandes et al., 2010). This source of WTC is particularly useful for small lakes, where the measurements at a single station can be representative of the whole lake (Crétaux et al., 2013).

In the absence of GNSS-derived WTC or MWR measurements, such as for CryoSat-2 mission or regions with invalid measurements, the WTC can be calculated from global grids of two single-level parameters provided by global atmospheric models, such as the ECMWF. These two parameters are the total column water vapour (TCWV, expressed in mm or, the equivalent, kg/m²) and two-meter temperature (T_0) that is the near-surface air temperature (Bevis et al., 1992, 1994).

$$WTC = - \left(0.101995 + \frac{1725.55}{T_m} \right) \frac{TCWV}{1000} \quad (4)$$

Eq. (4) represents the expression to compute the WTC in meters from global grids of atmospheric models, where T_m is the mean temperature of the troposphere in Kelvin, which can be modelled from T_0 according to Eq. (5) also in Kelvin (Mendes et al., 2000).

$$T_m = 50.440 + 0.789T_0 \quad (5)$$

Eqs. (4) and (5) allow to compute the WTC at the same level of the atmospheric parameters, which is the model orography. The orography heights can depart from the actual surface heights by hundreds of meters, depending on the region, so this first model-derived WTC can be affected by an error due to the use of a wrong altitude. With an appropriate height reduction, WTC can be computed at the surface level using an accurate DEM.

Due to its large variability in space and time, the dependence of water vapour with height is not easy to model. (Kouba, 2008) developed an empirical expression to model this dependence, represented in Eq. (6).

$$WTC(h_s) = WTC(h_0) e^{\frac{h_0 - h_s}{2000}} \quad (6)$$

In Eq. (6), h_0 and h_s are the orthometric heights in meters of the model orography and surface, respectively. This altitude modelling of the WTC still has some limitations, namely it should not be used to perform WTC height reductions larger than 1000 m (Kouba, 2008). This equation for the altitude modelling of the WTC needs further developments due to its limitations. In spite of its limitations, it is very relevant, namely over inland waters. Tropospheric corrections over these regions are often provided at orography level, so this reduction is crucial to compute the WTC at correct altitude over continental waters.

2.1.2.3. Data description

The analyses for each region of interest were performed using various data sources: CS-2 altimetry data, global grids of various parameters from an atmospheric model, mean lake levels and mean river profiles derived from satellite altimetry, a digital elevation model and a geoid model.

For all ROIs except for the Caspian Sea, the CS-2 L1B data were processed by isardSAT in the scope of the ESA funded SHAPE project, spanning the year 2015 or 2016, depending on the ROI. These are SAR mode data for the Amazon basin and Lake Vanern and SARIn mode reduced to SAR for Danube and Titicaca. This SAR L1B product has been produced using FBR Baseline C as input. These are pass files at 20 Hz containing data over and around each river or lake of interest. For simplification and reference to other data sets, when referring to these CS-2 pass files the sub-cycle of 27 or 29 days and pass number are used, as defined in the Radar Altimeter Data Base System (RADS). In the Caspian Sea, CS-2 1 Hz data from the CS-2 Geophysical Ocean Products available at the ftp server 131.176.221.36, under the scope of the ESA project CryoSat IPF/COP Maintenance and Evolution Support were used for the year 2014.

ECMWF operational model at $0.125^\circ \times 0.125^\circ$ spatial sampling and 6-h intervals was adopted (Miller et al., 2010). The following fields were used: sea level pressure (SLP) in the computation of the DTC and total column water vapour (TCWV) and 2-metre temperature (T0) in the computation of the WTC.

The Altimeter Corrected Elevations 2 (ACE2) digital elevation model, at its highest spatial resolution (3'') was adopted (Berry et al., 2008). This DEM is provided in tiles of $15^\circ \times 15^\circ$, so according to the location of each ROI some procedures are required, as merging and clipping. The European Improved Gravity model of the Earth by New techniques (EIGEN-6C4) geoid model, complete up to maximum degree and order 2190, has been selected (Förste et al., 2014).

For the river ROIs, mean river profiles have been derived and provided by Along-Track (ATK). For the Amazon basin ROI, this is a high water level profile for the year 2014. It has been derived from inter-calibrated, edited and filtered Jason-2 and SARAL data for distances between 400 km and 2100 km from the ocean. The remaining section, between 0 km and 400 km, has been extrapolated. Points along the profile were interpolated every 10 km using a 2nd order spline (Bercher et al., 2016).

For the Danube ROI, a mean river profile has been derived for the years 2010–2015 from edited and filtered Jason-2, SARAL and CryoSat-2 data for distances between 0 km and 2500 km from the river mouth in the Black Sea. It is important to note that the Danube profile is different from the Amazon one. While for the Amazon it is just a polyline along the central part of the river, for the Danube it is a set of points covering the main river path, also modelling river width.

For the lakes and closed sea regions, polygons from the Natural Earth dataset (<http://www.naturalearthdata.com/>) have been used to decide whether the along-track point was inside or outside the lake/sea.

Atmospheric pressure data from The International Surface Pressure Databank (ISPD) have been used for comparison with model-derived DTC, in the analysis of the dry tropospheric correction. GNSS-derived zenith total delays (ZTD) from the International GNSS Service (IGS) and from the EUREF Permanent Network (EPN) have been used to estimate GNSS-derived WTC for comparison with model-derived WTC.

2.1.2.4. Methodology

Considering the height dependence of the tropospheric corrections, the analysis of the DTC and WTC errors requires a proper inspection of the height variations within each ROI.

For this purpose, for each CS-2 measurement point in a given ROI, three altitudes have been considered and inspected: (i) the mean water level profile (hprofile) or mean lake/sea level (hmean), for a river or lake/sea, respectively; (ii) the interpolated altitude from the ACE2 DEM at its highest resolution (hdem) and (iii) the interpolated altitude from the ECMWF orography (horo). hprofile and hmean have been determined from altimeter data as described in Sections 2.1.2.3 and 2.1.3.1, respectively.

For this analysis, according to each river and the corresponding profile, CS-2 points up to 20 km and 2 km from the nearest point in the profile of the Amazon and the Danube, respectively, are considered, while for lakes/seas only points inside the water body are analysed. For each one of these examined CS-2 points, hprofile is equal to the height of the closest point in the river profile, hmean assumes the same value for all CS-2 measurements inside the lake or sea and hdem and horo are obtained with a bilinear interpolation from the ACE2 DEM and ECMWF orography, respectively.

For the computation of the tropospheric path delays, the expressions mentioned in Section 2.1.2.1 for the DTC and in Section 2.1.2.2 for the WTC were adopted. Both tropospheric corrections are computed at three different levels (hprofile or hmean, hdem and horo).

For the DTC, surface pressure grids are obtained from SLP grids using Eq. (2) at these three levels and for each model grid node, and these grids are then used to compute the DTC at the corresponding levels using Eq. (1). With these grids of DTC, for each CS-2 measurement, three DTC are interpolated in space and then interpolated at the measurement time instant using the two closest in time model grids, six hours apart. At each ROI and for each CS-2 point four DTC are analysed:

- (i) DTC alt – provided in the CS-2 altimetric data products;
- (ii) DTC oro – computed from SLP at orography level (horo);
- (iii) DTC hdem – computed from SLP at ACE2 DEM height (hdem);
- (iv) DTC profile – computed from SLP at hprofile level (for rivers) or DTC mean – at the mean water level (for lakes and Caspian Sea).

For the WTC, for each model grid node, the correction is firstly computed at the orography height, using Eqs. (4) and (5). With Eq. (6), WTC is computed by a height reduction at the other levels (hdem, hprofile or hmean). For each CS-2 measurement, various WTC are interpolated in space and time. Thus, for each CS-2 point, four WTC are analysed:

- (i) WTC alt – as provided in the CS-2 altimetric products;
- (ii) WTC oro – computed from TCWV and T_0 , at the level of model orography (horo);
- (iii) WTC hdem – computed from TCWV and T_0 , reduced to the ACE2 DEM height (hdem);
- (iv) WTC profile – computed from TCWV and T_0 , reduced to hprofile (for rivers) or WTC mean – reduced to the mean water level height (hmean), for lakes and Caspian Sea.

Firstly, the assessment of the errors due to the height dependence of the tropospheric corrections present on CS-2 products is performed through the comparison between the various corrections, computed at different levels.

Secondly, once these errors are corrected for, remaining errors in the tropospheric corrections are assessed through their comparison with tropospheric corrections derived from in situ independent observations, providing an independent assessment of model-derived corrections, once computed at the correct surface elevation.

At barometric stations available at each ROI, measurements of in situ surface pressure allow to derive the DTC at each station location using Eq. (1). DTC from SLP model fields is computed at each in situ measurement location by bilinear interpolation in space followed by linear interpolation in time. DTC computed from ECMWF at sea level is then reduced to surface elevation, allowing the comparison with DTC computed from in situ pressure data at station height, using directly Eq. (1).

On the other hand, GNSS-derived WTC at GNSS stations in the vicinity of each ROI, when available, are compared with the corresponding correction from ECMWF computed at the GNSS station height. The quantity estimated at each GNSS station is the zenith tropospheric delay (ZTD) at station level, which corresponds to the sum of the zenith hydrostatic delay (ZHD) and the zenith wet delay (ZWD). The quantity of interest for the altimetry over inland water regions is the zenith wet correction, which can be obtained from the ZTD at station level by computing the dry tropospheric correction or ZHD from SLP fields using Eq. (1) and reducing this DTC to the same station level. With both (ZTD and ZHD) estimated at the same level, ZWD or GNSS-derived WTC can be estimated with the same accuracy and compared to the corresponding correction computed from ECMWF, reduced to the same level.

Note that these independent comparisons are performed at stations within each ROI, but not exactly located over a river or over a lake. However, this is valid in this context. In this independent assessment the objective is to compare DTC/WTC computed from ECMWF and the corresponding corrections computed with in situ data, at the same level, to evaluate the model-derived DTC/WTC errors. Since as all corrections are computed at the same surface level, no altitude related errors will occur.

2.1.3. Assessment of tropospheric corrections present on CS-2 products

After introducing the application of satellite radar altimetry over inland water regions, with focus on the tropospheric corrections in Section 2.1.1 and the data and methodology to derive these corrections from an atmospheric model in Section 2.1.2, this section presents the assessment of the tropospheric corrections present on CS-2 products.

Firstly, a comparison between DTC and WTC present on CS-2 products and the corresponding corrections computed using the methodology presented in Section 2.1.2 is performed. Secondly, for the DTC a comparison with in situ pressure data is presented, while for the WTC a comparison with GNSS-derived WTC is performed, for the regions where GNSS data are available.

Tropospheric corrections present in altimeter products are often provided at sea level or at the height of the orography of the adopted atmospheric model. Over inland water regions, model orography can depart from the actual surface level by hundreds of meters, which induce DTC errors of several cm (2.5 cm per each 100 m). Thus, the analysis of the tropospheric corrections errors requires a proper inspection of the height variations in each region of interest. For this purpose, an analysis of the altitudes is performed within each ROI.

2.1.3.1. Altitude analysis

For an accurate retrieval of model-derived tropospheric corrections over continental water surfaces, which are initially computed at model orography level, the modelling of the height dependence of both tropospheric corrections is a crucial step. The altimetric level of interest over inland waters is the surface altitude of lake, reservoir or river, so the tropospheric corrections should be computed at this level, for a proper application of satellite altimetry over these regions. When the corrections are derived from atmospheric models, they are computed at model orography height, being the orography a smoothed representation of the surface relief. The orography is originally in the spectral domain, so it is obtained by means of a transformation between the spectral and the physical space domains. This transformation, when used to represent fields with sharp spatial gradients or discontinuities, such as the topography, can originate Gibbs oscillations in the vicinity of the discontinuities (Navarra et al., 1994).

Since any error in altitude has a direct impact in the corresponding corrections, particularly for the DTC, the altitude variations in each region of interest have been inspected by using three different altitudes, as mentioned in the methodology: the model orography, the ACE2 DEM and the mean river profile or mean lake/sea level.

Using data from Envisat and Saral/AltiKa for the period 2002.7 to 2016.2, extracted from RADS, mean lake levels of 3809.5 ± 0.6 m, 44.9 ± 0.3 m and -26.7 ± 0.4 m have been obtained for the Titicaca and Vanern lakes and the Caspian Sea, respectively.

Figs. 2-6 represent the five ROIs analysed in this study – Amazon and Danube rivers, Titicaca and Vanern lakes and Caspian Sea, respectively. The background field represents the altitude above geoid of the ACE2 DEM, at resolution of 5 arcminutes (left or top panel), or the altitude above geoid of the ECMWF model orography (right or bottom panel), while black points/lines represent the mean river profile or lake/sea borders. For each ROI, the colour scale is different, being saturated at certain values, in order to better observe the river, lake or sea and the surrounding relief. Note that the ECMWF operational model orography undergoes temporal changes, coincident with model updates (Miller et al., 2010). In the analyses performed in this study, the orography of the last model update, in May 12, 2015, has been used. Note that although in the figures a lower resolution version of the ACE2 DEM has been selected, in the analyses the model at its highest resolution (3") has been adopted.

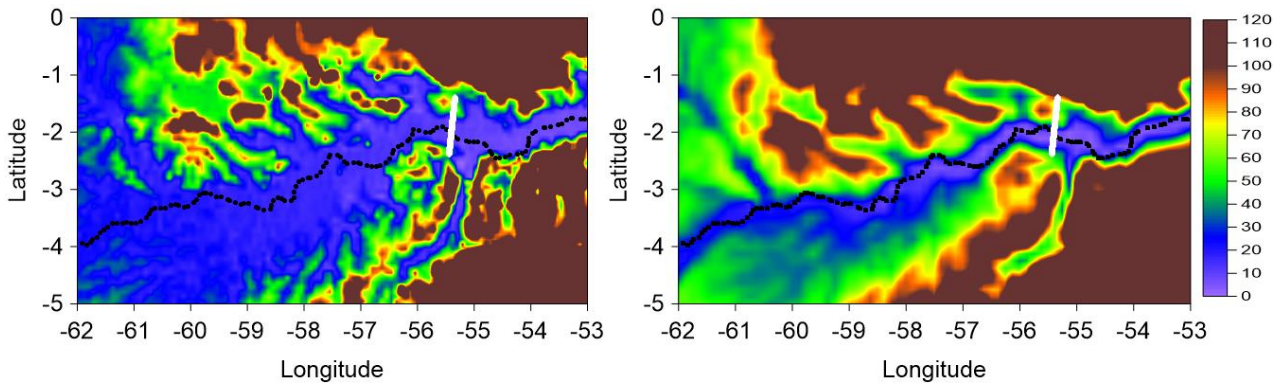


Figure 2. Altitudes in meters above geoid of the ACE2 DEM 5' (left panel) and of the ECMWF model orography (right panel), over the Amazon basin. Black points represent the mean river profile and white points represent pass 20 of CS-2 sub-cycle 62.

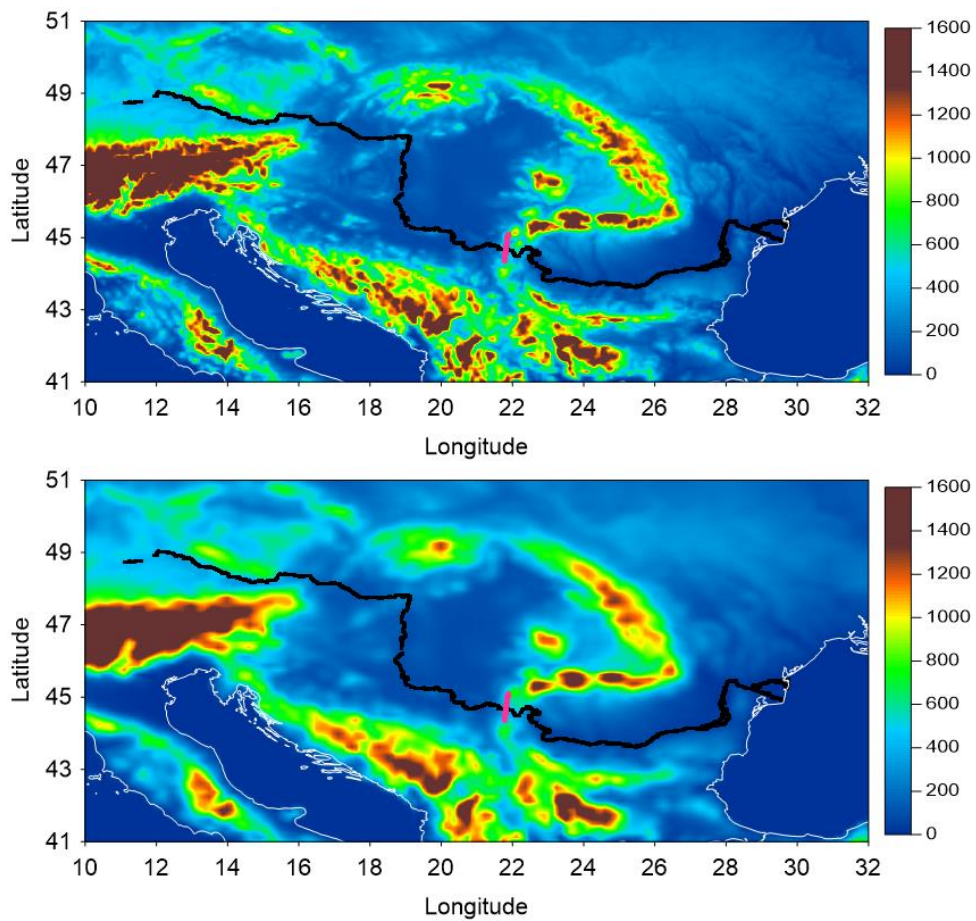


Figure 3. Altitudes in meters above geoid of the ACE2 DEM 5' (top panel) and of the ECMWF model orography (bottom panel), over the Danube river. Black points represent the mean river profile and pink points represent the pass 188 of CS-2 sub-cycle 62.

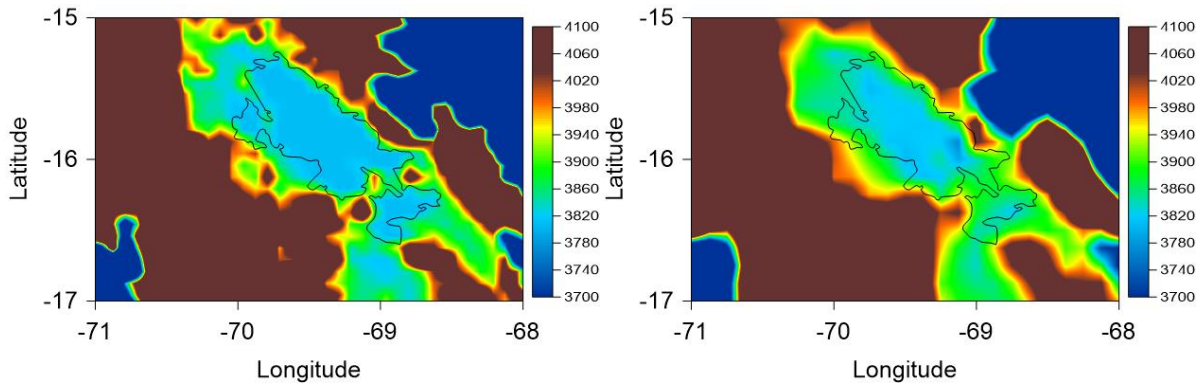


Figure 4. Altitudes in meters above geoid of the ACE2 DEM 5' (left panel) and of the ECMWF model orography (right panel), over Lake Titicaca. Black line represents the lake border.

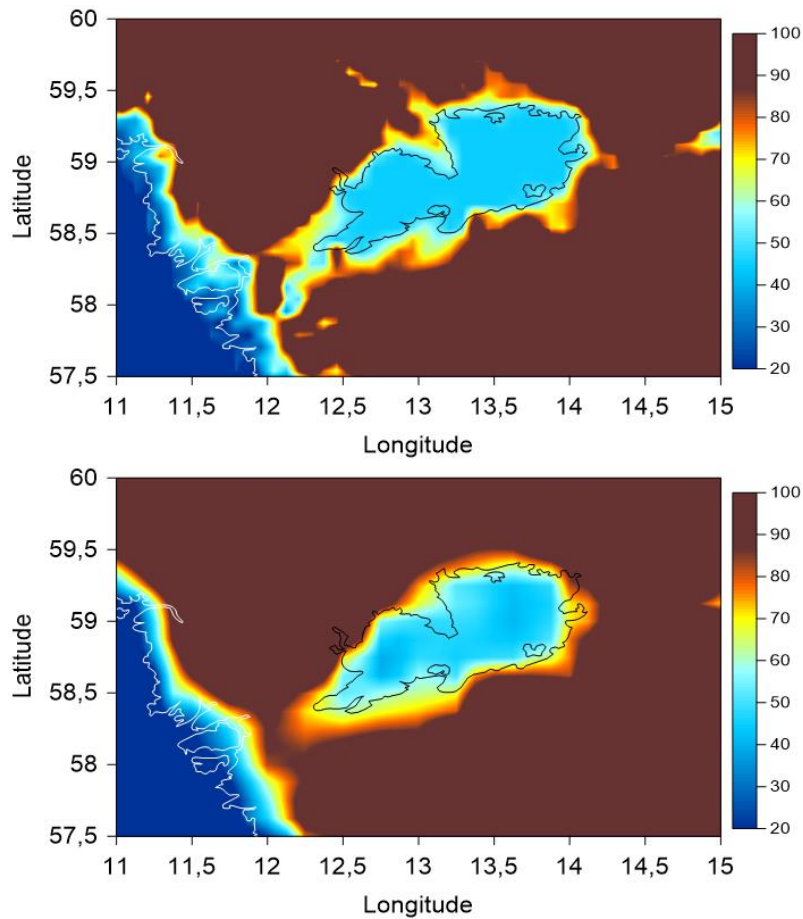


Figure 5. Altitudes in meters above geoid of the ACE2 DEM 5' (top panel) and of the ECMWF model orography (bottom panel), over the Vanern lake. Black line represents the lake border.

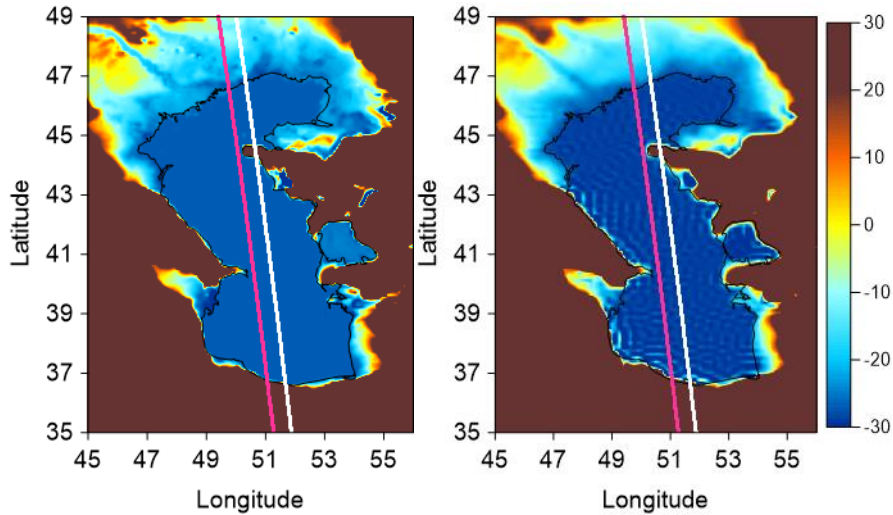


Figure 6. Altitudes in meters above geoid of the ACE2 DEM 5' (left panel) and of the ECMWF model orography (right panel), over the Caspian Sea. Black line represents the sea border and pink and white points represent passes 489 of CS-2 sub-cycles 51 and 52, respectively. Note that on the right panel Gibbs effects mentioned above can be observed on the ECMWF orography inside the Caspian Sea.

Fig. 7 shows examples of the analysis performed to inspect the altitudes of the ACE2 DEM (hdem) and of the ECMWF orography (horo) in comparison with the mean river profile (hprofile) or the mean lake/sea level (hmean). Altitudes above geoid in meters along the Amazon River profile are represented in the left panel, function of the distance to the ocean in kilometres. ACE2 DEM heights (blue) are closer to the mean river (red) profile heights, than the ECMWF orography (green) heights, however height errors up to 120 m exist in ACE2 in a narrow strip at about 700 km from the ocean, which corresponds to a region between longitudes 54°W and 55°W (see Fig. 2). Apart from this narrow strip, the standard deviation of the differences between hdem and hprofile is about 2.3 m, while for the differences between horo and hprofile the same value is almost 8 m.

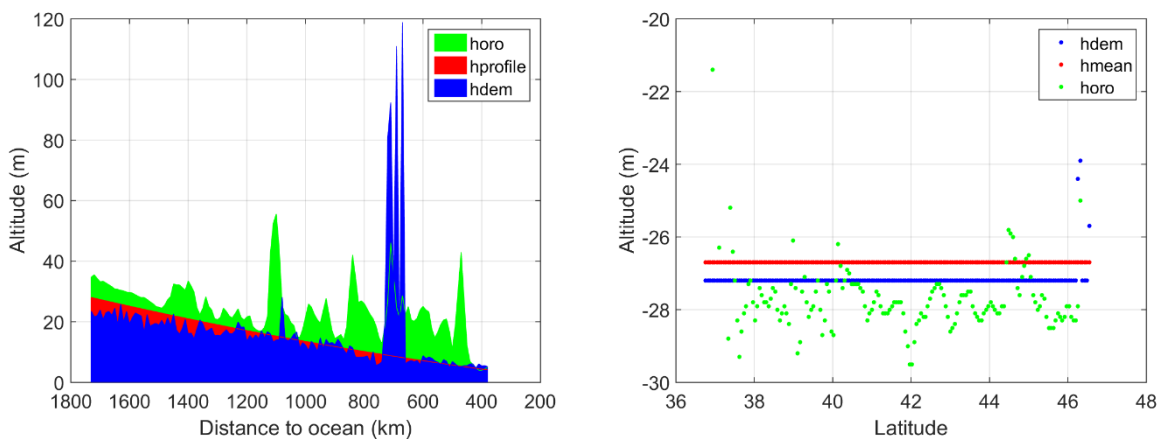


Figure 7. Various altitudes (hdem – blue, hprofile and hmean – red, horo – green) above geoid, in meters, along the Amazon river profile (left) and along CS-2 sub-cycle 51, pass 489 over the Caspian Sea (right). In the right panel, larger altitude values exist close to the sea border: -24 m for hdem and 61 m for horo.

The right plot of Fig. 7 represents the altitudes for CS-2 sub-cycle 51, pass 489, over the Caspian Sea (see Fig. 6). It is evident the proximity between h_{mean} and h_{dem} , with a constant difference of 0.1 m, apart from some CS-2 measurements close to the sea border. This altitude difference corresponds to an insignificant error in the tropospheric corrections. The altitudes interpolated from ECMWF orography (shown by the green points) over the Caspian Sea do not have a constant value and are noisy, due to the Gibbs effects mentioned above.

The overall results show a close proximity (0.1–0.5 m) between h_{dem} and h_{mean} over the Caspian Sea and lakes, apart from CS-2 points close to the lake/sea border. Considering only points inside the lake or sea, the standard deviation of the differences between h_{dem} and h_{mean} is 11, 4 and 1 m for Titicaca, Vanern and Caspian, while the same value of the differences between h_{oro} and h_{mean} is 34, 11 and 14 m for the same regions, respectively. Considering the same points inside the lake or sea, the maximum absolute value of the differences between h_{dem} and h_{mean} is 211 m, 93 m and 62 m for Titicaca, Vanern and Caspian, while the corresponding value of the differences between h_{oro} and h_{mean} is 168 m, 66 m and 624 m for the same regions, respectively. It can be observed that, although the standard deviation of the differences may not be very large, the maximum absolute differences between the orography and the mean lake level reach several hundreds of meters. Therefore, it is expected that these height differences induce systematic DTC errors in the range from 2 to 10 cm.

Table 1 shows the statistical parameters of the altitude differences over the Caspian Sea, considering only CS-2 points inside the sea polygon. Altitudes from ACE2 DEM are much closer to the h_{mean} , than altitudes from ECMWF orography over these lakes and closed sea, so tropospheric corrections over these water bodies are impacted by height errors when computed at the level of the ECMWF orography. For the computation of the tropospheric corrections over lakes/seas, errors in ACE2 altitudes are insignificant, apart from the narrow zones close to the sea/lake borders, where errors in these altitudes can reach dozens of metres (e.g. 62 m in the Caspian Sea, as shown in Table 1). Due to these facts, the best surface height to compute the tropospheric corrections for the lakes and the Caspian Sea is the mean water level derived from satellite altimetry measurements.

Table 1. Statistical parameters (minimum (min), maximum (max) and mean values and standard deviation (std)) of the altitude differences, considering only CS-2 points inside the Caspian Sea.

	Min (m)	Max (m)	Mean (m)	StD (m)
$h_{\text{dem}}-h_{\text{mean}}$	-9.40	61.50	-0.37	0.82
$h_{\text{oro}}-h_{\text{mean}}$	-59.70	623.40	0.95	13.91

The altitude analysis is different for the river ROIs, since the width of each river is not constant and some CS-2 points outside the rivers, over the surrounding areas, can be incorrectly considered. Table 2 shows the statistics of the altitude differences, considering only points in the Danube River mean profile. Analysing Fig. 3, it can be observed that the Danube ROI has some very narrow regions, with high mountains surrounding the river banks, such as that seen at the 12°–16°E longitude range (Germany and Austria) and also at longitude around 22° (border between Romania and Serbia).

Therefore, over these regions, the altitude values given by the altimetric surfaces under consideration will vary greatly for the CS-2 measurements close to the river. Unlike lakes or closed seas, the best set of CS-2 measurements for assessing the tropospheric corrections over rivers is a difficult choice. While for the lakes or seas, the polygons allow to choose only the CS-2 points over the water surfaces, for rivers the mean profiles only allow to compute the distance of each CS-2 point to the mean river profile.

Table 2. Statistical parameters of the altitude differences along the Danube River mean profile.

	Min (m)	Max (m)	Mean (m)	StD (m)
$h_{\text{profile}} - h_{\text{dem}}$	-100.13	74.49	-0.86	6.24
$h_{\text{profile}} - h_{\text{oro}}$	-368.74	20.82	-57.85	58.24

As observed in Table 2, for the Danube river, h_{dem} are much closer to the h_{profile} than h_{oro} , however height errors in ACE2 DEM larger than 100 m can be observed. As for lakes and the Caspian Sea, altitudes from ECMWF orography should not be used to compute suitable tropospheric corrections for these rivers. Values of the standard deviation of the differences between h_{profile} and h_{dem} and between h_{profile} and h_{oro} along the Danube river profile are around 6 and 58 m, respectively. The latter difference has an absolute mean value close to the standard deviation, which corresponds to a systematic error in the altitudes from ECMWF orography, relative to the altitudes of the Danube mean profile. Maximum absolute values for $h_{\text{profile}} - h_{\text{dem}}$ and for $h_{\text{profile}} - h_{\text{oro}}$ are 100 m and 369 m, respectively, inducing DTC errors of 2.5 cm and 9 cm respectively.

Overall, it can be concluded that altitudes from ACE2 DEM have systematic errors larger than 100 m in some regions, namely those close to the sea or lake borders or in narrow river basins. These systematic errors in altitude can induce errors e.g. larger than 2 cm in the DTC. The orography level is not recommended to compute the tropospheric corrections over these regions of interest, since altitudes from the ECMWF orography do not follow closely the river, lake or sea mean level at each ROI.

Despite the fact that the ACE2 DEM is a relatively good reference surface in the majority of the regions, considering the overall results, the best surface to compute the tropospheric corrections is the height of the closest point in the mean river profile, for rivers, and the mean level for lakes and seas.

Alternatively, if accurate altimeter derived surface heights are available, from tuned retracking algorithms, uncorrected for tropospheric corrections, these can also be a valid altimetric source to derive the tropospheric corrections.

2.1.3.2. Analysis of the DTC

Once the height variations in each ROI have been examined, the corresponding DTC errors have been analysed and the results are presented in this section.

DTC height dependence errors

The analysis of the DTC present on CS-2 products is here performed through the comparison with the corresponding correction computed at three different levels (hdem, horo and hmean for sea/lakes or hprofile for rivers), according to the methodology described in Section 2.1.2. This first analysis allows to inspect the DTC present in CS-2 products by comparing it with those computed at different levels, and therefore to understand the effect of the altitude errors in the DTC. For this purpose, the analysis over some individual CS-2 passes is first presented with two examples, followed by an overall analysis for the regions of interest, namely by means of the statistical parameters of the DTC differences.

Fig. 8 represents examples of this DTC analysis for two ROIs. On the left, the various DTC are represented (bottom panel) along with the corresponding height levels (top panel), both in meters, function of distance to the first point of the pass in kilometres, for CS-2 sub-cycle 62, pass 188, over the Danube River (see Fig. 3). On the right, the same DTCs are represented for CS-2 sub-cycle 51, pass 489, over the Caspian Sea (see also Fig. 6), function of latitude.

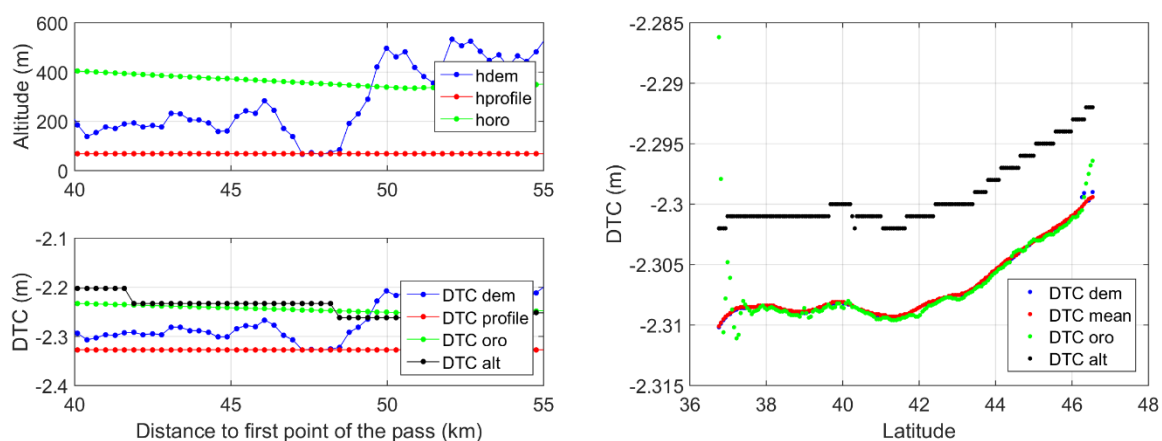


Figure 8. Various DTC (bottom left panel) and height surfaces (top left panel) for CS-2 sub-cycle 62, pass 188 (see also Fig. 3), over the Danube river. Various DTC in meters for CS-2 sub-cycle 51, pass 489 (see also Fig. 6), over the Caspian Sea (right panel).

Analysing the track over the Danube River, that intersects the river in a narrow region (between 45 and 50 km from the first point of the pass), it is possible to see the river width, where hdem (blue) is very close to hprofile (red). In the right panel, only points inside the Caspian Sea, for which hmean and hdem are very close (see right panel in Fig. 7) are considered. This analysis allows the inspection of the errors in the DTC related to its height dependence, which induce systematic errors, with varying magnitude depending on the zone.

In the example for the Danube River, the DTC computed at the orography level (green) and the DTC included in the altimetric products (black) are very close. Over the river, the DTC derived at the DEM surface level (blue) and at the level of the mean river profile (red) are also very close, while a difference of about 9 cm is observed between DTC computed at river level and DTC alt. This

difference is due to the height difference between the ECMWF orography used in DTC alt and the altitude of the river profile use in DTC profile which will always be of the same magnitude, thus it will be systematic. Even if CryoSat-2 would be making measurements over this region for a long time and DTC alt is derived in the same way, the error will not decrease.

Comparing the two panels on the left in Fig. 8, it is evident the well-known relation between altitude and DTC, according to Eqs. (1) and (2). It can also be observed that the DTC variation with height dominates the DTC signal, being much larger than the corresponding space/time variation. Since there is a quasi linear relationship between height errors and DTC errors, the results presented in the previous section for the height errors can be translated into the corresponding DTC errors.

For the example concerning the Caspian Sea, all DTC are similar, apart from the DTC present in the CS-2 products (black). The right panel of Fig. 8 shows a clear systematic difference, although small (0.7 cm), between DTC alt and the other ones.

Apart from the Caspian Sea, for the large majority of the tracks, as illustrated in the left panel in Fig. 8 for the Danube ROI, there is a close proximity between DTC alt and DTC oro, suggesting that, as expected, the DTC present in the CS-2 products is provided at the ECMWF model orography. On the contrary, for the Caspian Sea that has an altitude below sea level (-26.7 ± 0.4 m), the DTC present in the CS-2 products seems to be provided at the mean sea level (zero level), since the observed systematic differences in the DTC correspond to a difference in altitude of ~ 27 m.

For the overall analysis of the DTC and WTC differences, statistics are determined examining only points up to 20 km and 2 km from the river mean profile, for the Amazon and Danube rivers, respectively. For the Caspian Sea and lakes, only points inside the polygons are examined.

Table 3 shows the statistics of the DTC differences for the Amazon basin, in centimetres, analysing measurements up to 20 km from the mean river profile, considered representative of the errors in the river basin, with possible overestimation. On the other hand, considering that for the Danube, the river profile consists of a mesh of points over the river and not just a polyline, as for the Amazon, the points over the Danube basin have been selected considering only points up to a short distance (2 km) from the river profile. Table 4 shows the same statistics for the Caspian Sea, considering only CS-2 measurements inside the sea.

Table 3. Statistical parameters of the DTC differences considering CS-2 measurements up to 20 km from the Amazon mean river profile.

	Min (cm)	Max (cm)	Mean (cm)	StD (cm)
$DTC_{dem} - DTC_{alt}$	-3.51	2.91	-0.31	0.55
$DTC_{oro} - DTC_{alt}$	-2.02	1.34	-0.13	0.32
$DTC_{alt} - DTC_{profile}$	-0.33	3.49	0.35	0.50
$DTC_{dem} - DTC_{profile}$	-0.44	3.37	0.03	0.38
$DTC_{oro} - DTC_{profile}$	-0.27	2.42	0.22	0.42

Table 4. Statistical parameters of the DTC differences considering only CS-2 measurements inside the Caspian Sea.

	Min (cm)	Max (cm)	Mean (cm)	StD (cm)
DTC_{alt}-DTC_{mean}	0.56	6.16	0.73	0.18
DTC_{dem}-DTC_{mean}	-0.25	1.74	0.00	0.02
DTC_{oro}-DTC_{mean}	-1.64	15.29	0.03	0.37

Statistical parameters shown in Table 3 and Table 4 reinforce the observations above. As observed in the analysis of individual plots, the overall statistics show that, apart from the Caspian Sea, the DTC present in CS-2 products is closer to the one computed at the ECMWF orography level than to the DTC computed at ACE2 DEM height. For the Caspian sea, the mean value of 0.73 cm in the differences between DTC alt and DTC mean is correlated with a variation in DTC of ~ 27 m in altitude, suggesting that DTC alt for this closed sea is provided in CS-2 products at mean sea (zero) level. On the other hand, DTC hdem and DTC hmean are also very close, evidencing that the ACE2 DEM follows the lake/sea mean level or river profile altitude closely in most of the profiles. However, DTC computed at the level of ACE2 DEM height has large errors in some specific regions, namely close to lake borders and in certain narrow river basins.

Overall, results show that the mean and standard deviation of the analysed DTC differences are always small for all ROI. However, these statistical parameters are not representative of the DTC errors in some of these regions, since these errors are systematic, always having the same magnitude and sign at a given location. Therefore, the maximum and minimum values or the maximum absolute value of the differences give a more realistic idea of the magnitude of the errors, even if they occur over a small percentage of points in each region.

Although the overall results show that the DTC errors present in CS-2 products over the Amazon ROI are small, in some regions of interest they can reach several centimetres (e.g. 6 cm in the Caspian Sea). Differences between DTC computed at the level of the nearest point in the mean river profiles and corresponding correction computed at remaining levels are larger in the Danube, in comparison with the same analysis for the Amazon ROI. These larger values in the standard deviation of the differences are due to the large variation of the altitude within the 2-km buffer around the mean Danube river profile. Analysing the Danube ROI, as mentioned in Section 2.1.3.1, it is possible to identify two regions along the river where the altitude variations and consequently the DTC errors in the vicinity of the river are much larger. Although the mean and standard deviation of the differences are relatively small, the extreme values can be very large, reaching values larger than 10 cm.

For lakes Titicaca and Vanern, the errors in DTC alt can reach 6 cm, while the standard deviation of the differences is less than 1 cm. The ACE2 DEM errors cause DTC errors up to 4 cm in some narrow bands close to the lake or sea borders. Overall, both the DTC present in the CS-2 products and the DTC oro have errors in some parts of the lakes that may reach 2–6 cm. These are systematic errors that will affect all measurements over the same location in the same way. For the Caspian Sea,

a clear systematic error of about almost 1 cm is observed in the DTC provided in CS-2 products, related to the fact that in this ROI, these corrections are computed at sea level, when the surface altitude is -26.7 ± 0.4 m.

Although the overall results show that the DTC errors present in CS-2 products are small (mean and standard deviation of the differences small), in some zones either in lakes/seas or rivers they can be larger than 5 cm, namely in the Danube ROI and in the Caspian Sea.

For rivers, this analysis shows that the best altimetric practice for the computation of the DTC is the use of the river mean profile and the association of each measurement point to the height of the closest point in the river profile. If a river mean profile is available, this approach should produce DTC accurate to better than 1 cm. Although, overall the use of the ACE2 DEM leads to a better accuracy than the use of the model orography, large errors can occur in specific regions as for example in Amazon. Moreover, since these errors are height dependent they are systematic and will strongly affect the determination, for example, of water level time series (see e.g. Fig. 4 in (Fernandes et al., 2014)). For lakes or closed seas, this analysis shows that the best altimetric source for the computation of the DTC is the mean lake level. By estimating the tropospheric corrections of the points inside the lake at the mean lake level, DTC accurate to better than 1 cm should be obtained.

For the computation of the DTC at the level of the ACE2 DEM, two different ECMWF pressure fields have been used: (i) SLP followed by the height reduction from sea level to surface height; (ii) surface pressure followed by the height reduction from model orography to surface height. Results suggest that both ways of computing the dry path delay provide similar values. For this reason, the computation from SLP is usually preferred since it does not require the knowledge of the model orography, so all corrections at DEM level have been computed from this field.

Comparison with in situ pressure data

To evaluate the absolute errors of the dry path delay determined from ECMWF fields, the DTC derived from ECMWF using SLP, reduced to surface elevation, as provided in the ISPD data files, was compared with the DTC derived from pressure observations downloaded from The International Surface Pressure Databank, for the year 2013, the most recent epoch available in this data base. This comparison is performed at station location, for stations close to each ROI. Table 5 shows the root mean square, in centimetres, of these differences for each ROI.

Table 5. Root Mean Square (RMS) of the differences between DTC computed from SLP (ECMWF) reduced to surface elevation and DTC computed from pressure data from ISPD, in centimetres.

ROI	RMS (cm)
Amazon	0.7
Danube	0.6
Titicaca	0.5
Vanern	0.1
Caspian	0.8

RMS values of the differences between DTC computed from ECMWF SLP reduced to surface elevation and DTC computed from pressure data from ISPD are 0.1 cm, 0.5 cm, 0.6 cm, 0.7 cm and 0.8 cm for Vanern, Titicaca, Danube, Amazon and Caspian regions, respectively. In the Danube ROI, a very small number of stations (<1%) were rejected for having erroneous data.

These values indicate that the absolute errors in the ECMWF pressure fields and corresponding errors in the DTC are negligible in these regions.

Overall DTC assessment

Table 6 presents, for all analysed ROIs, the statistical parameters (mean and standard deviation, std) of the dry tropospheric correction once computed at the mean river profile or mean lake/sea level, as well as the maximum absolute errors present in CS-2 products related with the height dependence of the corrections. The third column represents the maximum absolute difference between DTC alt and DTC mean or DTC profile. This table does not intend to compare the errors in DTC alt related to the height dependence of the DTC with the mean and standard deviation of this correction computed at mean level (DTC profile or DTC mean), but rather to summarize a set of relevant statistics for each ROI. It summarizes the space–time variability of DTC computed at correct surface elevation within each ROI and the errors present in this correction provided in CS-2 products, which is the focus of this paper.

Table 6. Mean (in meters) and standard deviation (in centimetres) of the DTC computed at the level of mean river or mean lake (DTC profile or DTC mean) and maximum absolute error present in the DTC provided in CS-2 products, due to height dependence. The third column represents the maximum absolute difference between DTC alt and DTC mean or DTC profile.

ROI	Mean DTC (m)	StD DTC (cm)	Max DTC error (cm)
Amazon	-2.30	0.5	3.5
Danube	-2.30	3.0	10.8
Titicaca	-1.48	0.5	5.5
Vanern	-2.29	2.7	1.5
Caspian	-2.32	1.8	6.2

Results show that, once computed at the correct mean river profile or lake mean level, the DTC has a small space–time variation, with a standard deviation of 0.5 cm in the Amazon River and Lake Titicaca, 1.8 cm in the Caspian Sea, 2.7 cm in Lake Vanern and 3.0 cm in the Danube River. The DTC absolute values go from 1.48 m in Lake Titicaca to 2.32 m in the Caspian Sea.

Regarding the DTC uncertainties, comparison of Tables 5 and 6 demonstrate that the errors due to the height dependence of the correction are still significant, varying from a few cm up to 11 cm, while the corresponding errors for the corrections properly computed at surface height, using accurate surface height information, are smaller than 1 cm.

Statistics presented in Table 6 are related to different sets of CS-2 measurements according to each ROI and the corresponding spanning period. For the case of the Caspian ROI this period is the full

2014 year. Fig. 9 represents daily and monthly means of the DTC computed at mean sea level over the Caspian Sea function of time. It is important to note that, due to its geodetic orbit, over small regions of the Earth such as these ROIs, there are some days without any CS-2 measurements and other ones with a very few measurements. A challenge with CS-2 is the geodetic orbit, which makes time series of inland water difficult. For this reason, some noise is observed in daily means (blue points), however an annual signal in the DTC is clearly observed, mainly in monthly means (red points). Only 12 red points are observed, due to the spanning period, however they are enough to observe the annual signal of the DTC.

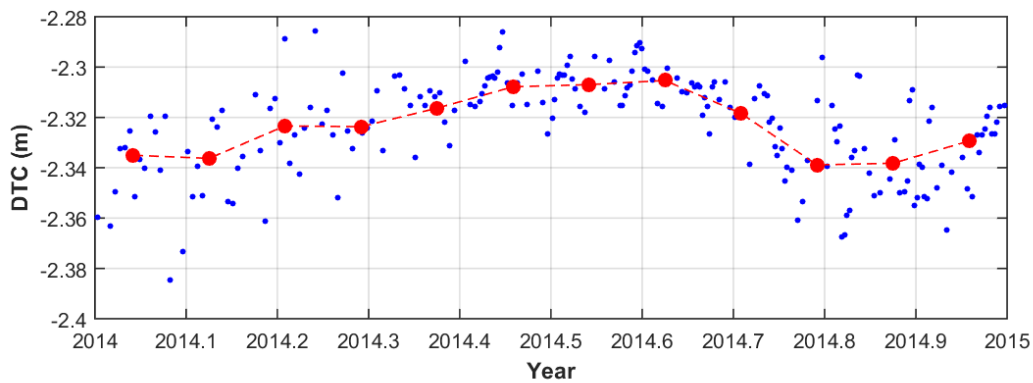


Figure 9. Daily (blue points) and monthly (red points) means of the DTC computed at mean sea level over the Caspian Sea, spanning the year 2014.

Note that in the representation of Fig. 9, as well as in the statistics in Table 6, only CS-2 measurements inside the Caspian Sea have been considered, all computed at the same level.

2.1.3.3. Analysis of the WTC

This section presents the analysis of the wet tropospheric corrections present in the CS-2 products over the analysed regions of interest.

WTC height dependence errors

As for the DTC, aiming at quantifying the errors in the wet tropospheric correction present in CS-2 products, a comparison with the corresponding WTC computed at different height levels has been performed, as mentioned in the methodology, and is presented in this section. For this and as for the DTC, an analysis over individual CS-2 passes is first presented, followed by an overall analysis for the various regions.

Fig. 10 illustrates two examples of the individual analysis of the WTC. In the left panel, various WTC are represented for CS-2 sub-cycle 62, pass 20, over the Amazon basin, function of distance to river profile (see Fig. 2). In the right panel, the same WTC are represented for CS-2 sub-cycle 52, pass 489, function of latitude, for the Caspian Sea (see Fig. 6). Unlike the DTC, there is no clear relation between WTC and altitude in these passes. As modelled by Eq. (6), the height dependence of the WTC is function not only of the surface elevation but also of the WTC itself. For the example in the Amazon, it is possible to identify the river, where the ACE2 DEM closely follows the mean river profile,

approximately for points with distances less than 20 km from the profile, where the WTC profile and WTC dem are very close. In the same example WTC alt is closer to WTC oro, than WTC dem. Over the Amazon River, there is a maximum difference between WTC alt and WTC profile of about 1.3 cm. In the example for the Caspian, all WTC are very close. The profile over the Caspian is a good illustration of the space time variability of the WTC over the closed sea, opposite to what happened for the DTC (Fig. 8, right panel).

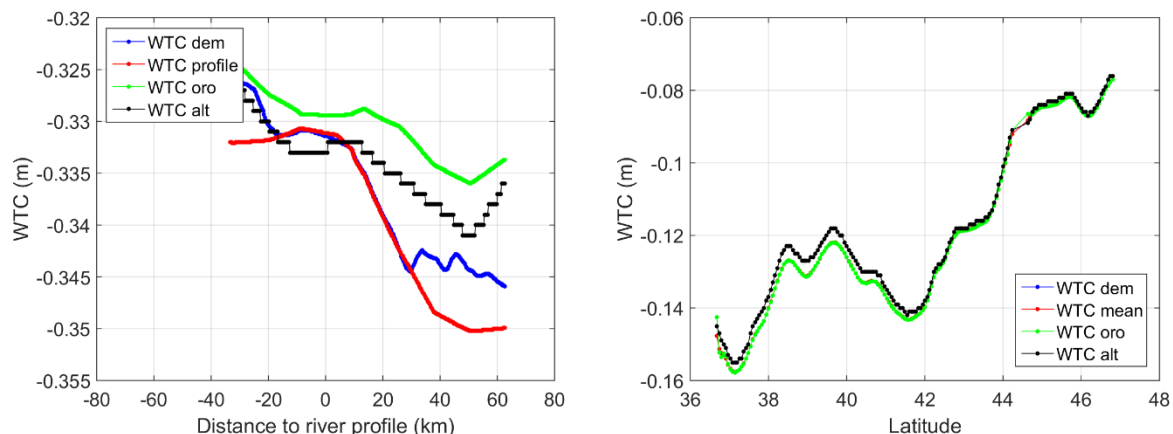


Figure 10. Various WTC for CS-2 sub-cycle 62, pass 20, over the Amazon river (left panel) function of distance to river profile and for CS-2 sub-cycle 52, pass 489, over the Caspian Sea (right panel), function of latitude. To represent both sides of the river, negative distances have been considered in one side of the Amazon.

Table 7 shows the statistical parameters of the WTC differences considering CS-2 measurements up to 2 km from the Danube river profile, while Table 8 shows the statistics considering only CS-2 measurements inside the Caspian Sea.

Table 7. Statistical parameters of the WTC differences considering CS-2 measurements up to 2 km from the Danube river profile.

	Min (cm)	Max (cm)	Mean (cm)	StD (cm)
$WTC_{dem} - WTC_{alt}$	-1.66	1.10	-0.07	0.27
$WTC_{oro} - WTC_{alt}$	-0.87	1.04	0.10	0.20
$WTC_{alt} - WTC_{profile}$	-0.40	1.84	0.16	0.31
$WTC_{dem} - WTC_{profile}$	-0.13	2.00	0.09	0.22
$WTC_{oro} - WTC_{profile}$	-0.14	2.38	0.25	0.31

Table 8. Statistical parameters of the WTC differences considering only CS-2 measurements inside the Caspian Sea.

	Min (cm)	Max (cm)	Mean (cm)	StD (cm)
$WTC_{alt} - WTC_{mean}$	-0.82	1.92	0.10	0.16
$WTC_{dem} - WTC_{mean}$	-0.05	0.21	0.00	0.00
$WTC_{oro} - WTC_{mean}$	-0.38	4.79	0.01	0.08

Statistical parameters in Table 7 reinforce the observations of Fig. 10, since overall results show that the WTC present in the CS-2 products is closer to WTC oro than to WTC dem. Considering the plots and the statistics presented above, the WTC errors related with the height dependence of the correction are larger in rivers than in lakes or Caspian Sea. On the other hand, these WTC errors are smaller in the Amazon than in the Danube, due to the fact that in the Danube region the height variations are higher than those in the Amazon region. When the zones with high altitude variation are rejected in the Danube, the extreme values of these values only reach 1.6 cm while for these zones the extreme values reach 2.4 cm.

In the left panel of Fig. 10, the step nature of the WTC present on CS-2 L1B products used in this analysis can be observed, most probably due to the fact that these corrections have been obtained by interpolation from 1 Hz observations.

Overall, results show that WTC errors of altitude are globally small, with standard deviations below 1 cm, however these errors can be larger than 1 and 2 cm in Amazon and Danube, respectively. The overall analysis of the WTC in the rivers allows to conclude that the WTC computed at the level of the closest point in the river profile shall minimize the errors due to the height dependence of the correction.

For the lakes Vanern and Titicaca, the four WTC are very similar with very small errors, lower than 0.6 cm. For the Caspian Sea, the four WTC are also very close, however WTC dem and WTC mean are much closer than all others. Although the values for the mean and standard deviation of the differences are lower than 0.2 cm, these errors can reach 2 cm (see Table 8).

For rivers, when computed at the level of the river mean profile it is expected to obtain WTC with negligible errors (<1 cm) related to the height dependence of the correction. Considering that the mean profile is the best representation of the surface height in the river basin, it is also the best reference surface for use in the WTC estimations from an atmospheric model (Eqs. (4)-(6)). For the lakes, errors in WTC present in CS-2 products due to height dependence are negligible. For the Caspian Sea, although values of mean and standard deviation of the differences are negligible, the maximum error can reach 2 cm, so the WTC should be computed at mean level derived from satellite altimetry measurements.

Comparison with GNSS-derived WTC

The comparison between GNSS-derived and ECMWF-derived WTCs is performed only for the Danube, Vanern and Caspian ROIs, since in the Amazon and Titicaca regions no GNSS stations are available. For this purpose, 25, 4 and 1 GNSS stations in the vicinity of the Danube river, Vanern lake and the Caspian Sea, respectively, have been selected. While for the Vanern and Caspian ROIs only a few GNSS stations exist, for the Danube River they have a good spatial distribution.

For the period of the CS-2 mission (2010–2016), WTC computed at two different altitudes are considered and two types of differences are computed: (i) differences between WTC obtained from GNSS and from ECMWF, both at station level (RMS of differences given by RMS1) and (ii) differences between WTC from GNSS at station level and WTC from ECMWF at orography height (RMS2). The obtained results are shown in Table 9. RMS2 indicates the error of the ECMWF-derived corrections

when reported at the orography level, while RMS1 shows the error in the model-derived WTC when reduced to surface height using Eq. (6). Considering the three regions, RMS1 is in the range from 0.7 to 1.5 cm, while RMS2 is in the range from 0.7 to 2.3 cm.

Table 9. Statistical parameters of the differences between ECMWF and GNSS-derived WTC, in centimetres.

ROI	No. of stations	RMS1 (cm)	RMS2 (cm)
Danube	25	0.8-1.5	0.8-2.3
Vanern	4	0.7-0.9	0.7-0.9
Caspian	1	1.1	1.1

These results are independent indicators that, for these regions, while the accuracy of model-derived WTC is 1–3 cm when referred to the orography model, when these WTC are reduced to surface height, even using a coarse expression such as Eq. (6), errors are reduced to values below 1.5 cm.

Overall WTC assessment

Table 10 presents, for all analysed ROIs, the statistical parameters (mean and standard deviation) of the wet tropospheric correction once computed at the mean river profile or mean lake level, as well as the maximum absolute errors present in CS-2 products related with the height dependence of the corrections. The third column represents the maximum absolute difference between WTC alt and WTC mean or WTC profile. As in Table 6, Table 10 does not intend to compare errors in the WTC due to height dependence with the mean and standard deviation of the same correction computed at mean level. It summarizes each ROI in terms of WTC errors in CS-2 products and space–time variability of the wet correction.

Table 10. Mean (in meters) and standard deviation (std, in centimetres) of the WTC computed at the level of mean river or mean lake (WTC profile or WTC mean) and maximum absolute error present in the WTC provided in CS-2 products, due to height dependence. The third column represents the maximum absolute difference between WTC alt and WTC mean or WTC profile.

ROI	Mean WTC (m)	STD WTC (cm)	Max WTC error (cm)
Amazon	-0.31	4.5	1.3
Danube	-0.11	5.3	1.8
Titicaca	-0.06	2.7	0.6
Vanern	-0.09	5.0	0.4
Caspian	-0.11	5.6	1.9

With a larger space–time variability when compared with the DTC, once computed at mean river profile or lake level, the standard deviation of the WTC goes from 2.7 cm in Lake Titicaca to 5–6 cm

in all other regions and absolute values vary from only 6 cm in Lake Titicaca, 9 cm in Lake Vanern, 11 cm in the Danube River and the Caspian Sea and 31 cm in the Amazon River.

Tables 9 and 10 demonstrate that for the WTC, unlike what happens with the DTC, the uncertainties due to the height dependence of the correction are of the same order of the corresponding absolute errors due to intrinsic model uncertainties of other origin, both in the range of 1–2 cm.

As in the previous DTC analysis, Fig. 11 represents daily and monthly means of the WTC computed at mean sea level, over the Caspian Sea. For the same reasons, some noise is observed in daily means (blue points), however a clear annual signal is also observed, mainly in monthly means (red points).

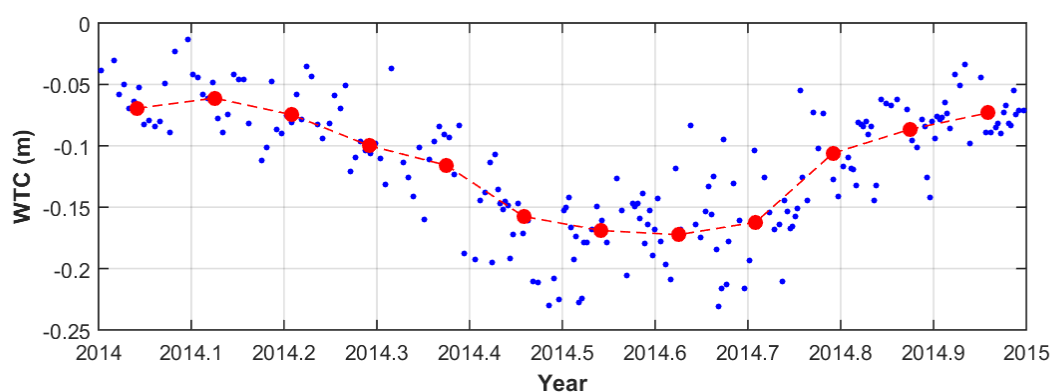


Figure 11. Daily (blue points) and monthly (red points) means of the WTC computed at mean sea level over the Caspian Sea, spanning the year 2014.

Any time series over inland waters using CS-2 measurements will be ever affected by spatial sampling, due to CS-2 geodetic orbit.

2.1.4. Conclusions

This study presents the analysis of the tropospheric corrections present on CS-2 products in five different regions of interest – Amazon and Danube rivers, lakes Titicaca and Vanern and the Caspian Sea.

Results indicate that, as expected, the CS-2 tropospheric corrections are referred to the ECMWF model orography, except for the Caspian Sea where corrections seem to be referred to mean sea level (zero level), with associated errors due to the uncertainties of this orography. Depending on the region, these height errors go from tens of meters to several hundreds of meters. These induce DTC uncertainties that can reach several centimetres (e.g. 11 cm in the Danube River) and WTC errors up to 2 cm. In the quantification of these uncertainties, small values for the mean and standard deviation are obtained, since large errors occur in a small percentage of points, e.g. in regions where the water body is surrounded by rough terrain. However, the errors related with the height dependence of the corrections are systematic, for a given location having always the same sign and magnitude, with a

stronger effect on the DTC. These systematic errors will affect the retrieval of the absolute water level (see e.g. Fig. 4 in (Fernandes et al., 2014)). Therefore, the adoption of adequate procedures to mitigate these errors is of major importance.

For rivers, considering that the mean profile is the best representation of the surface height in the river basin, it is also the best reference surface for use in the estimation of DTC and WTC from an atmospheric model. The same happens with lakes, where the corrections should be referred to the mean lake level. While mean lake level can easily be retrieved from satellite altimetry, the determination of mean river profiles can benefit from the use of water masks determined with external data such as satellite imagery.

For lakes or seas, the computation of model-derived corrections at mean lake level, previously determined from satellite altimetry, is recommended. For rivers, in the absence of an accurate mean river profile, an accurate DEM such as ACE2 can be used. Alternatively, if accurate altimeter derived surface heights are available, these can also be a valid altimetric source to derive the tropospheric corrections at each measurement point.

Results also show that, once computed at the correct mean river profile or lake mean level, the DTC has a small variation, with a standard deviation of 0.5 cm in the Amazon River and Lake Titicaca, 1.8 cm in the Caspian Sea, 2.7 cm in Lake Vanern and 3.0 cm in the Danube River. The DTC absolute values vary from 1.48 m in Lake Titicaca to 2.32 m in the Caspian Sea.

With a larger variability, once computed at mean lake level, the standard deviation of the WTC varies from 2.7 cm in Lake Titicaca to 5–6 cm in all other regions, with absolute values ranging from 6 cm in Lake Titicaca, 8 cm in Lake Vanern, 11 cm in the Danube River and the Caspian Sea to 31 cm in the Amazon River.

Results show that DTC errors in CS-2 products related with the height dependence of the correction are still significant, reaching 10 cm in certain regions. Dry path delays computed at surface level using accurate river profiles and mean lake levels are accurate to better than 1 cm, i.e. as accurate as those computed over open ocean.

For the analysed regions of interest, WTC errors of 1–2 cm were found, both related with its height dependence and due to model uncertainties of other origin. However, in regions with larger WTC variability, slightly larger errors may be found for the wet path delay.

Note that the systematic errors in the tropospheric corrections reported in this study are small compared to errors related to retracking and potential biases introduced by empirical retrackers. They are, however important to obtain accurate absolute water levels.

The fact that this study has been performed with CS-2 data, allowed the quantification of tropospheric path delay uncertainties present in altimetric products over continental water surfaces, with a spatial coverage only possible by geodetic missions such as CS-2. Despite that, results can be extended to other altimetric missions, namely Sentinel-3.

2.2. Independent Assessment of On-Board Microwave Radiometer Measurements in Coastal Zones Using Tropospheric Delays from GNSS (Article 2)

Abstract – Zenith tropospheric delays (ZTDs) computed at a network of 60 global navigation satellite system (GNSS) stations have been used to assess microwave radiometer (MWR) measurements from eight altimeter missions in coastal zones, where some of these observations become invalid. Results show that ZTDs are determined with an accuracy of a few millimetres; however, jumps are detected in some stations in standard products. The comparison between the MWR-derived wet tropospheric correction (WTC) and the GNSS-derived WTC at the nearby coastal stations illustrates the effect of land contamination in the MWR measurements and yields the distance from coast at which this contamination appears. This distance is different for the analysed altimetric missions, due to their different footprint sizes and different MWR retrieval algorithms, varying from 10 to 30 km. The root mean square of the differences between GNSS and MWR-derived WTC, at the closest distance at which no land contamination occurs, is in the range of 1.6–1.9 cm for all missions. This coastal assessment also shows the ability of the GNSS-derived path delay plus algorithm to remove this land contamination and to improve the WTC retrieval. Aiming at inspecting the long-term stability of the MWR measurements, the comparisons with GNSS show nonsignificant differences and drifts less than 0.3 mm/year. Therefore, the GNSS-derived WTC is a useful independent source to inspect the land effects on MWR observations and to monitor the stability of these instruments, thus contributing to the retrieval of precise water surface heights from satellite altimetry.

2.2.1. Introduction

In the last years, satellite radar altimetry has become a crucial remote sensing technique to monitor the ocean and continental waters at global and regional scales. The principal objective of this technique is to measure the range from the satellite to the water surface (Chelton et al., 2001). The difference between the orbit altitude of the satellite and the corrected range measurement from the altimeter allows one to derive the water surface height above a reference ellipsoid. These measurements have become essential in the understanding of the impact of climate change on water level evolution at global and regional scales, particularly in the coastal areas of the world (Willis et al., 2012).

Precise water surface height measurements (of 1–3 cm accuracy) are currently achieved globally over open-ocean using the state-of-the-art measuring techniques and accurate modelling of several effects. Various range and geophysical corrections are required to account for the effects in the radar pulse and echo backscatter due to the interaction of the signal with the dry and wet troposphere, the ionosphere, and the sea surface, and due to geophysical phenomena (dynamic atmospheric correction, tides), which must be accounted for in order to separate them from the signals of interest (Fernandes et al., 2015, 2016). A proper determination of the various corrections involved is of major

importance, in order to ensure the best final accuracy of the water levels derived from satellite radar altimetry, either over open-ocean or inland waters and coastal regions.

Amongst these corrections, the path delay induced by the presence of water vapor and liquid water in the troposphere, or wet tropospheric correction (WTC), is still one of the major error sources in satellite altimetry. The WTC has an absolute value up to 0.5 m, and it is highly variable in space and time. Due to its high variability, the most accurate way to account for this effect over open-ocean is through the measurements of microwave radiometers (MWRs) on-board the altimetric missions (Fernandes, et al., 2013).

On the contrary, MWR measurements over coastal, inland, and polar zones often fail to provide accurate wet corrections, due to the presence of surfaces, such as land, vegetation, or ice, which contaminate the MWR-derived WTC retrievals. The algorithms that compute the WTC from MWR observations were designed for water surfaces; thus when other surfaces are present in the MWR footprint, the corresponding measurements become invalid (Fernandes et al., 2015). For instance, as the MWR approaches the coast, the radiometrically warm land signal begins to fill the MWR field-of-view and consequently the retrieval errors increase.

The problem in the MWR measurements described above does not allow a proper direct use of these data in these regions, so alternative sources of data have been used, such as atmospheric models and global navigation satellite system (GNSS) stations distributed around the world, in combination with MWR measurements at valid points or third-party data scanning imaging MWR (SI-MWR) on-board other remote sensing satellites.

Various studies have been conducted aiming to develop improved methodologies for the computation of the WTC for coastal altimetry (see (Cipollini et al., 2017) for a review). Among these methods, in the context of this paper, two are of particular relevance, the GNSS-derived path delay plus (GPD+) algorithm (Fernandes et al., 2010, 2015, 2016) and the mixed pixel algorithm (MPA) (Brown, 2010).

Being the WTC one of the corrections applied to the altimeter range, any error or drift in this correction will directly impact sea level estimations. Thus, the independent monitoring of the MWR measurements is especially important for retrieving accurate global sea level from several altimetry missions either for open-ocean or mainly for coastal zones, where WTC from MWR becomes invalid.

Various methods are commonly used to validate or monitor the stability of radiometers on-board the altimeter missions such as the use of coincident radiosonde measurements (Obligis et al., 2006), ground-based water vapor radiometers (Somieski et al., 2006), the use of the hottest and coldest brightness temperatures (TBs) (Brown et al., 2004), and GNSS (Desai et al., 2004; Haines et al., 1998; Sibthorpe et al., 2011), with particular relevance in the context of this paper.

GNSS-derived tropospheric delays have been used in coastal altimetry studies for getting information about MWR performance. Drifts at the level of 1 mm/year in the TOPEX/Poseidon radiometer were detected using comparisons with WTC derived at terrestrial GNSS stations (Haines et al., 1998). On the other hand, systematic jumps in the Jason-1 radiometer of 4 mm were also detected using data from terrestrial stations (Desai et al., 2004). Estimates of tropospheric delays at coastal

GNSS stations have also been used to validate the WTC measurements from Jason-2 radiometer (Sibthorpe et al., 2011).

Building upon these studies, data from GNSS stations in coastal zones can be used to analyse the WTC derived from the on-board MWR of several altimetry missions and, therefore, to gather relevant information about these instruments, in particular, to evaluate their stability in these regions and to inspect the effect of land contamination on their measurements.

The main objectives of this paper are: 1) to exploit the potential of GNSS data to monitor the stability of the MWR measurements of the various altimetric missions in coastal regions and 2) to study the impact of land contamination on the MWR observations of these missions.

In spite of the high accuracy of a few millimetres (Pacione et al., 2011) and great potential of application of GNSS-derived zenith tropospheric delays (ZTDs), they may suffer from discontinuities (Bock et al., 2010) due to changes in parameter modelling (e.g., changes in the adopted reference system and parameters related with receiver corrections). For this reason, in this paper, ZTDs have been computed for a set of stations with a good spatial distribution, using the state-of-the-art methodologies, this way ensuring both their accuracy and long-term stability.

The various data sources involved in this paper are detailed in Section 2.2.2, while Section 2.2.3 presents the computation and analysis of the ZTD for a previously established network and the corresponding GNSS-derived WTC. Section 2.2.4 presents the application of the WTC derived from these ZTD to extract relevant information about the MWR measurements of eight altimetry missions: the so-called reference missions — TOPEX/Poseidon (TP), Jason-1 (J1), and Jason-2 (J2), the three European Space Agency (ESA) missions— ERS-1 (E1), ERS-2 (E2), and ENVISAT (EN), GeoSat Follow-On (GFO), and SARAL/AltiKa (SA). Since CryoSat-2 (C2) does not possess an on-board MWR, a WTC derived using only third-party data was also assessed in this section. Finally, Section 2.2.5 summarizes the main results and conclusions of this paper.

2.2.2. Data set description

Originally designed for applications over the ocean, WTC retrieved from MWR measurements becomes invalid close to the coast, over regions where plenty GNSS-derived tropospheric delays are available.

In this section, the various WTC sources used in this paper are detailed. First, the MWRs and the various missions that possess these instruments are described as well as the way how the wet correction can be derived from GNSS and atmospheric models. Second, an algorithm that combines various data sources to improve the WTC retrieval in coastal zones, where MWR observations are missing or invalid, is detailed.

2.2.2.1. MWR-Derived WTC

The passive MWR on-board the altimetric missions retrieve the WTC from the instantaneous measured TBs, at the nadir, in various channels (Fernandes et al., 2014). The accuracy of the MWR-derived WTC, namely, in coastal zones, depends on the MWR instrumental characteristics and on the algorithms that retrieve this tropospheric correction from MWR measurements.

Two main types of MWRs have been deployed in the altimetric satellites: three-band in the reference missions and two-band in the ESA missions (Fernandes et al., 2015).

In the reference missions, three channels are operated at frequencies of 18, 21, and 37 GHz for TOPEX/Poseidon and 18.7, 23.8, and 34 GHz for Jason-1 and Jason-2. The primary water vapor sensing frequency is at 23.8 GHz. Measurements at the 18.7 and 34 GHz frequencies primarily account for sea surface wind effects and cloud liquid content, respectively. The ESA missions (ERS-1/2 and EN), GFO, and SA two-band radiometers have been used: 23.8 and 36.5 GHz for the ESA missions (Fernandes et al., 2015), 22 and 37 GHz for GFO, and 23.8 and 37 GHz for SA.

The footprint of these radiometers is of the order of 20–45 km, depending on the instrument and frequency (Tournadre, 2006), except for AltiKa on-board SARAL, which is about 10 km (Tournadre et al., 2009).

The algorithms used to retrieve the WTC from the measured TBs of the various MWR channels assume surface emissivity values typical of water conditions. In the presence of surfaces with a different emissivity, such as land, vegetation, or ice, the MWR measurements become invalid. This is the case example of coastal and high-latitude regions.

2.2.2.2. WTC from GNSS

Another source to derive WTC is terrestrial GNSS stations, from which ZTD can be determined with an accuracy of a few millimetres (Pacione et al., 2011). GNSS-derived tropospheric delays have been used in applications such as the monitoring and validation of MWR measurements (Desai et al., 2004; Haines et al., 1998; Sibthorpe et al., 2011) and in the computation of the tropospheric path delays for coastal altimetry (Fernandes et al., 2010, 2016).

The total path delay caused by the troposphere in the zenith direction (ZTD) can be separated into the sum of the hydrostatic component, the zenith hydrostatic delay (ZHD) and the wet component, the zenith wet delay (ZWD), the equivalent to the WTC, according to the following equation:

$$ZTD = ZHD + ZWD \quad (1)$$

The hydrostatic component, due to the dry gases in the troposphere, accounts for nearly 90% of the total path delay, while the wet component accounts only for the remaining nearly 10% of the total delay. ZHD corresponds to an absolute mean value of 2.3 m at sea level and is usually modeled with high accuracy from surface pressure. Global grids of sea level pressure (SLP) provided by various atmospheric models [e.g., those from the European Centre for Medium-Range Weather Forecasts (ECMWF)] allow the estimation of the ZHD with an accuracy of 1–3 mm at global scale (Fernandes et al., 2013).

On the contrary, despite its low absolute value (lower than 50 cm), the wet component due to the presence of water vapor in the troposphere is much more variable both in space and time and, therefore, more difficult to determine (Fernandes et al., 2013).

Since the wet path delay is also a significant error source in GNSS measurements, it is common practice in GNSS processing to consider this component an additional unknown to be estimated. In GNSS processing, the tropospheric delay is determined according to (2), where STD is the measured slant total delay, E is the elevation angle of each GNSS satellite, and mf_h and mf_w are the mapping functions for the hydrostatic and wet components, respectively.

$$STD(E) = ZHDmf_h(E) + ZWDMf_w(E) \quad (2)$$

The mapping functions are known and relate the zenith delays with those in the slant direction. In (2), apriori ZHD is evaluated from the Vienna mapping functions 1 (VMF1) (Boehm et al., 2006). ZHD is equivalent to dry tropospheric correction (DTC).

In (2), ZWD is the unknown and the quantity given with high accuracy is indeed a combined ZTD value, as the sum of the apriori ZHD and the estimated ZWD. Thus, to get an accurate ZWD, an accurate ZHD (more accurate than the apriori value) needs to be subtracted from ZTD, using (1). Accurate ZHD can be estimated from surface pressure data given by an atmospheric model, as described in Section 2.2.2.3.

In summary, for each observation with a precise determination of ZTD from GNSS and ZHD derived from an atmospheric model (replacing the apriori value adopted in the GNSS processing), the corresponding ZWD (equivalent to WTC) is obtained from (1). All these values are referred to the GNSS station height. For application in satellite altimetry, they must be reduced to sea level.

2.2.2.3. Model-Derived Tropospheric Corrections

In the absence of wet path delay observations, the WTC from global meteorological models must be used (Fernandes et al., 2014). They can also be used in combination with other WTC data sources such as MWR valid measurements and coastal GNSS stations. The overall accuracy of WTC from meteorological models is worse than the corresponding values from MWR or GNSS; however, the quality of the recent models has been increasing significantly (Miller et al., 2010), particularly for the reanalysis product from ECMWF, the ERA Interim model (Dee et al., 2011).

For use in satellite altimetry, tropospheric corrections can be calculated from global grids of some single-level parameters provided by global atmospheric models.

DTC can be estimated with an accuracy of a few millimetres from surface atmospheric pressure p_s using the modified Saastamoinen model (Davis et al., 1985), according to (3), as described in (Fernandes et al., 2014)

$$DTC = - \frac{0.0022768p_s}{1 - 0.00266 \cos 2\varphi - 0.28 \times 10^{-6}h_s} \quad (3)$$

In (3), from which DTC results in meters, p_s is the surface pressure in hPa, φ is the geodetic latitude, and h_s is the surface height above the geoid, in meters (Fernandes et al., 2014). Surface

pressure (p_s) can be computed from SLP (p_0) using (4) that represents the pressure variation with altitude. Since p_0 is the SLP, then $h_0 = 0$

$$p_s = p_0 \exp \left[-\frac{g_m(h_s - h_0)}{RT_m} \right] \quad (4)$$

In (4), R is the specific constant for dry air, T_m is the mean temperature in kelvin of the layer between heights h_0 and h_s , and g_m is the mean gravity, given by the following equation. T_m can be estimated as the mean value of temperatures T_0 and T_s at heights h_0 and h_s , respectively.

$$g_m = 9.784(1 - 0.00266 \cos 2\varphi - 0.28 \times 10^{-6}h_s) \quad (5)$$

Using (3)–(5), ZHD (or DTC) can be computed from an atmospheric model with high accuracy and then used to replace the a priori value adopted in the GNSS processing.

For the WTC, two parameters are used: total column water vapor (TCWV, expressed in mm or, the equivalent, kg/m²) and near-surface air temperature in kelvin (two-meter temperature, T_0) (Bevis et al., 1992, 1994)

$$WTC(h_s) = -\left(0.101995 + \frac{1725.55}{T'_m}\right) \frac{TCWV}{1000} \quad (6)$$

Equation (6) allows the computation of WTC in meters at height h_s , using global grids of T_0 and TCWV from an atmospheric model. T'_m is the mean temperature in kelvin of the troposphere, which can be modelled from T_0 according to (7) (Mendes et al., 2000)

$$T'_m = 50.440 + 0.789T_0 \quad (7)$$

WTC computed from T_0 and TCWV using (6) and (7) is referred to the atmospheric model orography level. An empirical expression represented in (8) allows determining WTC at other heights, where h_0 and h_s are the orthometric heights of the model orography and surface, respectively (Kouba, 2008).

The determination of this expression was performed using a very small data set (1.5 years data set of 11 globally distributed GNSS stations), so it has some limitations; namely, it should not be used to perform WTC height reductions for heights above 1000 m (for more details see (Kouba, 2008)); however, at present, this equation is the only available in the literature

$$WTC(h_s) = WTC(h_0) e^{\frac{h_0 - h_s}{2000}} \quad (8)$$

The model orography may depart from the real surface height by hundreds of meters. For instance, a height difference of about 100 m corresponds to a variation in DTC of about 2.5 cm, so tropospheric corrections should be obtained by an appropriate height reduction, which is a crucial step for coastal and inland water studies (Fernandes et al., 2014).

2.2.2.4. GNSS-Derived Path Delay Plus (GPD+) Algorithm

In the last years, the University of Porto, Porto, Portugal, has been developing methods for improving the WTC retrieval by addressing the various error sources inherent to the MWR-derived WTC, namely, the land contamination in these measurements. These methods are based on data combination through space–time objective analysis of various wet path delay observations (Fernandes et al., 2016).

The GPD+ algorithm, the latest version of these methods, is based on a statistical technique that interpolates the wet path delay values from the nearby (in space and time) observations. This is performed at each altimeter ground-track point, when the MWR measurement is invalid. This algorithm can be applied not merely to missions with an MWR aboard the respective spacecraft, but also to those which do not possess an on-board MWR.

Hence, the GPD+ is wet path delay based on: 1) MWR-derived WTC measurements whenever they exist and are valid and 2) new WTC values estimated by data combination of all available observations in the vicinity of the estimation point (valid MWR measurements, GNSS-derived WTC at coastal and island stations, and WTC from SI-MWR), whenever the previous are considered invalid.

Moreover, the GPD+ version of these products corresponds to WTC calibrated with respect to the special sensor microwave imager (SSM/I) and the SSM/I sounder (SSM/IS) imaging radiometers, known for their stability and independent calibration (Wentz, 2013).

More details about this algorithm to improve the WTC retrieval, particularly in coastal zones, can be found in (Fernandes et al., 2010, 2015, 2016).

2.2.3. WTC derived from ZTD UPorto

In this paper, a network of coastal and island GNSS stations with long observation periods and ensuring a good geographical distribution have been chosen for calculating the ZTD (designated ZTD UPorto) at their locations, using the GPS analysis package developed at Massachusetts Institute of Technology (GAMIT) software (Herring et al., 2006).

ZTD available online from EUREF (European reference frame) permanent network (EPN) and International GNSS Service (IGS) are also available and have been compared to ZTD UPorto, allowing the assessment of the precision of the latter, in the absence of independent external information.

After this, the way how GNSS-derived WTC, at sea level, is derived from ZTD UPorto is described.

2.2.3.1. Computation of ZTD UPorto

ZTD UPorto has been computed for a set of 60 coastal GNSS stations with global distribution (Fig. 1) to cover regions with different variability patterns of the tropospheric and oceanic conditions. The period covered by these observations is from 1995 to 2016.

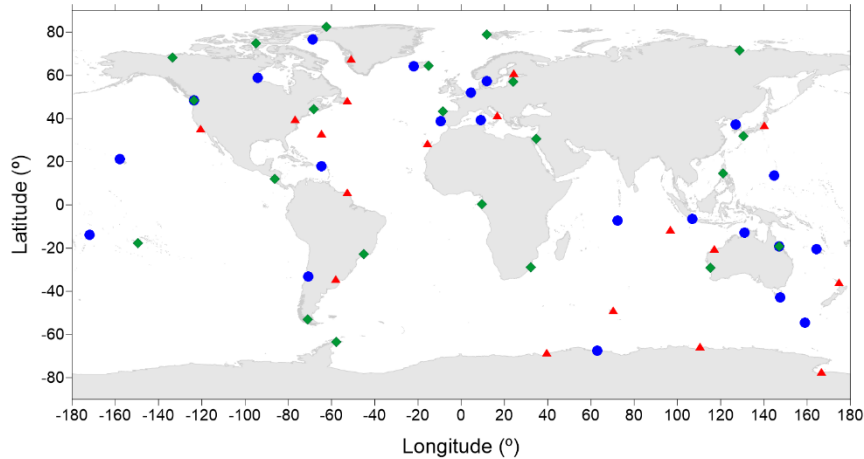


Figure 1. Spatial representation of the three subnetworks (UPorto-1—red triangles, UPorto-2—blue points, and UPorto-3—green squares).

In this calculation, phase measurements were used (double differences), at 30-s intervals, IGS precise satellite orbits and clock parameters, a cutoff elevation angle of 7° , and the VMF1 (Boehm et al., 2006). As a priori ZHD, the values present in the VMF1 grids were used. Atmospheric parameters were estimated at 30-min intervals using the “metutil” GAMIT routine.

The calculation time increases with the square of the number of stations included in the GAMIT network. At the time of the calculations, it was decided to build subnetworks, in order to optimize the computation time. This is a common strategy to handle, in an operational way, large networks of permanent stations. For this purpose, three subnetworks were created, designated hereafter by UPorto-1, UPorto-2, and UPorto-3, represented in Fig. 1, by red triangles, blue points, and green squares, respectively. This procedure ensures a good geographic distribution and similar observation periods within each subnetwork. Moreover, for validation purposes, three stations common to all networks were considered.

Hence, ZTD UPorto is a set of ZTDs for the UPorto network shown in Fig. 1, for each station covering the maximum period for which observations are available for that station, estimated as described above, at 30-min intervals.

2.2.3.2. Intercomparison of ZTD From Different Subnetworks

Aiming at assessing the uncertainties of ZTD UPorto retrievals, out of the 60 stations of the initial network, three were chosen simultaneously in different subnetworks (FALE in UPorto-1 and UPorto-2, while ALBH and TOW2 are present in all three subnetworks). These common stations allow the comparison between the ZTD of the same station computed in different subnetworks. On the other hand, this procedure allows observing the influence of network geometry on the estimated tropospheric parameters.

Fig. 2 represents differences in millimetres between ZTD computed at distinct subnetworks for the ALBH station, function of time. In Fig. 2 (top), ZTD differences between UPorto-1 and UPorto-2 are represented, where a similar behaviour is observed for the whole analysed period. ZTD differences UPorto2–UPorto3 and UPorto1–UPorto3 are shown in Fig. 2 (middle and bottom),

respectively. Contrary to the first observed differences, a similar behaviour of the differences is not observed during the whole period, being the ZTD differences much larger in the initial part of the analysed period. The same happens for the TOW2 station. Note that the vertical axes are saturated in the range $[-80, 80]$ mm.

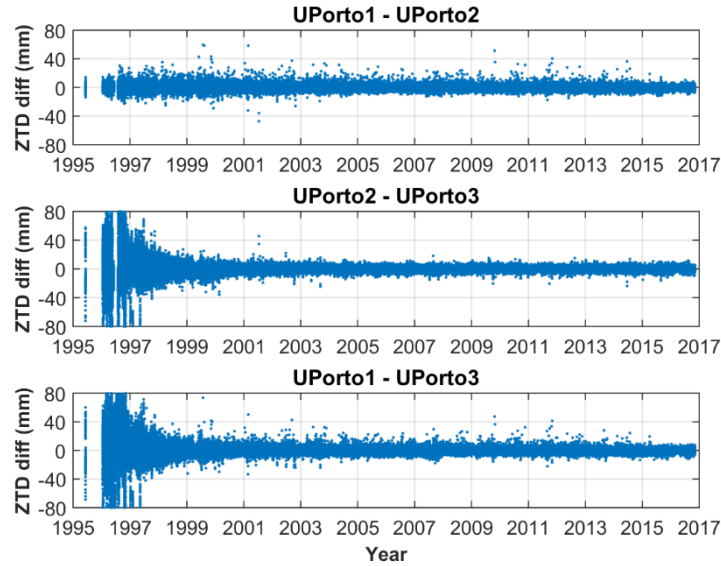


Figure 2. ZTD differences for the ALBH station between ZTD computed in different subnetworks. (Top) UPorto1–UPorto2. (Middle) UPorto2–UPorto3. (Bottom) UPorto1–UPorto3.

To inspect the origin of these large ZTD differences, the number of GNSS observations in the third subnetwork versus time has been examined. Fig. 3 shows the number of observations per day (blue, left axis) and the corresponding number of stations per day (red, right axis) for the UPorto-3 subnetwork. A small number of stations and consequently observations are clearly observed during the period of the large reported differences. The ZTD UPorto-3 computation in the initial part of the period is affected by the small number of stations, an indicator of an inadequate network geometry. The same problem does not occur in UPorto-1 and UPorto-2 subnetworks, for which a sufficiently large number of stations with global distribution exist for the whole period.

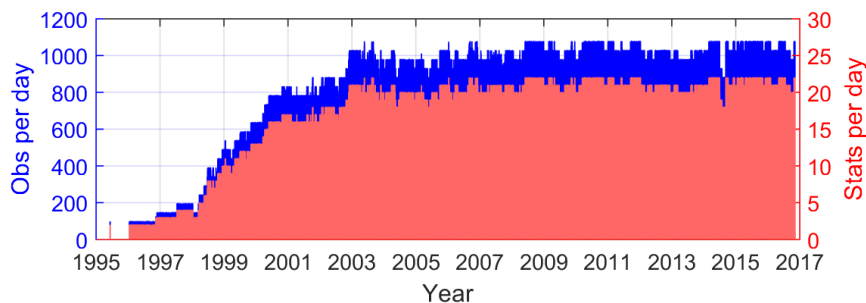


Figure 3. Number of observations and stations per day since beginning of 1995 to end of 2016 for the UPorto-3 subnetwork. (Left axis) (blue) Number of observations per day. (Right axis) (red) Number of stations per day.

While the influence of network geometry on station coordinates has been evaluated already (see (Ineichen et al., 1999)), the effect on tropospheric parameter estimation was recognized but had not

yet been quantified in detail (Brenot et al., 2014). Results present in Figs. 2 and 3 show the profound influence of the network geometry in the uncertainties of tropospheric delays retrieved from GNSS. When the number of stations becomes small, with poor spatial distribution, all stations observe the same satellite with similar viewing angles. Therefore, the same atmospheric conditions are observed, the retrieved ZTD becomes highly correlated and the corresponding uncertainties increase.

Since large ZTD differences obtained using UPorto-3 are observed at the beginning of the analysed period, due to its poor network geometry, ZTD UPorto-3 from 1995 to 1999 has been rejected and not used in the subsequent analyses performed in this paper. For the same analysis, in the common stations, only ZTD UPorto-1 was used.

Table 1 shows the root mean square (RMS) of these ZTD differences, in millimetres. For comparisons with ZTD UPorto-3, two values are presented: one considering the whole period (1995–2016) and other considering only the period from 1999 until the end of 2016.

Table 1. RMS (mm) of the ZTD differences for the common stations used in different subnetworks (UPorto-1, UPorto-2, and UPorto-3)

ZTD diffs (mm)	Time span	stations		
		ALBH	FALE	TOW2
UP1-UP2	1995-2016	2.5	3.4	3.5
UP2-UP3	1995-2016	9.2	-	12.7
	1999-2016	2.2	-	3.4
UP1-UP3	1995-2016	10.0	-	13.2
	1999-2016	2.4	-	3.6

ZTD differences between distinct subnetworks affected by an inappropriate network geometry show RMS values that can reach 1.3 cm. Rejecting the period affected by poor network geometry in UPorto-3, these RMS values are lower than 4 mm. As referred by several authors, at present, ZTD can be determined at station location with an accuracy of a few millimetres. These results show the importance of using an appropriate network geometry in ZTD computation.

2.2.3.3. Comparison of ZTD UPorto With IGS and EPN

At present, tropospheric delays determined by GNSS at international data centres became a routine product, being available for any user.

A way to evaluate the precision of ZTD estimates is by comparing tropospheric delays from different solutions, namely, IGS and EPN, when both are available. The comparisons were performed for stations where at least two solutions (UPorto, IGS, or EPN) were available.

Fig. 4 shows an example representing the differences between the three solutions (UPorto–IGS and UPorto–EPN) for station MAS1 located in Maspalomas, Gran Canaria, Spain. This is a station of the first subnetwork (see red triangles in Fig. 1) for which both IGS and EPN ZTD are available. In Fig. 4 (top), differences between UPorto and IGS ZTD are represented, while Fig.4 (bottom) represents

the corresponding differences between UPorto and EPN products. Note that on Fig. 4 (top and bottom), the time axis represents the period 2010–2015, while the vertical axes are saturated in the range $[-80, 80]$ mm.

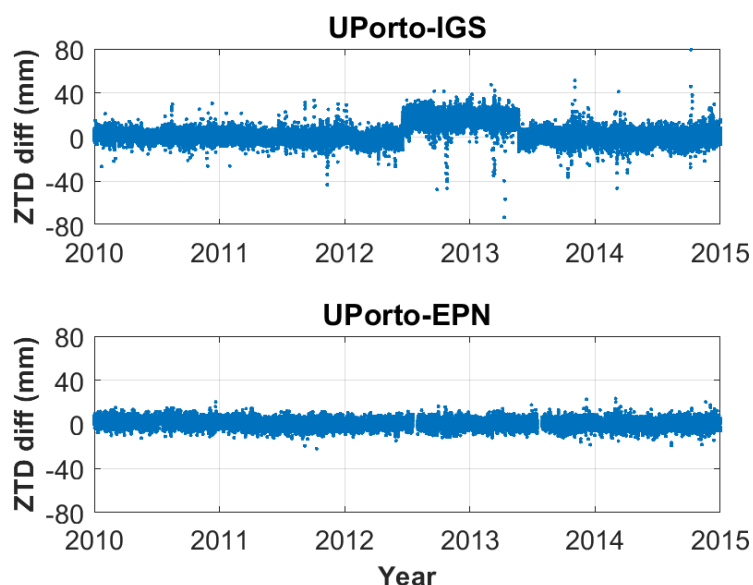


Figure 4. ZTD differences between UPorto and (Top) IGS and (bottom) EPN, in millimetres, for station MAS1, Gran Canaria, Spain.

In Fig. 4 (bottom), a homogeneous pattern is observed over the whole period. ZTD differences between UPorto and EPN have a constant behaviour over the whole period. The RMS of these differences for the various stations varies from 2 up to 6 mm. Two very small gaps can be observed, due to a lack in the EPN tropospheric products.

On the contrary, the top plot of Fig. 4 shows a clear jump of about 20 mm in the ZTD differences between UPorto and IGS from mid-2012 to mid-2013. Since the same jump is not observed in the differences with EPN (bottom graph), the origin of this jump is attributed to the ZTD from IGS. The same happens for other stations in different periods. Apart from some periods with jumps in ZTD IGS, the RMS of the ZTD differences between UPorto and IGS can reach a value up to 9 mm; however, in most stations, it is smaller than 5 mm.

ZTD differences are affected by the spatial variation of the ZTD. Stations at high latitudes have small values of RMS differences while those at low latitudes, corresponding to regions of large WTC variability, show larger RMS.

The results show that for some stations, ZTD provided by IGS has not been computed with a homogenous methodology over the whole period. The jumps observed in this comparison are due to changes and updates in the methodology adopted by IGS to estimate the ZTD. It should be noted that these jumps were present in some IGS stations at the time of the ZTD download. Later on, it was found that most of these stations have been reprocessed and the jumps have now been removed.

These jumps are not observed when comparing UPorto and EPN ZTD. However, ZTD provided by EPN is geographically limited due to the fact that it is a regional network; therefore, they cannot be used to evaluate MWR globally.

These results evidence the importance of having a global solution, derived by adopting a homogeneous procedure for the whole computation period. ZTD UPorto has been computed in order to ensure stable and homogeneous ZTD on a global network.

2.2.3.4. Separation of ZHD and ZWD and Reduction to Sea Level

ZTD UPorto has been computed at station height, while the required quantity for comparison with MWR-derived WTC is the corresponding ZWD (or WTC) at sea level.

Using the methodology presented in Section 2.2.2.3, ZHD for the same UPorto instants have been interpolated from the ERA Interim model, at the station locations. This was done by using SLP from ERA Interim, reduced to station height using (4) and further used in (3) to derive the ZHD at station height.

Due to the height dependence of the ZHD (DTC equivalent) (see (Fernandes et al., 2014)), ensure that all quantities referred to the same level (in this case station height) is crucial to avoid introduction of undesirable biases.

After this, using the GNSS-derived ZTD UPorto and the model-derived ZHD, the corresponding ZWD (or WTC) was determined using (1), at station location. This WTC is then reduced to sea level using (8), hereafter referred as WTC GNSS UPorto or simply WTC GNSS.

After these steps, the corresponding GNSS-derived UPorto WTC is given at sea level, for comparison with MWR-derived WTC. In Section 2.2.4, the GNSS-derived WTC values are those from the ZTD UPorto solution.

2.2.4. Assessment of MWR-derived WTC

As mentioned in Section 2.2.3, ZTD UPorto (and corresponding WTC GNSS) was computed using the same methodology throughout the whole period, so that they can be used as reference. Moreover, they were computed for a network with a good geographical distribution, in order to cover regions around the world with different atmospheric variability conditions.

Therefore, WTC GNSS consists of a set of WTC measurements at each station location (see Fig. 1) for the whole period of observations available for that station. As mentioned above, to minimize the systematic effects related to the WTC height dependence, WTC GNSS has been estimated at sea level. These data are geographically limited to the network defined above and temporally limited to the period of each station. On the contrary, WTC from satellite altimetry data is global, covering the whole period of each mission.

These WTC data sets allow the comparison between GNSS and MWR data, being this analysis possible only over coastal zones. It should be stressed that a collocated comparison is not possible, since there is no spatial overlap between terrestrial GNSS stations and valid ocean measurements from on-board MWRs.

For this purpose, at a first step, altimetry measurements up to 120 km from the GNSS stations are selected. Here, a large set of about 800 coastal stations belonging to several global and regional

networks are used, in order to allow other comparisons, e.g., with WTC derived from ZTD IGS or EPN. However, in the subsequent analysis, only the WTC from the UPorto solution has been used.

For instance, Fig. 5 represents altimetry measurements selected around the Iberian Peninsula for the EN orbit repeat cycle 73 (top) and Jason-2 cycle 10 (bottom). Red points represent the MWR measurements flagged as invalid. Fig. 5 shows only a representation of the selection of altimetry points for comparison with GNSS-derived WTC. The same procedure was applied to the eight altimetry missions, considering the whole period covered by each mission.

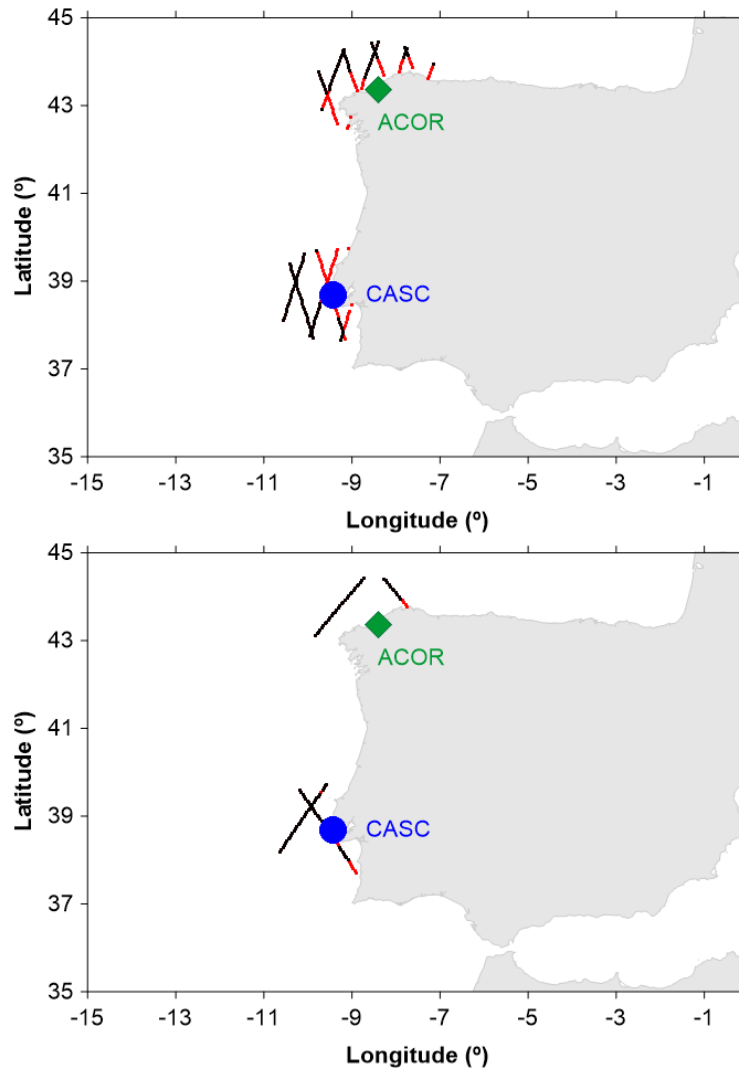


Figure 5. Selected altimetry measurements around the Iberian Peninsula for (Top) EN cycle 73 and (Bottom) J2 cycle 10.

For the epoch of each selected altimetry point, a value of WTC GNSS is interpolated in time, at the station location. Thus, for the same epoch, there are two values of WTC—one from MWR observations at the along-track point and one WTC GNSS, at the station location. For each pair of WTC (MWR and GNSS-derived WTC, relative to the same instant), since they are derived at different locations, the distance between these two measurements as well as the distance from coast of each altimeter point are computed and considered in the subsequent analysis.

The distances from coast used for this analysis were computed from a global netCDF grid with distances to the nearest global self-consistent, hierarchical, high-resolution geography database shoreline (Wessel et al., 1996).

This interpolation is performed for each GNSS station with surrounded altimetry measurements and then the whole set of stations is considered, in order to obtain representative results for the whole globe.

In this analysis, for each altimetry point, a value of WTC derived from the GPD+ algorithm is also considered. Thus, the whole set of noncollocated WTC differences (GNSS–MWR and GNSS–GPD) are analysed below for each mission, function of distance from coast and function of time.

2.2.4.1. Coastal Assessment

Comparisons between GNSS-derived WTC and those from MWR on-board the several altimetry missions are first analysed, function of distance to coast. This analysis aims at inspecting the land contamination of each MWR and the ability of GPD+ algorithm to remove this contamination and improve the WTC retrieval, either very close to the coast or up to dozens of kilometres from the coast. In addition, it aims to obtain relevant information for each mission, e.g., the distance from coast where land contamination disappears, useful for algorithms like GPD+.

For this purpose, the differences between GNSS-derived and MWR-derived WTCs and the differences between GNSS-derived WTC and WTC GPD+ are binned into classes of distance from coast of 5 km. For each class, RMS of these two differences as well as the number of measurements is computed.

For this analysis, two different sets of measurements are considered, based on validation flags associated with the altimetry data used. Since GPD+ provides valid WTC values for all points, irrespective of their distance from coast, in the comparison with the WTC GPD+, all altimetry points have been used. On the contrary, for the comparison with MWR, only altimetry points flagged as valid were used, except for the flag that rejects the measurements located at a distance from coast less than a given threshold. In this way, the selected MWR observations include those contaminated by land, but exclude, for example, ice contamination and outliers.

Figs. 6–13 represent the RMS (left axis) of the differences between WTC GNSS and MWR-derived WTC (red points) and the differences between WTC GNSS and GPD+ derived WTC (black points) for each class of distance to coast in kilometres. Red bars represent the number of measurements used to compute the RMS of the differences GNSS–MWR, while grey bars represent the number of points used to compute the RMS of the differences GNSS–GPD+. Note that left vertical axes are saturated in the range 1–3 cm, for all missions, and in some classes, grey bars are not observed because they are overlapped by red bars; however, grey bars are always higher than red bars. The axes of distance from coast are represented in the range 0–65 km.

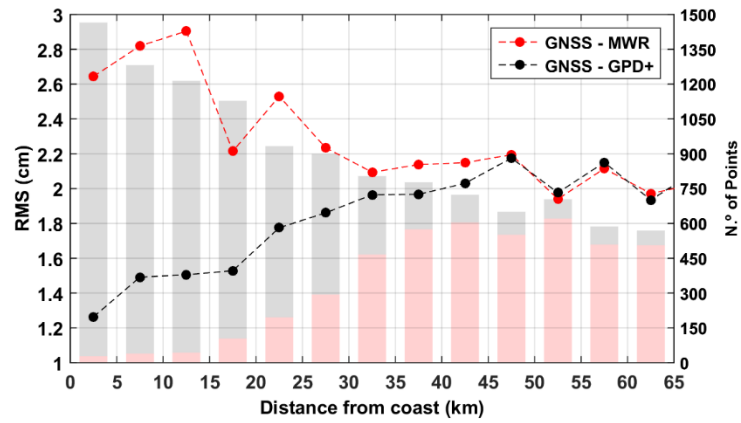


Figure 6. (Left axis) RMS (cm) of the WTC differences and (Right axis) number of altimetry measurements used for the ERS-1 mission.

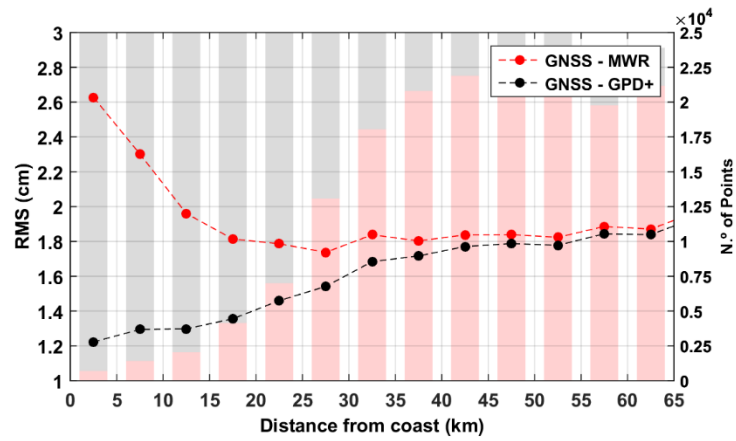


Figure 7. (Left axis) RMS (cm) of the WTC differences and (Right axis) number of altimetry measurements used for the ERS-2 mission.

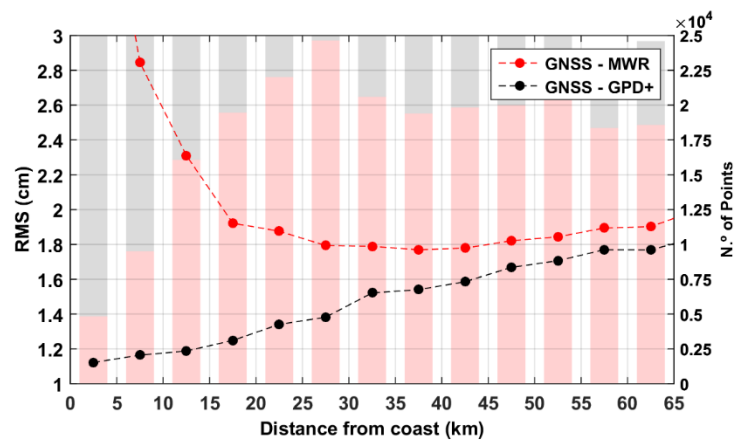


Figure 8. (Left axis) RMS (cm) of the WTC differences and (Right axis) number of altimetry measurements used for the EN mission.

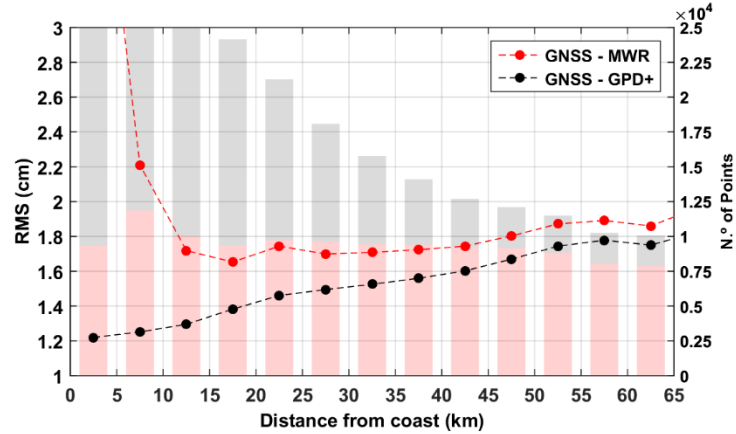


Figure 9. (Left axis) RMS (cm) of the WTC differences and (Right axis) number of altimetry measurements used for the SA mission.

It is important to note that the RMS values represented in Figs. 6–13 are affected by the fact that this is a noncollocated comparison. Large distances from coast induce large WTC differences, since they correspond to two observations several kilometres apart.

Figs. 6–8 represent these values for the ESA missions, ERS-1, ERS-2, and EN, respectively. Fig. 9 represents the same values for the MWR on-board SA satellite.

The results for ERS-2 are very similar to those for EN. Differences between GNSS and MWR are minimum for distances from coast at about 25–30 km, which indicates that land contamination on the MWR on-board ERS-2 and EN is observed only at distances from coast smaller than these values. The same behaviour is observed for SARAL at 15–20 km from coast which is in agreement with the footprint size, since this is smaller for the SARAL radiometer (about 10 km (Tournadre et al., 2009)) than for the MWR on-board the ESA missions (of the order of 20–45 km (Tournadre, 2006)).

Although the plot is similar to those obtained for ERS-2 and EN, results for the MWR on-board ERS-1 (see Fig. 6) are not significant due to the small number of GNSS observations for the period of this mission, as observed by the bar plots.

Very close to the coast, the RMS of the differences GNSS–MWR can be larger than 3 cm. On the contrary, the RMS of the differences GNSS–GPD+ is lower close to the coast and increase for larger distances due to the WTC spatial variation. In the first classes near the coast, where the differences are less affected by the WTC spatial variation, the RMS of the differences GNSS–GPD+ is not larger than 1.2 cm for the analysis using these four missions. It can be clearly observed that this algorithm is able to remove the land contamination in the MWR and the RMS values of the differences between GNSS and GPD+ are always lower than the corresponding values for the differences between GNSS and MWR.

These results are in agreement with the fact that compared to ESA missions, which also possess a 2-band MWR, SA has a smaller footprint size, showing land contamination up to a shorter distance from coast. The AltiKa radiometer is the MWR aboard altimetry missions with the best resolution (12 km for the 23.8 GHz channel and 8 km for the 37 GHz channel) (Valladeau et al., 2015).

Figs. 10–12 represent the same analysis for the reference missions TOPEX/Poseidon, Jason-1, and Jason-2, respectively. Fig. 13 represents the differences for the radiometer on-board GFO satellite and also the RMS values for comparison GNSS–GPD+ for C2 satellite.

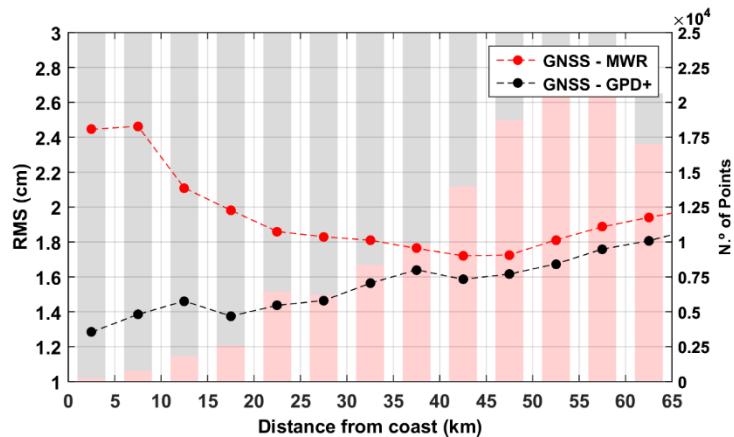


Figure 10. (Left axis) RMS (cm) of the WTC differences and (Right axis) number of altimetry measurements used for the TOPEX/Poseidon mission.

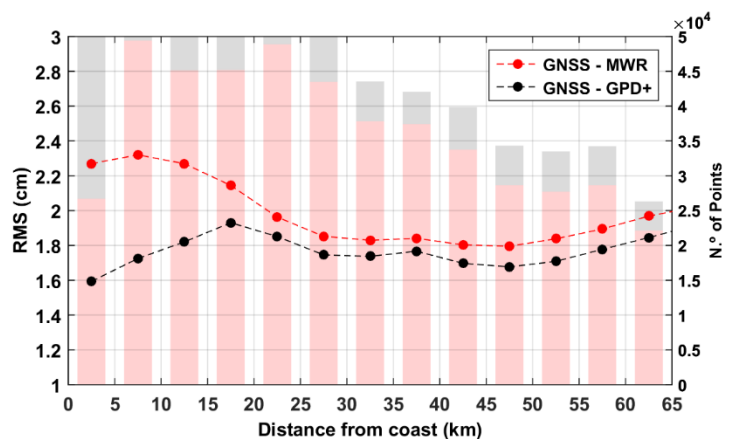


Figure 11. (Left axis) RMS (cm) of the WTC differences and (Right axis) number of altimetry measurements used for the Jason-1 mission.

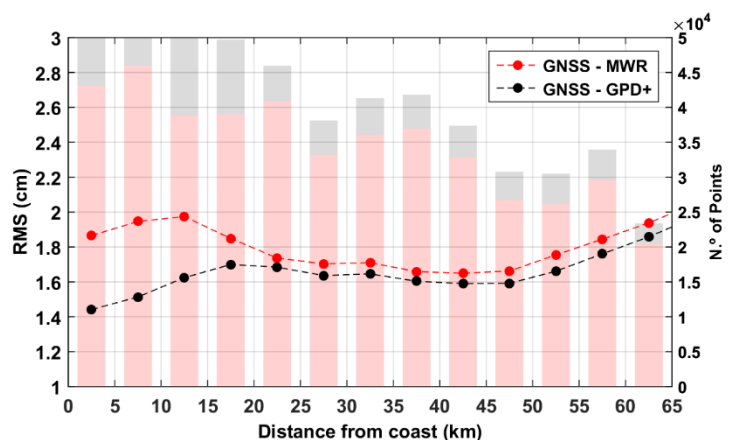


Figure 12. (Left axis) RMS (cm) of the WTC differences and (Right axis) number of altimetry measurements used for the Jason-2 mission.

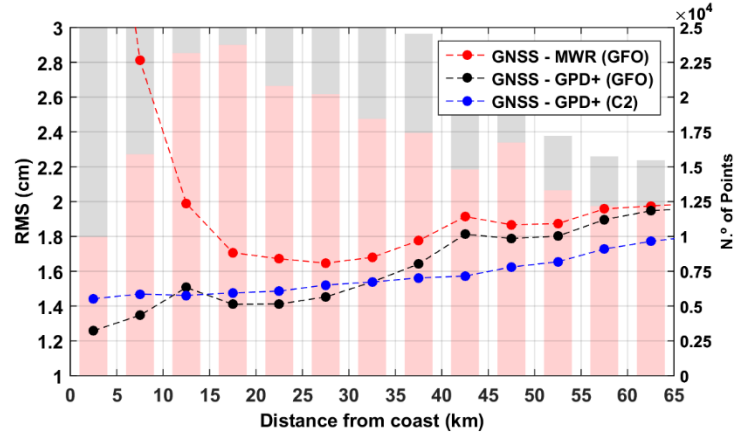


Figure 13. (Left axis) RMS (cm) of the WTC differences and (Right axis) number of altimetry measurements used for the GFO mission. Blue points represent the RMS of the differences between GNSS and GPD+ for the C2 mission.

As for the 35-day missions, the RMS values of the differences between GNSS and GPD+ are always lower than the corresponding values of the differences between GNSS and MWR. As observed in the bar plots, in the comparison for the TOPEX/Poseidon (see Fig. 10), the number of points is lower than those for other missions. For the first missions (ERS-1 and TOPEX/Poseidon), the number of measurements is small, due to a small number of GNSS stations and observations for the corresponding period in the UPorto network.

For the reference missions (Figs. 10–12), the RMS values of the differences between GNSS and the corresponding MWR close to the coast are lower than 2.5 cm (less than 2 cm for Jason-2), which does not happen for the ESA, SARAL, and GFO missions. This reveals that land contamination is less pronounced in radiometers on-board reference missions. The same analysis reveals that land contamination is only observed up to 25–30 km from the coast for TOPEX/Poseidon and Jason-1 and up to 20–25 km for Jason-2. The values found for Jason-2 are smaller than those reported in (Sibthorpe et al., 2011) (40 km); a possible indication that the criteria adopted in the detection of contaminated MWR observations is efficient (Fernandes et al., 2016) and also due to the fact that the Jason-2 data used in this paper are already enhanced near the coast (Brown, 2010).

As for ESA missions and SARAL, land contamination for GFO is more pronounced, with RMS of the differences between GNSS and MWR larger than 3 cm in the first class near the coast. For this satellite, the land contamination is observed up to 15–20 km from the coast.

These analyses through a noncollocated comparison between GNSS-derived WTC and the corresponding correction derived from MWR measurements, using a GNSS network with a good geographical distribution, are useful to inspect the land contamination, as shown above for ESA and reference missions, SA, and GFO. It is important to note that this is an independent coastal assessment of the MWR measurements, performed globally, only over coastal zones, where GNSS is available.

These results show that the GPD+ algorithm improves the retrieval of the WTC, mainly close to the coast, where MWR measurements are invalid due to land contamination. Fig. 13 also illustrates the RMS of the differences between GNSS-derived and GPD+ WTC (blue points) for C2. Since this

satellite does not carry any on-board MWR, the GPD+ WTC is solely based on third-party data. Thus, the RMS of the differences is slightly larger than those for GFO close to the coast, still within 1–2 cm.

It should be noted that GPD+ includes GNSS-derived observations as input data; thus, the RMS of the differences between GNSS and GPD+ does not provide an independent assessment of the GPD+ WTC. In spite of that, these results clearly show that GPD+ is efficient in removing the land contamination in the MWR observations, ensuring the continuity of the WTC in the open-ocean/coastal transition zone.

2.2.4.2. Long-Term Stability

In this section, the time evolution of the differences between GNSS-derived WTC and MWR-derived WTC and the time evolution of the differences between GNSS-derived WTC and GPD+ WTC are examined.

Due to a different time span and spatial coverage of each altimeter mission, a different set of altimetry measurements was used in the temporal analysis for each mission. Here, only MWR measurements flagged as valid have been considered, thus eliminating all possible error sources (contamination by land, ice, or rain and outliers).

For this analysis of the differences GNSS–MWR and GNSS–GPD+, function of time, the mean values of WTC differences are computed for predefined intervals of time. For the ESA missions and SARAL, mean values of WTC differences are computed for 35 and 385 days, while for the reference missions and GFO, mean values of WTC differences are computed for 10 and 370 days. These periods have been chosen according to each satellite repeat cycle. In both cases, the larger window size corresponds to 1 year and is applied to remove signals with periods less than or equal to one year, thus obtaining smoothed differences in time.

A linear fit has been applied to these nearly annual means (385 or 370 days). Values of slope in millimetres per year are computed, as well as the coefficient of determination.

As previously observed in the coastal analysis, results for ERS-1 mission are not significant, due to the very small number of points in the corresponding period of comparison with GNSS, so results for this mission are not shown here.

In the plots of these temporal analyses, vertical and horizontal axes are represented in the intervals $[-8, 8]$ mm and $[1995, 2017]$, respectively. In the same plots, averages of 35 or 10 days (small points), averages of 385 or 370 days (large points) and the linear lines fitted to the nearly annual means are represented. The same colour is used for each mission.

Fig. 14 represents the time evolution (averages) of the differences between GNSS and MWR (top) and the differences between GNSS and GPD+ (bottom) for ERS-2 (blue points), EN (red points), C2 (black points), and SARAL (green points).

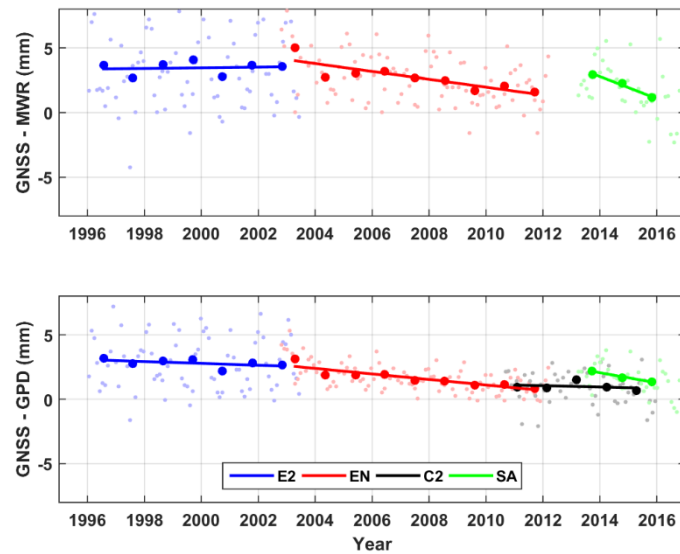


Figure 14. Time evolution (averages) of the WTC differences (Top) between GNSS and MWR and (Bottom) between GNSS and GPD+ for ERS-2, EN, C2, and SA missions.

C2 satellite does not possess an on-board MWR; however, GPD+ WTC is also computed for this mission using only third-party data. Time evolution of the differences between GNSS and GPD+ is also represented in Fig. 14 (bottom).

Tables 2 and 3 show the values of the linear fit to the nearly annual means for the differences GNSS–MWR and GNSS–GPD+, represented in Fig. 14 (top and bottom), respectively, for ESA missions, C2, and SA. The values of slope in millimetres per year, coefficient of determination, and the time span used to determine these values for each mission are given.

Table 2. Linear fitting values and time span for the 385-day averages of the GNSS–MWR differences for ESA missions and SA

Mission	Slope (mm/year)	R ²	Time span
E2	0.03	0.01	1996.0-2003.5
EN	-0.30	0.73	2002.8-2012.3
SA	-0.86	0.98	2013.2-2016.9

Table 3. Linear fitting values and time span for the 385-day averages of the GNSS–GPD differences for ESA missions, C2, and SA

Mission	Slope (mm/year)	R ²	Time span
E2	-0.07	0.25	1996.0-2003.5
EN	-0.21	0.81	2002.8-2012.3
C2	-0.05	0.08	2010.6-2016.0
SA	-0.40	0.98	2013.2-2016.9

Apart from SA, with a large absolute value of slope (0.86 and 0.40 mm/year, for GNSS–MWR and GNSS–GPD+, respectively) due to its small period of about three years, the remaining missions have absolute values of slope lower than 0.3 mm/year. The linear fit for SARAL mission has an R^2 very close to 1; however, these values are not significant, since only three points (green) are obtained for the 385-day averages, as observed in Fig. 14.

For the ERS-2 mission, these GNSS–MWR average differences are not well fit by a linear regression, showing a very small R^2 value; however, there is no significant drift in time, as observed in Fig. 14 (top). For the EN mission, the 385-day averages of differences GNSS–MWR have a slope of -0.30 mm/year with a value of R^2 larger than 0.70.

Concerning the differences GNSS–GPD+ [Fig. 14 (bottom) and Table 3], all the absolute values of the slope are lower than 0.21 mm/year, except for the SARAL mission, due to the reason already described. In the comparison with Table 2, overall values in Table 3 show smaller values of slopes for differences GNSS–GPD+ than for differences GNSS–MWR, showing that GPD+ WTC estimates are more stable than MWR measurements, when compared to the WTC derived from GNSS UPorto.

Comparing the two panels of Fig. 14, absolute mean values of differences GNSS–GPD+ (bottom) are smaller than absolute mean values of differences GNSS–MWR (top), in agreement with the results from previous coastal analysis.

For each mission, both 385-day averages of WTC differences have absolute values lower than 5 mm with a variation below 2 mm. Results shown in Fig. 14 also allow observing an alignment between consecutive missions, mainly between missions of the ESA group (ERS-2 and EN).

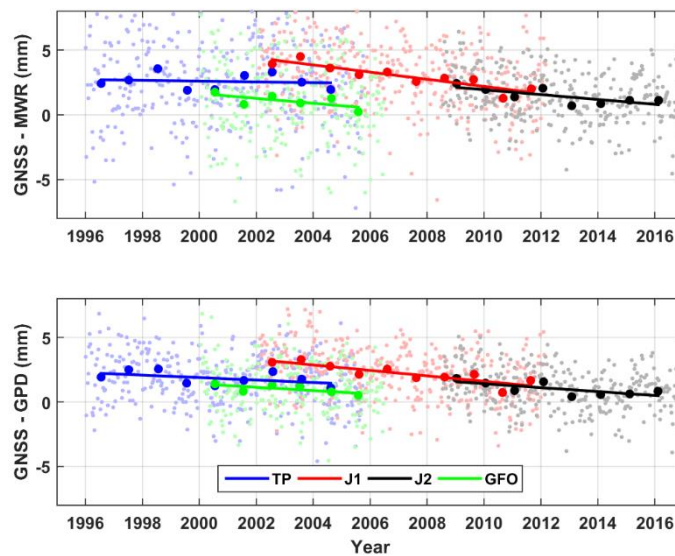


Figure 15. Time evolution (averages) of the WTC differences (Top) between GNSS and MWR and (Bottom) between GNSS and GPD+ for the reference missions and GFO.

Fig. 15 represents the time evolution (averages) of the differences GNSS–MWR (top) and GNSS–GPD+ (bottom), for TOPEX/Poseidon (blue points), Jason-1 (red points), Jason-2 (black points), and GFO (green points). Small points represent averages of 10 days, while large points represent 370-day averages. Tables 4 and 5 show the values (slope and coefficient of determination) of the linear fit to

the 370-day averages for the differences GNSS–MWR and GNSS–GPD+, respectively, and the time span for each mission.

Time evolution of the differences GNSS–MWR for the reference missions and GFO reveals absolute slopes lower than 0.28 mm/year. R^2 of the linear fit for TOPEX mission is very small, thus indicating that annual means are not well fit by a linear regression; however, as shown in Fig. 15 (top), these differences vary in a range of about 2 mm (approximately between 2 and 4 mm). These 370-day averages of WTC differences between GNSS and MWR are always smaller than 5 mm.

Table 4. Linear fitting values and time span for the 370-day averages of the GNSS–MWR differences for the reference missions and GFO

Mission	Slope (mm/year)	R^2	Time span
TP	-0.03	0.02	1996.0-2005.8
J1	-0.28	0.81	2002.1-2012.2
J2	-0.19	0.56	2008.5-2016.9
GFO	-0.19	0.44	2000.0-2006.5

Table 5. Linear fitting values and time span for the 370-day averages of the GNSS–GPD differences for the reference missions and GFO

Mission	Slope (mm/year)	R^2	Time span
TP	-0.10	0.24	1996.0-2005.8
J1	-0.21	0.74	2002.1-2012.2
J2	-0.15	0.52	2008.5-2016.9
GFO	-0.13	0.49	2000.0-2006.5

Concerning the time evolution of the differences GNSS–GPD+ for the reference missions and GFO, shown in Fig. 15 (bottom), slopes with absolute values lower than 0.21 mm/year are given in Table 5. Overall, differences GNSS–MWR are larger than differences GNSS–GPD+, as observed for the previous missions.

The temporal analysis of the differences GNSS–MWR and GNSS–GPD+ for the eight altimetry missions shows an alignment between consecutive missions of the same group (reference or ESA missions) and also very similar WTC differences in the common period. With common objectives, this shows that altimetry missions of each group (35-day and 10-day) are aligned, constituting uniform intercalibrated data sets.

For studies such as sea level variation, the long-term stability of all terms involved in the computation of the altimeter-derived sea level anomaly is of particular relevance. The recent requirements state that these terms, including the WTC, should be known to better than 0.3 mm/year (Ablain et al., 2015). This analysis reveals slopes with absolute values lower than 0.3 mm/year for the

time evolution of the differences between GNSS and MWR, with a bit smaller values for differences between GNSS and GPD+.

It should be recalled that to ensure long-term stability of the corrections, all radiometers used in this paper have been calibrated with respect to the SSM/I and the SSM/IS (Fernandes et al., 2016). This paper reveals a good performance of this calibration, being the observed differences (at millimetre level) mainly due to the space–time collocation errors and to the atmospheric variability.

It is important to note that in this analysis of the time evolution of the WTC differences, all altimetry contaminated measurements close to the coast were rejected, so the results presented in this section are not affected by land contamination, neither by other error sources such as ice contamination.

Any comparison between GNSS and MWR, either function of distance from coast or function of time, provides an independent assessment. However, the disadvantage is the lack of a common spatial coverage, since noncollocated data were compared, being the results presented here global, but only relative to coastal zones.

2.2.5. Conclusion

This paper presents the application of ZTD computed at the University of Porto using the state-of-the-art methodologies to assess the performance of MWR on-board several altimetry satellites over coastal zones. The computation of ZTD UPorto (and corresponding GNSS-derived WTC) was performed using a homogeneous methodology throughout the whole period of analysis.

Results show the profound influence of the network geometry in the uncertainty associated with the retrieval of the tropospheric delays. Geographical distribution is of major importance in ZTD computation over a network of stations. An accuracy of a few millimetres (2–6 mm) in ZTDs from GNSS is achieved only if a good geographical distribution is guaranteed, in order to avoid effects of network geometry.

Two types of independent comparisons between GNSS-derived WTC and MWR-derived WTC were performed: function of distance to coast and function of time.

The first analysis allows clearly observing the land contamination in the MWR measurements of the various satellites, which is less pronounced in the MWRs on-board the reference missions. This coastal contamination is observed up to 20–30 km from the coast for the ESA and reference missions. For the GFO, this effect is observed up to 15–25 km from the coast. Due to its smaller footprint size, the same effect is observed only up to 10–20 km from the coast for SA. It can be observed that the effect of the MPA implemented in Jason-1 and Jason-2 by (Brown, 2010) has a pronounced effect in the reduction of the RMS of the differences between GNSS-derived and MWR-derived WTCs in the classes near the coast but not in the distance from coast up to which the contamination is depicted.

Overall, the RMS of the differences between GNSS and MWR-derived WTC, for the closest distance at which no land contamination occurs, is in the range 1.6–1.9 cm, mainly due to the collocation errors and to the WTC variability.

Thus, GNSS-derived WTC is a useful independent source to inspect the land contamination on the MWR observations.

In parallel with the comparison between WTC GNSS and WTC derived from MWR, the same comparison was performed between WTC GNSS and WTC GPD+. This comparison reveals clearly that this algorithm removes the land contamination and improves the WTC retrieval over the whole range of analysed distances to coast, ensuring the continuity of the WTC in the open-ocean/coastal transition zones and around islands.

The temporal analysis reveals a long-term stability in the MWR measurements, with absolute values of slope with respect to GNSS lower than 0.3 mm/year. In agreement with the coastal analysis, differences between GNSS and GPD+ are slightly smaller than the corresponding differences between GNSS and MWR.

For some altimetry missions, the analyses performed with the GNSS-derived WTC using WTC UPorto (60 stations distributed around the world) were also repeated using WTC derived from ZTD computed from a global set of hundreds of stations from international and regional networks (IGS and EPN). Similar results have been achieved, indicating that once a global set of stable stations with a good global distribution is selected, the results are not very different. These results are not shown since the analysis with the WTC GNSS UPorto is representative of a global network, including zones with a different spatial variability of the wet correction.

In spite of the fact that GNSS-derived and MWR-derived WTCs are not collocated measurements, these results show that the former is a useful independent source to inspect the land effects on MWR observations and to monitor the stability of these instruments, thus contributing to the retrieval of precise water surface heights from satellite altimetry over coastal zones.

2.3. Impact of the New ERA5 Reanalysis in the Computation of Radar Altimeter Wet Path Delays (Article 3)

Abstract — Satellite altimetry allows the estimation of accurate water surface heights only with accurate determination of all involved terms, namely, the wet tropospheric correction (WTC) or its symmetric value, the wet path delay (WPD). WPD is best determined from onboard microwave radiometer (MWR) measurements; however, the corresponding WPD retrievals become invalid close to land (e.g., coastal and inland waters). Alternative WPD sources are numerical weather models (NWMs), e.g., from the European Centre for Medium-Range Weather Forecasts (ECMWF). NWMs provide the parameters at 6-h intervals; however, ERA5 (the latest ECMWF reanalysis) provides hourly atmospheric parameters at $0.25^\circ \times 0.25^\circ$. The best spatial resolution is provided by the ECMWF operational model at $0.125^\circ \times 0.125^\circ$. Motivated by this new and improved temporal resolution, the focus of this paper is the global assessment of the impact of different temporal resolutions of ERA5 in the WPD computation. The same assessment is also performed concerning the spatial resolution of ERA5 and operational models. Aiming to identify the best compromise between spatial/temporal resolutions, accuracy, and computational time, WPDs computed using various combinations of these

resolutions were inter-compared and compared with MWR-derived WPD. The results show that the global root mean square (RMS) of the differences between MWR and ERA5 is 1.2 cm and the effect of using 1-h intervals instead of 6-h intervals is small, significant only for latitudes 30°–60° S and 30°–60° N. Hourly intervals do not have a significant impact on the WPD from ERA5, being a temporal resolution of 3 h high enough to ensure the same accuracy of 1 h, showing that ERA5 cannot map the WPD short space and time scales.

2.3.1. Introduction

Satellite radar altimetry is a remote sensing technique, whose principal objective is to measure the range from the satellite to the water surface. The range can then be converted into the height of the water surface relative to the reference ellipsoid (Chelton et al., 2001), knowing the altitude of the satellite orbit relative to the same reference surface. These measurements allow the global determination of the water surface height and its monitoring, either at regional (Cipollini et al., 2017) or global scales (Legeais et al., 2018). This water-level measurement from satellite altimetry involves the determination of several parameters, namely, the effect of the atmosphere in the altimetric signals (Fernandes et al., 2014). Due to the presence of water (vapor and liquid) in the atmosphere, when the signal travels from the satellite to the earth's surface, it suffers a delay designated by wet path delay (WPD). The corresponding correction that needs to be accounted for in the altimeter observations is its opposite value, the wet tropospheric correction (WTC). Otherwise, any water surface height measurement derived from satellite altimetry would be affected by this undesirable error.

With a value of up to 50 cm, the WPD is highly variable, both in space and time (Vieira et al., 2019). It has long been recognized that due to this high variability, the best and most accurate way to measure this effect over the open ocean is from collocated microwave radiometer (MWR) measurements, a passive instrument onboard most of altimetric missions. However, WPD retrievals from MWR measurements become systematically invalid and cannot be used over some regions, such as coastal zones (Fernandes et al., 2018; Vieira et al., 2019b) and inland waters (Fernandes et al., 2014; Vieira et al., 2018). On the other hand, some satellites (e.g., CryoSat-2) do not possess an MWR in their payload. For these reasons, alternative sources for the wet correction are required, such as those computed using numerical weather model (NWM) parameters (Fernandes et al., 2014; Legeais et al., 2014). Although the overall accuracy of the WPD from NWM is worse than the corresponding path delays from MWR, in the absence of any other data source, the WPD from NWM must be used (Fernandes et al., 2014).

WPD may be computed from global grids of single-level atmospheric parameters (Fernandes et al., 2014), at the corresponding NWM orography height, as described in Section 2.3.2, or from 3-D model fields (Collecte Localisation Satellites (CLS), 2011), the latter approach being much more computationally intensive. The difference between these two approaches (from 2-D or 3-D atmospheric parameters) to derive WPD from NWM at its orography height will be assessed and presented in Section 2.3.2.

Concerning the available NWM for the WPD computation, the European Centre for Medium-Range Weather Forecasts (ECMWF) provides some products of interest that have been used in the context of tropospheric corrections for satellite altimetry. The quality of the models has been increasing (Miller et al., 2010), particularly for the ERA Interim (Dee et al., 2011) reanalysis model from ECMWF. ERA5, the latest reanalysis model (Copernicus Climate Change Service, 2018) produced by ECMWF, is the fifth major global reanalysis data set, after ERA Interim. Presently, only a first batch covering the period from 2000 to present was released and is freely available for any user via the Copernicus Climate Change Service (C3S) Climate Data Store (CDS) (Copernicus Climate Change Service, 2018). Compared to ERA Interim (available at $0.75^\circ \times 0.75^\circ$ spatial sampling and 6-h intervals), ERA5 has a much higher spatial ($0.25^\circ \times 0.25^\circ$) and temporal (1-h) resolutions and an improved troposphere modelling. It is the first ECMWF atmospheric model available at 1-h intervals.

Another ECMWF product of interest is the operational model, which has the finest spatial sampling ($0.125^\circ \times 0.125^\circ$). ERA Interim is more stable than ECMWF operational model (Legeais et al., 2014); however, the latter has been updated and improved several times, and for the latest years (after 2004), it provides similar or better results when compared with ERA Interim (Fernandes et al., 2014).

In the altimetry community, it was believed that the common temporal resolution of the available NWM (6 h) was poor for use in the context of the radar altimeter tropospheric corrections and a better temporal resolution was required. Motivated by the new and high temporal resolution of ERA5 (Copernicus Climate Change Service, 2018), the focus of this paper is the assessment of the impact of 1-h sampling atmospheric parameters used for the WPD computation, for application in satellite altimetry. The NWM-derived WPDs are mainly useful over non open-ocean surfaces, namely, coastal and continental waters. For this purpose, WPDs computed from ERA5 at different temporal resolutions are intercompared in Section 2.3.3. Similar comparisons are carried out concerning different spatial resolutions of ERA5 and ECMWF operational models, also presented in Section 2.3.3.

All above-mentioned analyses are inter-comparisons that allow the assessment (not independent) of different spatial and temporal resolutions of the same atmospheric model. To perform an independent assessment of the WPD derived from ERA5 at different resolutions (both temporal and spatial), Section 2.3.4 presents the comparison between the ERA5-derived WPD and those retrieved from valid onboard MWR measurements. This independent comparison is carried out for MWR onboard ENVISAT and Jason-2 satellites. Finally, Section 2.3.5 summarizes the main achievements of this paper.

2.3.2. WPD computation from NWM parameters

This section presents the methodology used to derive WPDs from atmospheric fields provided by the ERA5 and ECMWF operational models.

2.3.2.1. Computation from Single-Level Parameters

NWM-derived WPD can be calculated from the global grids of two single-level parameters provided by the corresponding model: total column water vapor (TCWV) and the near-surface air

temperature (2-m temperature, T_0). This computation is performed using (1), where TCWV is expressed in kg/m^2 (or the equivalent precipitable water, in mm), and WPD results in meters (Bevis et al., 1992, 1994)

$$WPD = \left(0.101995 + \frac{1725.55}{T_m} \right) \frac{TCWV}{1000} \quad (1)$$

In (1), T_m is the mean temperature of the troposphere, in kelvin at each point, which is modelled from T_0 , as given by (2), according to (Mendes, 1999)

$$T_m = 50.440 + 0.789T_0 \quad (2)$$

It is important to note that single-level parameters, such as TCWV, are provided at only one level (orography); however, TCWV is representative of the total column, from the top of atmosphere (TOA) down to the orography level. This total water vapor content is the same, which affects the path of the altimetric signals, from the satellite to the surface.

The single-level parameters (as TCWV and T_0 used for the WPD computation) available from an atmospheric model are relative to the height of the corresponding orography, usually a smoothed representation of a digital elevation model. Thus, WPDs computed using (1) and (2) are provided at the level of the same reference surface, the model orography. Apart from the comparisons with MWR in Section 2.3.4, all analyses presented in this paper were performed at the height of the corresponding atmospheric model orography in order to avoid the introduction of undesirable biases.

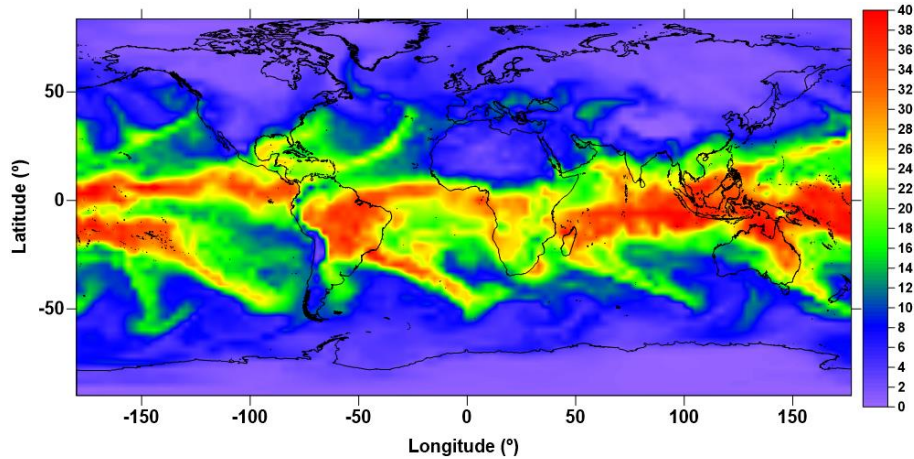


Figure 1. WPD mean (cm) computed from ERA5 single-level parameters, at the corresponding orography height, for the period 2010–2014 at $3^\circ \times 3^\circ$ spatial sampling.

As an example of the wet delay derived from an NWM (using single-level fields), Fig. 1 shows the global distribution of the WPD mean (cm), computed from (1) and (2), using TCWV and T_0 provided by ERA5. It was computed for the period 2010–2014, with grids every 6 h at $3^\circ \times 3^\circ$ spatial

sampling. Overall, the magnitude of the WPD is small over the polar regions and increases toward the equator (for more details about the WPD spatial distribution, see (Vieira et al., 2019)).

Another approach to derive the WPD from NWM is from 3-D atmospheric parameters provided at vertical levels (Collecte Localisation Satellites (CLS), 2011). This method involves the numerical integration of these parameters (of humidity and temperature) along the vertical profiles, from the TOA down to the surface. This approach requires much more computational power.

Section 2.3.2.2 will demonstrate that the use of WPD estimated from 2-D NWM parameters is adequate for the purpose of this study.

2.3.2.2. Comparison Between WPD Computed from Single-Level and 3-D Parameters

Two sets of WPD have been estimated from ERA5 for a time span of one year (2010). For each point on a grid $3^\circ \times 3^\circ$ every 6 h, two WPD values have been obtained at the height of the model orography: from 2-D and from 3-D parameters. The WPD computation from 3-D parameters is performed through numerical integration from the TOA down to the height of the model orography. This is performed using (3) as given in (Collecte Localisation Satellites (CLS), 2011), where P_{TOA} and P_{oro} are the corresponding pressures in hPa, respectively, q is the specific humidity in kg/kg, T is the temperature in kelvin, and WPD results in meters

$$WPD_h = \left(1.116454 \times 10^{-3} \int_{P_{TOA}}^{P_{oro}} q dp + 17.66543928 \int_{P_{TOA}}^{P_{oro}} \frac{q}{T} dp \right) \times (1 + 0.0026 \cos 2\varphi) \quad (3)$$

The analysis of the differences between these two WPD values allows to inspect their magnitude and spatial distribution. Fig. 2 shows the mean values of these WPD differences in millimetres computed for $3^\circ \times 3^\circ$ tiles. These differences have a global mean of 0.1 mm and a standard deviation of 1.6 mm.

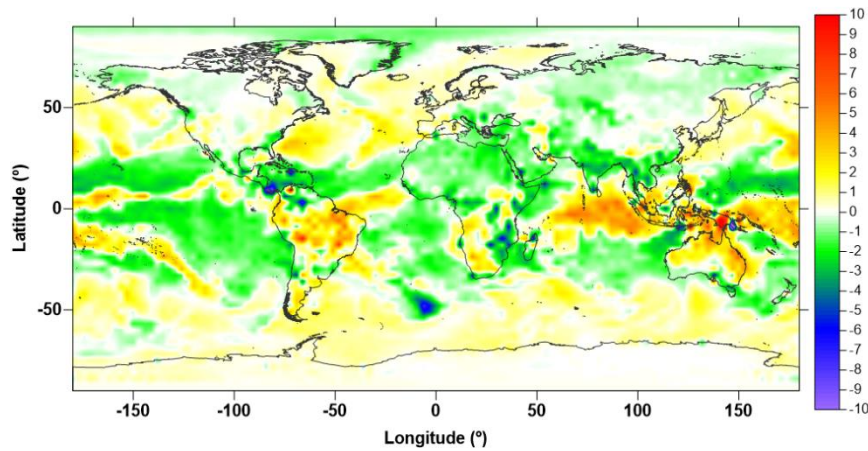


Figure 2. WPD mean differences (mm) between 2-D and 3-D approaches at orography height for the year 2010.

Observing Fig. 2, there are some regions with absolute WPD mean differences larger than 6 mm; however, the map is mainly green and yellow corresponding to WPD mean differences in the range $[-4, 4]$ mm. The root mean square (RMS) values of the same WPD differences reveal the maximum values of 1.1 cm in regions at low latitudes. The largest differences are in locations where WPD vertical variation is complex, namely due to its dependence on temperature, not well modelled by (1) and (2). The results show that although these WPD differences can exceed 1 cm, they are globally small. Therefore, in the interest of computational efficiency, the 2-D approach was adopted in this paper.

2.3.3. Inter-comparisons of NWM-derived WPD

The first analysis carried out in order to assess the impact of different resolutions in the WPD computation concerns the inter-comparisons of various NWM-derived WPDs. Using a time span of four years (2010–2014), several WPDs from ERA5 and ECMWF operational models, as shown in Tables 1 and 2, have been inter-compared.

For the ERA5 model, WPDs interpolated from single level atmospheric parameters at 2, 4, and 6-h intervals and at $0.6^\circ \times 0.6^\circ$ and $1.2^\circ \times 1.2^\circ$ spatial samplings have been considered. For the ECMWF operational model, WPDs interpolated from single-level atmospheric parameters at $0.25^\circ \times 0.25^\circ$, $0.50^\circ \times 0.50^\circ$ and $0.75^\circ \times 0.75^\circ$ spatial samplings have been compared. Other WPD values have been computed for the instants and grid points of the native resolution of each model (1 h and $0.3^\circ \times 0.3^\circ$ for ERA5 and 6 h and $0.125^\circ \times 0.125^\circ$ for ECMWF operational model), without any temporal or spatial interpolation, to be used as a reference in these inter-comparisons.

The ERA5 data have a native resolution of 0.28125° (31 km) and ECMWF recommends rounding the resolution to 0.25° . The ERA5 data used in this paper were requested in the NetCDF format with a spatial resolution of $0.3^\circ \times 0.3^\circ$, which is automatically interpolated to this regular grid (selected by the user).

2.3.3.1. Using Different Temporal Resolutions

For the inter-comparisons using different temporal resolutions, maintaining the same spatial resolution ($0.3^\circ \times 0.3^\circ$), only ERA5 was adopted and the following methodology was used: 1) for each grid point of the ERA5 model, a reference WPD value is computed using the corresponding atmospheric parameters, at the model native resolution; 2) for the same grid point, another WPD value is derived using the corresponding atmospheric parameters of the grids 1 h before and 1 h after (2-h interval), interpolated in time to the instant of the actual 1-h resolution grid; 3) another WPD value computed as the latter, but using the grids 2 h before and after (4-h interval); and 4) another WPD value interpolated in time using the grids 3 h before and after (6-h interval). All interpolated WPD values are obtained from the WPD computed using the atmospheric parameters at full resolution. All these WPD values are summarized in Table 1.

Table 1. Temporal resolutions used to compute various WPDs from ERA5 model

	Temporal resolution
NWM	ERA5
Reference WPD (not interpolated)	1-h
Interpolated WPD	2-h
	4-h
	6-h

Using these four global WPD values for a period of four years, three differences are calculated between the noninterpolated WPD and those interpolated using atmospheric parameters from ERA5 at 2, 4, and 6-h intervals. These global sets of WPD differences have been binned into classes of latitude and an RMS value is calculated for each WPD difference and for each class of latitude. Fig. 3 (top) shows these RMS values in cm for the latitude classes of 3° . Blue bars represent the rms of the differences between the non-interpolated WPD and those interpolated using ERA5 atmospheric parameters at 6-h intervals. Orange and green bars represent the corresponding values when 4 and 2-h intervals are used, respectively.

The same global sets of WPD differences were binned per day, computing daily weighted rms of the differences (weight function of the co-sine of latitude) for the whole globe. RMS of these daily and globally differences is shown in Fig. 3 (bottom) using the same colour code, allowing to observe the time evolution of the various WPD differences (rms) and providing a global rms for each difference.

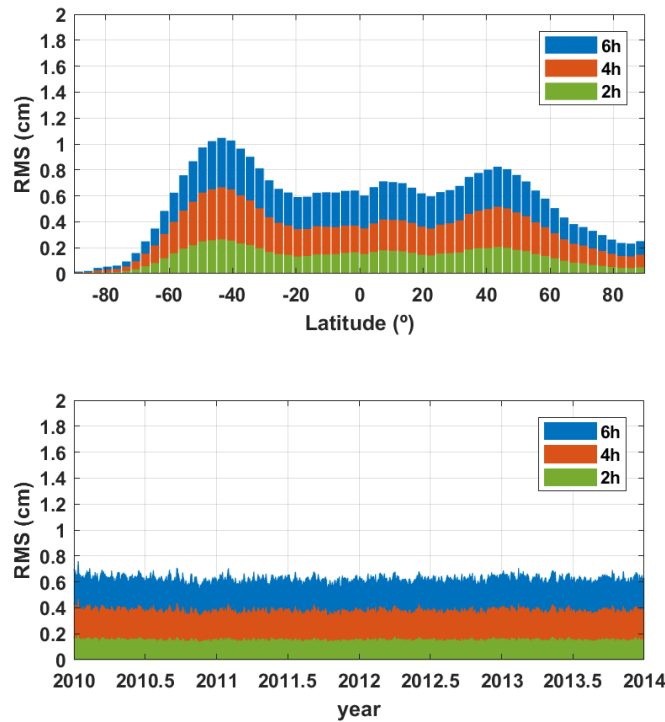


Figure 3. RMS (cm) of WPD differences function of latitude for classes of 3° (top) and function of time computed for weighted daily and global differences (bottom). WPD differences are between the reference values and those interpolated using different temporal resolutions, both from ERA5.

Fig. 3 shows that, as expected, the differences increase with the time interval between the consecutive WPD grids. These differences show the maximum values around latitudes $\pm 45^\circ$, larger in the southern hemisphere (latitudes 30° – 50° S), with a maximum rms value of about 1.0, 0.6, and 0.2 cm for the 6, 4, and 2-h intervals, respectively. These values are indicators of the effect of the time sampling used to compute WPD from ERA5. Fig. 3 (bottom) shows a constant pattern and the global RMS values for the WPD differences of about 0.6, 0.4, and 0.2 cm when 6, 4, and 2-h intervals are used, respectively.

To observe the spatial distribution of the differences between the reference (non-interpolated) WPD and the corresponding interpolated values using 6-h intervals (shown in blue in Fig. 3), Fig. 4 shows the same rms values computed for $3^\circ \times 3^\circ$ tiles. The largest differences observed in Fig. 3 (top) in the southern hemisphere are observed in Fig. 4 for latitudes around 45° S. Fig. 4 also shows the regions with rms values larger than 1 cm and zones where this value is small (such as South Atlantic Ocean close to the coast of Africa, South Pacific Ocean close to Peru and Chile and polar regions).

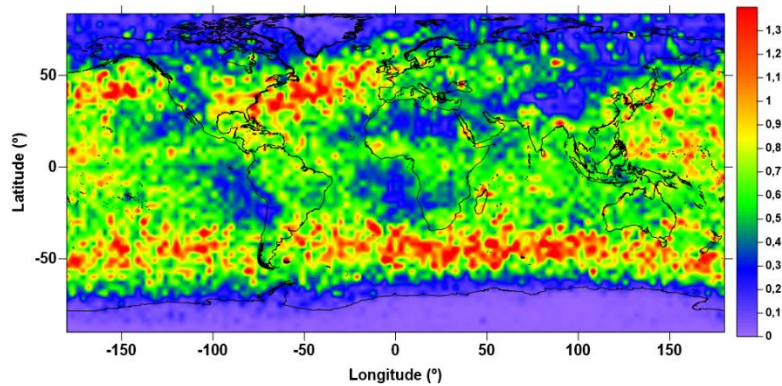


Figure 4. RMS (cm) of the WPD differences when WPD is interpolated from ERA5 grids 6-h apart.

These results show that when compared with WPD derived from ERA5 at its best temporal resolution, the use of atmospheric parameters at 6 h has an impact less than 1 cm (~ 0.6 cm) in the global WPD computation [see Fig. 3 (bottom)]; however, in some regions, this value can reach 1 cm [see Fig. 3 (top)] or even be larger than 1 cm (see Fig. 4).

The interpretation of these results needs some care. Since this is a comparison between different temporal resolutions, large differences can be associated with regions where the WPD is more variable in time or simply regions where the effect of using different temporal model resolutions is significant (irrespective of the WPD time variability). The identification of zones with latitudes around $\pm 40^\circ$ with the largest rms values (see Figs. 3 and 4) is mainly due to the second reason, as it will be confirmed and discussed in Section 2.3.4, after comparing with independent observations. When different temporal resolutions are compared, small differences mean that the different resolutions do not generate significantly different path delays. On the contrary, large differences mean that the different temporal resolutions generate different path delays, which can mean that one of them maps better the WPD than the other one, irrespective of its temporal variation.

The significant impact of ERA5 at 1 h, instead of 6 h, observed in some latitude bands (not necessarily with the highest WPD temporal variability) can be associated with regions where there is a larger amount of input data to the ERA5 reanalysis data assimilation (Zhang et al., 2018).

2.3.3.2. Using Different Spatial Resolutions

For the inter-comparison using different spatial resolutions, ERA5 and ECMWF operational models were examined. The following methodology was adopted: 1) for all grid points of each model, a WPD value is computed at the native resolution of the NWM using the corresponding atmospheric parameters, adopted as the reference WPD values; 2) for the same grid points, a WPD value is interpolated in space, from WPD values at the four neighbouring grid points, which are the corners of a square with centre in the previously mentioned grid points and with size twice the highest resolution of each model ($0.6^\circ \times 0.6^\circ$ for ERA5 and $0.25^\circ \times 0.25^\circ$ for ECMWF operational); 3) another WPD value computed as the latter, but taking a square with a size of four times the models' resolution ($1.2^\circ \times 1.2^\circ$ for ERA5 and $0.50^\circ \times 0.50^\circ$ for ECMWF operational); 4) another WPD value computed as the latter, only for the ECMWF operational model, considering a square with a size of six times the model resolution ($0.75^\circ \times 0.75^\circ$). All these WPD values obtained from different spatial resolutions are summarized in Table 2.

Table 2. Spatial resolutions used to compute various WPDs from era5 and ECMWF operational models

NWM	Spatial resolution	
	ERA5	Operational
Reference WPD (not interpolated)	$0.3^\circ \times 0.3^\circ$	$0.125^\circ \times 0.125^\circ$
	$0.6^\circ \times 0.6^\circ$	$0.25^\circ \times 0.25^\circ$
Interpolated WPD	$1.2^\circ \times 1.2^\circ$	$0.50^\circ \times 0.50^\circ$
		$0.75^\circ \times 0.75^\circ$

Using these global sets of WPD for the period from 2010 to 2014, differences have been calculated between the reference WPD and those interpolated using different spatial resolutions, as explained earlier.

As in the analysis using different temporal resolutions, these WPD differences were binned into classes of latitude (3°) and, for each day, calculating the rms for each class. Fig. 5 (top) shows these values for ERA5, function of latitude. The maximum rms of about 1.3 and 0.8 cm for the differences between the reference WPD and those interpolated at $1.2^\circ \times 1.2^\circ$ (blue) and at $0.6^\circ \times 0.6^\circ$ (orange), respectively, is observed in the equatorial region. Concerning the time evolution of the global and daily rms [see Fig. 5 (bottom)], the same differences have the global rms of about 0.8 and 0.4 cm, respectively. This time evolution also reveals the existence of an annual signal in these differences, with maximum values during boreal summer, due to the WPD seasonal variability. The largest differences are observed in periods of year where WPD reaches its maximum variability.

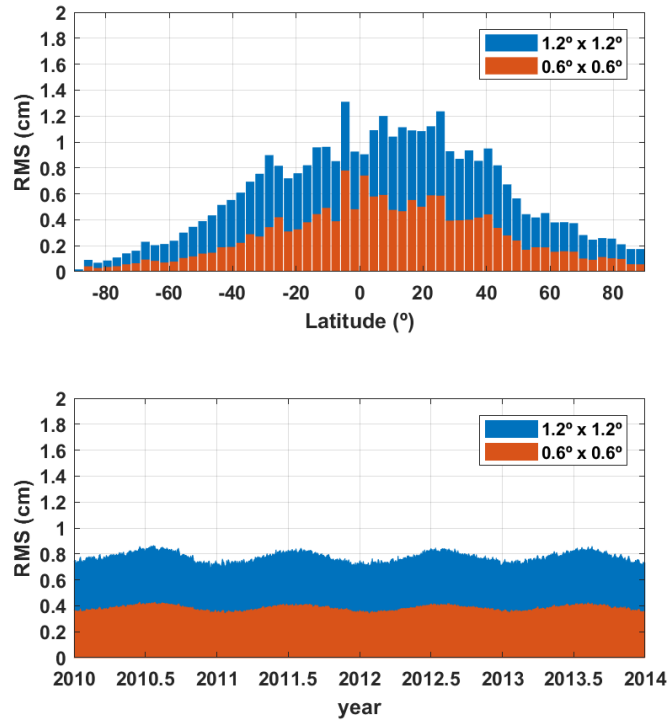


Figure 5. RMS (cm) of WPD differences function of latitude for classes of 3° (left) and function of time computed for each day (right). WPD differences are between the reference values and those interpolated using different spatial resolutions, both from ERA5.

The same RMS values represented in blue in Fig. 5 were computed globally for $3^\circ \times 3^\circ$ tiles and shown in Fig. 6. Fig. 6 allows to observe the spatial pattern of these differences (rms). The most striking feature is the latitudinal dependence of these differences, in agreement with Fig. 5 (top). RMS larger than 1.0 cm is observed in some regions, with the highest values mainly over land and coastal zones at latitudes around 50° S– 50° N. The significance of these values (represented in Figs. 5 and 6) will be discussed again in Section 2.3.4, after an independent assessment of the various spatial resolutions.

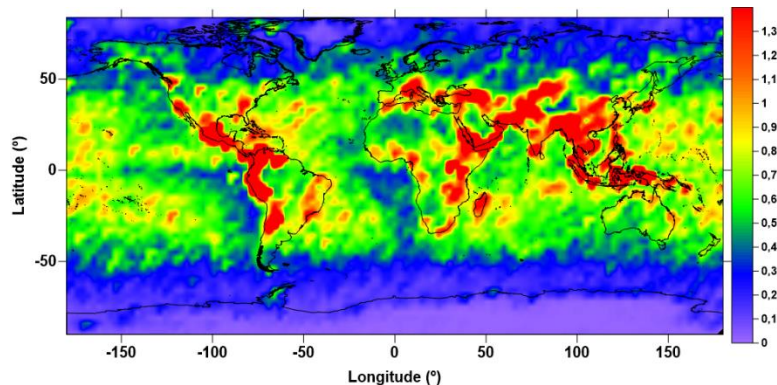


Figure 6. RMS (cm) of the WPD differences when WPD is interpolated from ERA5 at $1.2^\circ \times 1.2^\circ$ spatial sampling.

Regarding the same analysis using WPD from the ECMWF operational model, Fig. 7 (top) shows the maximum rms values of about 1.6, 1.0, and 0.4 cm for WPD differences between the WPD reference values and those interpolated at $0.75^\circ \times 0.75^\circ$, $0.50^\circ \times 0.50^\circ$, and $0.25^\circ \times 0.25^\circ$, respectively. The

same differences calculated globally and daily [see Fig. 7 (bottom)] have the rms values of about 0.7, 0.5, and 0.2 cm.

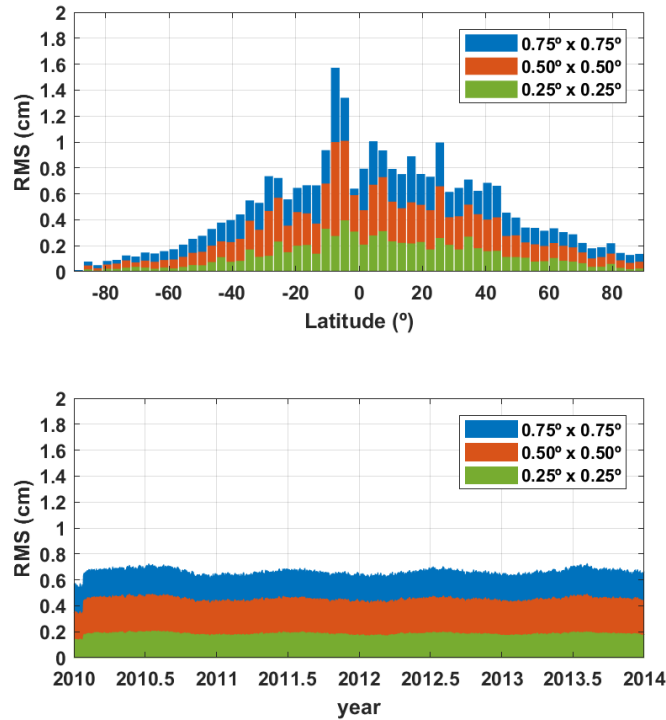


Figure 7. RMS (cm) of (Top) WPD differences function of latitude for classes of 3° and (Bottom) function of time computed for each day. WPD differences are between the reference values and those interpolated using different spatial resolutions, both from ECMWF operational model.

The results represented in Fig. 7 (bottom) show a jump in the beginning of 2010, after which the three WPD differences become larger. This jump occurs in the same instant of an upgrade in the ECMWF operational model (January 26, 2010), with a corresponding change in the model orography. This can mean that this change leads to a better modelling of the troposphere. When WPD differences between different spatial samplings are examined, low differences mean that the increase in spatial resolution does not conduct to significant improvement in the modelling of the WPD spatial variation. On the contrary, large differences indicate a better modelling of the WPD spatial variation, only depicted by the finest resolutions.

The results of this section reveal the global WPD differences with rms smaller than 0.8 cm [see Figs. 5 and 7 (bottom)]; however, values larger than 1 cm exist in some regions [see Figs. 5 and 7 (top)]. Concerning ERA5, when $0.6^\circ \times 0.6^\circ$ spatial sampling is used, differences have a global rms of about 0.4 cm, being smaller than 0.8 cm over the equator. Regarding the ECMWF operational model, when $0.75^\circ \times 0.75^\circ$ spatial sampling is considered, differences have a global rms of about 0.7 cm and rms values can reach 1.6 cm close to the equator. Concerning these differences using the $0.50^\circ \times 0.50^\circ$ spatial sampling, the rms values are not larger than 1 cm.

The focus of this study is the assessment of the impact of using different NWM resolutions in order to determine the best compromise between the accuracy of the NWM-derived WPD and also the corresponding computational time. Being the above-mentioned results related with the ability of

the atmospheric models to resolve the atmosphere, with respect to the water vapor distribution and variability, there is interest in the identification of regions with different WPD temporal and spatial variabilities (Stum et al., 2011). This is of great relevance for some existing algorithms to improve the WPD retrieval (Fernandes et al., 2010, 2015, 2016), allowing to improve the knowledge of WPD spatial and temporal correlations, crucial in the combination of different WPD sources.

All the results presented in this section are provided by inter-comparisons between various NWM-derived WPD, using different temporal and spatial resolutions of the models. For a complete analysis, an independent assessment is required, namely using WPD retrieved from an external and more accurate source (e.g., measurements from MWR).

2.3.4. Independent comparison between MWR and ERA5-derived WPD

For an independent evaluation of the impact of using different resolutions of ERA5 in the WPD computation, this section presents a comparison with the measurements retrieved from MWR onboard ENVISAT and Jason-2. MWR provides WPDs over the open ocean with enough accuracy for satellite altimetry studies (errors of less than 1 cm) (Brown, 2010; Keihm et al., 1995). These altimetry data are provided by the Radar Altimeter Database System (RADS) (Scharroo, 2016). Using a time span of one full year (2010), WPDs from these MWRs have been compared with those computed from ERA5 considering different spatial and temporal model samplings. For each along-track measurement of MWR, three WPD values are interpolated from ERA5: 1) using $0.3^\circ \times 0.3^\circ$ and 1 h, the best resolutions; 2) $0.3^\circ \times 0.3^\circ$ and 6 h, as the former, but degrading the temporal resolution; 3) $0.6^\circ \times 0.6^\circ$ and 6 h, as the second, but degrading the spatial resolution. For these comparisons, only MWR-derived WPD measurements flagged as valid and with latitudes in the range $[-60^\circ, 60^\circ]$ were used. The validity criteria consider only open-ocean points absent of land, ice, and rain contamination (Fernandes et al., 2016). Since MWR-derived WPD measurements are provided at sea level, for this comparison, all ERA5-derived WPD values are reduced to sea level using an empirical expression (Kouba, 2008). Anyway, note that over open ocean, the ERA5 orography is very close to the sea level (differences smaller than 1 m).

The various WPD differences between the MWR-derived WPD and those interpolated from ERA5 were binned into classes of latitude (3°), and rms values were calculated for each class. These rms values, function of latitude, for WPD differences between MWR onboard ENVISAT and ERA5 (left) and between MWR onboard Jason-2 and ERA5 (right) are shown in Figs. 8 and 10. Fig. 8 shows the effect of using the same spatial sampling ($0.3^\circ \times 0.3^\circ$) and different temporal resolutions (1 or 6 h), while Fig. 10 shows the effect of using the same temporal resolution (6 h) and different spatial samplings ($0.3^\circ \times 0.3^\circ$ or $0.6^\circ \times 0.6^\circ$), when compared with an independent WPD source.

2.3.4.1. Impact of the Temporal Resolution

Concerning the use of different temporal resolutions, the results shown in Fig. 8 reveal that the rms of differences between the MWR- and ERA5-derived WPDs is in the range 0.6–1.7 cm, depending on the latitude band. However, a small effect is detected when WPD values are interpolated from 1-h sampled parameters (green), instead of 6-h sampled parameters (orange). This small effect

corresponds to rms differences lower than 0.2 cm, only in some regions (approximately 30°–60° S and 30°–60° N). These results are in agreement with those shown in Fig. 3 (top), where the WPD differences are larger in the same latitude bands. These regions do not necessarily represent the highest WPD temporal variability (Stum, 1994). On the contrary, the largest differences observed in Section 2.3.3 (see Figs. 3 and 4) are due to the effect of using different temporal resolutions of the ERA5, shown to be significant only for these regions.

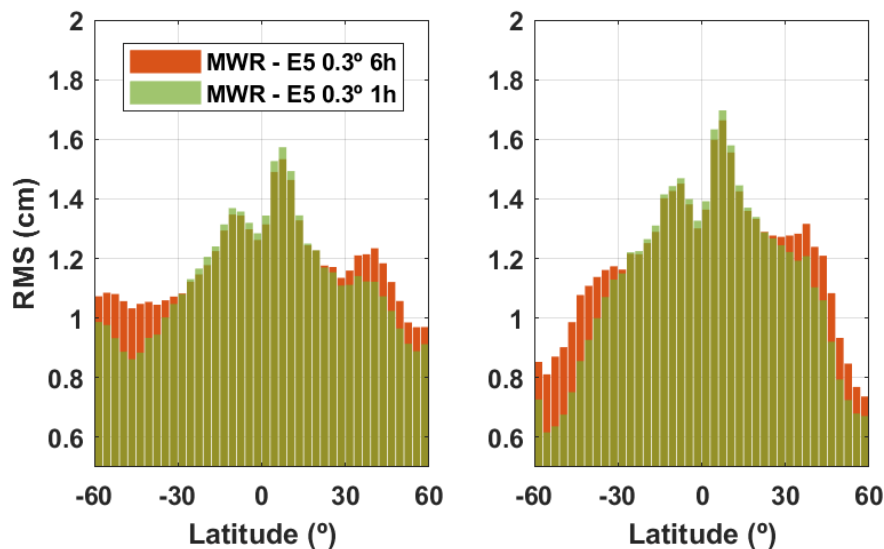


Figure 8. RMS (cm) of the WPD differences between (Left) MWR onboard EnviSat and (Right) Jason-2 and ERA5 at different temporal resolutions (1- and 6-h intervals), maintaining the same spatial resolution (0.3° × 0.3°).

To confirm the global results shown in Fig. 8, Fig. 9 shows an example of an ENVISAT partial track, where WPD derived from its MWR is represented in black, while WPD derived from ERA5 is represented in orange (6 h) and green (1 h). Fig. 9 confirms that overall, there are no large differences between the two WPD derived from ERA5, showing similar behaviour to the path delay retrieved from MWR. For high variations well detected by the MWR, as observed for latitudes close to 24° N, using 1-h intervals, the NWM-derived WPD is slightly closer to the WPD retrieved from the MWR than the corresponding 6-h interval values. However, even using the highest temporal resolution, the WPDs derived from ERA5 are not able to detect this large variation. It has long been recognized that the WPD computed from meteorological models has poorer accuracy than the MWR valid measurements, because such models often cannot map the atmospheric humidity small space and time scales (Stum, 1994). Thus, these results confirm the small effect of using 1-h intervals, instead of 6-h intervals, and the inability of the ERA5 to detect short time scales of the WPD, even at 1-h resolution.

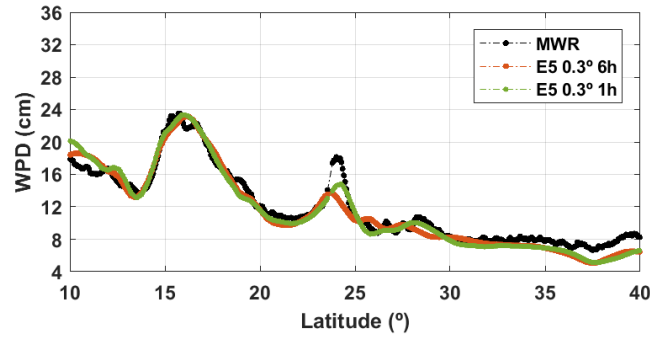


Figure 9. Example of the WPD (cm) from ENVISAT MWR (black) and interpolated from ERA5 at $0.3^\circ \times 0.3^\circ$ and 1-h (green) and $0.3^\circ \times 0.3^\circ$ and 6-h (orange), showing only the effect of the temporal resolution.

2.3.4.2. Impact of the Spatial Resolution

Regarding the effect of the spatial resolution in the computation of the WPD from ERA5, when compared with independent measurements from onboard MWR (ENVISAT and Jason-2), Fig. 10 shows very small differences between WPDs interpolated from ERA5 at $0.3^\circ \times 0.3^\circ$ and $0.6^\circ \times 0.6^\circ$. The results show that there is no significant effect when WPD derived from ERA5 is interpolated at $0.6^\circ \times 0.6^\circ$, instead of $0.3^\circ \times 0.3^\circ$, proving that ERA5 cannot detect the WPD short space scales, even with its finest spatial resolution. Fig. 10 shows that the rms of the differences between the MWR- and ERA5-derived WPDs in all cases is in the range 0.7–1.7 cm, depending on latitude.

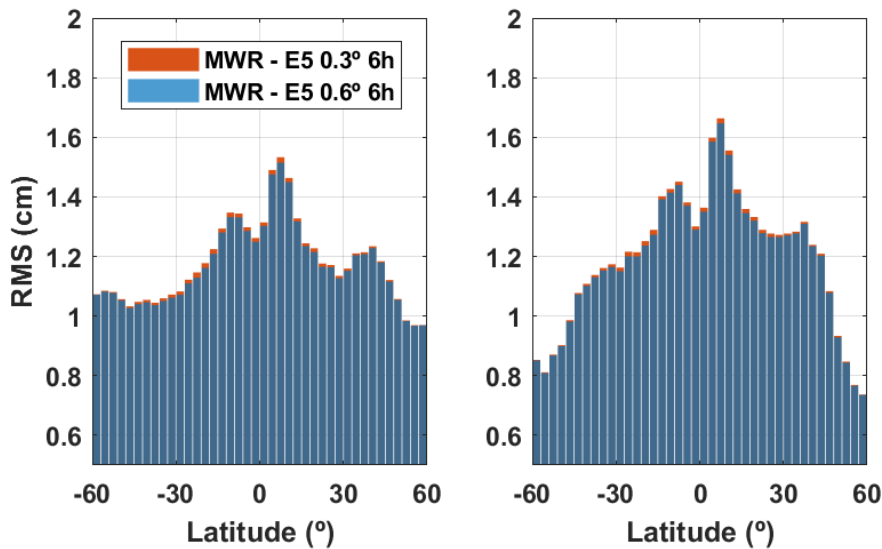


Figure 10. RMS (cm) of the WPD differences between (Left) MWR onboard ENVISAT and (Right) Jason-2 and ERA5 at different spatial resolutions ($0.3^\circ \times 0.3^\circ$ and $0.6^\circ \times 0.6^\circ$), maintaining the same temporal resolution (6-h intervals).

Fig. 11 shows an example for the same partial track of ENVISAT, where significant differences between WPDs interpolated at $0.3^\circ \times 0.3^\circ$ or $0.6^\circ \times 0.6^\circ$ are not observed, confirming the global results represented in Fig. 10 (left). These results indicate that to optimize the calculation time, $0.6^\circ \times 0.6^\circ$ spatial sampling may be used, since a finer spatial resolution does not significantly improve the

ERA5-derived WPD. Note that a reduction of resolution from $0.3^\circ \times 0.3^\circ$ to $0.6^\circ \times 0.6^\circ$ corresponds to a data reduction of 1/4, very relevant in terms of computational effort.

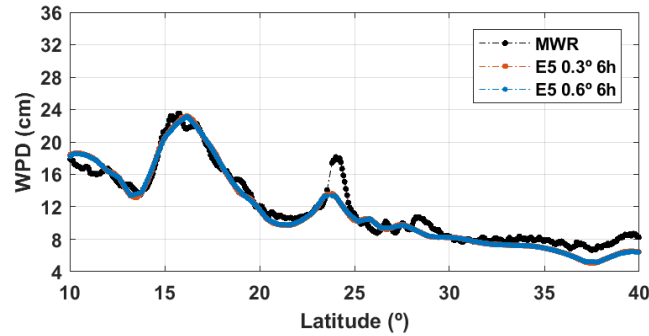


Figure 11. Example of the WPD (cm) from ENVISAT MWR (black) and interpolated from ERA5 at $0.3^\circ \times 0.3^\circ$ and 6 h (orange) and $0.6^\circ \times 0.6^\circ$ and 6 h (blue), showing only the effect of the spatial resolution.

Globally, the three WPD differences represented in Figs. 8 and 10 have rms values around 1.2 cm, without very significant global differences between them. Depending on latitude, these rms values vary between 0.6 and 1.7 cm. These numbers are indicators of the actual accuracy of WPD derived from ERA5 when compared with a more accurate source (MWR).

The previous analyses with NWM inter-comparisons show a global rms of about 0.6 cm when 6-h intervals are used [see Fig. 3 (bottom)] and a global rms of about 0.4 cm when $0.6^\circ \times 0.6^\circ$ spatial sampling is used [see Fig. 5 (bottom)]. These last two rms values (0.6 and 0.4 cm) are very low compared with the global RMS value of the differences between MWR and ERA5 (1.2 cm). For this reason, the effect of using different spatial ($0.3^\circ \times 0.3^\circ$ or $0.6^\circ \times 0.6^\circ$) and temporal (1-h or 6-h) resolutions to derive WPD from ERA5, when compared with that from MWR, is insignificant or very small. These results are explained by the fact that NWM is not able to model the smallest spatial and temporal scales of the WPD variability (Stum, 1994), showing that the same happens for the latest reanalysis from ECMWF.

In general, models cannot represent variability on scales smaller than those defined by the spacing grid ($0.25^\circ \times 0.25^\circ$ for ERA5). In fact, models do not represent the grid scale very well, being the effective resolution of models somewhat larger than the grid scale.

Defining the effective resolution as the smallest scale that the model can resolve fully, spectral analyses have been shown that the effective resolution is estimated as eight times the model grid spacing. Defining the effective useful resolution as the scale required to map at least 50% of the field variability of that scale, the same analyses show that the effective useful resolution is four times the grid resolution (Abdalla et al., 2013). Regarding the ERA5 reanalysis, these two definitions of effective horizontal resolutions are around 2.3° and 1.1° (considering the native resolution of 0.28125°).

The analysis shown in Fig. 10 was extended to other spatial resolutions (1.2° , 1.8° , and 2.4°) using the same period of ENVISAT data, and the results (not shown) indicate that using 0.3° , 0.6° , or 1.2° spatial samplings, the ERA5 does not generate a significantly different WPD. Only using a spatial resolution worse than 1.2° , the differences with MWR measurements become significantly larger. This

value agrees with the definition of effective useful resolution, as described earlier (Abdalla et al., 2013) and explains the results shown in Figs. 10 and 11.

This independent comparison with MWR-derived WPD also confirms that the results present in Section 2.3.3, shown in Figs. 5 and 6, do not have a physical meaning. Large differences observed may be only due to interpolation errors in areas of high WPD gradient, since the spatial resolutions of $0.3^\circ \times 0.3^\circ$, $0.6^\circ \times 0.6^\circ$, and $1.2^\circ \times 1.2^\circ$ do not generate WPD significantly different.

Figs. 8 and 10 allow also to observe that, mainly for latitudes near $\pm 60^\circ$, the differences between MWR onboard ENVISAT and ERA5 (left) are larger than the differences between MWR onboard Jason-2 and ERA5 (right). This is because missions as Jason-2 (the so-called reference missions) and those as ENVISAT (European Space Agency missions) have different spatial coverages, due to their orbit repeat cycles (10 and 35 days, respectively).

The analysis presented in Section 2.3.3 is global (includes both ocean and land). On the contrary, the analysis presented in this section is only performed over open ocean (where valid MWR measurements exist), which is the regions of interest for satellite altimetry. For these reasons, the results of Sections 2.3.3 and 2.3.4 are not directly comparable. Thus, the same inter-comparisons shown in Section 2.3.3 were performed only for oceanic regions and the results similar to the global ones are achieved. Only the rms of the differences between various ERA5-derived WPDs computed for latitude bands is a bit different, but it remains smaller than the rms of the differences between MWR and ERA5 (0.6–1.7 cm).

2.3.5. Conclusion

This paper describes the impact of using atmospheric parameters from NWM (ERA5 and ECMWF operational models) at different spatial and temporal resolutions in the computation of the WPD for application in satellite altimetry, with a particular interest in the new and high temporal resolution of the ERA5 (1-h intervals).

NWM-derived WPDs used in the analyses of this paper are those computed using single-level parameters; however, it is shown that the impact of using this approach instead of using atmospheric parameters on vertical levels (3-D) is small. This comparison shows the differences at the orography height with a global mean of 0.1 mm and a standard deviation lower than 2 mm, while the rms computed for $3^\circ \times 3^\circ$ tiles is lower than 1.1 cm.

Inter-comparisons between various NWM-derived WPD reveal differences with the global rms values of about 0.6, 0.4, and 0.2 cm, when 6-, 4-, and 2-h intervals, instead of the native 1-h values, are used in the WPD computation from ERA5, respectively. However, using 6-h intervals, the rms can be larger than 1 cm in some regions (mainly at latitudes around $\pm 50^\circ$ and in the southern hemisphere). For the spatial resolution, the same analysis reveals the WPD differences with a global rms of about 0.4 cm when $0.6^\circ \times 0.6^\circ$ spatial sampling of ERA5 is used instead of the original $0.3^\circ \times 0.3^\circ$ spacing, being the maximum of this rms smaller than 0.8 cm close to the equator. Using the ECMWF operational model, the results show the WPD differences with the global rms values of about 0.2, 0.5, and 0.7 cm when $0.25^\circ \times 0.25^\circ$, $0.50^\circ \times 0.50^\circ$, and $0.75^\circ \times 0.75^\circ$ spatial samplings are used in place of

the original $0.125^\circ \times 0.125^\circ$ spacing. However, the same values can reach 0.4, 1.0, and 1.6 cm in some regions (mainly over coastal zones at low latitudes, where spatial WPD variability seems to be large).

Independent comparisons with WPD derived from MWR (onboard ENVISAT and Jason-2) show an insignificant effect when WPD is interpolated from ERA5 at $0.6^\circ \times 0.6^\circ$, instead of $0.3^\circ \times 0.3^\circ$ spatial sampling, indicating that to optimize the computational time, $0.6^\circ \times 0.6^\circ$ spatial sampling may be used. This shows that the effective useful spatial resolution of the ERA5 is a bit worse than its native resolution. Concerning the temporal sampling, the effect of using 1-h intervals instead of 6-h intervals is significant only in some regions (latitude bands around $30^\circ\text{--}60^\circ$ S and $30^\circ\text{--}60^\circ$ N) and this effect is smaller than 0.2 cm in the rms values of the differences between MWR and ERA5. These results show that 1-h intervals do not have a significant effect on the WPD accuracy from ERA5, being a temporal resolution of e.g., 3 h enough to remove this small effect of only 0.2 cm in the rms and to ensure the same accuracy of using 1-h intervals. This is due to the inability of the model to represent the smaller scales of variability, both in space and time.

Overall, the results indicate that the observed differences in the inter-comparisons of various ERA5-derived WPDs are small when compared with the differences between the WPD retrieved from MWR and those from ERA5, which were shown to have a global rms value of 1.2 cm, varying in latitude between 0.6 and 1.7 cm.

As recognized for the previous atmospheric models, the results obtained from the independent comparisons show that ERA5 cannot map the WPD small space and time scales, evidencing the limitations of the latest ECMWF reanalysis, being the measurements from MWR, whenever valid, the most accurate way to measure the effect of the wet troposphere in satellite altimetry.

Results of this paper provide relevant information to ensure that when NWM-derived WPDs are used in satellite altimetry, the best compromise is achieved between accuracy and computational time.

3. Modelling the Altitude Dependence of the Wet Path Delay for Coastal Altimetry Using 3-D Fields from ERA5 (Article 4)

Abstract – Wet path delay (WPD) for satellite altimetry has been provided from external sources, raising the need of converting this value between different altitudes. The only expression available for this purpose considers the same altitude reduction, irrespective of geographic location and time. The focus of this study is the modelling of the WPD altitude dependence, aiming at developing improved expressions. Using ERA5 pressure level fields (2010–2013), WPD vertical profiles were computed globally. At each location and for each vertical profile, an exponential function was fitted using least squares, determining the corresponding decay coefficient. The time evolution of these coefficients reveals regions where they are highly variable, making this modelling more difficult, and regions where an annual signal exists. The output of this modelling consists of a set of so-called University of Porto (UP) coefficients, dependent on geographic location and time. An assessment with ERA5 data (2014) shows that for the location where the Kouba coefficient results in a maximum Root Mean Square (RMS) error of 3.2 cm, using UP coefficients this value is 1.2 cm. Independent comparisons with WPD derived from Global Navigation Satellite Systems and radiosondes show that the use of UP coefficients instead of Kouba’s leads to a decrease in the RMS error larger than 1 cm.

3.1. Introduction

The presence of water in the atmosphere plays a key role in the Earth’s climate, being crucial for human life. With economic and social impacts, remote sensing techniques have been developed to measure and monitor the water vapor content in the troposphere, namely its vertical distribution (Chaboureaud et al., 1998). However, the water vapor content in the atmosphere is itself an undesirable factor for some remote sensing techniques, as satellite radar altimetry, whose final purpose is not to measure the atmospheric properties.

Satellite altimetry’s main objective is the measurement of the sea surface height (SSH) above a reference surface (Chelton et al., 2001), allowing applications as the monitoring of the mean sea level (Ablain et al., 2015; Legeais et al., 2018), at global or regional scales. The SSH depends on the measurement of the range between the satellite orbit and the sea surface and on the satellite altitude above the same reference surface. Contrary to what happens in the vacuum, the propagation of the radar signals through the atmosphere is affected by its constituents (Fernandes et al., 2014). One of these effects is the path delay induced by the wet troposphere, which, in the context of satellite altimetry, is one of the atmospheric corrections to be considered: the wet tropospheric correction

(WTC). Since this delay leads to an additional path induced by the wet troposphere, the WTC is a negative value in the altimetric equations involved in the SSH estimation. Mainly due to the presence of water vapor in the troposphere, the WTC has a maximum absolute value of 0.5 m. Hereafter, for simplification, its absolute value, the wet path delay (WPD) is adopted.

Accurate determination of SSH from satellite altimetry, either over the ocean or continental waters, depends on the accuracy of all terms involved in its computation, namely the WPD. It is known that the water vapor concentration is highly variable in the atmosphere, both in space and time, and its greatest concentration is near the ground and in the tropics (Vieira et al., 2019). Due to this complex 4-D variation, for altimetry applications over open-ocean, the WPD is best determined from collocated measurements provided by Microwave Radiometers (MWR), passive instruments on board most of altimetric missions (Brown, 2010). Satellite altimetry has been used over coastal (Cipollini et al., 2017; Fernandes et al., 2018; Handoko et al., 2017) and inland waters (Fernandes et al., 2014; Vieira et al., 2018), however the WPD retrievals from MWR measurements become invalid and cannot be used over these regions (Vieira et al., 2019b). The current algorithms that compute the WPD from MWR measurements have been tuned to conditions only over ocean surfaces (Thao et al., 2015). When different surfaces (e.g., land) are present in the footprint of the MWR, the algorithms will return the corresponding ocean-like WPD, resulting in invalid values over e.g., coastal and continental waters.

Alternative sources to provide valid WPD values for these zones can be the Global Navigation Satellite Systems (GNSS) ground stations (Fernandes et al., 2013; Vieira et al., 2019b) and Numerical Weather Models (NWM) (Fernandes et al., 2014; Legeais et al., 2014), e.g., those from the European Centre for Medium-Range Weather Forecasts (ECMWF). These different WPD sources have been used together in order to develop improved WPD products for satellite altimetry, with significant impacts over coastal zones (Fernandes et al., 2010, 2015, 2016). Since these WPD sources are different in terms of spatial coverage, temporal sampling, reference surface and accuracy, appropriate procedures are required to handle the different observations and to retrieve the best WPD estimation (Stum et al., 2011).

Designed for applications over the ocean, altimetric missions are mainly focused on the sea surface and, for this reason, MWR-derived WPD measurements refer to the sea level. On the contrary, WPD derived from an NWM are computed at the level of its orography (usually a smoothed representation of a digital elevation model), which can depart from the actual surface by hundreds of meters (Fernandes et al., 2014). The path delays derived from GNSS are available at each station height (Fernandes et al., 2013), which for some coastal and island stations can be larger than 2000 m. Due to the differences between these three data types (MWR, NWM, and GNSS), namely their reference surfaces, the modelling of the height dependence of the WPD is crucial information to better combine these different WPD sources for altimetry application over coastal and inland waters. Over coastal zones, all measurements must refer to the sea level, while over continental waters they must refer to the level of the corresponding water body. Therefore, an expression to reduce the WPD from GNSS station height and orography level to sea level (over coastal zones) and to water body height (over inland waters) is required.

At present, there is an expression for the altitude reduction of the WPD developed by Kouba (Kouba, 2008), however this equation has some limitations due to the complex 4-D variation of the WPD, since it assumes that this altitude dependence is the same over the whole globe.

For real-time applications like aircraft navigation and positioning, similar approaches for the modelling of this height dependence that provide WPD (or equivalent values) without meteorological measurements are used (Böhm et al., 2015; W. Li et al., 2018; Yao et al., 2018). As these approaches were not developed for altimetry applications, they have precisions of various centimetres.

The focus of this research is the modelling of the height dependence of the WPD, aiming to derive improved expressions to account for its complex 4-D variation, required for regions of interest, as coastal and continental waters. These expressions are crucial for the retrieval of accurate WPD measurements over the latter regions, such as rivers and lakes, very important for obtaining accurate absolute water levels.

For this modelling, global WPD estimations at vertical profiles are required, which can be obtained from various sources, such as NWM, GNSS tomography, or radiosondes (RS). The RS network is the primary in-situ observing system for monitoring the atmosphere, giving unique information on the distribution and variability of water vapor in the troposphere. RS measurements provide vertical profiles of the meteorological variables required for the WPD retrieval (pressure, temperature, and humidity), as well as the geopotential height. Usually, radiosondes are expected to measure WPD with an uncertainty up to 1.2 cm (Niell et al., 2001). However, the use of radiosondes is restricted by their high operational costs, decreasing sensor performance in cold dry conditions, and their poor spatial coverage (Z. Li et al., 2003).

GNSS is an operational tool for measuring the atmospheric water vapor, allowing the estimation of WPD at the station height with an accuracy of some millimetres (Fernandes et al., 2013). The advantages of GNSS are that it makes continuous measurements possible and the spatial density of the current GNSS networks is higher than that of the radiosonde network. Concerning the GNSS tomography in which the 3-D water vapor content is estimated, it takes advantage of observing the wet delays in the slant direction. If a network of GNSS stations is available, a vertical discretization of the water vapor content can be achieved. The disadvantage of the GNSS tomography is its spatial coverage (a regional portion of the troposphere, covered by the GNSS network) (Benevides et al., 2017; Flores et al., 2000).

Only NWM provide global data at a regular temporal sampling. For this reason, WPD vertical profiles computed from NWM were selected. For this purpose, the latest reanalysis model from ECMWF (Copernicus Climate Change Service, 2018), ERA5, was used. This new reanalysis provides hourly atmospheric fields at $0.25^{\circ} \times 0.25^{\circ}$ spatial sampling on 137 vertical levels (from the surface up to an altitude around 80 km).

This study is performed in three main steps. First, the errors introduced when applying the Kouba expression globally (using a constant coefficient) are assessed. This provides a quantification of the magnitude of the errors and their spatial distribution. For this, global WPD vertical profiles from ERA5 are computed and analysed. Exploiting the knowledge acquired in the first step, improved

expressions for the vertical variation of the WPD are determined in the second step, from WPD at ERA5 vertical levels, considering regional and temporal dependent coefficients. The last step of this study is an assessment (selecting ERA5 data not used in the modelling) and a validation (using radiosondes and GNSS data). This allows to inspect the significance of this improved modelling in the handling of wet path delays for satellite altimetry in regions such as coastal and inland waters.

Section 3.2 presents the different data and methodologies adopted in this study, both for the WPD computation and for the modelling of its vertical distribution, while Section 3.3 presents the results and the discussion of this work. Finally, Section 3.4 summarizes the main achievements of this research and its impact on the wet tropospheric correction for coastal altimetry.

3.2. Data and Methods

The modelling described in this paper was performed using global atmospheric variables on vertical levels from ERA5 every 3h, for a time span of 4 years (2010–2013). Data from the same model for a different time span (2014) were used for its assessment. For validation purposes, GNSS and radiosondes data over the year 2014 were used. This section describes these data and the methodologies used to derive WPD from them, both at vertical profiles and at a single vertical level (e.g., GNSS station altitude or ERA5 orography height), as well as the methods used for the modelling of the WPD altitude dependence.

3.2.1. Data Sources for WPD Estimation

In this section, the computation of WPD from atmospheric fields provided by NWM is described. The same computation is also performed using in-situ atmospheric measurements from radiosondes. The methodology to derive WPD from GNSS data is also addressed. Together with radiosonde measurements, they are used as independent observations to validate the modelling proposed in this paper.

3.2.1.1. Numerical Weather Models (NWM)

The computation of wet delays from NWM for application in satellite altimetry is commonly performed from products provided by ECMWF, as the operational model with a spatial resolution of $0.125^{\circ} \times 0.125^{\circ}$ and temporal sampling of 6h or the ERA Interim reanalysis (Dee et al., 2011) with the same temporal resolution and a slightly worse spatial sampling ($0.75^{\circ} \times 0.75^{\circ}$). ERA Interim is more stable than the ECMWF operational model (Legeais et al., 2014), however the latter has been updated and improved and after 2004 it provides similar or better results than ERA Interim (Fernandes et al., 2014). More recently, ECMWF released the fifth and the latest major global reanalysis ERA5 (Copernicus Climate Change Service, 2018), which is freely available for any user via the Copernicus Climate Change Service (C3S) Climate Data Store (CDS). In this study, the ERA5 reanalysis was adopted.

When compared with its predecessor (ERA Interim), ERA5 has higher spatial ($0.25^{\circ} \times 0.25^{\circ}$) and temporal (1h) resolutions and an improved troposphere modelling. It is the first ECMWF model available at 1h intervals. Previous studies (Vieira et al., 2019a) show that this new and improved temporal resolution has a small impact in the WPD computation for satellite altimetry, when

compared with the common temporal resolution of 6h. As recognized for the previous atmospheric models, ERA5 also cannot map the WPD small space and time scales, evidencing the limitations of the latest ECMWF reanalysis, even with atmospheric variables at 1h intervals (Vieira et al., 2019a). In spite of these limitations, when compared with its predecessor ERA Interim, ERA5 shows a global reduction of the WPD Root Mean Square (RMS) error of 0.2 cm. For some latitude bands, the improvement can reach 0.4 cm, illustrating the considerable impact of the new reanalysis in the computation of radar altimeter wet path delays.

The WPD retrieval from an NWM such as ERA5 can be performed from two types of data: single level (SL) variables provided at surface level and those provided at vertical levels (3-D). The first ones are variables available at a single vertical level (the orography height of the corresponding NWM). Some of these fields are representative of the total atmospheric column (integrated variables). The single level variables are provided at global regular grids and allow the computation of the WPD for the same spatial and temporal resolutions, at the corresponding NWM orography height. WPD values for along-track satellite altimeter observations must be obtained interpolating in space and time the gridded products, further reduced to the height of interest (e.g., sea level or water body height).

The computation from SL variables can be performed from two atmospheric fields—Total Column Water Vapor (TCWV) and two-meter temperature (T_0), according to Equations (1) and (2):

$$WPD = \left(0.101995 + \frac{1725.55}{T_m} \right) \frac{TCWV}{1000} \quad (1)$$

Equation (1) proposed by (Bevis et al., 1992, 1994) allows the computation of WPD in meters, using TCWV in kg.m^{-2} . TCWV is a measure of the total water vapor contained in a vertical column of atmosphere, part of the altimetric signal path. Using the density of water equal to 1000 kg.m^{-3} , TCWV is equivalent to the height of a column of water expressed in millimetres ($1 \text{ kg.m}^{-2} = 1 \text{ mm}$), designated as precipitable water. Thus, TCWV corresponds to the height the water would occupy if the vapor was condensed into liquid and spread evenly across the column. Typically, with maximum values around 75 kg.m^{-2} for low latitudes (or 75 mm of precipitable water), TCWV is related with WPD through the simple relation: $WPD = 6.4 \times TCWV$, with TCWV and WPD in the same length units (Bevis et al., 1992; Stum et al., 2011). For the TCWV maximum value of 7.5 cm, the corresponding WPD is around 48 cm. However, this relation is not accurate enough.

The term T_m in Equation (1) is the mean atmospheric temperature, in Kelvin, which can be obtained from the near-surface temperature (T_0), by means of a linear relation according to e.g., Equation (2) proposed by (Mendes, 1999).

$$T_m = 50.440 + 0.789T_0 \quad (2)$$

In Equations (1) and (2), T_0 and T_m are in Kelvin, TCWV in millimetres and the WTC results in meters. Adopting these two equations, WPD can be derived from an NWM single level variable, the so-called 2-D approach, leading to a less intensive computation. Note that thanks to the use of the integrated TCWV field, the estimated WPD value is representative of the total signal path. The disadvantage of this approach is the fact that it only allows the WPD computation at a single vertical level (the NWM orography height).

The second type of data provided by NWM for WPD computation are the atmospheric variables available at vertical levels (3-D fields). At each grid point, irrespective of its altitude, ERA5 provides atmospheric variables on 137 model levels (ML), from the surface up to 0.01 hPa (around an altitude of 80 km). These variables are also interpolated to standard levels, such as pressure levels (PL), which correspond to 37 levels (1, 2, 3, 5, 7, 10, 20, 30, 50, 70, 100, 125, 150, 175, 200, 225, 250, 300, 350, 400, 450, 500, 550, 600, 650, 700, 750, 775, 800, 825, 850, 875, 900, 925, 950, 975, and 1000 hPa), from an altitude around 45–50 km (1 hPa) down to the surface at 1000 hPa. Unlike model levels, which, for each point, correspond to different pressure values, the pressure levels are always the same, irrespective of the location or the corresponding surface height. For regions where the surface height is above the lowest pressure level, the atmospheric variables for PL below the surface height are extrapolated.

As an example, Figure 1 shows the temperature (T) and the specific humidity (q) at the location with coordinates 00° , 120°E provided by ERA5 on 1 January 2010, at 00:00 UTC. Blue points are the variables provided on model levels (137), while orange points represent the variables on pressure levels (37). Pressure in hPa is represented in the vertical axes, for which the 1000 hPa level is close to the surface, while pressures of 500 and 200 hPa correspond to altitudes around 6 and 12 km, respectively. These values are approximate, since the correspondence between pressure and altitude depends on the geographic location.

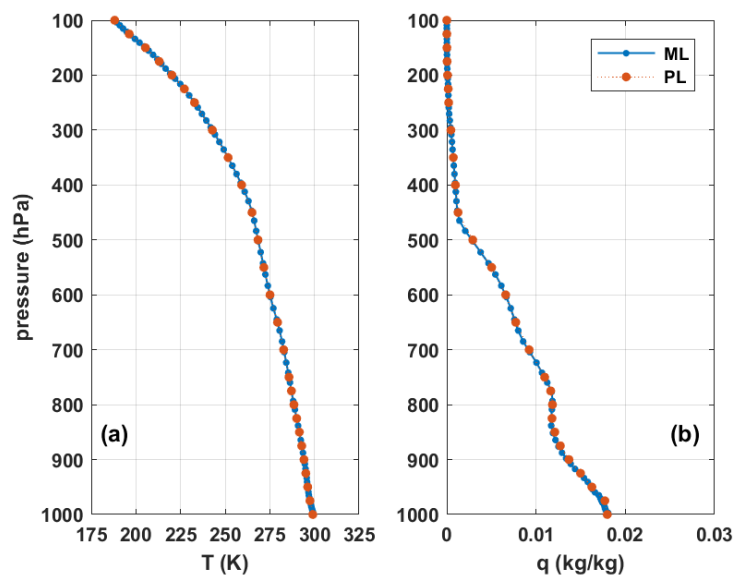


Figure 1. Atmospheric variables provided by ERA5 on 1 January 2010, at 00:00 UTC on model levels (blue) and on pressure levels (orange): (a) temperature (T) in Kelvin and (b) specific humidity (q) in kg/kg at location 00° , 120°E .

Observing Figure 1b, the specific humidity has a complex vertical distribution and becomes negligible for levels above 300–200 hPa (~10 km). On the contrary, Figure 1a shows a linear temperature decrease with altitude up to an height of about 10 km, with a mean temperature lapse rate of -6.5 K/km (Boehm et al., 2007; Lagler et al., 2013). Figure 1 shows that the pressure levels (orange), even being less (37) than the ML (137), are enough to describe the atmospheric vertical profiles well. These characteristics are common for the entire globe. The results shown in Section 3.3 demonstrate that the use of PL, instead of ML, provides similar global results, without significant WPD differences. Moreover, the estimations with PL are much more computationally efficient.

The WPD retrieval from these 3-D variables (either on ML or on PL) can be accomplished from a numerical integration of these two variables (temperature and specific humidity), according to Equation (3) (Collecte Localisation Satellites (CLS), 2011). This numerical integration is performed from the level at the top of atmosphere (TOA), with pressure P_{TOA} , down to the level at surface (with pressure P_{surf}). In Equation (3), q and T are the specific humidity in kg/kg and the temperature in Kelvin, respectively, φ is the latitude, the pressures are given in hPa, and the WPD at the lowest (surface) level results in meters.

$$WPD = \left(1.116454 \times 10^{-3} \int_{P_{TOA}}^{P_{surf}} q dp + 17.66543928 \int_{P_{TOA}}^{P_{surf}} \frac{q}{T} dp \right) \times (1 + 0.0026 \cos 2\varphi) \quad (3)$$

For a less intensive computation, ERA5 data on levels up to 200 hPa (approximately 20 pressure levels) are adequate, since the specific humidity of the upper levels is negligible and the corresponding WPD is null.

The WPD from the so-called 3-D approach was computed using Equation (3) from ERA5 data on vertical pressure levels in a global grid of $5^\circ \times 5^\circ$. Figure 2 shows examples of WPD profiles at three different locations (only PL above the surface were considered). Grey points represent all WPD vertical profiles, every 3h, over one complete year (2010) and the solid line represents the corresponding annual mean profile. Mean profiles for January (squares with dashed line) and for July (circles with dotted line) are also shown, representative of winter and summer conditions, respectively.

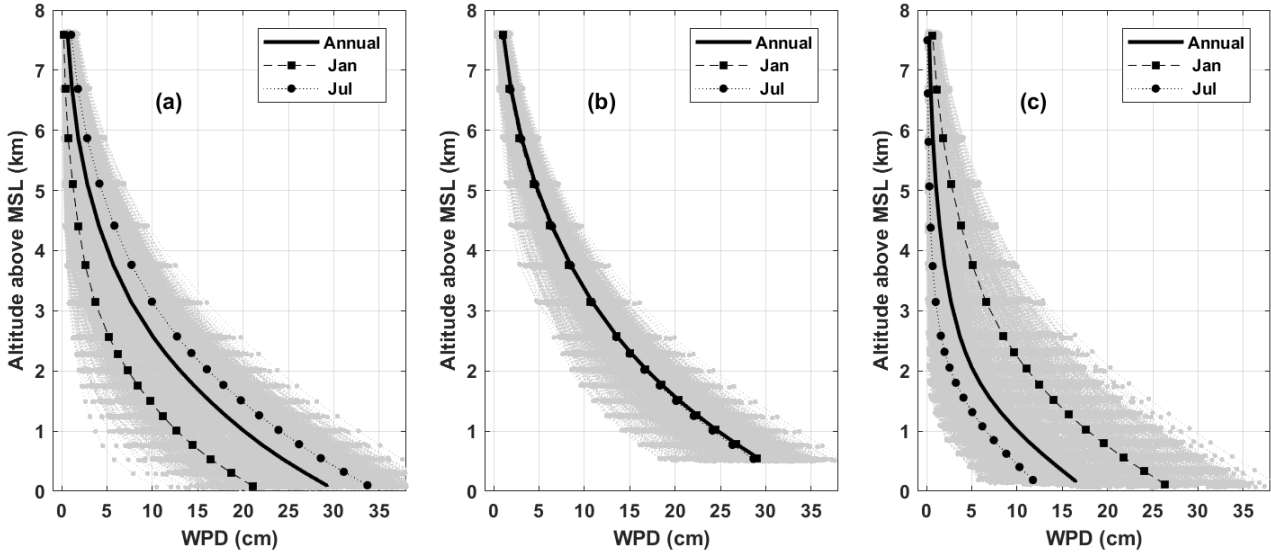


Figure 2. Wet path delay (WPD) vertical profiles at (a) 10°N, 90°W; (b) 00°, 100°E; (c) 25°S, 65°E. Grey profiles represent those every 3h over the year 2010, solid line represents the annual mean profile, squares with dashed line and circles with dotted line represent the mean profiles for January and July, respectively.

Considering three distinct locations and two different months (opposite seasons), Figure 2 illustrates different WPD vertical distributions, varying both with the geographic location and period of the year. WPD has a seasonal variability with largest values in the boreal summer (Vieira et al., 2019), which can be observed in Figure 2. WPD is larger in July than in January at the location in the northern hemisphere (a) and, on the contrary, it is larger in January than in July at the location in the southern hemisphere (c). The profiles shown in Figure 2 could also be obtained from ML variables. The impact of using different (ML or PL) levels is presented in Section 3.3.

Figure 2 allows to observe the typical curves of the WPD change with altitude, varying with the geographic location and period of the year, suggesting the need for inclusion of temporal and spatial dependent terms in the modelling of the WPD variation with altitude. Figure 2 also shows the WPD exponential decrease with altitude, according to the water vapor vertical distribution, with its greatest concentration near the ground.

3.2.1.2. Radiosondes (RS)

At present, there are several methods to obtain the atmospheric humidity from observations, usually divided into two types: ground and space-based measurements. Among these observations, radiosondes and satellites are two common platforms supporting sensors to measure the vertical and horizontal distribution (3-D) of water vapor in the troposphere.

The vertical variables provided by atmospheric models, as above described, are also derived from radiosondes. These are balloon-borne instruments, which measure these variables in-situ, but with a limited spatial coverage. Radiosondes have provided detailed measurements of global atmospheric water vapor since 1905 (many years before the first altimetry mission). At present, there are over 2700 stations distributed all over the world. These provide essential variables to study the characteristics of atmospheric humidity for weather prediction and global climate change, as well as for different validation purposes, namely space-based measurements of total column water vapor (Kalakoski et

al., 2016). However, radiosondes measurements inadequately resolve the temporal and spatial variability of atmospheric water vapor, which occurs at scales much finer than the spatial and temporal variability of e.g., temperature or winds (Anthes, 1983).

Radiosondes data used in this paper are from the National Climatic Data Centre Integrated Global Radiosonde Data (IGRA) version 2 (Durre, 2016). IGRA consists of radiosonde and pilot balloon observations at globally distributed stations. Observations are available at standard and variable pressure levels. Variables include pressure, temperature, geopotential height, relative humidity, dew point depression, wind direction and speed, and elapsed time since launch (Durre et al., 2018). The variables of interest for this study are the temperature, humidity, altitude, and pressure. For validation purposes, WPD vertical profiles were computed from these in-situ vertical measurements at each radiosonde location and at each sounding time, using Equation (3).

There are many ways to express atmospheric humidity values. Radiosondes usually measure relative humidity (RH). These are the observations provided by IGRA, while those required in Equation (3) are specific humidity values. The methodology used to convert the RH radiosondes measurements into specific humidity can be found in (Nievinski et al., 2010).

Usually, radiosondes are expected to retrieve WPD with an uncertainty up to 1.2 cm and better than 0.6 cm for low ranges of wet delay (Niell et al., 2001). WPD is calculated for each radiosonde profile, assuming that the measured pressure, temperature, and humidity were obtained along a vertical ascent (although the horizontal motion of almost all radiosonde trajectories is significant). Moreover, there is a decreasing sensor performance in cold dry conditions (increasing altitude) (Z. Li et al., 2003). For these two reasons, the uncertainty of the RS-derived WPD is expected to increase with altitude. On the other hand, the WPD decreases exponentially with altitude, so in terms of absolute values this increasing uncertainty can be small.

Figure 3 shows the spatial coverage of the radiosondes from IGRA, where blue points represent the 2788 radiosondes since 1905 until 2018. Green diamonds represent the 93 radiosondes with valid measurements of temperature and humidity, as reported in the original sounding, over the year 2014. Within this subset of RS with valid measurements of interest for this study, 20 sites were selected (represented by red triangles) for the validation task. This selection aimed at ensuring a good geographic distribution allowed by the available RS represented by green squares, at low latitudes. Here the WPD is more variable and, thus, the effect of this modelling can be more significant.

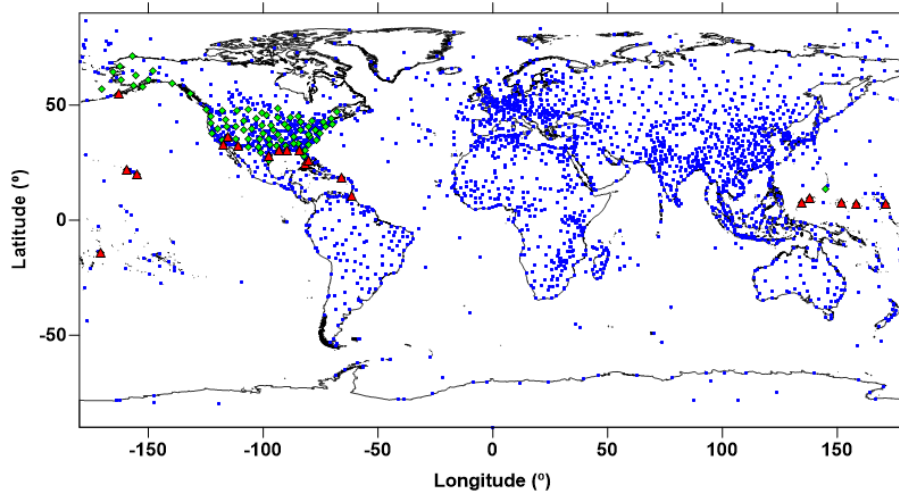


Figure 3. Spatial representation of the radiosondes (RS) network from Integrated Global Radiosonde Data (IGRA). Blue points represent all RS since 1905, green squares represent the RS with valid measurements of temperature and humidity over the year 2014, and red triangles represent those selected for the validation.

3.2.1.3. GNSS Stations

In the context of the tropospheric corrections for satellite altimetry, despite their poor spatial resolution, GNSS data have been widely used to derive these corrections (Fernandes et al., 2013; Vieira et al., 2019b). The increasing number of GNSS stations in coastal zones has been useful for the retrieval of tropospheric corrections in these zones, where the WPD retrieval from MWR measurements become invalid and cannot be used (Vieira et al., 2019b). The GNSS-derived WPD have been adopted for assessment, validation, and monitoring purposes (Desai et al., 2004; Haines et al., 1998; Kalakoski et al., 2016; Sibthorpe et al., 2011; Vieira et al., 2019b) and also to develop improved methodologies to provide valid WPD measurements in regions where MWR-derived WPD are invalid (Fernandes et al., 2010, 2015, 2016).

The WPD is not a direct estimation from GNSS. The quantity derived from this technique is the zenith tropospheric delay (ZTD), which is the total tropospheric delay in the zenith direction due to the dry and wet troposphere. The dry component of the total delay can be computed from surface pressure fields provided by atmospheric models with high accuracy (Fernandes et al., 2013). Using the total delay from GNSS and subtracting the dry delay computed from NWM, both with high accuracy, the WPD can be obtained. This way, at the location of each GNSS station and for each instant, a WPD with an error less than 1 cm is estimated. In terms of vertical reference, these WPD estimations are relative to the corresponding GNSS station height, which is not the level of interest for coastal satellite altimetry application. After the WPD derivation from GNSS, the corresponding estimations must be reduced to the altitude of interest (sea level or water body height), this being a crucial step. Therefore, the modelling of the vertical dependence of the WPD is an important procedure to ensure a better use of GNSS-derived WPD in satellite altimetry.

For more details about the estimation of WPD from GNSS see e.g., (Fernandes et al., 2013; Vieira et al., 2019b).

3.2.2. Modelling the Altitude Dependence of the WPD

There is, presently, only one expression available for modelling the WPD vertical dependence, which is the one proposed by Kouba (Kouba, 2008). This expression has many limitations since it considers the same dependence, irrespective of geographic location and WPD variability. Building upon this expression and considering the complex WPD variation, this section presents the developed methodology in view to derive improved expressions, taking into account the different patterns of the WPD vertical variation function of location and time.

3.2.2.1. The Kouba Formulation

To compare wet delays at different heights and in the absence of a convenient transformation, Kouba (Kouba, 2008) developed an exponential decay function to transform wet delays between different altitudes, at the same planimetric point:

$$WPD_i = WPD_0 e^{\frac{h_0 - h_i}{2000}} \quad (4)$$

where WPD_0 is the known wet delay at height h_0 , and WPD_i is the wet delay to be calculated at height h_i . The Kouba empirical decay coefficient (1/2000) was obtained from the WPD values spanning 1.5 years at a single location (22.13°N, 159.66°W) and at only two levels (ellipsoidal heights 18 and 1168 m). This dataset, considered adequate in the context of the Kouba's study, is not enough to characterize the complex 4-D WPD variation.

From the analysis of this expression, the following values can be withdrawn: for a WPD of 30 cm at an altitude of 0 m, reducing this value with the Kouba expression to an altitude of 1000 m, the corresponding WPD is 18.2 cm. For empirical decay coefficients of, for example, 1/1500 or 1/2500, the corresponding WPD is 15.4 or 20.1 cm, respectively. Therefore, the effect of using different decay coefficients can lead to WPD differences of several centimetres.

3.2.2.2. Modelling Using ERA5 Data on Pressure Levels

After analysing the sensitivity of the Kouba expression concerning its decay coefficient and given the high 4-D WPD variation, new decay coefficients will be modelled in this section. Hereafter, for simplification, instead of a decay coefficient (which for Kouba is 1/2000), an inverse decay coefficient (α) is introduced.

In a 5°×5° grid, WPD vertical profiles were computed from atmospheric variables on PL from ERA5, over 4 years, as described in Section 3.2.1.1. A temporal sampling of 3h was used, considered to be adequate for the WPD computation (Vieira et al., 2019a). At each location and for each WPD vertical profile, an α coefficient is determined using least squares, setting the initial coefficient to the Kouba value (2000). Since the main application of this modelling is satellite altimetry over coastal and inland waters, only the altitudes below 4000 m are of interest. For this reason, only pressure levels with altitudes below 4000m were considered. On the other hand, only the pressure levels above surface were selected, as those below the surface are generated by extrapolation. For regions where the surface height is larger than 4000 m (e.g., Himalayas region), the corresponding vertical profiles will be empty and the initial coefficient (2000) was considered for these cases.

Thus, for each point in a $5^{\circ} \times 5^{\circ}$ grid, an α coefficient was determined every 3h, from the beginning of 2010 to end of 2013. Analysing the time series of these coefficients at each point and observing that some regions exhibit an annual signal, as will be addressed in Section 3.3, three sets of coefficients were developed:

- UP-01: a single coefficient for each location (non-time-dependent), computed as the mean at each point;
- UP-04: four seasonally averaged coefficients for each location;
- UP-12: 12 monthly averaged coefficients for each location.

The computation of the UP-04 and UP-12 coefficients was performed by binning the coefficients into classes of time intervals (3 months and 1 month, respectively), spanning the four analysed years. Results in Section 3.3 will show that using data for only one year, the obtained coefficients are very similar, without significant differences from those obtained using the 4-year dataset. For this reason, the time span used for this modelling (4 years) is considered appropriate, since additional years do not generate different coefficients.

3.2.2.3. Assessment and Validation

After introducing Kouba's expression and developing the UP modelling, the proximity of the WPD vertical profiles computed from ERA5 data on PL and those derived from WPD at only one vertical level, followed by different altitude reductions (both Kouba and UP) was analysed. For this purpose, ERA5 data on PL for a different period, i.e., for a time span not used in the UP modelling was selected.

Two WPD vertical profiles were considered, at each $5^{\circ} \times 5^{\circ}$ grid point, every 3h: the first one computed from ERA5 data on pressure levels from Equation (3) and the second one estimated at ERA5 orography level from Equations (1) and (2), further reduced to the upper pressure levels using the different modelling approaches (Kouba, UP-01, UP-04, and UP-12). The differences between the computed WPD vertical profiles from ERA5 data (temperature and humidity fields) and those reduced from the values at surface level will provide a global quantification of the ability of the different modelling approaches to describe the WPD vertical distribution, knowing only one WPD value at surface level.

The validation of the various expressions was performed by means of independent data from radiosondes and GNSS stations.

For the validation from radiosondes, a similar procedure used in the assessment with ERA5 was adopted. Two WPD vertical profiles were selected. The first one was computed from temperature and humidity data from radiosondes on their vertical levels and the other one from the WPD at the lowest RS level and then reduced to the upper levels using the different coefficients. This validation was performed by means of independent in-situ atmospheric measurements up to an altitude of 4 km, however it was spatially limited to the network coverage of the RS with valid temperature and humidity measurements.

For the validation using GNSS data, two single level WPD values were selected: one derived from GNSS at the corresponding station level, and the other one computed at ERA5 orography level from

Equations (1) and (2) further reduced to the corresponding station height, using the different altitude reductions. This validation was performed at only one level, while the validation with radiosondes was carried out along various vertical profiles in a range of altitudes up to 4 km, so the significance of the validation from RS data is larger than that from GNSS. Moreover, the validation with GNSS data is only useful for GNSS stations with altitudes significantly different from the altitude of the ERA5 orography at the location of the corresponding GNSS station. The validation with GNSS is also limited to the corresponding network spatial coverage. The assessment with ERA5 is the only method that allows a global inspection of the different vertical modelling.

3.3. Results and Discussion

This section provides a description of the experimental results at each step of this study, as well as the corresponding interpretation and the corresponding discussion.

3.3.1. Comparison between WPD Computed Using Different ERA5 Data

As described above, ECMWF provides 3-D variables both at model and pressure levels and the first ones lead to a significantly larger computational effort. Before adopting the second ones in this study, an assessment was carried out to inspect the impact of this choice, both in terms of accuracy and computational time. For this purpose, the following WPD were compared at the level of the ERA5 orography: the WPD computed using Equation (3) from temperature and humidity variables provided at pressure and model levels (37 and 137 vertical levels, respectively). For completeness, the WPD retrieved from single level variables using Equations (1) and (2) was also considered. Thus, for a time span of one complete year (2010), three WPD were considered for each point, at the level of ERA5 orography.

To consider the three values at the same vertical reference (ERA5 orography level), when the orography height is between two consecutive pressure levels, the corresponding WPD value from PL data was interpolated to the orography level using the WPD at the corresponding consecutive pressure levels. When the orography height was below the lowest pressure level, the WPD value from data on PL was extrapolated to the orography height. The same procedures were not required for the ML, since the corresponding vertical levels were always above the orographic surface. Thus, the three WPD values computed at each point using different ERA5 data (SL, ML, and PL) under comparison were relative to the same altitude, avoiding the introduction of biases.

Statistical parameters (mean and standard deviation in centimetres) of the differences between these three WPD values were calculated. These statistics reveal very small differences, with standard deviation values not larger than 2 mm and an absolute mean up to 1 mm. Concerning the differences between the two computations using 3-D variables (on model and pressure levels) the mean is null, and the standard deviation is 1 mm, showing an insignificant effect. As suggested by Figure 1, these results indicate that there is no significant impact when the WPD is computed using data on ERA5 pressure levels, instead of denser data on model levels. For this reason and in the interest of computational time, the estimation from data on PL was adopted in this study.

Regarding the differences between the WPD retrieval from single level variables (SL) and those using 3-D variables, there is a small bias (absolute mean of 1 mm). For the case of data on PL, this should be due to the interpolation and extrapolation errors, while for the data on ML, this is due to the altitude of the lowest model level. Computing the global differences between the ERA5 orography height and the altitude of the lowest model level (the first level, closest to the surface), the absolute mean is 9.7 m. This indicates that the lowest model level is systematically 9.7 m above the ERA5 orography height, leading to a very small bias (1 mm).

Considering a compromise between accuracy and computational time, the ERA5 data on pressure levels were selected for this modelling.

3.3.2. Modelling

Using the pressure levels above the surface and up to an altitude of 4 km, WPD vertical profiles have been estimated globally, every 3h, for a time span of 4 years. Building upon these vertical profiles, the α coefficient (derived from the empirical decay coefficient in the expression proposed by Kouba (Kouba, 2008)) was computed every 3h at each grid point using least squares. Figure 4 represents the time evolution of these α coefficients at three different locations: (a) one point in the northern hemisphere with coordinates 10°N, 90°W; (b) one point in the equator with coordinates 00°, 100°E; (c) one point in the southern hemisphere with coordinates 25°S, 65°E. Three geographic locations, the same as in Figure 2, were chosen to be representative of the global distribution and variability of the α coefficients (which describe the WPD vertical variation). The location in the equator (b) shows a low variability, while the other two locations show high variability.

Analysing Figure 4, the most striking feature is the clear annual signal observed in the coefficients, more pronounced at locations not over the equator, as illustrated in Figure 4a,c. The signals shown in these panels are not in phase, since they are relative to locations at different hemispheres. The first one is maximum when the second one is minimum. Another striking feature is the high variation of the α coefficients, even for small periods, evidencing the high vertical variation of the WPD. This variability represents an additional difficulty in this modelling.

The three UP modelling approaches (UP-01, UP-04 and UP-12), as described in Section 3.2, are represented in Figure 4 by orange lines, purple squares, and green circles, respectively. Figure 4a,c shows that the use of a single non-time-dependent coefficient (UP-01) is not enough to account for the variability that the coefficients determined every 3h show.

Assuming an additional temporal dependence (UP-04 and UP-12), the corresponding modelled coefficients can still be very different from those determined every 3h, evidencing again the difficulty of this modelling.

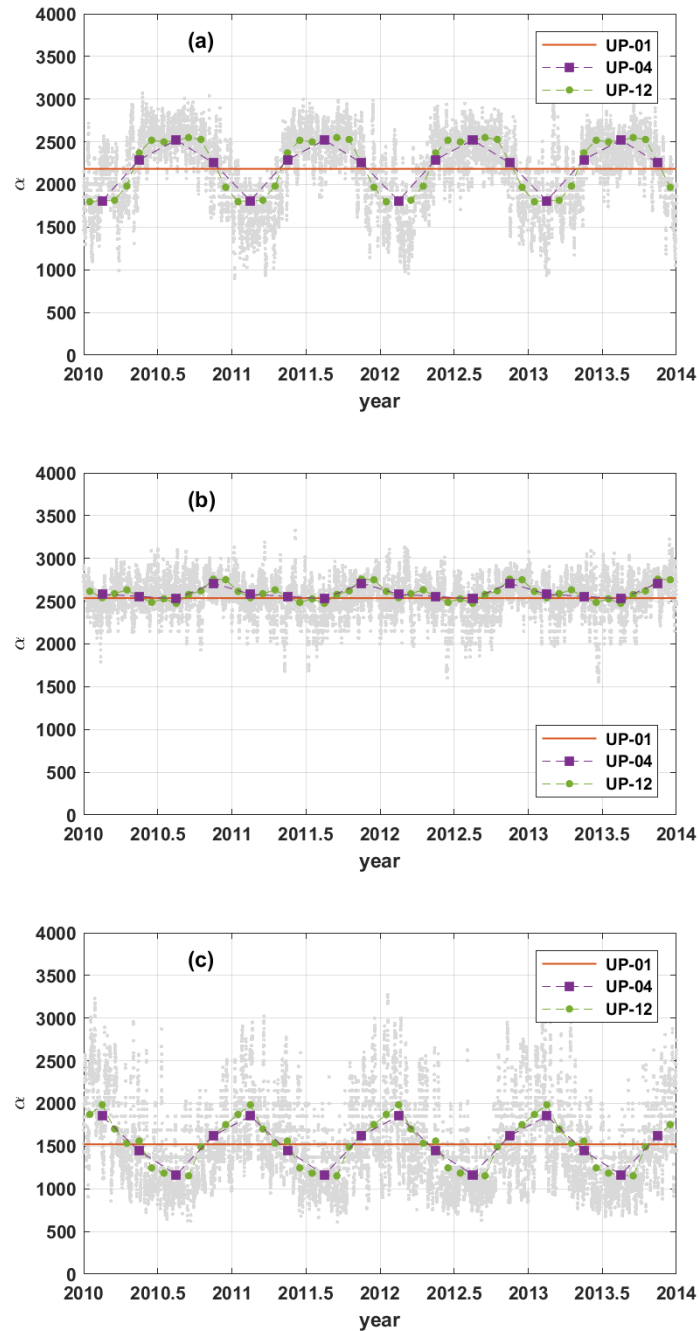


Figure 4. Time evolution of the α coefficients at locations: (a) 10°N , 90°W ; (b) 00° , 100°E ; (c) 25°S , 65°E . Grey points represent the α coefficients every 3h, orange line represents the overall mean (UP-01) and purple squares and green points represent the seasonally averaged (UP-04) and monthly averaged coefficients (UP-12), respectively.

Considering only the spatial dependence of this modelling, Figure 5 shows the spatial representation of the α coefficients derived as the mean for each point, non-time-dependent (UP-01). The colour scale of the α coefficient is saturated in the range [1500–2500] in order to have a scale centered in 2000 (white), however the minimum and maximum coefficients are 1165 and 2705, respectively. The most striking feature of this spatial representation is that there are many regions where the α coefficient is very different from that proposed by Kouba. To understand the impact of

having different coefficients, taking the example given in Section 3.2, for a WPD of 30 cm at the zero level, the reduced values at an altitude of 1000 m are 12.7 and 20.7 cm using an α coefficient of 1165 and 2705, respectively. The two WPD at the example level of interest corresponding to the minimum and maximum α and maximum α coefficients found in the results of this modelling have a difference of 8 cm, a very significant value regarding the accuracy of the WPD derived from the different sources. These values are important indicators of the need of having a vertical modelling of the WPD, dependent on geographic location.

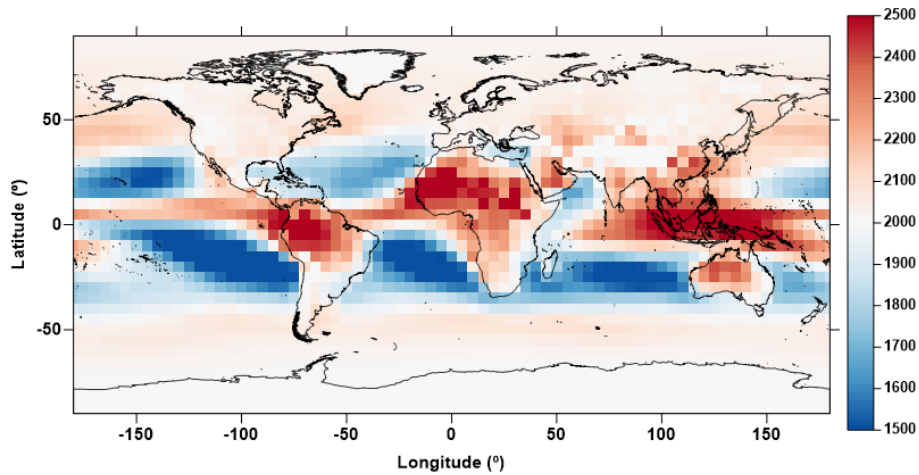


Figure 5. Spatial representation of the α coefficient, computed as the mean for each point (UP-01) in a $5^\circ \times 5^\circ$ grid.

In Figure 5, regions represented in white are those where the α coefficient derived from ERA5 3-D PL data is close to that suggested by Kouba. These regions are mainly over the poles, where the WPD at surface level is small and, for this reason, there is a narrow range of WPD variation, from a small value at surface height (a few cm) up to zero at a certain altitude. The same happens over high regions and for altitudes above 4 km, where the Kouba value is assumed by default in the UP modelling. The WPD is more variable in low latitude regions due to the complex wet equatorial climate, with larger temperatures than in the poles, generating a high evaporation rate and large concentrations of water vapor in the troposphere.

The spatial representation of the α coefficient in Figure 5 gives some information about the atmospheric water vapor concentration. Since this coefficient describes the exponential decrease of the WPD with altitude, according to Equation (4), a small α coefficient makes the WPD vanish more rapidly with altitude, while a large coefficient represents a slower decrease. This means that, when compared with the total atmospheric column at each point, a small α coefficient indicates a larger near-surface water vapor concentration, than a large α coefficient. Thus, regions represented in blue in Figure 5 have larger near-surface water vapor concentrations than regions represented in red.

In summary, UP modelling consists of three sets of α coefficients in a $5^\circ \times 5^\circ$ grid: UP-01, a single coefficient for each point (2701 coefficients represented in Figure 5); UP-04, four seasonally averaged coefficients for each point (10,804 in total); UP-12, 12 monthly averaged coefficients for each point (32,412 in total).

A larger number of coefficients (both in space and time) would certainly lead to a better modelling of the vertical distribution of WPD, however, it is important to find a compromise between accuracy and computational effort. An increasing number of coefficients means an increasing time of computation in the handling of the WPD provided from different sources. The significance of using the different modelling approaches here presented will be addressed below, in view to assess and validate the impact of using the various improved procedures.

3.3.3. Assessment with ERA5 Data

The assessment carried out using ERA5 data on PL allows a global inspection of the impact of adopting different sets of coefficients in the WPD estimation, when compared with the corresponding WPD retrieved from the original ERA5 PL fields. Five global sets of WPD vertical profiles were considered: one computed at pressure levels adopting the corresponding variables from ERA5 and the other four computed at only one level (ERA5 orography level) further reduced to the various PL using the Kouba and each of the three UP models.

Figure 6 represents the RMS, in centimetres, of the differences between these two WPD vertical profiles (up to 4 km), considering ERA5 data over the year 2014, selecting for the altitude reduction only the α coefficient proposed by Kouba (2000). The largest differences, where the performance of the Kouba coefficient is worst, are observed for low latitudes, represented by dark blue. The maximum RMS value of 3.2 cm is observed at 5°S, 150°E (Papua New Guinea region). The Indonesia region, together with the central Pacific, are the regions where the Kouba coefficient has the largest errors, when compared with WPD retrieved from ERA5 data on PL. The coastal zones, as the Indonesia region (Handoko et al., 2017) and the central America, are the critical regions where better vertical modelling is required.

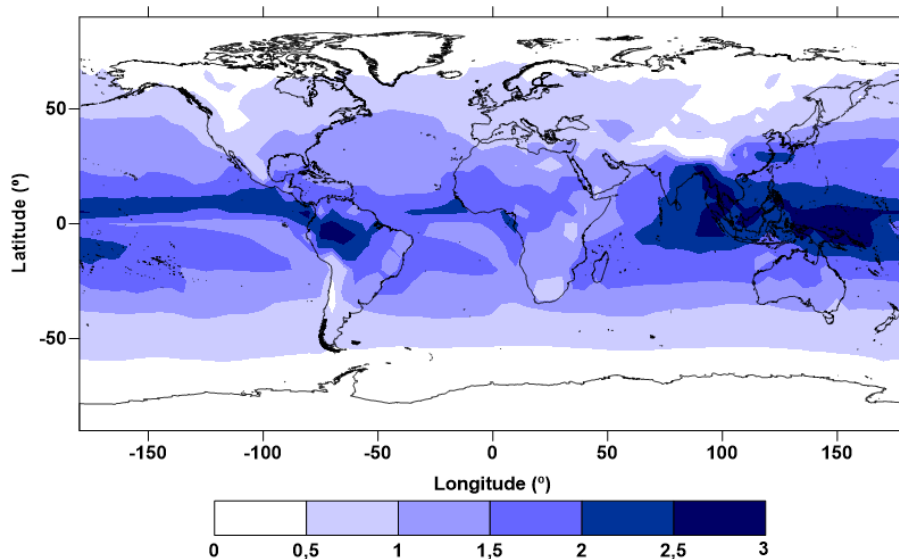


Figure 6. Root Mean Square (RMS) (cm) of the WPD differences between 3-D (WPD retrieved from the original ERA5 PL fields) and 2-D with Kouba reduction, using profiles every 3h in a 5°×5° grid over the year 2014.

Figure 7 represents the same as Figure 6, but using UP-01 coefficients for the altitude reduction, instead of Kouba. The clearest observation is the RMS decrease when a spatially dependent coefficient (UP-01) is used, in place of a single coefficient (Kouba). This RMS decrease is clearer over the

Indonesia region. To the maximum RMS difference of 3.2 cm observed at 5°S, 150°E in Figure 6 (with the Kouba approach) corresponds a value of 1.2 cm in the UP-01 modelling, leading to an RMS decrease of 2 cm at this location. Using UP-01, the maximum RMS WPD difference is 2.5 cm at the location with coordinates 25°N, 90°E, where the corresponding Kouba value is 2.7 cm.

The most significant impact of this modelling observed in the Indonesian region, considering only a dependence on geographic location and neglecting the dependence on time (UP-01), is due to the low temporal variability of the WPD over this region. Despite its large absolute values, over this region WPD has a small temporal variability, when compared with the surrounding regions (Vieira et al., 2019) (see the vertical profile of Figure 2b, representative of the WPD variability in this region).

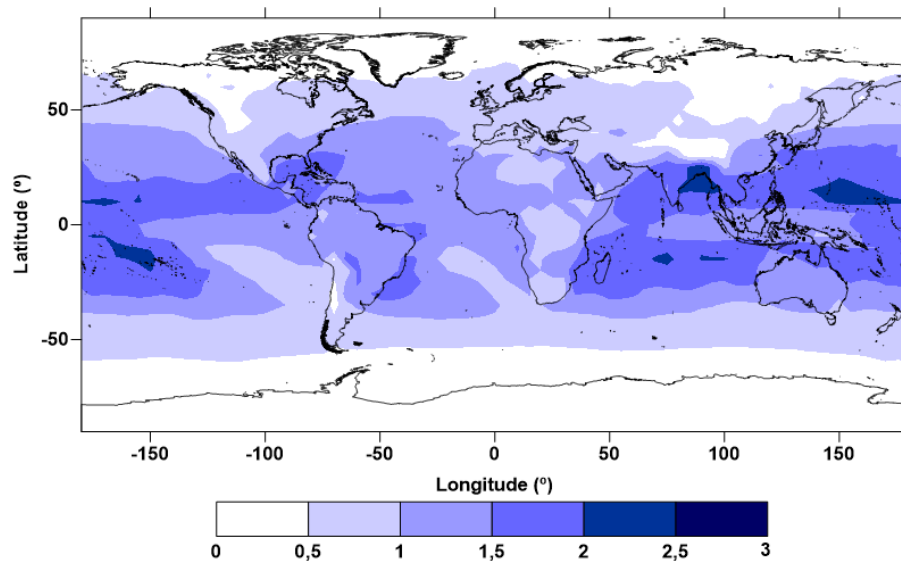


Figure 7. RMS (cm) of the WPD differences between 3-D and 2-D with UP-01 reduction, using profiles every 3h in a 5°×5°grid over the year 2014.

Figure 8 illustrates the same assessment using the UP modelling which considers a temporal dependence of the α coefficients (UP-04 and UP-12), in the left and right panels, respectively. Here, the decrease in the analysed statistical parameter is not so clear, however the maximum values are 2.2 and 2.1 cm, using UP-04 and UP-12, respectively. Moreover, in the region where the additional temporal modelling has the most significant impact (25°N,90°E, Bay of Bengal region), the RMS errors are 2.7, 2.5, 1.7, and 1.4 cm when Kouba, UP-01, UP-04, and UP-12 are used, respectively. When compared with Kouba, the UP seasonally and monthly coefficients lead to an RMS decrease of 1 and 1.3 cm, respectively, at this location. When compared with a single, non-time-dependent coefficient (UP-01), there is an RMS decrease of 0.8 and 1.1 cm when the two time-dependent modelling approaches are adopted, respectively.

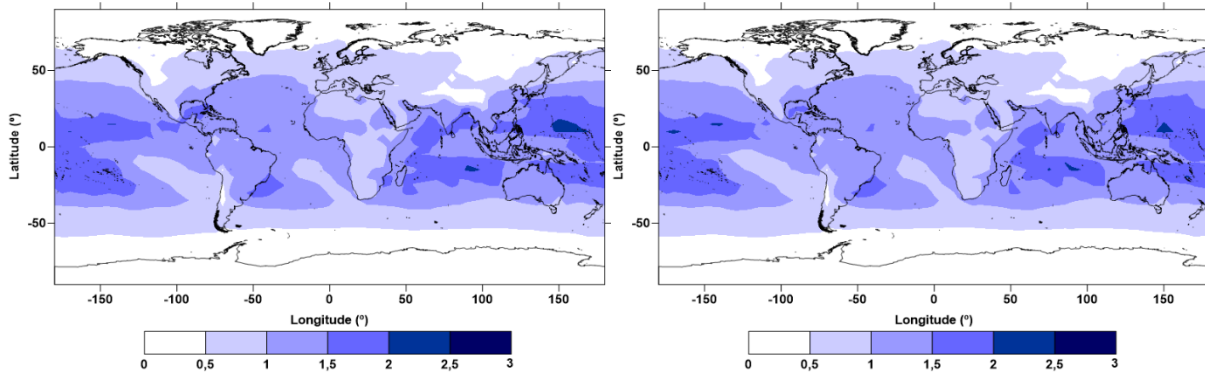


Figure 8. RMS (cm) of the differences between WPD computed with 3-D approach and that computed at surface level and then reduced with UP-04 (left) and UP-12 (right) coefficients

It is important to highlight again that the ERA5 data selected for this assessment are not used in the UP modelling, since they refer to different time spans. However, the evaluation presented here is affected by the fact that the various analysed WPD are not completely independent and they are not observations. For a complete analysis, a validation by means of independent WPD values from in situ observations is required. This is presented in the next subsection, selecting measurements from radiosondes and GNSS. However, it is important to highlight that the assessment using ERA5 data allows a global analysis, not possible with the data from these independent sources.

3.3.4. Validation with RS and GNSS

Figure 9 shows the RMS in cm of the differences between WPD computed using data from RS at vertical levels (temperature and humidity) and those using only the WPD at the lowest level of each RS and then reduced to the upper levels through the different modelling approaches: Kouba (blue), UP-01 (orange), UP-04 (purple), and UP-12 (green). These differences are exclusively due to the altitude reduction, since the initial WPD is the same at the lowest level of the RS vertical profile.

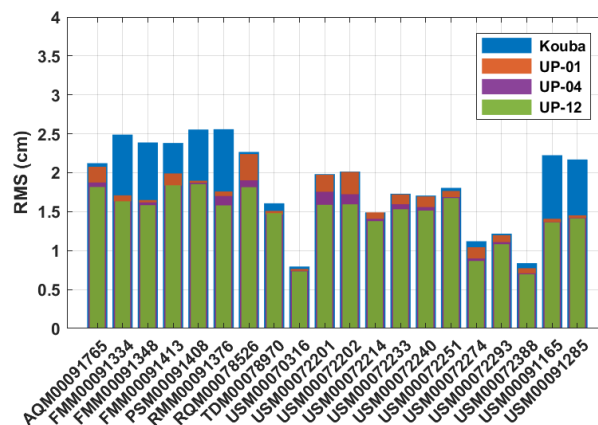


Figure 9. RMS (cm) of the differences between WPD computed with 3-D approach using atmospheric variables from IGRA and those computed at lowest level and then reduced with Kouba (blue bars), UP-01 (orange bars), UP-04 (purple bars), and UP-12 (green bars) coefficients.

The horizontal axis of Figure 9 represents a set of 20 radiosondes selected among the available sites with valid temperature and humidity data. Observing Figure 9, the most significant decrease in the RMS error occurs from Kouba (blue bars) to UP-01 (orange bars), corresponding to the use of

spatially dependent coefficients instead of a single coefficient. This effect is significant in radiosondes FMM, PSM, and RMM in the region of Indonesia and in the last two USM in Hawaii, as illustrated in Figure 3. This is in agreement with the results shown in Figure 6 and Figure 7, where the most significant impact of spatially dependent coefficients (UP-01), in comparison with Kouba, is mainly over the Indonesia region and central Pacific.

Moreover, in some regions the additional modelling of the temporal dependence (UP-04 and UP-12) also has a significant impact, when compared with UP-01, as observed mainly in radiosondes RQM, USM00072201, and USM00072202 in central America. The small differences observed in some radiosondes are due to the small WPD values at surface level (e.g., USM00070316 in the northern hemisphere, with a latitude larger than 50°).

These independent in situ data show that the RMS error decrease can be larger than 1 cm in some regions, when using the UP coefficients instead of Kouba’s single coefficient.

A similar validation was performed using GNSS stations, however this is limited in terms of vertical levels, since it was carried out at only one level, the altitude of each station. Moreover, the differences achieved in this comparison are due to the altitude reduction but also due to the differences between GNSS and ERA5. On the other hand, this validation is significant only for GNSS stations with altitudes very different from the ERA5 orography, at the corresponding GNSS location. Figure 10 shows the RMS in cm of the differences between WPD derived from GNSS and that computed from ERA5 data at the corresponding orography level and then reduced to the altitude of the station, adopting the different modelling approaches represented by the same colours. The results given in Figure 10 are very similar to those given in the validation with radiosondes. This comparison with GNSS does not give additional significant information. It is important to note that WPD derived from ERA5 have an accuracy worse than those derived from GNSS. The WPD value (from ERA5) is the same in the different altitude reductions, so even with an improved methodology the initial value has a low accuracy. The results shown in Figure 10 are affected by this issue, which does not happen in the validation using RS.

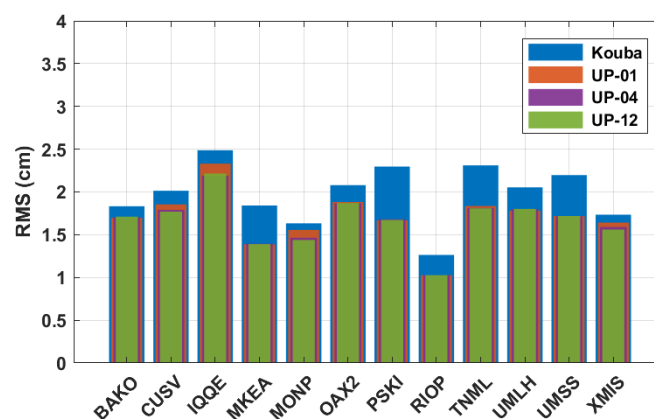


Figure 10. RMS (cm) of the differences at Global Navigation Satellite Systems (GNSS) station height between WPD derived from GNSS and those computed at ERA5 orography level using single level atmospheric variables and then reduced with Kouba (blue bars), UP-01 (orange bars), UP-04 (purple bars), and UP-12 (green bars) coefficients to the height of each GNSS station (identified by its four characters).

The global assessment with ERA5 data and mainly the validation with in situ radiosondes at vertical levels show the significant impact of the modelling presented in this study, when compared with the only modelling available so far (Kouba, 2008). The new UP models must be adopted to reduce WPD values at undesirable altitudes, e.g., those provided at the level of NWM orography in some altimetry products (Fernandes et al., 2014; Vieira et al., 2018). One of the applications of these models will be the integration in the GNSS-derived Path Delays Plus (GPD+) algorithm (Fernandes et al., 2010, 2015, 2016), which provides valid WPD measurements whenever the corresponding path delay derived from MWR is invalid or inexistent. This method combines different data sources (e.g., GNSS) in the vicinity of each along-track point with invalid or inexistent MWR-derived WPD. These new models will be implemented in this algorithm to better combine the different data sources, properly referring the wet correction to the levels of interest for satellite altimetry application (e.g., sea level in coastal oceanic regions (Liu et al., 2012; Roblou et al., 2011; Vignudelli et al., 2019)).

The modelling proposed in this study was performed using global 3-D WPD estimations from ERA5. It has long been recognized that the WPD derived from meteorological models has worse accuracy than observations from dedicated instruments (Vieira et al., 2019a), however, atmospheric models provide global data to compute 3-D WPD and the quality of the recent models has been increasing significantly.

The option to follow the expression proposed by Kouba for this modelling, deriving improved decay coefficients dependent on geographic location and time (period of the year), was based on the observed exponential variation of the WPD with altitude, as represented in Figure 2. Other types of modelling approaches/functions can be attempted in future work, however, due to the highly WPD vertical variation, as depicted in Figure 4, the development of improved models, namely using piecewise functions, will be difficult. Moreover, models with a larger number of coefficients will result in WPD altitude reduction procedures computationally more intensive.

3.4. Conclusions

This study presents the modelling of the altitude dependence of the WPD, crucial to better combine the different WPD sources in coastal and continental waters. This way, improved WPD estimations lead to improved water surface height retrievals from satellite altimetry.

This modelling was performed from ERA5, the latest ECMWF reanalysis, shown to be considerably better than ERA Interim in the computation of radar altimeter wet path delays. When compared to ERA Interim, ERA5 leads to a global reduction of the WPD RMS error of 0.2 cm, with values up to 0.4 cm for some latitude bands.

Following the unique expression available for this altitude reduction, the decay coefficient of this exponential expression was modelled, considering a dependence on geographic location and period of the year. This was performed by means of WPD vertical profiles, computed globally, from temperature and humidity 3-D fields provided by ERA5. This modelling consists of an exponential function with variable coefficients. Three models were developed, with different sets of coefficients: UP-01, a single coefficient for each point (non-time-dependent), computed as the mean at each point;

UP-04, four seasonally averaged coefficients for each location, and UP-12, 12 monthly averaged coefficients for each point.

Analysing the time evolution of the coefficients at each location, the first striking feature is the large variation of these coefficients, due to the high WPD vertical variability, which makes this modelling difficult. In some regions, a clear annual signal in the coefficients is observed, suggesting the inclusion of a temporal dependence.

After the modelling, a global assessment using ERA5 data for a different time span was carried out. When compared with an invariable coefficient (Kouba), the most significant RMS error decrease appears when only spatially dependent coefficients (UP-01) are used. This assessment also shows that for the location where the Kouba coefficient has the maximum RMS error of 3.2 cm (around the Indonesia region), this value is reduced to 1.2 cm when UP coefficients are adopted. The most significant impact of this modelling is an RMS decrease of 2 cm. In some regions (e.g., Bay of Bengal), the modelling of the additional temporal dependence (UP-04 and UP-12) has an impact when compared with UP-01. In the region where this temporal modelling has the most significant impact, the RMS error is 2.7, 2.5, 1.7, and 1.4 cm when Kouba, UP-01, UP-04, and UP-12 are considered, respectively. Selecting UP-04 and UP-12 instead of UP-01, the RMS decrease is 0.8 and 1.1 cm, respectively. This assessment also reveals many regions where the additional temporal coefficients have no impact (e.g., European region).

Finally, independent comparisons with radiosondes and GNSS data show that the RMS error decrease can be larger than 1 cm, when UP coefficients are used instead of Kouba. The validation with in-situ measurements obtained from radiosondes is more significant than that with GNSS, since the former are available at various vertical levels and only the altitude reduction is evaluated. On the contrary, the validation with GNSS data was performed at only one vertical level (GNSS station height) and the comparison is affected by the altitude reduction and the expected differences between GNSS and ERA5 derived WPD.

In order to better combine the different WPD data sources (e.g., in the GPD+ algorithm) for satellite altimetry application over coastal and inland waters, the models developed in this study may be adopted, thus contributing to a better retrieval of water surface heights over these regions of interest.

4. An enhanced Neural Network-based retrieval of the Wet Tropospheric Correction for Sentinel-3 (Article 5)

Abstract – Sentinel-3 (S3) mission is currently composed of two operating satellites (S3A and S3B), equipped with Microwave Radiometers (MWR), performing brightness temperature (TB) measurements at 23.8 and 36.5 GHz to determine the Wet Tropospheric Correction (WTC) of the altimeter observations. The two MWR-derived WTC present in S3 products, retrieved from 3- and 5-input neural network algorithms, suggest that improvements are required. This paper aims at developing an enhanced WTC retrieval algorithm for open-ocean, considering a suitable learning for the S3 and a better accounting for the contribution of the surface to the WTC retrieval. Adopting a purely empirical approach, the learning database has been built using 1-year (2017) of valid S3A measurements, ERA5-derived WTC, and sea surface temperature (SST) interpolated from ERA5. Results show that, instead of seasonal tables as adopted in S3, SST from ERA5 introduces relevant information on the surface contribution to the WTC, becoming the fifth input (vertical temperature decrease) redundant. The proposed algorithm is a 4-input neural network: TB at 23.8 and 36.5 GHz, altimeter backscattering coefficient and SST. Comparisons with reference and independent WTC sources show that WTC derived from the proposed algorithm (instead of those available in the S3 products) leads to a decrease in the RMS values of the WTC differences with respect to these independent WTC by about 1 mm globally, while this decrease can reach almost 1 cm locally. This study proposes a new algorithm for Sentinel-3, which proved to be a significant enhancement over the current algorithms (firstly designed for EnviSat).

4.1. Introduction

Sentinel-3 is a land and ocean mission from the European Space Agency (ESA) currently composed of two operational satellites: Sentinel-3A (S3A) launched on 16 February 2016 and Sentinel-3B (S3B) launched on 25 April 2018. Two other satellites (Sentinel-3C and Sentinel-3D) are planned for the future to overlap with S3A and S3B, in order to generate a coherent and consistent earth observation dataset (Quartly et al., 2020). Thus, this multi-instrument mission provides remote sensing data continuity for the ESA missions ERS-1, ERS-2, EnviSat and CryoSat-2.

Sentinel-3 has been planned with multiple objectives, including the measurement of the global sea surface topography. This supports oceanic studies such as the global monitoring of the sea level rise (Cazenave, 2018) associated with the climate changes, important for the evaluation and anticipation of its impacts (Bronselaeer et al., 2018; Garner et al., 2018). For this purpose, each Sentinel-3 satellite makes use of various sensing instruments, namely a dual-frequency Synthetic Aperture

Radar (SAR) ALtimeter (SRAL) and a 2-channel Microwave Radiometer (MWR). Other instruments are part of the mission payload, e.g. sensors for sea and land surface temperature, as well as for land and ocean colour, supporting an additional environmental and climate monitoring (Donlon et al., 2012).

Focusing on the SRAL and MWR instruments, together they form the Sentinel-3 Surface Topography Mission (STM) in the frame of the European Commission Copernicus program. These two instruments (combined with auxiliary data and modelling) collect data and allow the mapping of the global sea surface heights (SSH).

According to the straightforward measuring principle of satellite altimetry, the SSH above a reference ellipsoid is obtained at each along-track point by subtracting the range measured by the SRAL from the satellite altitude above the same reference ellipsoid (Chelton et al., 2001).

The SSH measurement is not merely the output of a single instrument, but it is derived from a measurement system. An accurate determination of the sea surface heights from satellite radar altimetry (e.g. from SRAL and MWR on board Sentinel-3 satellites) needs a set of corrections to be used together with the range measured by the altimeter and the orbit altitude (Chelton et al., 2001). Therefore, ensuring a proper determination of these corrections and combining them with the range measurement and the precise location of the spacecraft makes it possible to determine SSH globally with an accuracy of a few centimetres over the open oceans. Satellite altimetry has been also used over coastal regions, however over these zones the determination of accurate SSH is still challenging due to errors in altimeter waveform retrievals and in most of the corrections and auxiliary data (Vignudelli et al., 2019).

Among these corrections, the effect of the wet troposphere in the SRAL pulses is of particular interest for this study. When these radar pulses travel from the instrument on the satellite to the targeted surface, they suffer the effect of the atmospheric refractivity. This effect is due to the interaction of the pulses with the atmospheric constituents in the dry troposphere (dry gases), wet troposphere (water vapor and cloud liquid droplets) and ionosphere (electrons).

Concerning the wet troposphere, this effect causes a delay due to the presence of atmospheric water vapor and liquid water, designated by Wet Path Delay (WPD) (Fernandes et al., 2014; Legeais et al., 2014; Vieira et al., 2019). In the computation of the corrected SSH, this delay is considered as the Wet Tropospheric Correction (WTC), which is the opposite and negative value of the WPD ($WPD = |WTC|$). In this way, any error in the wet tropospheric correction (as well as in any other altimetric term) directly impacts the water level determination from satellite (Thao et al., 2014). If not taken properly into consideration, errors in WTC can be wrongly interpreted as SSH variations.

WPD is mostly owing to the water vapor in the troposphere, so its value is maximum (WPD up to 50 cm) for the largest water vapor content. Additionally, this water vapor amount increases with increasing atmospheric temperature. Thus, WTC depends on atmospheric vertical profiles of humidity, temperature and pressure (Obligis et al., 2006).

The sensing of atmospheric water vapor is a difficult task, due to its high variation, both in space and time. For this reason, the WPD has the same high variation (Vieira et al., 2019), becoming its

accurate measurement a challenge. Globally WPD (absolute value of WTC) ranges in a small interval (0-50 cm), however its standard deviation ranges from 10 to 15 cm in the tropics (Fernandes et al., 2021).

In the altimetry context, the most accurate way to determine the WPD is from dedicated MWR measurements. Due to the WTC variation, the best way to determine this correction is by means of MWR measurements collocated with the altimeter instrument. However, WTC is still considered one of the main contributors to the error budget of the SSH estimation (Ablain et al., 2019), contributing to 50% of the global mean sea level error budget (Ablain et al., 2009).

For satellite altimetry applications, WTC has also been derived from other sources, e.g. coastal and island Global Navigation Satellite Systems (GNSS) stations (Fernandes et al., 2013; Sibthorpe et al., 2011; Vieira et al., 2019b) and Numerical Weather Models (NWM) (Legeais et al., 2014; Vieira et al., 2019a). Since the state-of-the-art WTC retrieval algorithms from MWR measurements are tuned only for atmospheric states over oceanic surfaces, the corresponding retrievals become invalid over other surfaces (e.g. land and ice) (Vieira et al., 2019b) and cannot be used. For this reason, the alternative WTC sources mentioned above gain relevance over these regions. At the moment NWM cannot map the WTC short space and time scales (Vieira et al., 2019a) and, for this reason, their accuracy is worse than that from MWR. However, over some regions (e.g. inland waters (Vieira et al., 2018)) NWM can be the only source available and should be used (Fernandes et al., 2014, 2021). Moreover, the quality of the atmospheric models commonly used to compute the tropospheric corrections has been increasing over time, by means of improved data and assimilation methodologies.

Vertical integral of atmospheric water vapor (Total Column Water Vapor, TCWV) products from scanning imaging MWR on board remote sensing satellites are other data of extreme importance for the estimation of altimeter WTC. Data from some of these sensors (e.g. the Special Sensor Microwave Imager (SSM/I), SSM/I Sounder (SSM/IS), Along Track Scanning Radiometer (ATSR-E) and Global Precipitation Measurement (GPM) Microwave Imager (GMI)), known by their stability and independent calibration, have been used combined with altimeter MWR (Fernandes et al., 2016), as well as for purposes of validation, monitoring and calibration of the MWR-derived WTC.

Concerning the MWR measurements, two different instruments have been deployed on the altimetry missions, with three or just two frequencies (e.g. MWR on board Sentinel-3 satellites, which perform brightness temperature (TB) measurements, at 23.8 and 36.5 GHz). The 3-channels MWR, used in the reference missions (TOPEX/Poseidon (TP), Jason-1 (J1), Jason-2 (J2) and Jason-3 (J3)), have been shown to be near-optimum for measuring the wet troposphere delay (Keihm et al., 1995). Regarding the 2-frequency MWR, the lack of a third frequency has been addressed with improved methodologies and additional parameters (Eymard et al., 1996; Obligis et al., 2006, 2009; Picard et al., 2015).

The WTC retrieval from these collocated TB measurements is itself a complex step, since the brightness temperatures are nonlinearly related to the water vapor content. The retrieval of geophysical parameters from radiometric measurements is commonly difficult, mainly because of

this nonlinearity of the relation between the brightness temperatures and the geophysical parameters of interest (Obligis et al., 2006).

This nonlinear relation between TB and WTC has been empirically established using statistical regression methods, such as parametric methods (Brown, 2010; Keihm et al., 1995) and neural network (NN) techniques (Obligis et al., 2006, 2009; Picard et al., 2015). NN are particularly well suited for addressing nonlinear problems, while the parametric regression lacks flexibility and robustness to optimally adjust the data. It has been shown that the neural network methods are better suited for the retrieval of the wet tropospheric correction than the traditional parametric regression (Thao et al., 2015).

The neural network algorithm, first developed for Envisat (Obligis et al., 2006) and later improved (Obligis et al., 2009) is now used in Sentinel-3. In this way, two MWR-derived WTC are present in the S3 products: one derived from three inputs (Obligis et al., 2006) and another one from five inputs (Obligis et al., 2009). The three inputs are the brightness temperatures at 23.8 and 36.5 GHz and the Ku-band ocean backscatter coefficient (not corrected for the atmospheric attenuation). The five inputs are these three inputs plus the sea surface temperature and the atmospheric temperature decrease rate between the surface and 800 hPa pressure level.

Previous studies (Fernandes et al., 2018) indicate that the MWR-derived WTC present in current Sentinel-3 products is worse than that of the reference missions and EnviSat, suggesting that there is scope for improvement of this range correction.

The objective of this article is to exploit the S3-derived WTC (and the corresponding retrievals) and to develop an improved algorithm for the WTC retrieval from MWR measurements over open ocean, better tuned for Sentinel-3. This is performed mainly in two steps: 1) considering a suitable learning, temporally closer to the S3 mission period and 2) better account for the contribution of the surface in the MWR measurements (a weakness in the 2-band MWR such as that of S3). The second point is addressed by means of computing the inputs from atmospheric model fields (instead of a static climatology or seasonal tables as adopted in S3 products) and testing of new/alternative inputs and different combinations of inputs in order to fix a better algorithm. Once the contribution of the atmospheric water vapor and cloud liquid water in the WTC is properly accounted for by TB at 23.8 and 36.5 GHz, respectively, the effect of the surface (emissivity and temperature) in these TB measurements is carefully handled by means of including additional inputs, such as σ_0 or wind speed (with information on changes in the surface emissivity owing to wind-induced sea surface roughness) and sea surface temperature.

Section 4.2 presents an overview of the different WTC retrieval algorithms used in the various altimetry missions, with a focus on those used in the Sentinel-3 products (inherited from the previous ESA missions). Building upon these state-of-the-art retrieval schemes, an improved algorithm is developed and described in Section 4.3, while the performance of this proposed algorithm against that adopted in S3 products is shown in Section 4.4 (using independent data). Finally, Section 4.5 summarizes the main findings and conclusions of this paper.

4.2. MWR-derived WTC retrieval algorithms

Satellite-borne microwave radiometers have been widely used to acquire information about several atmospheric and surface properties for different applications. This includes the sensing of atmospheric water vapor and cloud liquid water, as well as the wet path delay for satellite altimetry (mainly dependent on atmospheric water vapor) over ocean surfaces, to correct the altimeter range for the excess path delay due to the wet troposphere.

Satellite remote sensing of atmospheric water vapor is not a straightforward procedure. At present, microwave brightness temperature measurements are used to retrieve the water vapor in the atmosphere, as well as other related geophysical parameters, by a retrieval technique. For this reason, the payload of the altimetric satellites includes a microwave radiometer to measure the range delay of the altimeter signal mainly due to the water vapor in the troposphere.

The microwave radiation measured by a nadir-looking radiometer can be expressed as a brightness temperature (or blackbody temperature) which corresponds to the sum of three contributions (frequency dependent): atmosphere, surface and the cosmic background (Grody, 1976). Resulting from these contributions, the TB measurements by a satellite-based downward-looking MWR depend on the atmospheric (temperature and absorption) and surface (temperature and emissivity) properties. In the microwave region of the spectrum, the scattering is negligible for cloud droplets, ice and snow particles in the atmosphere (De Angelis et al., 2016).

On the other hand, the atmospheric absorption profiles depend on three atmospheric components: oxygen (well determined from atmospheric pressure and temperature), water vapor and liquid water. Therefore, the MWR measurements depend on two surface (temperature and emissivity) and four atmospheric profiles (temperature, pressure, water vapor and liquid water) properties. In addition, changes in the surface emissivity due to wind-induced roughness of the sea surface make the surface emissivity dependent on surface wind speed. An altimeter-derived parameter related to the wind-generated roughness of the sea surface is described later.

The ability to retrieve these properties from satellite measurements is determined by the atmospheric properties and the consequent interaction with different signals in the selected spectral band. Due to these properties, the WPD can be retrieved from brightness temperatures measured near the 22.235 GHz water vapor absorption line. The reference missions (TP, J1, J2 and J3) have a three-channel radiometer (18, 21 and 37 GHz for TP and 18.7, 23.8 and 34 GHz for J1, J2 and J3) while the ESA missions (including Sentinel-3 and SARAL) only have two frequencies (23.8 and 36.5 GHz). The brightness temperatures that an MWR measures at 18-37 GHz when it receives the upwelling emitted radiance ranges from ~125–150 K (over calm water surfaces) to ~300 K (over near blackbody land surfaces, such as the Amazon rainforest) (Brown et al., 2004).

The three MWR frequencies of the reference missions have shown to be the most well-suited for measuring the wet path delay. These three channels contain mainly information on the surface, atmospheric water vapor and cloud liquid water, respectively. Thus, the combination of these three channels ensures an accurate retrieval of the WPD in all non-heavy precipitation weather conditions (Brown et al., 2004). The atmospheric opacity and absorption increase with increasing frequency, so

the atmosphere is more transparent for the low frequencies and a better sensing of the surface is performed with the ~18 GHz channel (not available in Sentinel-3). The opposite happens for ground-based MWR, where the high frequencies are more sensitive to changes in the lower troposphere and close to the ground (Sahoo et al., 2015).

Since the wet tropospheric delay is largely due to the atmospheric water vapor, the 23.8 GHz channel (near the water vapor absorption line) has the major contribution in the WPD retrieval. The other two frequencies (window channels) are less sensitive to atmospheric water vapor, so they have a lower weight in the same retrieval.

In order to quantify this weight in the WTC retrieval, the lack of the 37 GHz channel (not able to correct for the effects of cloud liquid) increases the uncertainties in the WPD (and consequently in the WTC) to 2 cm, while the lack of the 18 GHz (not able to correct for the effects of the surface) increases these uncertainties to about 1.5 cm (dependent on surface emissivity) (Keihm et al., 1995). These figures show the small contribution of each window channel, compared with that of the band near the 22.235 GHz water vapor absorption line.

4.2.1. From MWR measurements to WTC

The conversion of raw MWR data into altimeter wet tropospheric corrections can be divided into three levels of processing (Brown et al., 2004). Firstly, in the antenna temperature calibration (Ruf et al., 1995), the raw data are converted into antenna temperatures. Secondly, in the antenna pattern correction (APC) (Janssen et al., 1995), the antenna temperatures are corrected for contributions from the sidelobes of the antenna pattern. The brightness temperature is derived from the antenna temperature by quantifying and removing all undesirable contributions, such as the side lobe contamination and a small contribution from the cosmic background (cold space). And thirdly, the brightness temperatures at each MWR frequency are converted to wet tropospheric corrections by a retrieval algorithm (Ruf et al., 1996). This paper addresses this third step.

Concerning the last step of this processing chain, two methods are generally used to retrieve the WTC from the brightness temperature measurements: statistical procedures (traditional parametric regression or neural networks) and physical retrieval methods (Desportes et al., 2010; Hermozo et al., 2019).

The first approach is based on a statistical relationship established between the measured brightness temperatures (in some cases plus other additional inputs) and the WTC values. The second method uses a radiative transfer model (RTM) in an iterative procedure to modify an assumed WTC until the simulated TB match the observations within the observational uncertainty (Cadeddu et al., 2013). This is performed by means of an assimilation scheme, combining atmospheric state data (from a model) and measurements.

For operational purposes, the wet tropospheric correction is widely retrieved using statistical methods. The computational expense of the physical methods is several orders of magnitude larger than the statistical ones. Moreover, the estimation errors of these methods were found to be of the same magnitude as those obtained from statistical retrievals, confirming the reliability of the

statistical procedures (Cadeddu et al., 2009). From here onwards, this paper focuses on the statistical methods.

Regarding the statistical approaches, two regression methods have been applied in the context of altimeter wet tropospheric corrections: log-linear regression in the reference missions (three-band MWR) and neural networks in the ESA missions (two-channel MWR). Previous studies show that, for the WTC retrieval using the same inputs, the neural networks are better suited than the log-linear regression (Thao et al., 2015).

4.2.2. Algorithms used in the reference missions

The WTC retrieval algorithm from MWR measurements for the reference missions was firstly developed for TOPEX/Poseidon (Keihm et al., 1995) and then adopted for the next reference missions (Brown, 2010; Brown et al., 2004). This retrieval is based on a two-step statistical inversion algorithm (Keihm et al., 1995). It was designed to be globally applicable and to consider the sea surface emissivity and wind speed effects on the WTC retrieval and the nonlinearities between the water vapor and the 3-channel brightness temperatures.

This statistical algorithm determines coefficients dependent on stratified values of wind speed and initial estimates of WTC, becoming this procedure more robust and flexible for the nonlinear problems. A second (and final) estimation of the WTC is determined using coefficients stratified in the initial WTC.

The algorithm makes use of a global data base archive: radiosonde, sea surface temperature, wind speed and corresponding collocated simulated brightness temperatures (ensuring a global representation of atmospheric and surface scenes over open ocean).

In spite of some limitations due to large errors for anomalous conditions, the first algorithm developed for TP was established, predicting an overall WTC accuracy of 1.2 cm (Keihm et al., 1995), while the uncertainty of the follow on Jason-1 was demonstrated to be less than 0.9 cm (Brown et al., 2004).

The coefficients for the MWR algorithms are determined prelaunch and require a posterior on-orbit adjustment.

4.2.3. Sentinel-3 Algorithm

For the first ESA missions (ERS-1/2), the corresponding MWR algorithms were established using a direct log-linear function of the two radiometer TB measurements and the altimeter-derived wind speed (Eymard et al., 1996). The lack of a third band in the radiometers on the ESA missions has been overcome using additional inputs in the corresponding algorithms, as the altimeter wind speed (Eymard et al., 1996) or the altimeter backscatter coefficient (Obligis et al., 2006).

One of the altimeter measurements is the power of the returned signal, designated as backscattering coefficient (σ_0), related to the wind-generated sea surface roughness. The roughness of the sea surface increases with increasing wind speed, making the power of the returned signal weaker, since a greater fraction of the radiation that reaches the sea surface is reflected away from the antenna. Thus, σ_0 is inversely related to wind speed. In this way, the estimation of wind speed from

altimeter is performed by means of measurements of σ_0 and possibly significant wave height (Lillibridge et al., 2014). For nadir-viewing, σ_0 is not dependent on the wind direction, so wind direction cannot be derived from altimeters, only the wind speed is inferred from the backscatter coefficient.

Due to the nonlinear relation of the measurements, neural networks have been extensively adopted to retrieve geophysical parameters from satellite-based measurements. A neural network for regression purposes is itself a statistical algorithm, however it is easy to implement, is robust and is able to represent the nonlinear relations without a priori information (Obligis et al., 2006).

According to these advantages of the NNs relative to the traditional parametric approaches, an innovation of the ERS MWR algorithms was performed for the retrieval of EnviSat MWR products, showing a significant improvement with respect to the previous ESA missions (Eymard et al., 1996). On the one hand, to better account for the nonlinear relation between TB and WTC, instead of a log-linear combination, a neural network approach was adopted. On the other hand, in order to avoid uncertainties coming from the wind speed retrieval (Witter et al., 1991), the altimeter backscatter coefficient (σ_0) in the Ku band (not corrected for the atmospheric attenuation) is used as the third input, in place of the wind speed (Obligis et al., 2006). Thus, this algorithm is based on a neural network with three inputs, both EnviSat MWR TBs and the backscatter coefficient. Hereafter, this algorithm is mentioned as 3I.

Previous studies have shown that some specific regions of the globe have atmospheric temperature profiles systematically different from the global mean, characterized by a strong temperature inversion and an accumulation of water vapor near the surface (Sun, 1993). This means that the same column water vapor content (and consequently the same WTC), but with different vertical distributions can originate distinct TB measurements. Aiming at better accounting for these effects, a new algorithm was developed (henceforth designated as 5I) and described in (Obligis et al., 2009). Similar to the previous algorithm, this incorporates two extra inputs: the sea surface temperature and the atmospheric temperature lapse rate (γ_{800}), describing the linear decreasing of atmospheric temperature with altitude, between the surface and the 800 hPa pressure level. In the formulation of the 5I algorithm, these two extra fields are used from four seasonal tables at $2^\circ \times 2^\circ$ spatial resolution (for SST) and from a climatological table at $1^\circ \times 1^\circ$ spatial resolution (for γ_{800}).

The two wet tropospheric corrections provided in the Sentinel-3 products seem to be derived from these algorithms (3I and 5I), originally designed for EnviSat, without a proper tuning for Sentinel-3.

(Thao et al., 2015) show that the best results are obtained when the brightness temperature at 18 GHz is used instead of the backscattering coefficient, which is not possible for the ESA missions, including Sentinel-3. This fosters the need to develop improved algorithms, in view to overcome this instrumental limitation. Additionally, the same studies show that better results are achieved when a neural network algorithm is used instead of a log-linear regression (Thao et al., 2015). Thus, for this paper only the neural network formalism will be addressed.

The statistical retrieval algorithms adopted in the ESA missions are formulated on a database that contains estimated values of WTC from an atmospheric model and corresponding collocated

simulated brightness temperatures, being these simulations performed over a range of atmospheric states provided by 3D fields from an atmospheric model. The uncertainty of this semi-empirical method comes from the database and the radiative transfer model (modelling component).

Other retrieval configurations have been tested by other authors, such as a purely empirical relationship (Picard et al., 2015), where measured brightness temperatures and altimeter backscatter coefficient are used instead of simulated ones. This configuration avoids bias and errors due to differences between simulated and measured parameters. The uncertainty of a purely empirical method comes from the database and measurements (instrumental component). The configuration using measurements instead of simulations proved to have performances closed to what it was initially expected using simulations (Picard et al., 2015). The simulations are critical in the prelaunch phase, since no on-orbit measurements are available.

Thus, accurate retrieval of the path delay correction requires firstly well calibrated brightness temperatures and any additional inputs and secondly a precise inversion algorithm to establish the relation between these parameters and the WTC.

Both current algorithms (either parametric or neural networks) are derived for pure ocean surfaces (based on sea surface emissivity conditions), so they do not consider the very strong and variable land radiation. Between 18 and 34 GHz, the ocean has an emissivity around 0.4-0.5, while land typically has an emissivity above 0.9 at these frequencies.

4.3. A new Sentinel-3 WTC retrieval algorithm

Building upon the current WTC retrieval algorithms used in Sentinel-3, several algorithms have been implemented for this mission, which are described in this section. Two main aspects have been addressed. On a first step, a suitable learning database has been established. After this, different input configurations have been tested in order to find a better suited retrieval algorithm for the Sentinel-3 mission.

4.3.1. Learning Database

The learning database for this study was created as follows: 104030 S3A points randomly were chosen over the year 2017, ensuring a good distribution in time and geographic location. The following criteria were used: surface type equal to zero (ocean measurements), quality flags of TB23.8, TB36.5 and σ_0 equal to zero (valid measurements), latitude between 50°N and 50°S (to avoid sea ice) and distance from coast larger than 30 km (to avoid land contamination) (Fernandes et al., 2018). S3A data here used were released in 2020 (latest processing Baseline 4) (EUMETSAT, 2020).

Here, a purely empirical approach has been adopted (Picard et al., 2015), considering valid measurements of TBs and σ_0 from S3A, instead of simulations given by a radiative transfer model (semi-empirical approach).

For each point of the learning database mentioned above, a WTC value at sea level was computed/space-time interpolated from the state-of-the-art NWM ERA5 global fields at pressure levels, at 3h intervals and 0.25°x0.25° spatial sampling (Copernicus Climate Change Service (C3S),

2018a). This computation is performed from vertical integration of temperature and humidity profiles, as adopted in (Collecte Localisation Satellites (CLS), 2011; Vieira et al., 2019a, 2019c).

For the same learning dataset, additional parameters were obtained. Sea surface temperature at single level from ERA5 (Copernicus Climate Change Service (C3S), 2018b) at 6h intervals and $0.5^\circ \times 0.5^\circ$ spatial resolution was also interpolated for locations and instants of the learning points.

On the other hand, making use of the atmospheric temperature provided by ERA5 at pressure levels (Copernicus Climate Change Service (C3S), 2018a), global grids of γ_{800} were computed every 6h, at $0.5^\circ \times 0.5^\circ$ spatial sampling. For each grid point, γ_{800} is estimated by adjusting a linear fit to the temperature in the 9 lowest ERA5 pressure levels (between 1000 and 800 hPa). From these grids, γ_{800} is also interpolated for the S3A points in the learning database.

Since the backscatter coefficient only describes the modulus of the wind speed (not the direction) and it is used not corrected for the atmospheric attenuation, an alternative input can improve the WTC retrieval. On the other hand, the quality of the atmospheric models has been increasing, so the wind speed from ERA5 (Copernicus Climate Change Service (C3S), 2018b) is also considered as an additional input, in place of the backscatter coefficient.

To fully describe the horizontal wind speed, ERA5 provides two fields: u_{10} and v_{10} , the eastward and northward components of the 10 m wind, respectively. Both components are available at a height of ten meters above the sea surface, in meters per second. Together, these parameters give the speed and direction of the horizontal wind. Hence, u_{10} and v_{10} are also interpolated for the S3A points in the learning database.

In summary, 8 values are associated to each S3A point in the learning dataset: TB23.8, TB36.5 and σ_0 (valid measurements from S3A products), SST, γ_{800} , u_{10} , v_{10} and WTC computed and interpolated from ERA5. As described in section 4.2, each of the inputs accounts for the different effects in the upward emitted radiance received by an on-board MWR: atmospheric water vapor (TB23.8), atmospheric cloud liquid water (TB36.5), changes in the surface emissivity owing to wind-induced sea surface roughness (σ_0 or wind speed) and sea surface temperature. In addition, γ_{800} accounts for the effects of the vertical atmospheric changes in the TB measurements (Obligis et al., 2009).

Fig. 1 represents the absolute value of these WTC (WPD) versus each S3A measurement: TB23.8 (top left), TB36.5 (top right) and σ_0 (bottom). Fig. 2 shows the same WPD values versus the various additional parameters obtained from ERA5: SST (top left), γ_{800} (top right), u_{10} (bottom left) and v_{10} (bottom right).

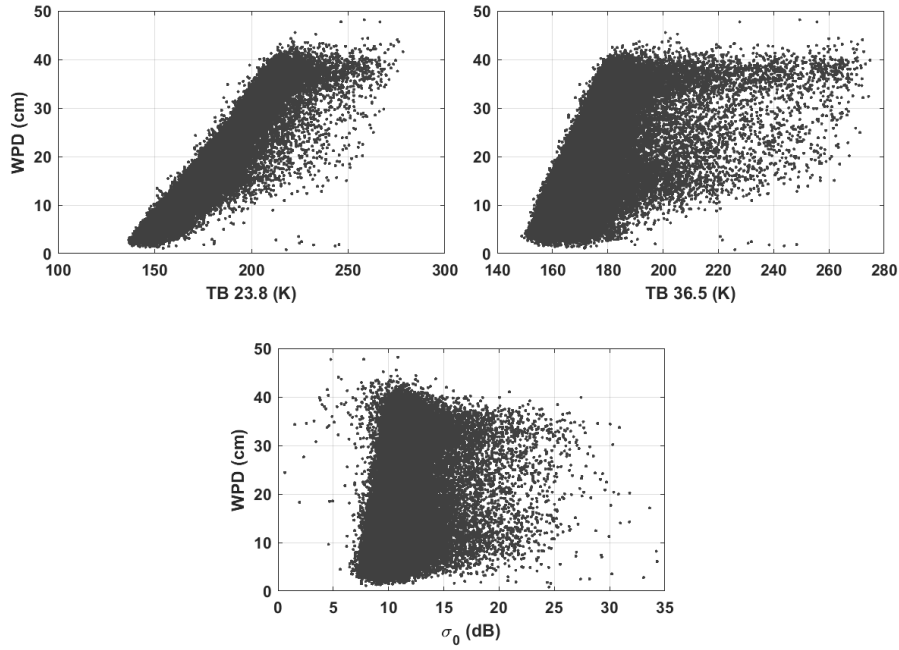


Figure 1. WPD computed from ERA5 versus S3A valid measurements stored in the learning database.

Figs. 1 and 2 allow to observe the nonlinear relation between the different geophysical parameters, as stated above, evidencing that the WTC retrieval from the different parameters is a difficult procedure, requiring robust statistical techniques. The most striking observation from Fig. 1 is the correlation between WTC and TB23.8, since this frequency is more sensitive to atmospheric water vapor and it has the highest weight in the WTC retrieval.

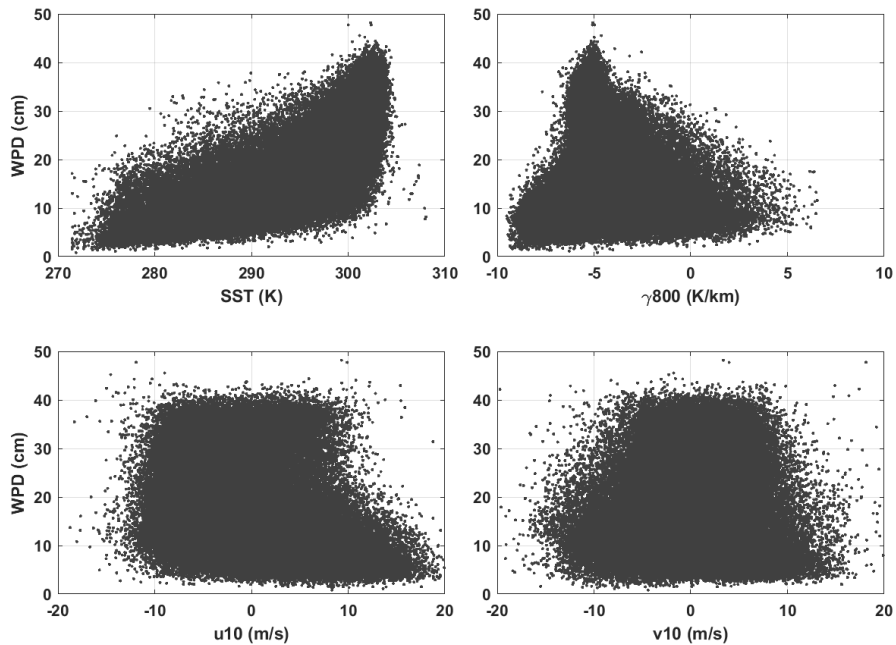


Figure 2. WPD computed from ERA5 versus additional inputs computed/interpolated from ERA5 stored in the learning database.

According to the radar equation (Chelton et al., 2001), σ_0 depends on the radar scattering characteristics of the sea surface, i.e. on the wind-induced sea surface roughness. As shown in the bottom panel of Fig. 1, a typical altimetric measurement of σ_0 is about 10 dB. This parameter ranges from about 20 dB at low wind speed to about 5 dB at high wind speed (Chelton et al., 2001). Concerning the wind speed, bottom panels of Fig. 2 show that the absolute values of each component range from 0 up to around 20 m/s, which means a wind speed up to about 30 m/s.

It is important to note that, since the near-surface wind speed is estimated from altimetric measurements of σ_0 , these two quantities are equivalent for the WTC retrieval, providing redundant information about the sea surface roughness (and consequently changes in the sea surface emissivity).

Fig. 3 illustrates the spatial representation of the three S3A measurements included in the learning database. This corresponds to mean values for 2017, computed for $2^\circ \times 2^\circ$ tiles of TB23.8 in K (top panel), TB36.5 in K (middle panel) and backscatter coefficient in dB (bottom panel). As described above, only S3A points over open-ocean (distance from coast larger than 30 km) and between latitudes 50°S and 50°N were selected.

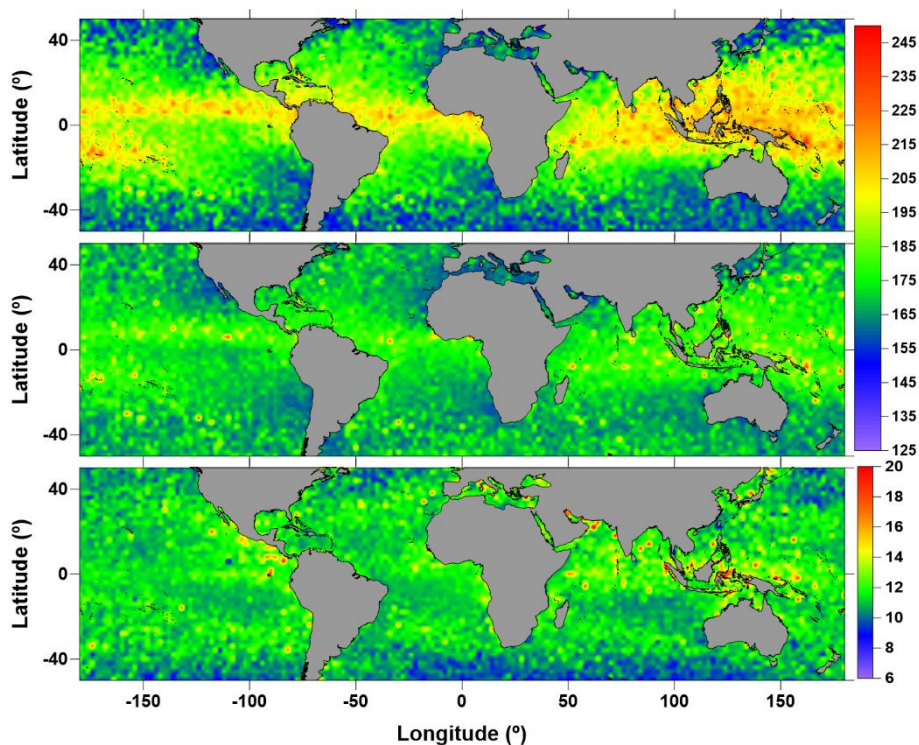


Figure 3. Spatial representation of mean values of TB23.8 (top panel), TB36.5 (middle panel) and σ_0 (bottom panel) from Sentinel-3A measurements considering the 104030 points over the year 2017 in the learning dataset. Brightness temperatures are in K, while σ_0 is in dB.

Fig. 4 represents the annual mean (2017) of WTC in centimetres over the ocean, computed at sea level from integration of temperature and specific humidity profiles provided from ERA5 on pressure levels. The absolute WTC annual mean ranges from a few centimetres (at high latitudes) to about 35 cm in the western tropical Pacific Ocean and eastern tropical Indian Ocean, as illustrated in Fig. 4.

As observed in the top left panels of Fig. 1 and Fig. 3, the TB measurement at 23.8 GHz has a very similar spatial pattern as the one of the WTC (Fig. 4), due to the dominant contribution of the water vapor to the WTC. Therefore, the TB23.8 (more sensitive to this atmospheric gas) becomes the input with the largest contribution to the WTC retrieval.

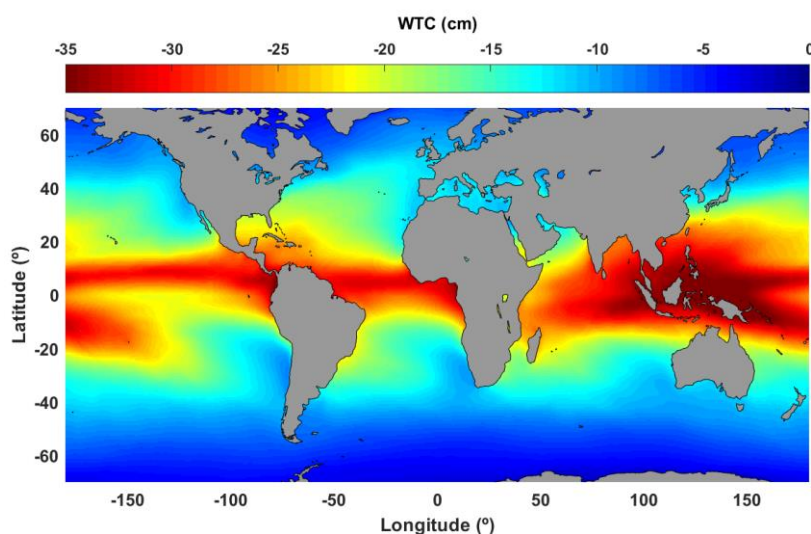


Figure 4. Annual mean of WTC in cm computed from vertical integration of temperature and humidity profiles from ERA5 on pressure levels, at 6h intervals and $0.5^\circ \times 0.5^\circ$ spatial sampling over the year 2017.

The top panel of Fig. 5 shows the annual mean of SST for the year 2017, where the most evident feature is the clear dependence on latitude. This global representation was performed using SST from ERA5, at 6h intervals and $0.5^\circ \times 0.5^\circ$ spatial resolution. The sea surface temperature as input for the WTC retrieval algorithm without TB measurements at ~ 18 GHz is an additional and alternative information, due to the dependence on the surface (temperature and emissivity) properties.

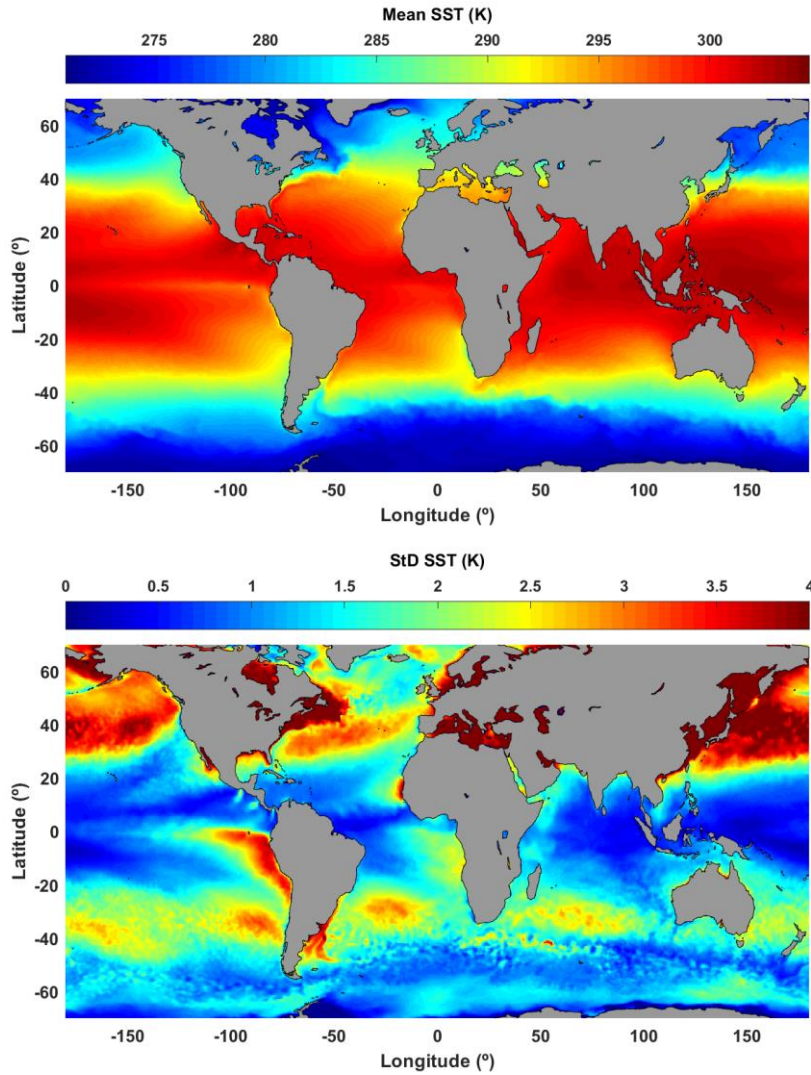


Figure 5. Mean (top panel) and standard deviation (bottom panel) for the year 2017 of SST in K from ERA5 at single level, every 6h, at $0.5^\circ \times 0.5^\circ$ spatial sampling.

The bottom panel of Fig. 5 shows the standard deviation of the SST, considering the same data as in the top panel of the same figure. The pattern of the SST variation shows the regions where fine temporal resolution SST information can improve the WTC retrieval (where SST is more variable). Over these regions, SST from four seasonal tables at $2^\circ \times 2^\circ$ spatial resolution, as used in (Obligis et al., 2009), cannot be enough to describe the effect of the SST temporal variation in the MWR measurements. This point will be discussed later on.

Fig. 6 illustrates the annual mean (top panel) and standard deviation (bottom panel) of the γ_{800} (year 2017). This is computed using the global temperature field provided by ERA5 at pressure levels, using only the levels between surface and 800 hPa. The top panel of Fig. 6 clearly shows the regions of the globe where the atmospheric temperature profiles are systematically different from the global mean. Considering the data used in Fig. 6, the global mean of the atmospheric temperature decreasing with altitude (between the surface and the level at 800 hPa) is -4.8 K/km. However, over some specific regions, this value can be positive, i.e., the temperature increases with altitude, from the surface up

to 800 hPa. These regions are mainly some coastal zones of America and Africa (California, Peru, Mauritania and Namibia) as previously identified (Obligis et al., 2009).

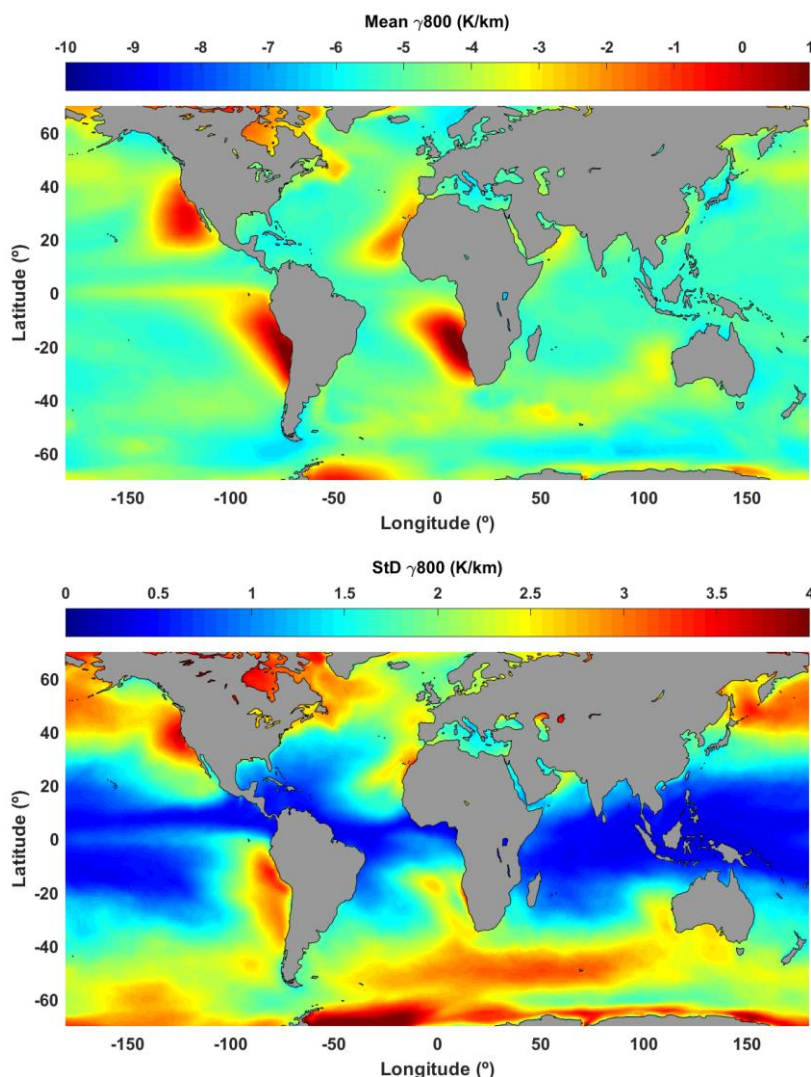


Figure 6. Mean (top panel) and standard deviation (bottom panel) for year 2017 of γ_{800} in K/km computed using temperature from ERA5 at pressure levels, every 6h, at $0.5^\circ \times 0.5^\circ$ spatial sampling.

The bottom panel of Fig. 6 shows the spatial pattern of the temporal variation of the γ_{800} , evidencing a strong positive correlation with temperature. γ_{800} is more variable where the SST is also more variable. Additionally, the SST is more variable (bottom panel of Fig. 5) where the SST itself is low in the extratropical regions (top panel of Fig. 5). Thus, a strong correlation between SST and γ_{800} exists.

Fig. 7 represents the annual mean of the zonal component of horizontal speed of air moving towards the east (u_{10}) in m/s, where a strong pattern is visible, with westward winds at low latitudes (mainly blue) and eastward winds at high latitudes (mainly red).

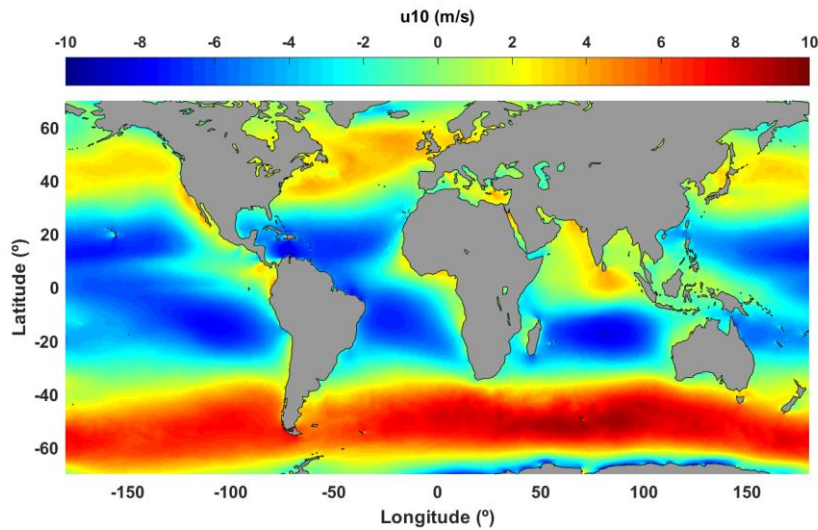


Figure 7. Mean for the year 2017 of u10 in m/s from ERA5 at single level, every 6h, at $0.5^\circ \times 0.5^\circ$ spatial sampling.

Fig. 8 illustrates the annual mean of the horizontal speed of air moving in the north-south direction (v10), in metres per second. The untypical regions observed in Fig. 6, are the same where the meridional component of the wind (Fig. 8) has a strong pattern. Winds towards the equator can be observed, both from north (blue) and from south (red), due to the Hadley cell tropical atmospheric circulation, which makes the air to rise near the Equator (Zhou et al., 2020), evidencing the strong correlation between SST and γ_{800} .

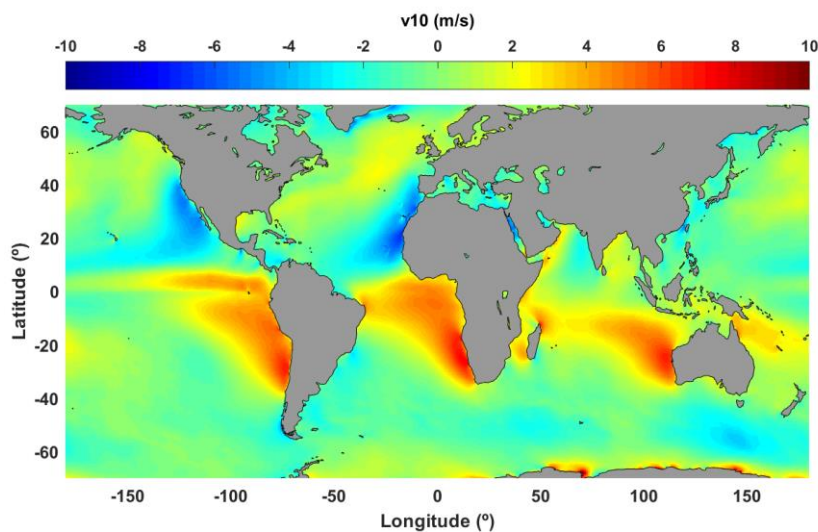


Figure 8. Mean for the year 2017 of v10 in m/s from ERA5 at single level, every 6h, at $0.5^\circ \times 0.5^\circ$ spatial sampling.

The values shown in Figs. 5 to 8 were computed using single level fields from ERA5, at 6h intervals and $0.5^\circ \times 0.5^\circ$ spatial resolution (1460 global grids for each component over the year 2017).

Figs. 3-8 show patterns that will help to discuss the results in section 4.4.

Considering this learning database, the following can be pointed out: TB23.8 ranges from 137 to 277 K (mean 179 K); TB36.5 ranges from 151 to 279 K (mean 172 K); differences between the two WTC values provided in the Sentinel-3 products (computed from 3I and 5I algorithms) and that computed from ERA5 have RMS values of 1.50 and 1.43 cm, respectively. Therefore, the non-significant

difference between both WTC suggests that the corresponding algorithms are not well tuned for Sentinel-3. Additionally, contrary to other missions such as Jason-3, Sentinel-3 wet tropospheric corrections do not show an improvement over a correction only derived from third-party data (Fernandes et al., 2018).

Near-surface air temperature from the latest ECMWF reanalysis (Copernicus Climate Change Service (C3S), 2018b) reveals that the increase in global temperatures over the last three decades is about 0.2°C per decade. This temperature increase induces an increase in global atmospheric water vapor of about 0.35 mm/decade (roughly 2.2 mm/decade for the WTC). This means that the global absolute mean increase of the WTC over the altimetry era (since 1991) is almost 1 cm. These figures allow to note the impact of the climate changes in the WTC, evidencing the importance of having a learning dataset for the WTC algorithms temporally close to the mission of interest.

Due to the climate changes and the corresponding impacts in the atmosphere, algorithms (and the corresponding adjusted coefficients) obtained some time ago may not be valid for current and future missions. The same happens for some auxiliary data, e.g. seasonal and climatological tables for SST and γ_{800} . It is thus important to keep the algorithms and the auxiliary data up to date.

4.3.2. Learning of different Algorithms

The retrieval algorithm adopted in this study is a neural network with a single hidden layer of eight neurons similar to the architecture adopted by (Obligis et al., 2006, 2009). The transfer function for each input is the sigmoid function, while the output is linked with a linear function. The retro-propagation algorithm is the Levenberg–Marquardt algorithm.

After establishing the architecture configuration, the learning procedure applied over the learning database estimates the weight and bias values associated to each connection and neuron, respectively.

In the scope of the research described in this paper, different networks (with the same architecture) have been established with different combinations of input parameters:

- UP3S0: TB23.8, TB36.5 and σ_0 , same as in the 3I algorithm (Obligis et al., 2006);
- UP4S0: TB23.8, TB36.5, σ_0 and SST;
- UP5S0: TB23.8, TB36.5, σ_0 , SST and γ_{800} , same as in the 5I algorithm (Obligis et al., 2009);
- UP3WS: TB23.8, TB36.5, u10 and v10;
- UP4WS: TB23.8, TB36.5, u10, v10 and SST;
- UP5WS: TB23.8, TB36.5, u10, v10, SST and γ_{800} ;

UP3WS, UP4WS and UP5WS consider as inputs 4, 5 and 6 parameters, respectively, since wind speed from ERA5 is described through two components (two separated fields). For a direct comparison between using wind speed (two inputs) instead of backscatter coefficient (one input), this terminology has been assumed. Thus, UP3WS, UP4WS and UP5WS are as UP3S0, UP4S0 and UP5S0, respectively, using wind speed from ERA5 instead of σ_0 .

Contrary to the WTC provided in Sentinel-3 products, where climatological tables are adopted (Obligis et al., 2006, 2009), here any additional input (u10, v10, SST and γ_{800}) is interpolated from ERA5 at 6h intervals and 0.5°x0.5° spatial sampling. Hence, some improvements are expected, since

small space and time scales (as far as ERA5 allows) of these geophysical parameters are expected to be resolved.

In summary, six algorithms with different combinations of inputs (UP3S0, UP4S0, UP5S0, UP3WS, UP4WS, UP5WS) have been tuned and can be applied to any set of along-track S3 points. Their operational implementation requires the geographic coordinates and instants from the S3 products and the additional inputs are interpolated from global grids provided by ERA5.

4.4. Evaluation of the different Sentinel-3 Wet Tropospheric Corrections

For the purpose of assessment and validation, the same Sentinel-3A data used in the learning phase (latest processing Baseline 4) are used to apply the different retrieval algorithms. In order to ensure a temporal independence, while data over the year 2017 were used in the learning step, S3A data over the year 2018 are used for the analysis of the performance of each algorithm.

For this evaluation, eight WTC are analysed: 3I and 5I (as available in the S3 products and described in section 4.2), UP3S0, UP4S0, UP5S0, UP3WS, UP4WS and UP5WS (output from the different algorithms tuned in the scope of this paper and described in section 4.3).

4.4.1. Comparison with Scanning Imaging MWR

A comparison has been performed using independent WTC derived from Scanning Imaging MWR (SIMWR). SIMWR-derived WTC is computed from the corresponding TCWV products (Stum et al., 2011). These data are known for their stability and independent calibration, suitable to be adopted as reference. All independent SIMWR as described in (Lázaro et al., 2020), available for this comparison are used (dependent on temporal and spatial overlapping between SIMWR and S3). For more details about these data see e.g. (Fernandes et al., 2016; Lázaro et al., 2020).

For each S3A along-track point, measurements from SIMWR have been selected in its vicinity (whenever available). For each pair of non-located WTC (one from MWR and other from SIMWR), distance and time difference between them are available. For this comparison, only SIMWR points with distances to S3A points smaller than 25 km and time difference lower than 30 minutes have been used, ensuring a closer proximity, both in location and time. In this way, WTC differences due from the non-collocation are minimized and these reference WTC can be considered collocated with S3.

Considering a full year (2018) and the same criteria as mentioned in Section 4.3 for the selection of S3A points, differences have been computed between the SIMWR-derived WTC and those derived from the tuned algorithms, as well as those available in the Sentinel-3 products (3I and 5I). Fig. 9 illustrates the global RMS values of these differences.

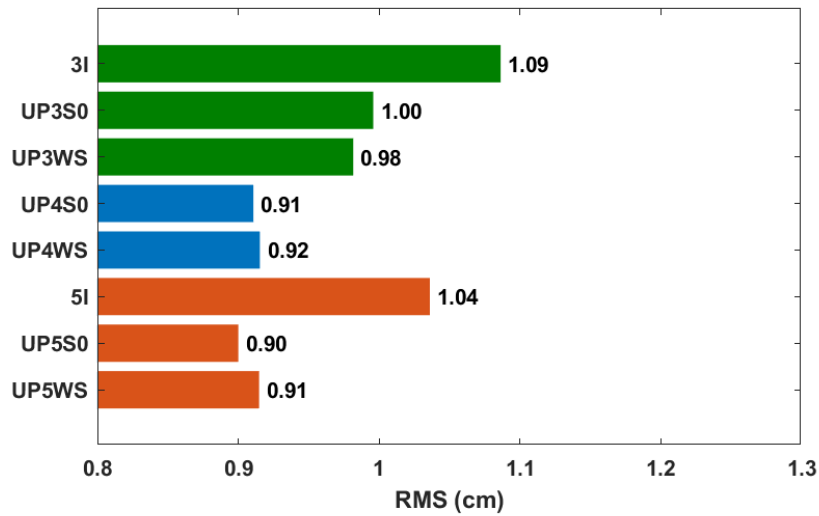


Figure 9. Global RMS of the WTC differences between SIMWR and the various S3 MWR retrievals.

Globally, when the retrievals of the algorithms tuned in the scope of this study are used instead of those available in the S3A products (3I and 5I), an RMS decrease of about 1 mm is observed, when compared with SIMWR (1.4 mm for 5I versus UP5S0). No significant difference is achieved when wind speed interpolated from ERA5 (two components) is used instead of the altimeter σ_0 . Relative to the 3 inputs algorithms (green bars), when only the SST is included (blue bars), the decrease of the RMS values is globally almost 1 mm. Concerning the algorithms used in the S3 products, when 5I is used instead of 3I, only an RMS decrease of 0.5 mm is observed. The inclusion of additional inputs (not derived from altimetry) is more significant in the UP algorithms than in the 3I/5I algorithms. Any UP algorithm is globally better than the two currently available in S3 products, when compared with SIMWR.

Still regarding the use of wind speed from ERA5 instead of σ_0 , although the global difference is not significant, an important result is observed from Fig. 9. Concerning the 4 and 5-input algorithms (blue and orange bars, respectively), the RMS value when σ_0 is used is slightly smaller than the RMS value when WS is used. The same does not happen for the 3-input algorithms (green bars), where the RMS of the differences SIMWR-UP3S0 is larger than that of the differences SIMWR-UP3WS, i.e. the use of WS instead of the backscatter coefficient improves the WTC retrieval (which does not happen using 4 and 5 inputs). This suggests that when the two components of wind speed are used as input without SST, the contribution of surface in the MWR measurements is better estimated in regions where u_{10} has a strong pattern (see Fig. 7), where the SST is more variable (Fig. 5). When the SST is included as input, this contribution is already present in the SST and the use of WS instead of σ_0 does not incorporate additional information on the surface contribution. This observation will be confirmed below in a spatial analysis.

The RMS of WPD differences were spatially and globally computed for $5^\circ \times 5^\circ$ tiles and are represented in Fig. 10. In order to evaluate the reduction of RMS of WPD differences when different algorithms are used, differences between the corresponding RMS values were computed.

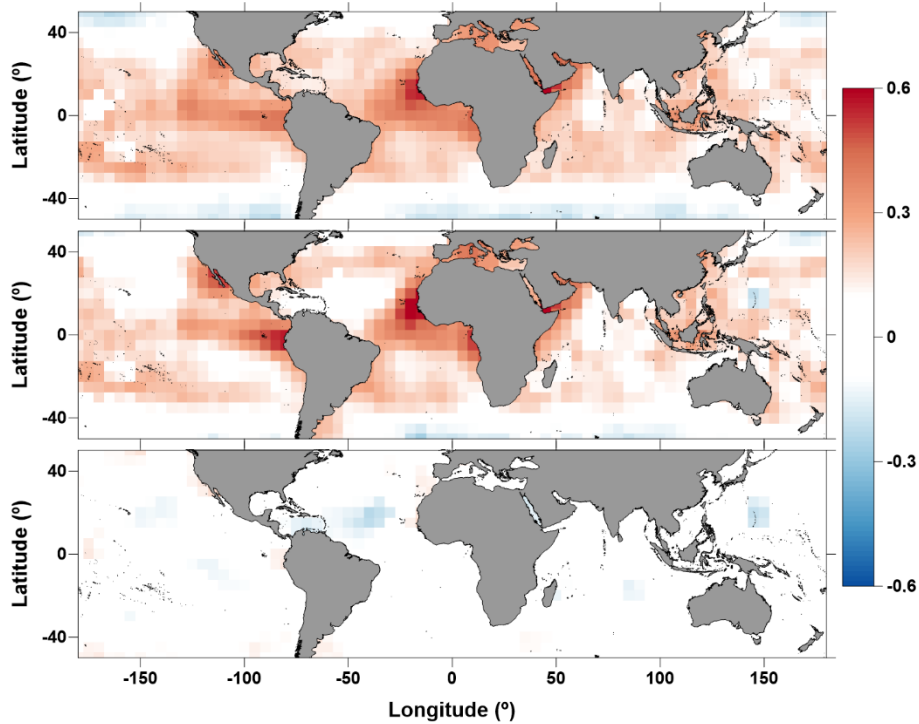


Figure 10. Differences (in cm) between RMS of WPD differences for 3I-UP3S0 (top panel), 3I-UP3WS (middle panel) and UP3S0-UP3WS (bottom panel).

Fig. 10 shows the RMS differences for 3I-UP3S0, 3I-UP3WS and UP3S0-UP3WS in the top, middle and bottom panels, respectively. Thus, when compared with SIMWR, positive differences (red) mean that UP3S0 is better than 3I (top panel), UP3WS is better than 3I (middle panel) and UP3WS is better than UP3S0 (bottom panel). A slight zonal band around 50°S in blue in the top panel of Fig. 10 is less pronounced in the middle panel of the same figure, showing the very small effect of using the two components of WS without SST, as described above. This impact is not observed in the bottom panel, because it is very small.

Fig. 11 represents the same as Fig. 10, concerning the 5-input algorithms. The top and middle panels of Figs. 10 and 11 show clearly the improvement of the UP algorithms over those used in the S3A products, with a pattern mainly red (RMS of the differences SIMWR-UP smaller than the RMS of the differences SIMWR-3I/5I). The very few regions with negative differences (RMS of the differences SIMWR-UP larger than the RMS of the differences SIMWR-3I/5I) are depicted with blue colour, most of them with a very light blue (differences very close to zero).

Although the global improvement in the RMS of WPD differences is small, around 1 mm (Fig. 9), when UP retrievals are used instead of 3I and 5I, the RMS decrease when compared with SIMWR can reach 0.8 and 0.9 cm over some regions, respectively (Figs. 10 and 11).

Once SST is used as input, the effect of using wind speed (two components) instead of backscatter coefficient is very small and negligible, not showing any spatial pattern (bottom panel of Fig. 11), as observed in the global RMS values (Fig. 9).

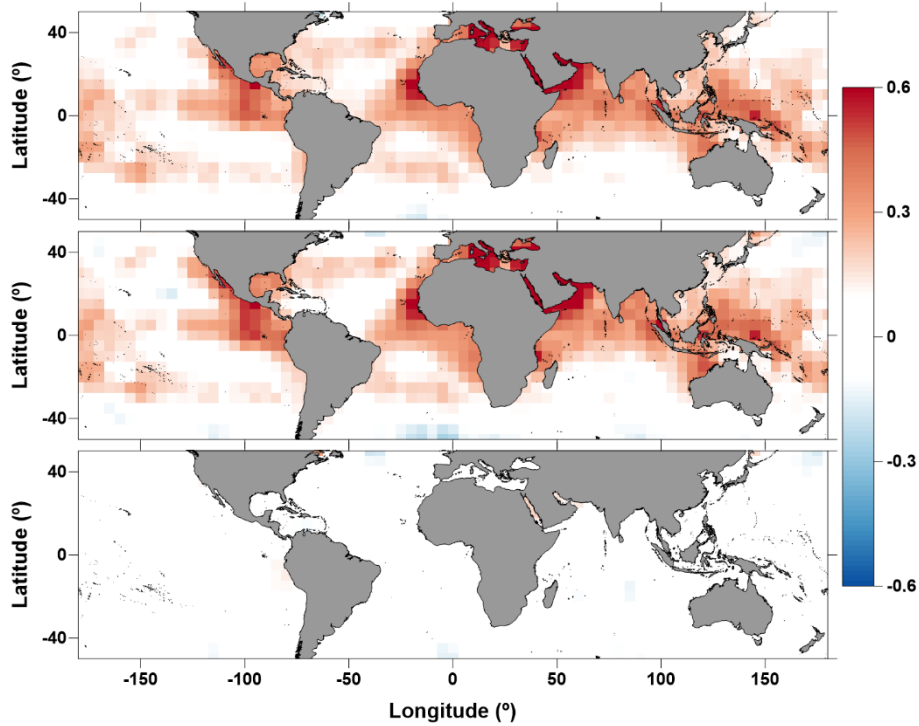


Figure 11. Differences (in cm) between RMS values for 5I-UP5S0 (top panel), 5I-UP5WS (middle panel) and UP5S0-UP5WS (bottom panel).

Another important observation from Figs. 9 and 11 is the insignificant effect when the fifth input (γ_{800}) is included in the UP algorithms. There is no significant difference between UP4 and UP5 algorithms, when compared with SIMWR. Fig. 12 shows the RMS differences for UP3S0-UP4S0 (top panel) and UP4S0-UP5S0 (bottom panel), showing the effect of the inclusion of the SST and γ_{800} as inputs, respectively.

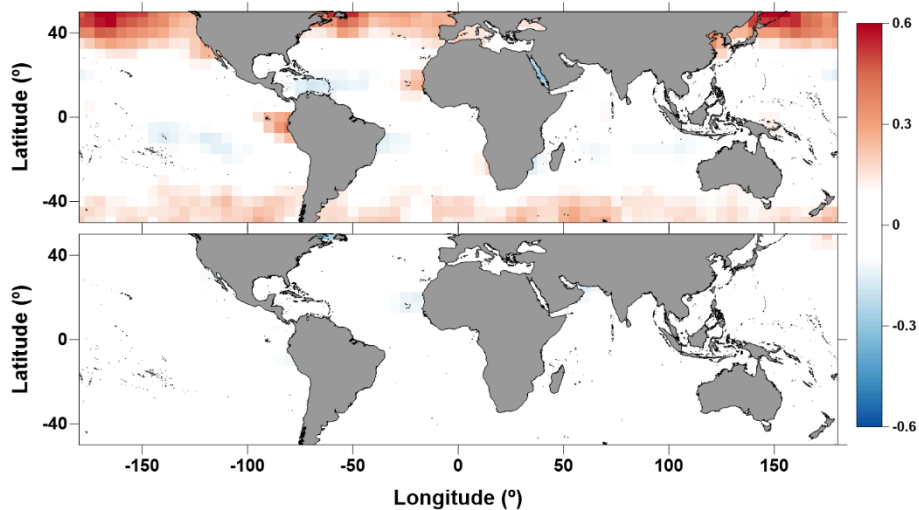


Figure 12. Differences (in cm) between RMS values for UP3S0-UP4S0 (top panel) and UP4S0-UP5S0 (bottom panel).

The regions where the inclusion of the SST has a significant impact in the improvement of the WTC retrieval are represented with red colour in the top panel of Fig. 12. The inclusion of the SST interpolated from global grids every 6h, will improve the retrieval where the SST is temporally more

variable. This improvement can reach 0.9 cm in some regions, i.e. the entire improvement from 5I to UP5S0. For this reason, the top panel of Fig. 12 has the same spatial pattern of the bottom panel of Fig. 5 (standard deviation of the SST considering grids at 6h intervals over one complete year).

The bottom panel of Fig. 12 illustrates the effect of the fifth input, when compared with the algorithm with four inputs. Once the SST variability is accounted for and included, the addition of the γ_{800} does not improve the WTC retrieval, as shown in Fig. 9 and in the bottom panel of Fig. 12. The temporal variation of the γ_{800} (bottom panel of Fig. 6) and the same variation of SST (bottom panel of Fig. 5) have a very similar spatial pattern. This means that the variability of the SST already includes information on the vertical decrease rate of the atmospheric temperature, becoming the addition of the fifth input redundant to the learning. Since the sea surface temperature plays an essential role in the Hadley Cell changes, the temperature vertical profiles directly depend on the temperature at sea level.

It is important to note again the predominant contribution of the TB at 23.8 GHz in the WTC retrieval. Any other input (accounting for information on atmospheric cloud liquid water and surface) has a small contribution, when compared with TB23.8. This reinforces some of these results, regarding small impacts when different inputs or combinations of inputs are used.

When the spatial patterns of the improvements of the UP retrievals over those provided in the S3 products (top and middle panels of Figs. 10 and 11) are analysed, a pronounced improvement over some near coastal regions is observed. The RMS values computed as explained before but considering only along-track points with distances from coast between 30 and 250 km are represented in Fig. 13. While the global improvement from 3I/5I to UP retrievals (when compared with SIMWR) represented in Fig. 9 is about 1 mm, this improvement can reach 2.4 mm when only regions with distances from coast in this range are considered.

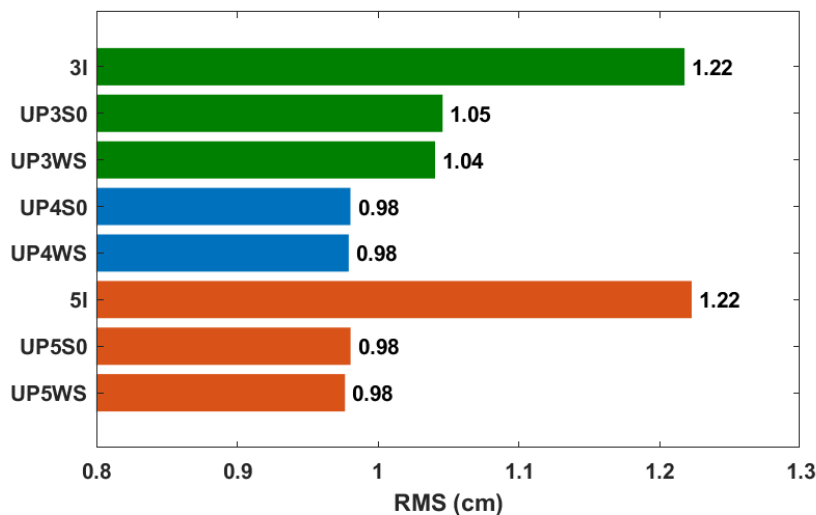


Figure 13. RMS of the WTC differences between SIMWR and the various MWR retrievals, considering only S3A along-track points with distances from coast in the range 30-250 km.

Fig. 13 reveals a pattern very similar to Fig. 9, however the differences between RMS values (3I/5I versus UP) are more pronounced. On the other hand, the small effect observed in Fig. 9 when 5I is used instead of 3I is not observed. Fig. 13 reinforces again that 3I and 5I algorithm are not well tuned for Sentinel-3, since the inclusion of two additional inputs does not improve the WTC retrieval (3I and 5I with the same RMS value when compared with an independent source). Fig. 13 also shows that any UP algorithm is better than 3I or 5I and, once SST is included, the addition of the fifth input has no impact (the same RMS of 0.98 cm).

Aiming to identify a better compromise between accuracy and input parameters, this comparison with independent SIMWR data reveals that the best algorithm is UP4S0. Thus, this paper proposes a WTC retrieval algorithm with 4 input parameters: TB23.8, TB36.5, σ_0 and SST interpolated from ERA5.

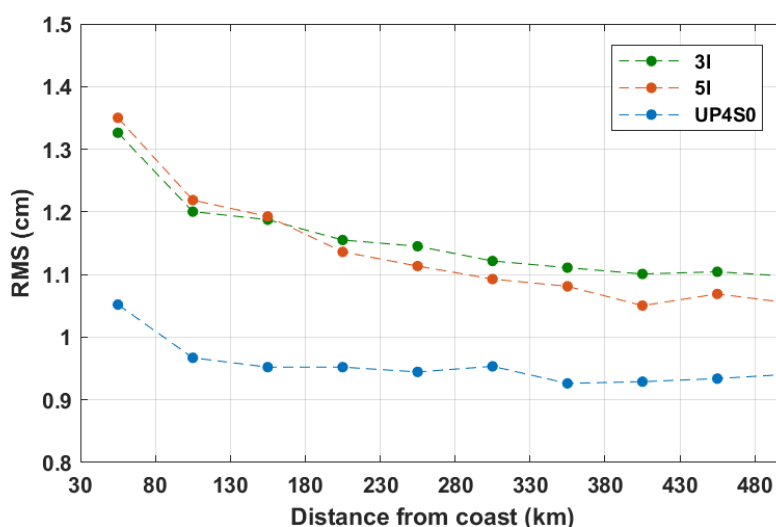


Figure 14. RMS of the WTC differences between SIMWR and 3I (green), 5I (orange) and UP4S0 (blue) function of distance from coast.

Fig. 14 illustrates the RMS values, function of distance from coast, of the WPD differences between SIMWR and three S3A algorithms: 3I (green points), 5I (orange points) and UP4S0 (blue points). These RMS values (the same as represented in Figs. 9 and 13) are computed for classes of distance from coast of 50 km, between 30 and 500 km. As illustrated in Fig. 14, the improvement of UP algorithm over 3I and 5I is more pronounced at distances from coast in the band 30-150 km (almost 3 mm in RMS). For distances from coast in the range 30-250 km (Fig. 13), the 5I algorithm does not seem to be better than the 3I. A slightly improvement of the 5I algorithm relative to the 3I is noticeable only for distances from coast larger than 250 km. This suggests that the tables for the additional inputs used by the 5I algorithm are not suitable, mainly for distances from coast smaller than 250 km. The low performance of the 5I over 3I at distances from coast between 30 and 250 km can be due to the coarse spatial resolution ($2^\circ \times 2^\circ$) of the seasonal tables used for SST.

Fig. 14 reinforces the better performance of the UP4S0 algorithm globally, over those adopted in Sentinel-3 products, with a global RMS of the WPD differences between SIMWR and UP4S0 smaller than 1 cm.

4.5. Conclusion

After analysing the current algorithms adopted in the Sentinel-3 products, this paper describes an improved algorithm for the retrieval of the wet tropospheric correction from MWR measurements over open ocean, better tuned for Sentinel-3.

Originally designed for EnviSat mission, S3 products provide two different MWR-derived WTC, retrieved from 3- and 5-input neural network algorithms (3I and 5I, respectively), where the second should be an improved version of the first one. Since the MWR on board Sentinel-3 (and other ESA missions) does not possess a third band near 18 GHz to account for the surface contribution in the MWR measurements (as is the case of the reference missions), these algorithms with additional inputs appeared to overcome this instrumental limitation. The main point of these algorithms is the use of parameters able to include the contribution of the sea surface (emissivity and temperature) in the MWR measurements, such as the altimeter σ_0 (describing the changes in the sea surface emissivity due to wind-induced sea surface roughness) and sea surface temperature. Moreover, a fifth input is also used, describing the atmospheric temperature vertical decrease (γ_{800}).

In the scope of the research described in this paper, various neural network algorithms have been tested with the same architecture (a single hidden layer of eight neurons) and different combinations of input parameters. These new WPD retrieval algorithms have been tuned specifically for the Sentinel-3 mission, by adopting a suitable learning for this mission. Additionally, in order to better account for the contribution of the surface in the TB measurements, while the algorithms adopted in the S3 products assume seasonal and climatological tables for the additional inputs, parameters interpolated from ERA5 are used here, attempting to include some small space and time scales of these geophysical parameters (as far as the atmospheric model allows).

A comparison with independent WPD from scanning imaging microwave radiometers shows that the best configuration is a neural network with 4 inputs: TB at 23.8 and 36.5 GHz, σ_0 and SST interpolated from ERA5 (UP4S0). It has been shown that once the small-time scales of the SST are included, the fifth input γ_{800} adopted by 5I becomes redundant and unnecessary. The same comparison shows that the global RMS of the WPD differences between SIMWR and the proposed algorithm is lower than 1 cm. Globally, the use of this algorithm instead of those adopted in the S3 products can reduce the RMS of the WPD differences between S3 MWR and SIMWR by about 1 mm, while reaching almost 1 cm over some regions. Results indicate that the two MWR-derived WTC provided in the S3 products (3I and 5I) are not significantly different, suggesting that a proper learning was not used and these algorithms were simply inherited from EnviSat.

These results are more pronounced for distances from coast between 30 and 250 km, where the improvement of the UP algorithm over those adopted in Sentinel-3 products in RMS is globally almost 3 mm. For the same range of distances from coast, 5I is not better than 3I. This only happens for distances from coast larger than 250 km, where 5I is slightly better than 3I (a global effect less than 0.5 mm in the RMS).

The inclusion of the two components of the wind speed from ERA5 instead of σ_0 has been tested, however a significant global impact was not achieved.

The performance of the WTC algorithm here described against those adopted in the Sentinel-3 data records shows a substantial improvement in the quality of the WTC. Therefore, this paper proposes the use of a new WTC retrieval algorithm, originally designed for Sentinel-3 and providing improved wet tropospheric corrections for this mission, as the UP4S0 here described. These improved corrections will allow the estimation of more accurate sea surface heights from the SRAL instrument aboard Sentinel-3, in particular for distances from coast shorter than 150 km. This shall also contribute to the estimation of improved WTC such as the GNSS-derived Path Delay Plus (GPD+) WTC (Fernandes et al., 2016, 2018; Lázaro et al., 2020) which extend the validity of this crucial range correction to all surface types.

5. Conclusions

Earth observation and monitoring, particularly over the oceans and water bodies, is increasingly important and satellite radar altimetry is a robust technique with a wide range of applications that can help to understand Earth's dynamics processes. The determination of the sea level from this technique depends directly on the ability to compute accurately tropospheric path delays, becoming the corrections of these effects crucial to get accurate water surface height measurements.

This thesis addresses the tropospheric corrections of the altimeter observations, aiming at improving their retrievals, with particular focus over coastal regions and inland waters. Any improvement in the estimation of these corrections, directly translates into an improvement in the sea level determination, provided that all required terms are properly considered.

Apart from some preventable wrong procedures, the state-of-the-art estimation of the DTC over coastal and inland waters is easily performed with centimetric accuracy. Results show that systematic errors related with the DTC height dependence still exist in some altimetry products, however, once computed at the correct water level, adopting appropriate procedures, the DTC has errors below 1 cm.

On the contrary, the estimation of the WTC over coastal and continental waters is more challenging and, for this reason, more attention has been dedicated to this correction. Thus, the focus of this thesis is the WTC.

The GNSS-derived WTC proves to be a useful independent source to monitor the stability of the microwave radiometers aboard the altimeter missions and to inspect the land effects on MWR observations, determining the distance from coast at which this contamination occurs. This distance ranges from 10 to 30 km for the analysed altimetric missions, depending on their footprint sizes and MWR retrieval algorithms. This study also shows the ability of the GNSS-derived path delay plus algorithm to remove this land contamination and to improve the WTC retrieval.

The global assessment of the impact of ERA5 in the WTC computation indicates that the global RMS of the differences between MWR and ERA5 is 1.2 cm and the effect of using 1h intervals instead of 6h intervals is small. Hourly intervals have a very small impact on the WTC from ERA5, being a temporal resolution of 3h high enough to ensure the same level of accuracy of 1 h. This study also shows that the latest ECMWF reanalysis, like its predecessors, cannot map the WTC small space and time scales.

Concerning the first main objective of this study, the modelling of the WTC altitude dependence, aiming at developing improved expressions, revealed to be a very difficult task, due to the high WTC vertical variation. The time evolution of the modelled coefficients shows regions where they are highly variable. A modelling dependent on geographic location and period of the year has been

developed. Results show that the most significant error decrease with respect to the adoption of a single coefficient occurs when only spatially dependent coefficients are used. Independent comparisons show that the developed modelling is a significant improvement, leading to a decrease in the error larger than 1 cm.

Regarding the second main objective of this thesis, the MWR-derived WTC present in Sentinel-3 products suggests that improvements are required. In the sequel, an enhanced WTC retrieval algorithm for open-ocean for this mission, considering a suitable learning and a better accounting for the contribution of the surface to the WTC retrieval was developed. Results show that the current algorithms do not use the best combination of inputs, using a fifth unnecessary parameter. The developed algorithm proved to be a significant enhancement over the current algorithms (firstly designed for a former mission), leading to a decrease in the errors by about 1 mm globally, while this decrease can reach almost 1 cm over some regions. These results are more pronounced for distances from coast between 30 and 250 km, where the improvement of the proposed algorithm over those adopted in Sentinel-3 products is globally almost 3 mm.

In the future work, various topics of research will be subject of study. On one hand, the coastal zones are of increasing interest, due to the sea level rise and, on the other hand, these zones are more challenging for the WTC retrieval. Concerning the second objective relative to the open ocean, it is expected to improve the WTC retrieval from MWR over coastal regions (ocean/land transition), by means of a proper handling of the contribution of different surfaces in the brightness temperature measurements and the land contamination in the corresponding WTC retrievals. This will be performed by exploring different methodologies and the steps before the WTC retrieval (the antenna pattern correction). Since the atmospheric attenuation in the returned signal is derived also from the brightness temperatures, this correction also can be of interest in future work. New instruments in the recent missions, such as the high frequencies in the MWR on board Sentinel-6, as well as the collocated GNSS-Radio Occultation (GNSS-RO) instrument, with highly accurate temperature and humidity information, combined with each other, can also be a topic for the future work. Other topics of interest, such as the effect of the global warming in the atmospheric humidity, and consequently in the WTC and its retrieval will also be of interest, aiming at better modelling the effect of the troposphere in satellite altimetry.

The work performed in the scope of this thesis contributes to the retrieval of precise water surface heights from satellite altimetry, by means of better tropospheric corrections estimations. Thus, the contribution of this space technique to the climate crisis is more and more reliable. A better accuracy will foster a proper use and management of the water resources, as well as a better monitoring of the climate changes and their impacts.

References

- Abdalla, S., Isaksen, L., Janssen, P. A. E. M., & Wedi, N. (2013). Effective spectral resolution of ECMWF atmospheric forecast models. *ECMWF Newsl.*, 137, 19–22.
- Ablain, M., Cazenave, A., Larnicol, G., Balmaseda, M., Cipollini, P., Faugère, Y., Fernandes, M. J., Henry, O., Johannessen, J. A., Knudsen, P., Andersen, O., Legeais, J., Meyssignac, B., Picot, N., Roca, M., Rudenko, S., Scharffenberg, M. G., Stammer, D., Timms, G., & Benveniste, J. (2015). Improved sea level record over the satellite altimetry era (1993–2010) from the Climate Change Initiative project. In *Ocean Science* (pp. 67–82). doi: 10.5194/os-11-67-2015
- Ablain, M., Cazenave, A., Valladeau, G., & Guinehut, S. (2009). A new assessment of the error budget of global Mean Sea Level rate estimated by satellite altimetry over 1993–2008. *Ocean Science*, 5(2), 193–201. doi: 10.5194/os-5-193-2009
- Ablain, M., Meyssignac, B., Zawadzki, L., Jugier, R., Ribes, A., Cazenave, A., & Picot, N. (2019). Uncertainty in Satellite estimate of Global Mean Sea Level changes, trend and acceleration. *Earth System Science Data Discussions*, 11, 1189–1202. doi: 10.5194/essd-2019-10
- Anthes, R. A. (1983). Regional models of the atmosphere in middle latitudes. *Monthly Weather Review*, 111(6), 1306–1335. doi: 10.1175/1520-0493(1983)111<1306:RMOTAI>2.0.CO;2
- Benevides, P., Nico, G., Catalao, J., & Miranda, P. M. A. (2017). Analysis of Galileo and GPS Integration for GNSS Tomography. *IEEE Transactions on Geoscience and Remote Sensing*, 55(4), 1936–1943. doi: 10.1109/TGRS.2016.2631449
- Benveniste, J., Cazenave, A., Vignudelli, S., Fenoglio-Marc, L., Shah, R., Almar, R., Andersen, O., Birol, F., Bonnefond, P., Bouffard, J., Calafat, F., Cardellach, E., Cipollini, P., Le Cozannet, G., Dufau, C., Fernandes, M. J., Frappart, F., Garrison, J., Gommenginger, C., ... Wöppelmann, G. (2019). Requirements for a coastal hazards observing system. *Frontiers in Marine Science*, 6, 348. doi: 10.3389/fmars.2019.00348
- Bercher, N., Fabry, P., Ambrózio, A., Restano, M., & Benveniste, J. (2016). Validation of CryoSat-2 SAR and SARin modes over rivers for the SEOM/SHAPE project. *Presentation at Living Planet Symposium 2016. May 10 2016, Prague, Czech Republic.*
- Berry, P. A. M., Smith, R. G., & Benveniste, J. (2008). ACE2: The New Global Digital Elevation Model. In S. P. Mertikas (Ed.), *Gravity, Geoid and Earth Observation* (Vol. 135, pp. 231–237). Chania, Greece: Springer. doi: 10.1007/978-3-642-10634-7_30
- Bevis, M., Businger, S., Chiswell, S., Herring, T. A., Anthes, R. A., Rocken, C., & Ware, R. H. (1994). GPS Meteorology: Mapping Zenith Wet Delays onto Precipitable Water. *Journal of Applied Meteorology*, 33(3), 379–386. doi: 10.1175/1520-0450(1994)033<0379:GMMZWD>2.0.CO;2
- Bevis, M., Businger, S., Herring, T. A., Rocken, C., Anthes, R. A., & Ware, R. H. (1992). GPS meteorology: Remote sensing of atmospheric water vapor using the global positioning system. *Journal of Geophysical Research*, 97(D14), 15787–15801. doi: 10.1029/92JD01517
- Birkett, C. (1995). The contribution of TOPEX/POSEIDON to the global monitoring of climatically sensitive lakes. *Journal of Geophysical Research*, 100(C12), 25,125-179,204. doi: 10.1029/95jc02125
- Birkett, C., & Beckley, B. (2010). Investigating the Performance of the Jason-2/OSTM Radar Altimeter over Lakes and Reservoirs. *Marine Geodesy*, 33, 204–238. doi: 10.1080/01490419.2010.488983
- Birkett, C., Reynolds, C., Beckley, B., & Doorn, B. (2011). From research to operations: The USDA global reservoir and lake monitor. In S. Vignudelli, A. G. Kostianoy, P. Cipollini, & J. Benveniste

- (Eds.), *Coastal Altimetry* (pp. 19–50). Germany: Springer-Verlag: Berlin/Heidelberg. doi: 10.1007/978-3-642-12796-0_2
- Bock, O., Willis, P., Lacarra, M., & Bosser, P. (2010). An inter-comparison of zenith tropospheric delays derived from DORIS and GPS data. *Advances in Space Research*, 46(12), 1648–1660. doi: 10.1016/j.asr.2010.05.018
- Boehm, J., Heinkelmann, R., & Schuh, H. (2007). Short note: A global model of pressure and temperature for geodetic applications. *Journal of Geodesy*, 81(10), 679–683. doi: 10.1007/s00190-007-0135-3
- Boehm, J., Werl, B., & Schuh, H. (2006). Troposphere mapping functions for GPS and very long baseline interferometry from European Centre for Medium-Range Weather Forecasts operational analysis data. *Journal of Geophysical Research: Solid Earth*, 111(2). doi: 10.1029/2005JB003629
- Böhm, J., Möller, G., Schindelegger, M., Pain, G., & Weber, R. (2015). Development of an improved empirical model for slant delays in the troposphere (GPT2w). *GPS Solutions*, 19(3), 433–441. doi: 10.1007/s10291-014-0403-7
- Brenot, H., Walpersdorf, A., Reverdy, M., Van Baelen, J., Ducrocq, V., Champollion, C., Masson, F., Doerflinger, E., Collard, P., & Giroux, P. (2014). A GPS network for tropospheric tomography in the framework of the Mediterranean hydrometeorological observatory Cévennes-Vivarais (southeastern France). *Atmospheric Measurement Techniques*, 7(2), 553–578. doi: 10.5194/amt-7-553-2014
- Bronselaer, B., Winton, M., Griffies, S. M., Hurlin, W. J., Rodgers, K. B., Sergienko, O. V., Stouffer, R. J., & Russell, J. L. (2018). Change in future climate due to Antarctic meltwater. *Nature*, 564(7734), 53–58. doi: 10.1038/s41586-018-0712-z
- Brown, S. (2010). A novel near-land radiometer wet path-delay retrieval algorithm: Application to the Jason-2/OSTM Advanced Microwave Radiometer. *IEEE Transactions on Geoscience and Remote Sensing*, 48(4), 1986–1992. doi: 10.1109/TGRS.2009.2037220
- Brown, S., Ruf, C. S., Keihm, S., & Kitiyakara, A. (2004). Jason microwave radiometer performance and on-orbit calibration. *Marine Geodesy*, 27(1–2), 199–220. doi: 10.1080/01490410490465643
- Cadeddu, M. P., Liljegren, J. C., & Turner, D. D. (2013). The atmospheric radiation measurement (ARM) program network of microwave radiometers: Instrumentation, data, and retrievals. *Atmospheric Measurement Techniques*, 6(9), 2359–2372. doi: 10.5194/amt-6-2359-2013
- Cadeddu, M. P., Turner, D. D., & Liljegren, J. C. (2009). A neural network for real-time retrievals of PWV and LWP from arctic millimeter-wave ground-based observations. *IEEE Transactions on Geoscience and Remote Sensing*, 47(7), 1887–1900. doi: 10.1109/TGRS.2009.2013205
- Calmant, S., & Seyler, F. (2006). Continental surface waters from satellite altimetry. *Comptes Rendus - Geoscience*, 338(14–15), 1113–1122. doi: 10.1016/j.crte.2006.05.012
- Calmant, S., Seyler, F., & Cretaux, J. F. (2008). Monitoring continental surface waters by satellite altimetry. *Surveys in Geophysics*, 29(4–5), 247–269. doi: 10.1007/s10712-008-9051-1
- Cazenave, A. (2018). Global sea-level budget 1993-present. *Earth Syst. Sci. Data*, 10, 1551–1590. doi: 10.5194/essd-10-1551-2018
- Cazenave, A., Bonnefond, P., Dominh, K., & Schaeffer, P. (1997). Caspian sea level from Topex-Poseidon altimetry: Level now falling. *Geophysical Research Letters*, 24(8), 881–884. doi: 10.1029/97GL00809

- Cazenave, A., Palanisamy, H., & Ablain, M. (2018). Contemporary sea level changes from satellite altimetry: What have we learned? What are the new challenges? *Advances in Space Research*, 62(7), 1639–1653. doi: 10.1016/j.asr.2018.07.017
- Chaboureaud, J. P., Chédin, A., & Scott, N. A. (1998). Remote sensing of the vertical distribution of atmospheric water vapor from the TOVS observations: method and validation. *Journal of Geophysical Research Atmospheres*, 103(D8), 8743–8752. doi: 10.1029/98JD00045
- Chander, S., Ganguly, D., Dubey, A. K., Gupta, P. K., Singh, R. P., & Chauhan, P. (2014). Inland water bodies monitoring using satellite altimetry over Indian region. *International Archives of the Photogrammetry, Remote Sensing and Spatial Information Sciences - ISPRS Archives*, XL-8(1), 1035–1041. doi: 10.5194/isprsarchives-XL-8-1035-2014
- Chelton, D. B., Ries, J. C., Haines, B. J., Fu, L.-L., & Callahan, P. S. (2001). Satellite Altimetry. In L. L. Fu & A. Cazenave (Eds.), *Satellite Altimetry and Earth Sciences: A Handbook of Techniques and Applications* (pp. 1–131).
- Cipollini, P., Benveniste, J., Birol, F., Joana Fernandes, M., Obligis, E., Passaro, M., Ted Strub, P., Valladeau, G., Vignudelli, S., & Wilkin, J. (2017). Satellite altimetry in coastal regions. In *Satellite Altimetry Over Oceans and Land Surfaces* (pp. 343–380). doi: 10.1201/9781315151779
- Cipollini, P., Calafat, F. M., Jevrejeva, S., Melet, A., & Prandi, P. (2017). Monitoring Sea Level in the Coastal Zone with Satellite Altimetry and Tide Gauges. *Surveys in Geophysics*, 38(1), 33–57. doi: 10.1007/s10712-016-9392-0
- Coe, M. T., & Birkett, C. M. (2004). Calculation of river discharge and prediction of lake height from satellite radar altimetry: Example for the Lake Chad basin. *Water Resources Research*, 40(10), W102051–W1020511. doi: 10.1029/2003WR002543
- Collecte Localisation Satellites (CLS). (2011). *Surface Topography Mission (STM) SRAL/MWR L2 Algorithms Definition, Accuracy and Specification*. Ramonville St-Agne, France. Retrieved from <https://sentinel.esa.int/web/sentinel/user-guides/sentinel-3-altimetry/document-library/>
- Copernicus Climate Change Service. (n.d.). *Climate Data Store (CDS)*. ERA5: Fifth Generation of ECMWF Atmospheric Reanalyses of the Global Climate. Retrieved from <https://cds.climate.copernicus.eu/cdsapp#!/home>
- Copernicus Climate Change Service (C3S). (2018a). *ERA5 hourly data on pressure levels from 1979 to present*.
- Copernicus Climate Change Service (C3S). (2018b). *ERA5 hourly data on single levels from 1979 to present*. European Union. doi: 10.24381/cds.adbb2d47
- Crétau, J.-F., Bergé-Nguyen, M., Calmant, S., Romanovski, V. V., Meyssignac, B., Perosanz, F., Tashbaeva, S., Arsen, A., Fund, F., Martignago, N., Bonnefond, P., Laurain, O., Morrow, R., & Maisongrande, P. (2013). Calibration of Envisat radar altimeter over Lake Issykkul. *Advances in Space Research*, 51(8), 1523–1541. doi: 10.1016/j.asr.2012.06.039
- Crétau, J.-F., & Birkett, C. (2006). Lake studies from satellite radar altimetry. *Comptes Rendus - Geoscience*, 338(14–15), 1098–1112. doi: 10.1016/j.crte.2006.08.002
- Crétau, J.-F., Calmant, S., Romanovski, V., Perosanz, F., Tashbaeva, S., Bonnefond, P., Moreira, D., Shum, C. K., Nino, F., Bergé-Nguyen, M., Fleury, S., Gegout, P., Del Abarca, R., & Maisongrande, P. (2011). Absolute calibration of Jason radar altimeters from GPS kinematic campaigns over lake Issykkul. *Marine Geodesy*, 34(3–4), 291–318. doi: 10.1080/01490419.2011.585110
- Davis, J. L., Herring, T. A., Shapiro, I. I., Rogers, A. E. E., & Elgered, G. (1985). Geodesy by radio interferometry: Effects of atmospheric modeling errors on estimates of baseline length. *Radio*

Science, 20(6), 1593–1607. doi: 10.1029/RS020i006p01593

- De Angelis, F., Cimini, D., Hocking, J., Martinet, P., & Kneifel, S. (2016). RTTOV-gb - Adapting the fast radiative transfer model RTTOV for the assimilation of ground-based microwave radiometer observations. *Geoscientific Model Development*, 9(8), 2721–2739. doi: 10.5194/gmd-9-2721-2016
- Dee, D. P., Uppala, S. M., Simmons, A. J., Berrisford, P., Poli, P., Kobayashi, S., Andrae, U., Balmaseda, M. A., Balsamo, G., Bauer, P., Bechtold, P., Beljaars, A. C. M., van de Berg, L., Bidlot, J., Bormann, N., Delsol, C., Dragani, R., Fuentes, M., Geer, A. J., ... Vitart, F. (2011). The ERA-Interim reanalysis: configuration and performance of the data assimilation system. *Quarterly Journal of the Royal Meteorological Society*, 137(656), 553–597. doi: 10.1002/qj.828
- Desai, S. D., & Haines, B. J. (2004). Monitoring measurements from the Jason-1 microwave radiometer and independent validation with GPS. *Marine Geodesy*, 27(1–2), 221–240. doi: 10.1080/01490410490465337
- Desportes, C., Obligis, E., & Eymard, L. (2010). One-dimensional variational retrieval of the wet tropospheric correction for altimetry in coastal regions. *IEEE Transactions on Geoscience and Remote Sensing*, 48(3), 1001–1008. doi: 10.1109/TGRS.2009.2031494
- Donlon, C., Berruti, B., Buongiorno, A., Ferreira, M.-H., Féménias, P., Frerick, J., Goryl, P., Klein, U., Laur, H., Mavrocordatos, C., Nieke, J., Rebhan, H., Seitz, B., Stroede, J., & Sciarra, R. (2012). The Global Monitoring for Environment and Security (GMES) Sentinel-3 mission. *Remote Sensing of Environment*, 120, 37–57. doi: <https://doi.org/10.1016/j.rse.2011.07.024>
- Durre, I. (2016). Integrated global radiosonde archive v2. *Dataset Description, Version 1. 0*, 15.
- Durre, I., Yin, X., Vose, R. S., Applequist, S., & Arnfield, J. (2018). Enhancing the data coverage in the integrated Global Radiosonde Archive. *Journal of Atmospheric and Oceanic Technology*, 35(9), 1753–1770. doi: 10.1175/JTECH-D-17-0223.1
- Escudier, P., Couhert, A., Mercier, F., Mallet, A., Thibaut, P., Tran, N., Amarouche, L., Picard, B., Carrere, L., Dibarboue, G., Ablain, M., Richard, J., Steunou, N., Dubois, P., Rio, M.-H., & Dorandeu, J. (2017). Satellite radar altimetry principle, accuracy, and precision. In *Satellite Altimetry Over Oceans and Land Surfaces* (pp. 343–380). doi: 10.1201/9781315151779
- EUMETSAT. (2020). *Copernicus Online Data Access REProcessed (CODAREP)*. Retrieved from <https://codarep.eumetsat.int>
- Eymard, L., Tabary, L., Gerard, E., Boukabara, S., & Cornec, A. Le. (1996). The microwave radiometer aboard ERS-1. II. Validation of the geophysical products. *IEEE Transactions on Geoscience and Remote Sensing*, 34(2), 291–303. doi: 10.1109/36.485108
- Fernandes, M. J., & Lázaro, C. (2016). GPD+ Wet tropospheric corrections for CryoSat-2 and GFO altimetry missions. *Remote Sensing*, 8(10), 851. doi: 10.3390/rs8100851
- Fernandes, M. J., & Lázaro, C. (2018). Independent assessment of Sentinel-3A wet tropospheric correction over the open and coastal ocean. *Remote Sensing*, 10(3), 484. doi: 10.3390/rs10030484
- Fernandes, M. J., Lázaro, C., Ablain, M., & Pires, N. (2015). Improved wet path delays for all ESA and reference altimetric missions. *Remote Sensing of Environment*, 169, 50–74. doi: 10.1016/j.rse.2015.07.023
- Fernandes, M. J., Lázaro, C., Nunes, A. L., Pires, N., Bastos, L., & Mendes, V. B. (2010). GNSS-derived path delay: An approach to compute the wet tropospheric correction for coastal altimetry. *IEEE Geoscience and Remote Sensing Letters*, 7(3), 596–600. doi: 10.1109/LGRS.2010.2042425

- Fernandes, M. J., Lázaro, C., Nunes, A. L., & Scharroo, R. (2014). Atmospheric corrections for altimetry studies over inland water. *Remote Sensing*, 6(6), 4952–4997. doi: 10.3390/rs6064952
- Fernandes, M. J., Lázaro, C., & Vieira, T. (2021). On the Role of the Troposphere in Satellite Altimetry. *Remote Sensing of Environment*, 252. doi: 10.1016/j.rse.2020.112149
- Fernandes, M. J., Nunes, A. L., & Lázaro, C. (2013). Analysis and inter-calibration of wet path delay datasets to compute the wet tropospheric correction for CryoSat-2 over ocean. *Remote Sensing*, 5(10), 4977–5005. doi: 10.3390/rs5104977
- Fernandes, M. J., Pires, N., Lázaro, C., & Nunes, A. L. (2013). Tropospheric delays from GNSS for application in coastal altimetry. *Advances in Space Research*, 51(8), 1352–1368. doi: 10.1016/j.asr.2012.04.025
- Flores, A., Ruffini, G., & Rius, A. (2000). 4D tropospheric tomography using GPS slant wet delays. *Annales Geophysicae*, 18(2), 223–234. doi: 10.1007/s00585-000-0223-7
- Förste, C., Bruinsma, S. L., Abrikosov, Oleg, Lemoine, Jean- Michel, Marty, Jean Charles, Flechtner, F., Balmino, G., Barthelmes, F., & Biancale, R. (2014). EIGEN-6C4 the latest combined global gravity field model including GOCE data up to degree and order 2190 of GFZ Potsdam and GRGS Toulouse. *EIGEN-6C4: The Latest Combined Global Gravity Field Model Including GOCE Data up to Degree and Order 2190 of GFZ Potsdam and GRGS Toulouse*.
- Francis, C. R. (2007). *CryoSat Mission and Data Description; CS-RP-ESA- SY-0059; ESTEC: Noordwijk, The Netherlands*. 82.
- Garner, A. J., Weiss, J. L., Parris, A., Kopp, R. E., Horton, R. M., Overpeck, J. T., & Horton, B. P. (2018). Evolution of 21st Century Sea Level Rise Projections. *Earth's Future*, 6(11), 1603–1615. doi: 10.1029/2018EF000991
- Goddijn-Murphy, L., Woolf, D. K., & Marandino, C. (2012). Space-based retrievals of air-sea gas transfer velocities using altimeters: Calibration for dimethyl sulfide. *Journal of Geophysical Research: Oceans*, 117(8). doi: 10.1029/2011JC007535
- Grody, N. C. (1976). Remote Sensing of Atmospheric Water Content From Satellites Using Microwave Radiometry. *IEEE Transactions on Antennas and Propagation*, 24(2), 155–162. doi: 10.1109/TAP.1976.1141324
- Haines, B. J., & Bar-Sever, Y. E. (1998). Monitoring the TOPEX microwave radiometer with GPS: stability of columnar water vapor measurements. *Geophysical Research Letters*, 25(19), 3563–3566. doi: 10.1029/98GL02757
- Hamlington, B. D., Gardner, A. S., Ivins, E., Lenaerts, J. T. M., Reager, J. T., Trossman, D. S., Zaron, E. D., Adhikari, S., Arendt, A., Aschwanden, A., Beckley, B. D., Bekaert, D. P. S., Blewitt, G., Caron, L., Chambers, D. P., Chandanpurkar, H. A., Christianson, K., Csatho, B., Cullather, R. I., ... Willis, M. J. (2020). Understanding of Contemporary Regional Sea-Level Change and the Implications for the Future. *Reviews of Geophysics*, 58(3). doi: 10.1029/2019RG000672
- Handoko, E., Fernandes, M. J., & Lázaro, C. (2017). Assessment of altimetric range and geophysical corrections and mean sea surface models-Impacts on sea level variability around the Indonesian seas. *Remote Sensing*, 9(2). doi: 10.3390/rs9020102
- Hermozo, L., Eymard, L., Karbou, F., Picard, B., & Pardé, M. (2019). A 1D-Var approach to retrieve Clear-Sky Wet tropospheric correction from current and future altimetry missions. *Journal of Atmospheric and Oceanic Technology*, 36(3), 473–489. doi: 10.1175/JTECH-D-17-0133.1
- Herring, T. A., King, R. W., & McClusky, S. C. (2006). GAMIT Reference Manual – GPS Analysis at MIT - Release 10.3. *Dep. of Earth, Atm. and Planetary Sciences, MIT*.

- Ineichen, D., Gurtner, W., Springer, T., Engelhard, G., Luthardt, J., & Ihde, J. (1999). Euvn-combined gps solution. *Mitteilungen Des Bundesamtes Für Kartographie Und Geodasie*, 23–46.
- IPCC, I. P. on C. C. (2019). *Sea Level Rise and Implications for Low-Lying Islands, Coasts and Communities*. Retrieved from <https://www.ipcc.ch/srocc/chapter/chapter-4-sea-level-rise-and-implications-for-low-lying-islands-coasts-and-communities/>
- Janssen, M. A., Ruf, C. S., & Keihm, S. J. (1995). TOPEX/Poseidon Microwave Radiometer (TMR): II. Antenna Pattern Correction and Brightness Temperature Algorithm. *IEEE Transactions on Geoscience and Remote Sensing*, 33(1), 138–146. doi: 10.1109/36.368214
- Kalakoski, N., Kujanpää, J., Sofieva, V., Tamminen, J., Grossi, M., & Valks, P. (2016). Validation of GOME-2/Metop total column water vapour with ground-based and in situ measurements. *Atmospheric Measurement Techniques*, 9(4), 1533–1544. doi: 10.5194/amt-9-1533-2016
- Keihm, S. J., Janssen, M. A., & Ruf, C. S. (1995). TOPEX/Poseidon Microwave Radiometer (TMR): III. Wet Troposphere Range Correction Algorithm and Pre-Launch Error Budget. *IEEE Transactions on Geoscience and Remote Sensing*, 33(1), 147–161. doi: 10.1109/36.368213
- Kouba, J. (2008). Implementation and testing of the gridded Vienna mapping function 1 (VMF1). *Journal of Geodesy*, 82(4–5), 193–205. doi: 10.1007/s00190-007-0170-0
- Lagler, K., Schindelegger, M., Böhm, J., Krásná, H., & Nilsson, T. (2013). GPT2: Empirical slant delay model for radio space geodetic techniques. *Geophysical Research Letters*, 40(6), 1069–1073. doi: 10.1002/grl.50288
- Lázaro, C., Fernandes, M. J., Vieira, T., & Vieira, E. (2020). A coastally improved global dataset of wet tropospheric corrections for satellite altimetry. *Earth System Science Data Discussions*, 1–31. doi: 10.5194/essd-2019-171
- Legeais, J. F., Ablain, M., & Thao, S. (2014). Evaluation of wet troposphere path delays from atmospheric reanalyses and radiometers and their impact on the altimeter sea level. *Ocean Science*, 10(6), 893–905. doi: 10.5194/os-10-893-2014
- Legeais, J. F., Ablain, M., Zawadzki, L., Zuo, H., Johannessen, J. A., Scharffenberg, M. G., Fenoglio-Marc, L., Fernandes, M. J., Andersen, O. B., Rudenko, S., Cipollini, P., Quartly, G. D., Passaro, M., Cazenave, A., & Benveniste, J. (2018). An improved and homogeneous altimeter sea level record from the ESA Climate Change Initiative. *Earth Syst. Sci. Data*, 10, 281–301. doi: 10.5194/essd-10-281-2018
- Li, W., Yuan, Y., Ou, J., & He, Y. (2018). IGGtrop-SH and IGGtrop-rH: Two improved empirical tropospheric delay models based on vertical reduction functions. *IEEE Transactions on Geoscience and Remote Sensing*, 56(9), 5276–5288. doi: 10.1109/TGRS.2018.2812850
- Li, Z., Muller, J. P., & Cross, P. (2003). Comparison of precipitable water vapor derived from radiosonde, GPS, and Moderate-Resolution Imaging Spectroradiometer measurements. *Journal of Geophysical Research Atmospheres*, 108(20). doi: 10.1029/2003JD003372
- Lillibridge, J., Scharroo, R., Abdalla, S., & Vandemark, D. (2014). One-and two-dimensional wind speed models for ka-band altimetry. *Journal of Atmospheric and Oceanic Technology*, 31(3), 630–638. doi: 10.1175/JTECH-D-13-00167.1
- Liu, Y., Weisberg, R. H., Vignudelli, S., Roblou, L., & Merz, C. R. (2012). Comparison of the X-TRACK altimetry estimated currents with moored ADCP and HF radar observations on the West Florida Shelf. *Advances in Space Research*, 50(8), 1085–1098. doi: 10.1016/j.asr.2011.09.012
- Mendes, V. B. (1999). Modeling the neutral-atmosphere propagation delay in radiometric space techniques. In *Modeling the Neutral-atmosphere Propagation Delay in Radiometric Space*

Techniques. University of New Brunswick, Fredericton, New Brunswick, Canada.

- Mendes, V. B., Prates, G., Santos, L., & Langley, R. B. (2000). An evaluation of the accuracy of models of the determination of the weighted mean temperature of the atmosphere. *ION 2000 National Technical Meeting*, 433–439.
- Miller, M., Buizza, R., Haseler, J., Hortal, M., Janssen, P., & Untch, A. (2010). Increased resolution in the ECMWF deterministic and ensemble prediction systems. *ECMWF Newsl*, 124, 10–16.
- Navarra, A., Stern, W. F., & Miyakoda, K. (1994). Reduction of the Gibbs oscillation in spectral model simulations. *Journal of Climate*, 7(8), 1169–1183. doi: 10.1175/1520-0442(1994)007<1169:ROTG0I>2.0.CO;2
- Niell, A. E., Coster, A. J., Solheim, F. S., Mendes, V. B., Toor, P. C., Langley, R. B., & Upham, C. A. (2001). Comparison of measurements of atmospheric wet delay by radiosonde, water vapor radiometer, GPS, and VLBI. *Journal of Atmospheric and Oceanic Technology*, 18(6), 830–850. doi: 10.1175/1520-0426(2001)018<0830:COMOAW>2.0.CO;2
- Nievinski, F. G., & Santos, M. C. (2010). Ray-tracing options to mitigate the neutral atmosphere delay in GPS. *Geomatica*, 64(2), 191–207.
- Obligis, E., Eymard, L., Tran, N., Labroue, S., & Femenias, P. (2006). First three years of the microwave radiometer aboard Envisat: In-flight calibration, processing, and validation of the geophysical products. *Journal of Atmospheric and Oceanic Technology*, 23(6), 802–814. doi: 10.1175/JTECH1878.1
- Obligis, E., Rahmani, A., Eymard, L., Labroue, S., & Bronner, E. (2009). An improved retrieval algorithm for water vapor retrieval: Application to the envisat microwave radiometer. *IEEE Transactions on Geoscience and Remote Sensing*, 47(9), 3057–3064. doi: 10.1109/TGRS.2009.2020433
- Oziel, L., Baudena, A., Ardyna, M., Massicotte, P., Randelhoff, A., Sallée, J.-B., Ingvaldsen, R. B., Devred, E., & Babin, M. (2020). Faster Atlantic currents drive poleward expansion of temperate phytoplankton in the Arctic Ocean. *Nature Communications*, 11(1). doi: 10.1038/s41467-020-15485-5
- Pacione, R., Pace, B., Vedel, H., De Haan, S., Lanotte, R., & Vespe, F. (2011). Combination methods of tropospheric time series. *Advances in Space Research*, 47(2), 323–335. doi: 10.1016/j.asr.2010.07.021
- Papa, F., Durand, F., Rossow, W. B., Rahman, A., & Bala, S. K. (2010). Satellite altimeter-derived monthly discharge of the Ganga-Brahmaputra River and its seasonal to interannual variations from 1993 to 2008. *Journal of Geophysical Research: Oceans*, 115(12). doi: 10.1029/2009JC006075
- Passaro, M., Rose, S. K., Andersen, O. B., Boergens, E., Calafat, F. M., Dettmering, D., & Benveniste, J. (2018). ALES+: Adapting a homogenous ocean retracker for satellite altimetry to sea ice leads, coastal and inland waters. *Remote Sensing of Environment*, 211, 456–471. doi: 10.1016/j.rse.2018.02.074
- Picard, B., Frery, M. L., Obligis, E., Eymard, L., Steunou, N., & Picot, N. (2015). SARAL/AltiKa Wet Tropospheric Correction: In-Flight Calibration, Retrieval Strategies and Performances. *Marine Geodesy*, 38, 277–296. doi: 10.1080/01490419.2015.1040903
- Quartly, G. D., Nencioli, F., Raynal, M., Bonnefond, P., Garcia, P. N., Garcia-Mondéjar, A., de la Cruz, A. F., Cretaux, J. F., Taburet, N., Frery, M. L., Cancet, M., Muir, A., Brockley, D., Mcmillan, M., Abdalla, S., Fleury, S., Cadier, E., Gao, Q., Escorihuela, M. J., ... Lucas, B. (2020). The roles of the S3MPC: Monitoring, validation and evolution of sentinel-3 altimetry observations. *Remote Sensing*, 12(11). doi: 10.3390/rs12111763
- Roblou, L., Lamouroux, J., Bouffard, J., Lyard, F., Le Hénaff, M., Lombard, A., Marsaleix, P., De Mey, P., & Birol, F. (2011). Post-processing altimeter data towards coastal applications and integration

- into coastal models. In *Coastal Altimetry* (pp. 217–246). doi: 10.1007/978-3-642-12796-0_9
- Ruf, C. S., Dewan, R. P., & Subramanya, B. (1996). Combined microwave radiometer and altimeter retrieval of wet path delay for the geosat follow-on. *IEEE Transactions on Geoscience and Remote Sensing*, 34(4), 991–999. doi: 10.1109/TGRS.1996.508416
- Ruf, C. S., Keihm, S. J., & Janssen, M. A. (1995). TOPEX/Poseidon Microwave Radiometer (TMR): I. Instrument Description and Antenna Temperature Calibration. *IEEE Transactions on Geoscience and Remote Sensing*, 33(1), 125–137. doi: 10.1109/36.368215
- Sahoo, S., Bosch-Lluis, X., Reising, S. C., & Vivekanandan, J. (2015). Radiometric information content for water vapor and temperature profiling in clear skies between 10 and 200 GHz. *IEEE Journal of Selected Topics in Applied Earth Observations and Remote Sensing*, 8(2), 859–871. doi: 10.1109/JSTARS.2014.2364394
- Scharroo, R. (2016). *RADS. RADS Version 4.2.4 User Manual*. Retrieved from <https://github.com/remkos/rads>
- Sharifi, M. A., Forootan, E., Nikkhoo, M., Awange, J. L., & Najafi-Alamdari, M. (2013). A point-wise least squares spectral analysis (LSSA) of the Caspian Sea level fluctuations, using TOPEX/Poseidon and Jason-1 observations. *Advances in Space Research*, 51(5), 858–873. doi: 10.1016/j.asr.2012.10.001
- Sibthorpe, A., Brown, S., Desai, S. D., & Haines, B. J. (2011). Calibration and validation of the Jason-2/OSTM advanced microwave radiometer using terrestrial GPS stations. *Marine Geodesy*, 34(3–4), 420–430. doi: 10.1080/01490419.2011.584839
- Somieski, A., Buerki, B., Geiger, A., Kahle, H.-G., Pavlis, E. C., Becker-Ross, H., Florek, S., & Okruss, M. (2006). Tropospheric water vapor from solar spectrometry and comparison with Jason microwave radiometer measurements. *Journal of Geophysical Research Atmospheres*, 111(9). doi: 10.1029/2005JD005767
- Stum, J. (1994). A comparison between TOPEX microwave radiometer, ERS 1 microwave radiometer, and European Centre for Medium-Range Weather Forecasting derived wet tropospheric corrections. *Journal of Geophysical Research*, 99(C12), 24927–24939. doi: 10.1029/94JC01104
- Stum, J., Sicard, P., Carrère, L., & Lambin, J. (2011). Using objective analysis of scanning radiometer measurements to compute the water vapor path delay for altimetry. *IEEE Transactions on Geoscience and Remote Sensing*, 49(9), 3211–3224. doi: 10.1109/TGRS.2011.2104967
- Sun, J. (1993). Effects of vertical distribution of water vapor and temperature on total column water vapor retrieval error. *Journal of Geophysical Research*, 98(C4), 7069–7079. doi: 10.1029/93jc00010
- Thao, S., Eymard, L., Obligis, E., & Picard, B. (2014). Trend and variability of the atmospheric water vapor: A mean sea level issue. *Journal of Atmospheric and Oceanic Technology*, 31(9), 1881–1901. doi: 10.1175/JTECH-D-13-00157.1
- Thao, S., Eymard, L., Obligis, E., & Picard, B. (2015). Comparison of Regression Algorithms for the Retrieval of the Wet Tropospheric Path. *IEEE Journal of Selected Topics in Applied Earth Observations and Remote Sensing*, 8(9), 4302–4314. doi: 10.1109/JSTARS.2015.2442416
- Timmermans, B. W., Gommenginger, C. P., Dodet, G., & Bidlot, J.-R. (2020). Global Wave Height Trends and Variability from New Multimission Satellite Altimeter Products, Reanalyses, and Wave Buoys. *Geophysical Research Letters*, 47(9). doi: 10.1029/2019GL086880
- Tong, X., Pan, H., Xie, H., Xu, X., Li, F., Chen, L., Luo, X., Liu, S., Chen, P., & Jin, Y. (2016). Estimating water volume variations in Lake Victoria over the past 22 years using multi-mission altimetry and remotely sensed images. *Remote Sensing of Environment*, 187, 400–413. doi:

10.1016/j.rse.2016.10.012

- Tournadre, J. (2006). Improved level-3 oceanic rainfall retrieval from dual-frequency spaceborne radar altimeter systems. *Journal of Atmospheric and Oceanic Technology*, 23(8), 1131–1149. doi: 10.1175/JTECH1897.1
- Tournadre, J., Lambin-Artru, J., & Steunou, N. (2009). Cloud and rain effects on AltiKa/SARAL ka-band radar altimeter-part I: Modeling and mean annual data availability. *IEEE Transactions on Geoscience and Remote Sensing*, 47(6), 1806–1817. doi: 10.1109/TGRS.2008.2010130
- UN, U. N. (2020). *Sustainable Development Goals*. Retrieved from <https://www.un.org/sustainabledevelopment/sustainable-development-goals/>
- Valladeau, G., Thibaut, P., Picard, B., Poisson, J. C., Tran, N., Picot, N., & Guillot, A. (2015). Using SARAL/AltiKa to Improve Ka-band Altimeter Measurements for Coastal Zones, Hydrology and Ice: The PEACHI Prototype. *Marine Geodesy*, 38, 124–142. doi: 10.1080/01490419.2015.1020176
- Vieira, E., Lázaro, C., & Fernandes, M. J. (2019). Spatio-temporal variability of the wet component of the troposphere – Application to satellite altimetry. *Advances in Space Research*, 63(5), 1737–1753. doi: 10.1016/j.asr.2018.11.015
- Vieira, T., Fernandes, M. J., & Lázaro, C. (2018). Analysis and retrieval of tropospheric corrections for CryoSat-2 over inland waters. *Advances in Space Research*, 62(6), 1479–1496. doi: 10.1016/j.asr.2017.09.002
- Vieira, T., Fernandes, M. J., & Lázaro, C. (2019a). Impact of the new ERA5 Reanalysis in the Computation of Radar Altimeter Wet Path Delays. *IEEE Transactions on Geoscience and Remote Sensing*, 57(12), 9849–9857. doi: 10.1109/TGRS.2019.2929737
- Vieira, T., Fernandes, M. J., & Lázaro, C. (2019b). Independent Assessment of On-Board Microwave Radiometer Measurements in Coastal Zones Using Tropospheric Delays from GNSS. *IEEE Transactions on Geoscience and Remote Sensing*, 57(3), 1804–1816. doi: 10.1109/TGRS.2018.2869258
- Vieira, T., Fernandes, M. J., & Lázaro, C. (2019c). Modelling the altitude dependence of the wet path delay for coastal altimetry using 3-D fields from ERA5. *Remote Sensing*, 11(24). doi: 10.3390/rs11242973
- Vignudelli, S., Birol, F., Benveniste, J., Fu, L.-L., Picot, N., Raynal, M., & Roinard, H. (2019). Satellite Altimetry Measurements of Sea Level in the Coastal Zone. *Surveys in Geophysics*, 40(6), 1319–1349. doi: 10.1007/s10712-019-09569-1
- Villadsen, H., Deng, X., Andersen, O. B., Stenseng, L., Nielsen, K., & Knudsen, P. (2016). Improved inland water levels from SAR altimetry using novel empirical and physical retracers. *Journal of Hydrology*, 537, 234–247. doi: 10.1016/j.jhydrol.2016.03.051
- Wentz, F. J. (2013). SSM/I version-7 calibration report. *SSM/I Version-7 Calibration Report*.
- Wessel, P., & Smith, W. H. F. (1996). A global, self-consistent, hierarchical, high-resolution shoreline database. *Journal of Geophysical Research B: Solid Earth*, 101(4), 8741–8743. doi: 10.1029/96jb00104
- Willis, J. K., & Church, J. A. (2012). Regional sea-level projection. *Science*, 336(6081), 550–551. doi: 10.1126/science.1220366
- Witter, D. L., & Chelton, D. B. (1991). A Geosat altimeter wind speed algorithm and a method for altimeter wind speed algorithm development. *Journal of Geophysical Research*, 96(C5), 8853. doi: 10.1029/91JC00414
- WMO, W. M. O. (2020). *The State of the Global Climate 2020*. Retrieved from <https://public.wmo.int/en/our-mandate/climate/wmo-statement-state-of-global-climate>

- Yao, Y. Bin, & Hu, Y. F. (2018). An empirical zenith wet delay correction model using piecewise height functions. *Annales Geophysicae*, 36(6), 1507–1519. doi: 10.5194/angeo-36-1507-2018
- Zakharova, E. A., Kouraev, A. V, Cazenave, A., & Seyler, F. (2006). Amazon River discharge estimated from TOPEX/Poseidon altimetry . *Comptes Rendus - Geoscience*, 338(3), 188–196. doi: 10.1016/j.crte.2005.10.003
- Zhang, Y., Xu, J., Yang, N., Lan, P., Zhang, Y., Xu, J., Yang, N., & Lan, P. (2018). Variability and Trends in Global Precipitable Water Vapor Retrieved from COSMIC Radio Occultation and Radiosonde Observations. *Atmosphere*, 9(5), 174. doi: 10.3390/atmos9050174
- Zhou, C., Lu, J., Hu, Y., & Zelinka, M. D. (2020). Responses of the Hadley circulation to regional sea surface temperature changes. *Journal of Climate*, 33(2), 429–441. doi: 10.1175/JCLI-D-19-0315.1